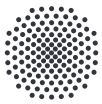

University of Stuttgart
Germany

Dissertation

From ground state properties to high energy spectroscopy:

Extending the application of DMFT for correlated quantum materials

Von der Fakultät Mathematik und Physik der Universität Stuttgart zur Erlangung der Würde eines Doktors der Naturwissenschaften (Dr. rer. nat.) genehmigte Abhandlung

Vorgelegt von

Michael Thobias Schmid

aus Ostfildern

Hauptbericht:	Prof. Dr. Maria Daghofer
Mitbericht:	Prof. Dr. Philipp Hansmann
Prüfungsvorsitz:	Prof. Dr. Hidenori Takagi

Tag der Einreichung:	30. Juni 2020
Tag der mündlichen Prüfung:	27. Juli 2020

Institut für funktionelle Materie und Quantentechnologien

der Universität Stuttgart

2020

Statutory Declaration

I assure that this thesis is a result of my personal work and that no other than the indicated aids have been used for its completion. Furthermore I assure that all quotations and statements that have been inferred literally or in a general manner from published or unpublished writings are marked as such. Beyond this I assure that the work has not been used, neither completely nor in parts, to pass any previous examination.

Stuttgart, 30 June 2020 Michael Schmid

Abstract

Strongly correlated electron systems exhibit rich physical phenomena reaching from superconductivity, Kondo- and, Mott physics to novel magnetic phases, which lie beyond most single-particle approaches such as density functional theory (DFT) or static mean-field theory. For many transition metal oxides (TMOs) such as Ca_2RuO_4 or LiV_2O_4 this is often a result of the partially filled d shells, leading to many-body wave functions, which cannot expressed as a single-slater determinant. Moreover, within this compounds there is often no clear hierarchy of energy scales, e.g. strong spin-orbit coupling, Hund's coupling, and crystal-field splitting, making the description with minimal models difficult. The breakdown of the single-particle picture triggered the development of numerous numerical methods (DMFT, DMRG, VCA, ...) within the last decades, all aimed at tackling the aforementioned phenomena with complementary approximations. One of the most prominent methods for describing real compounds has become dynamical mean-field theory (DMFT), which in many cases has proven to describe local electronic phenomena in good agreement with experimental results.

In this thesis we perform state of the art DFT+DMFT calculations in its single shot approach to complement theoretical $\boldsymbol{k}$-resolved one-particle spectral functions to neutron and x-ray diffraction experiments on Ca_2RuO_4. In the experiment small DC currents were applied to a Ca_2RuO_4 single-crystal resulting in the stabilization of new nonequilibrium phases. Based on experimentally refined structures, DFT calculations are performed to extract a tight binding model by projecting the correlated t_{2g}-subspace onto maximally localized Wannier orbitals. Within our

DMFT calculations spin-orbit coupling (SOC) and the spherical invariant Coulomb interaction are added to calculate spectral functions. The results indicate a semimetallic state with partially gapped Fermi surface in the nonequilibrium phases with elongated RuO_6 octahedra.

Additionally, we extend the DFT+DMFT scheme by a discretization scheme to obtain core-level spectroscopy data, such as XAS or RIXS spectra. This concept is based on the discretization of the DMFT hybridization function to construct an Anderson impurity model of finite bath sites. The discretized model is then extended by the core levels and core-valence interaction. To include sufficiently large amounts of bath sites, despite using an exact diagonalization (ED) solver, we choose the natural orbital basis as the single particle basis of choice to compute RIXS and XAS spectra.

Inhaltsangabe

Stark korrelierte Elektronensysteme besitzen eine Vielzahl an Phänomenen, die mittels herkömmlicher Einteilchennäherunge, wie Bandstrukturrechnungen nicht erklärt werden können. Prominente Beispiele sind etwa Supraleitung, Kondo- und Mottphysik oder neuartige magnetische (exitonische) Phasen, wie sie gerade in Übergangsmetalloxiden (sogenannten TMOs), wie Ca_2RuO_4 oder LiV_2O_4, zu finden sind. Die Ursache dieser ist häufig durch das Auftreten konkurrierender Energieskalen, bspw. zwischen Kristallfeldaufspaltung, Spin-Bahnkopplung und Hund's Kopplung, begründet. Neuartige numerische Methoden, wie sie etwa in den letzten Jahrzehnten entwickelt wurden, sind daher unabdingbar um den physikalischen Ursachen auf den Grund zu gehen. Eine dieser Methoden, die in den letzen Jahren an Popularität gewonnen hat, ist die dynamische Molekularfeldtheorie (DMFT). Ihr entscheidender Erfolg liegt darin, dass in vielen Fällen die experimentelle Sachlage von lokalen elektronischen Phänomenen gut reproduziert werden konnte.

In der vorliegenden Arbeit werden ausgehend von DFT+DMFT Rechnungen $\boldsymbol{k}$-aufgelöste einteilchen Spektralfunktionen für Ca_2RuO_4 untersucht und anschließend mit experimentellen Befunden verglichen. Neue Röntgen-und Neutronenbeugung-experimente legen nahe, dass unter anliegen eines schwachen Gleichstromes neue Nichtgleichgewichtsphasen von Ca_2RuO_4 stabilisiert werden können. Ausgehend von den experimentellen Strukturdaten werden Bandstrukturrechnungen mit anschließender Projektion auf sogenannte Wannierorbitale ausgeführt. Diese erlauben

es ein effektives t_{2g} Modell zu konstruieren, welches dann Ausgangspunkt einer DMFT Rechnung ist. Unsere Ergebnisse zeigen, dass einer der Nichtgleichgewichtsphasen einen semimetallischen Zustand, mit einer partiell isolierender Fermifläche anstrebt.

Zusätzlich wird das DFT+DMFT Verfahren zur Bestimmung von röntenspektroskopischen Methoden, wie XAS und RIXS, herangezogen. Hierzu wird die DMFT Hybridisierungsfunktion diskretisiert um das darunterliegende Anderson-Störstellen-Modell für eine endliche Anzahl an Bädern zu konstruieren. Das Modell wird anschließen mit den fehlenden Kernniveaus, sowie einer Kern-Valenz Wechselwirkung ergänzt um mittels eines exakten Diagonalisierungsverfahren die XAS und RIXS Spektren zu berechnen.

Contents

Chapter 1 Introduction

"Whether we like it or not, modern ways are going to alter and in part destroy traditional customs and values."

Werner Heisenberg (1901-1976)

The beginning of quantum theory goes back to the beginning of the twentieth century, where Max Plank first introduced the concept of quantized energy levels to describe the black body radiation spectrum [1]. Planck's formula was actually so successful that it absolutely matched Rubens latest measurement [2]. A concept which Einstein a bit later transferred (in 1905) to describe the photoelectric effect, where he concluded that light can be interpreted as quanta of specific energy [3]. The new concept sparked new experiments, like the famous Stern-Gerlach experiments investigating the magnetic moments of silver atoms [4], the discovery of the Compton effect in 1923 [5] and ultimatively lead to the formulation of modern quantum mechanics itself by Heisenberg in 1925 to 1927 [6, 7]. One year earlier Schrödinger found his famous equation [8]

$$i\hbar \frac{d}{dt} |\psi(t)\rangle = \hat{\mathcal{H}} |\psi(t)\rangle , \tag{1.1}$$

from which he successfully derived the stationary states of the Hydrogen atom as eigenvalues. From this it became clear that describing microscopic systems like

atoms, molecules or solids, with classical physics is not working, since the fundamental laws behind or experiments cannot be explained correctly. Heisenberg's quantum mechanics, however, can [9].

While classical physics assigns each particle a momentum vector $\boldsymbol{p}$ and position vector $\boldsymbol{r}$ spanning the phase space, quantum mechanics on the other hand introduces the concept of particle-wave dualism [10], where particles are described by many-body wave functions of the corresponding Hilbert space $|\psi\rangle \in H$, and observables $\hat{A}$ as linear, hermitian operators. Moreover the wave function can only be interpreted in statistical terms, as the overlap with another wave function $\langle\phi|\psi\rangle$ gives the probability of observing the state $|\phi\rangle$ given $|\psi\rangle$. This also implies that the product of a wave function $\psi(\boldsymbol{r},t)$ with its complex conjugate $\psi^*(\boldsymbol{r},t)$ is the position probability density $W(\boldsymbol{r},t) = \psi(\boldsymbol{r},t)\psi^*(\boldsymbol{r},t)$, which is normalized to $\int W(\boldsymbol{r},t)\,\mathrm{d}\boldsymbol{r} = 1$ [11–14].

Another difference to the classical description manifests, especially when many quantum particles are considered, namely the indistinguishably of identical particles and the resulting spin-statistics theorem [15]. As a result particles with integer spin are framed bosons and their wave functions are symmetric under exchange of particles or permutation. Particles with half-integer spin are called fermions, whose wave function is antisymmetric under permutation. The corresponding statistics are the boson- or fermi-static. Within the framework of second quantization this is implemented by using the commutator or anticommutator.

1.1 The many-body problem

When systems with sufficiently more than one or two particles are considered, one typically speaks of many-body systems. In these systems the particles can interact with each other. Archetypal examples for many-body problems are solids. Ideal solids consist of positively charged nuclei with negative electrons embedded in a crystalline lattice. The corresponding many-body Hamiltonian can then be sorted

into electron-, ion- and electron-ion part, i.e.

$$\mathcal{H} = \mathcal{H}_\mathrm{e} + \mathcal{H}_\mathrm{i} + \mathcal{H}_\mathrm{ie}, \tag{1.2a}$$

$$\mathcal{H}_\mathrm{e} = -\sum_{i=1}^{N_\mathrm{e}} -\frac{\hbar}{2m}\nabla_{\boldsymbol{r}_i}^2 + \frac{1}{2}\sum_{i\neq j} V_\mathrm{e}(\boldsymbol{r}_i - \boldsymbol{r}_j), \tag{1.2b}$$

$$\mathcal{H}_\mathrm{i} = -\sum_{i=1}^{N_\mathrm{i}} \frac{\hbar}{2M}\nabla_{\boldsymbol{R}_i}^2 + \frac{1}{2}\sum_{i\neq j} V_\mathrm{i}(\boldsymbol{R}_i - \boldsymbol{R}_j), \tag{1.2c}$$

$$\mathcal{H}_\mathrm{ie} = \sum_{i=1}^{N_\mathrm{e}}\sum_{j=1}^{N_\mathrm{i}} V_\mathrm{ie}(\boldsymbol{r}_i - \boldsymbol{R}_j). \tag{1.2d}$$

Here N_e (N_i) is the number of electrons (ions) in the system, m (M) the electron (ion) mass, and $\boldsymbol{r}_i$ ($\boldsymbol{R}_i$) are the coordinates of the electrons (ions). The subscript of the Coulomb interaction $V(\bullet)$ indicates the electron-electron (ee), ion-ion (i), or electron-ion (ie) interaction term. Although relativistic effects are neglected, many-body Hamiltonians of the form (1.2a) describe the physical problem quite extensively. Of course, there are compounds where for example spin-orbit coupling is quite strong and hence must be included into the Hamiltonian. The only drawback when trying to solve the stationary Schrödinger equation is the sheer number of coupled equation. Even numerically this task is already for minor problems cumbersome and one has to resort to approximations. The first approximation we consider is the Born-Oppenheimer approximation, which takes into account that the ion mass is rather big compared to the electron mass $M/m \sim 10^4$, so the wave function can be factorized into an electron and ionic part. When the ions are also treated as static, i.e. no lattice vibrations, Hamiltonian (1.2a) can be reduced to the form

$$\begin{aligned}\mathcal{H} = \sum_\sigma \int \mathrm{d}\boldsymbol{r}\, \psi_\sigma^\dagger(\boldsymbol{r}) \left[-\frac{\hbar^2\boldsymbol{\nabla}^2}{2m_\mathrm{e}} + \sum_\ell \frac{-e^2}{4\pi\varepsilon_0}\frac{Z_\ell}{|\boldsymbol{r}-\boldsymbol{R}_\ell|}\right]\psi_\sigma(\boldsymbol{r}) \\ + \frac{1}{2}\sum_{\sigma,\sigma'}\int \mathrm{d}\boldsymbol{r}\,\mathrm{d}\boldsymbol{r}'\psi_\sigma^\dagger(\boldsymbol{r})\psi_{\sigma'}^\dagger(\boldsymbol{r}')\left[\frac{e^2}{4\pi\varepsilon_0}\frac{1}{|\boldsymbol{r}-\boldsymbol{r}'|}\right]\psi_{\sigma'}(\boldsymbol{r}')\psi_\sigma(\boldsymbol{r}),\end{aligned} \tag{1.3}$$

when expressed in field-operators $\hat{\psi}^\dagger(\boldsymbol{r})$. Under this assumption the electron-ion interaction part is lattice periodic and becomes a constant. Instead of solving the Hamiltonian in the full configuration space one only needs to take into account

the primitive unit cell. In that sense solids can then be understood as a sequence of infinite repeating unit cells. Nonetheless this Hamiltonian, which now only describes the pure electronic problem, still inherits the same problems from the previous Hamiltonian (1.2a), i.e. there are still to many degrees of freedom to solve the general case.

1.2 Localized and itinerant electrons

The electronic Hamiltonian, as given in equation (1.3), can be further split into a Hamiltonian of the form $\mathcal{H} = \mathcal{H}_0 + \mathcal{H}_{\text{int}}$, where $\mathcal{H}_0$ contains only the single-particle terms (first line) and $\mathcal{H}_{\text{int}}$ two-particle terms (bottom line). It can be shown that the eigenfunctions of $\mathcal{H}_0$ are given by Bloch functions $\psi_{n,\boldsymbol{k}} = \mathrm{e}^{\mathrm{i}\boldsymbol{k}\boldsymbol{r}} u_{n,\boldsymbol{k}}(\boldsymbol{r})$, where n labels the band index, $\boldsymbol{k}$ the quasi-momentum and $u_{n,\boldsymbol{k}}(\boldsymbol{r})$ is a lattice periodic function. The bandstructure of a system is then a result of the corresponding discrete set of eigenvalues $\varepsilon_n(\boldsymbol{k})$. Describing the formation of bands with Bloch states is sometimes called free electron approximations and stresses the itinerant nature of electrons. The opening of a gap or description of a band insulator then follow the treatment of independent, noninteracting electrons in the presence of a weak lattice periodic potential [16, 17].

The localized nature of electrons is taken into account within the tight-binding approximations, especially for d orbitals in transition metal oxides this description seems to be a suitable starting point. The approach considers so called localized Wannier functions, which are technically Fourier transformed Bloch function. The Wannier functions describe orbitals centered around a lattice site $\boldsymbol{R}_i$, which rapidly decay when going further away from it. The movement of electrons from one electron site to another is then described by a hopping amplitude $t^{ii'}_{m\sigma,m'\sigma}$. Using this basis and the framework of second quantization then allows us to rewrite the

Hamiltonian in the form

$$\mathcal{H}_0 = -\sum_{ii'}\sum_{\sigma,\sigma'}\sum_{mm'} t^{ii'}_{m\sigma,m'\sigma'} c^\dagger_{im\sigma} c_{i'm'\sigma'}, \tag{1.4a}$$

$$\mathcal{H}_{\text{int}} = \frac{1}{2}\sum_{ii'jj'}\sum_{\sigma,\sigma'}\sum_{mm'}\sum_{pp'} U^{mpm'p'}_{ii'jj'} c^\dagger_{im\sigma} c^\dagger_{i'p\sigma'} c_{j'p'\sigma'} c_{jm'\sigma}, \tag{1.4b}$$

where $c^\dagger$ and c are the creation and annihilation operator of an electron in the Wannier basis, σ the spin index, i, j the lattice sites, and m, p the band index. The Coulomb interaction is represented by the tensor U, whose actual values are given by the above overlap integrals. Hamiltonian (1.4a) is conventionally called a tight-binding Hamiltonian of the full lattice. As we will see later (chapter 5.1) by assuming $i = i' = j = j'$ one realizes the well known Hubbard model [18], which already inherits a plethora of phenomena observed in solids.

1.3 Solving the many-body problem?

Although the original Hamiltonian (1.2a) was reduced to a generalized form of the Hubbard model, we still need a method allowing us to solve the Hamiltonian. At this point it should also be stressed that for a numerical treatment solving does not mean that we want to calculate all eigenenergies or eigenvectors, since this is not possible. However, the computation of the groundstate or the lowest excited states already allow access to quantities which can be compared to experiments. One of the most used methods in solid state physics in order to gain a first understanding of experimentally obtained data is probably density functional theory (DFT). DFT reduces the complexity of solving the many-body Hamiltonian to a set of coupled single-particle Schrödinger equations. Unfortunately, this comes at the cost of loosing all information about excited states, so only ground state properties are accessible [19]. Moreover, DFT tends to underestimate the localized nature of electrons. When working with transition metal oxides the localization, stemming from strong correlation, is quite important, especially for trying to understand so called Mott insulators [20].

Instead of advancing from the ab inito side (e.g. DFT) to tackle the many-body problem, one can search for minimal models which describe specific physical phenomena, e.g. Mott physics, correctly. One of most prominent models is probably the Hubbard model, which describes the hopping of electrons on a lattice in presence of a local Coulomb interaction. It should, however, be stressed that despite its simplicity the Hubbard model – or also other models – are still not analytically solvable. This requires capable numerical methods such as dynamical mean-field theory (DMFT), which gives an exact solution of the Hubbard model in infinite dimensions (see chapter 5). Within this $d \to \infty$ limit it was shown that the Hubbard model can be mapped onto an Anderson impurity model [21] and solved selfconsistently [22]. Although this method, is well suited to describe local electronic physics and Mott physics one needs to find the relevant model parameters – hoppings t and interaction values U – in order to describe real materials.

To get the best of both worlds, ab initio and minimal models, one can combine DFT and DMFT into a method known as DFT+DMFT. Within the last decades this combination has become quite popular and successfully applied to real materials. The idea of DFT+DMFT approach is to derive the material specific parameters for real compounds with DFT, e.g. by Wannier projections [23], to construct a multi-orbital Hubbard model, which is then slefconsistently solved via DMFT. Within this thesis we use the DFT+DMFT approach to obtain one-particle spectral functions for Ca_2RuO_4 and LiV_2O_4 (see chapter 6 and 7).

1.4 Structure of this thesis

This thesis is structured in two parts. The first part mainly discusses fundamental concepts and methods, reaching from density functional theory, Wannier projections, Green's functions to transition metal oxides, and crystal-field theory. Since the level-splitting in presence of a crystal-field is important it will be discussed in more detail for a cubic, tetragonal, orthorombic and trigonal crystal-field for a d^1

configuration.

The second part of the thesis starts with the concepts of dynamical mean-field theory and a short discussion of the analytical continuation, which is needed when performing calculations on the Matsubara axis and then going back to the real axis. The subsequent chapter investigates properties of Ca_2RuO_4 and is one of the main parts of this thesis. The chapter elaborates on the calculations covering most of the theoretical work published in [24]. Multiple DFT+DMFT calculations were performed to support our experimental collaborators with high quality data for recent experiments investigating the stabilization of nonequilibrium phases when small DC currents are applied. Further figures covering this material can be found in appendix C. Chapter 7 discusses how DMFT calculations can be extended to obtain core-level spectroscopic spectra, e.g. XAS or RIXS. Following a recent publication [25] we extend the discretization scheme to the natural orbital basis, which allows us to restrict the configuration space quite severely, so an exact diagonalization solver can be applied. The discretization scheme is then successfully tested for the Bethe model and the two dimensional Hubbard model. In a last attempt we try to apply this scheme to LiV_2O_4 in order to obtain XAS and RIXS spectra.

Within the appendices A to D further figures concerning Ca_2RuO_4, LiV_2O_4 are shown. Moreover a brief introduction into core-level spectroscopic methods such as XAS and RIXS are presented to support the underlying formulas and discussions in the main chapters.

Part I.

Basics

Chapter 2 From density functional theory to minimal models

2.1 Absolute basics

The following section is based on the textbooks [14, 26, 27].

2.1.1 Quantum statistics

Starting from the Hamiltonian of N_e electrons in the presence of a potential $V(\boldsymbol{r}_i)$, i.e., just one-particle interactions,

$$H_0 = \sum_{i=1}^{N_e} \frac{\boldsymbol{p}_i^2}{2m} + V(\boldsymbol{r}_i) \tag{2.1a}$$

$$= \sum_{k\sigma} \varepsilon(k) c_{k\sigma}^\dagger c_{k\sigma} \tag{2.1b}$$

often the properties of the system in thermodynamic equilibrium and its excitations out of it are of great interest. Quantum statistics provides us with the mathematical tools how to describe this. Rather than introducing the whole topic, we restrict ourselves to the important features and the grand-canonical ensemble, i.e., neither the energy nor the the particle number of a system is fixed. Instead of these the chemical potential μ and the inverse temperature $\beta = 1/(k_\mathrm{B}T)$ are specified. Consequently the Hamiltonian from above is extended by an additional chemical

potential part

$$\mathcal{H} = H_0 - \mu\hat{N}, \tag{2.2}$$

where $\hat{N}$ is the total number operator $\hat{N} = \sum_{i\sigma} \hat{n}_{i\sigma}$.

When dealing with quantum systems consisting of many particles the description of pure quantum states ψ, as in the single-particle quantum mechanics, is often not valid since we are dealing with situations where often it is a priori not clear which particular state describes the whole system. Instead it is common to introduce the concept of mixed states, i.e., a statistical ensemble of quantum states. The density operator $\hat{\varrho}$ which is defined as

$$\hat{\varrho} \equiv \mathrm{e}^{-\beta\mathcal{H}} \tag{2.3}$$

then describes the quantum system in this mixed state. Since the Hamiltonian–given a specific choice of basis–can be expressed as a matrix, so can the density operator, justifying the framing as density matrix. Additionally the partition function Ξ, which shows the statistical properties of the quantum system, can be defined via

$$\Xi \equiv \mathrm{tr}\left[\varrho\right] = \mathrm{tr}\left[\mathrm{e}^{-\beta\mathcal{H}}\right], \tag{2.4}$$

Armed with these it is possible to express the grand-canonical potential Ω as

$$\Omega = -\frac{1}{\beta}\ln\Xi. \tag{2.5}$$

It is a characteristic state function for the grand-canonical ensemble, from whom we can derive all thermodynamic quantities.

Since every observable A in quantum mechanics can be written as an operator $\hat{A}$, the expectation value on a statistical ensemble is then given by

$$\langle\hat{A}\rangle = \frac{\mathrm{tr}\left[\hat{A}\hat{\varrho}\right]}{\Xi}. \tag{2.6}$$

2.1.2 Field-operators

In the framework of second quantization it is also possible to express many-body Hamiltonians with so called field-operators, which are defined as

$$\hat{\psi}_\sigma(\boldsymbol{r}) = \sum_i \phi_i(\boldsymbol{r})\hat{a}_{i\sigma}, \tag{2.7a}$$

$$\hat{\psi}_\sigma(\boldsymbol{r}) = \int \mathrm{d}\alpha\, \phi_\alpha(\boldsymbol{r})\hat{a}_{\alpha\sigma}, \tag{2.7b}$$

where $\hat{a}_{i\sigma}$ annihilates a particle of spin σ and the single-particle wavefunction $\phi_i(\boldsymbol{r}) = \langle \boldsymbol{r}|i\rangle$. Hence a field-operator annihilates or creates a particle at the position $|\boldsymbol{r}\rangle$. The following relations are valid

$$[\hat{\psi}_\sigma(\boldsymbol{r}),\hat{\psi}_{\sigma'}(\boldsymbol{r}')]_\pm = [\hat{\psi}^\dagger_\sigma(\boldsymbol{r}),\hat{\psi}^\dagger_{\sigma'}(\boldsymbol{r}')]_\pm = 0, \tag{2.8a}$$

$$[\hat{\psi}_\sigma(\boldsymbol{r}),\hat{\psi}^\dagger_{\sigma'}(\boldsymbol{r}')]_\pm = \delta_{\sigma,\sigma'}\delta(\boldsymbol{r}-\boldsymbol{r}'). \tag{2.8b}$$

The $\pm$ in the subscript indicates that when working with fermion systems the anti-commutator must be used. On the other hand for bosonic systems the commutator is applied.

2.1.3 Consequences

Let $\mathcal{H}$ be the electronic Hamiltonian of a solid, i.e. describing the behavior of electrons in presence of Coulomb interaction and a lattice periodic potential. Then $\mathcal{H}$ can be split in a single-particle part and a multi-particle (here two-particle) part

$$\mathcal{H} = \mathcal{H}_\mathrm{T} + \mathcal{H}_\mathrm{V} + \mathcal{H}_\mathrm{C} \tag{2.9a}$$

$$= \underbrace{\sum_{i=1}^{N}\left(-\frac{\hbar^2}{2m}\boldsymbol{\nabla}_i^2 + V_\mathrm{ext}(\boldsymbol{r}_i)\right)}_{\text{single-particle part}} + \underbrace{\frac{1}{2}\sum_{i\neq j}^{N}\frac{e^2}{4\pi\varepsilon_0}\frac{1}{|\boldsymbol{r}_i-\boldsymbol{r}_j|}}_{\text{two-particle part}}. \tag{2.9b}$$

Expressed in field-operators we find

$$\mathcal{H}_{\mathrm{T}} = \int \mathrm{d}\boldsymbol{r}\, \hat{\psi}^{\dagger}(\boldsymbol{r}) \left[-\frac{\hbar^2}{2m} \boldsymbol{\nabla}_r^2 \right] \hat{\psi}(\boldsymbol{r}), \tag{2.10a}$$

$$\mathcal{H}_{\mathrm{V}} = \int \mathrm{d}\boldsymbol{r}\, V(\boldsymbol{r}) \hat{\psi}^{\dagger}(\boldsymbol{r}) \hat{\psi}(\boldsymbol{r}), \tag{2.10b}$$

$$\mathcal{H}_{\mathrm{C}} = \frac{1}{2} \frac{e^2}{4\pi\varepsilon_0} \int \mathrm{d}\boldsymbol{r} \int \mathrm{d}\boldsymbol{r}'\, \hat{\psi}^{\dagger}(\boldsymbol{r}) \hat{\psi}^{\dagger}(\boldsymbol{r}') \frac{1}{|\boldsymbol{r} - \boldsymbol{r}'|} \hat{\psi}(\boldsymbol{r}') \hat{\psi}(\boldsymbol{r}). \tag{2.10c}$$

The particle-density operator can also be expressed via field-operators

$$\hat{n}(\boldsymbol{r}) = \sum_{i=1}^{N} \delta(\boldsymbol{r} - \boldsymbol{r}_i) = \hat{\psi}^{\dagger}(\boldsymbol{r}) \hat{\psi}(\boldsymbol{r}), \tag{2.11}$$

so we can rewrite equation (2.10b) as

$$\mathcal{H}_{\mathrm{V}} = \int \mathrm{d}\boldsymbol{r}\, V(\boldsymbol{r}) \hat{n}(\boldsymbol{r}). \tag{2.12}$$

Let us define the expectation value of (2.11) as

$$n(\boldsymbol{r}) \equiv \langle \psi | \hat{n}(\boldsymbol{r}) | \psi \rangle\,, \tag{2.13}$$

then equation (2.12) can be rewritten to

$$\langle \mathcal{H}_{\mathrm{V}} \rangle = \int \mathrm{d}\boldsymbol{r}\, V(\boldsymbol{r}) n(\boldsymbol{r}), \tag{2.14}$$

which will be later used extensively. In this form the expectation value of the single-particle potential can be interpreted as a functional of the particle density, i.e. so called density functional

$$V[n(\boldsymbol{r})] \equiv \langle \mathcal{H}_{\mathrm{V}} \rangle\,. \tag{2.15}$$

2.2 Density Functional Theory (DFT)

Solving many-electron systems in general is not possible, at least not analytically. Therefore approximation methods are inevitable to capture at least the correct physics qualitatively. Probably the most prominent approximation are Hartree-Fock

or mean-field approximations. According to this approximation we start with the product of two operators

$$AB = (A - \langle A\rangle)(B - \langle B\rangle) + A\langle B\rangle + \langle A\rangle B - \langle A\rangle\langle B\rangle$$

and linearize it

$$AB \xrightarrow{\text{HF}} A\langle B\rangle + \langle A\rangle B - \langle A\rangle\langle B\rangle\,,$$

so no fluctuations around thermodynamic expectation values or higher correlations are included [14].

The basic idea of DFT is to express the groundstate properties of a system of electrons in an external field as functionals of the groundstate electron density.

2.2.1 Hohenberg-Kohn theorems

In order to derive the DFT functional, two important theorems – which will be proven subsequently – are of great importance. The discussion will follow [26–28].

The Hohenberg-Kohn theorems typically are known under the following formulation:

1. The groundstate energy of a many-body system (nondegenerate) is a unique functional of the particle density

$$E_0 = E[n_0(\boldsymbol{r})]. \tag{2.16}$$

2. The functional $E[n(\boldsymbol{r})]$ has its minimum relative to variations $\delta n(\boldsymbol{r})$ of the particle density at the equilibrium density $n_0(\boldsymbol{r})$

$$E_0 = E[n_0(\boldsymbol{r})] = \min E[n(\boldsymbol{r})], \qquad \left.\frac{\delta E[n(\boldsymbol{r})]}{\delta n(\boldsymbol{r})}\right|_{n(\boldsymbol{r})=n_0(\boldsymbol{r})} = 0. \tag{2.17}$$

Subsequently, both theorems will be proven. The first theorem is proven by contradiction. Assume the many-body Hamiltonian given in equation (2.9a). Here we use a slightly different notation, namely

$$\mathcal{H} = \mathcal{H}_\text{T} + \mathcal{H}_\text{V} + \mathcal{H}_\text{C} \equiv T + V + U. \tag{2.18}$$

The groundstate energy is given via

$$E_0 = \langle \psi_0 | \mathcal{H} | \psi_0 \rangle \,, \tag{2.19}$$

with the corresponding density

$$n_0(\boldsymbol{r}) = |\psi_0(\boldsymbol{r})|^2. \tag{2.20}$$

Now we want to show that this is unique, i.e., there is no other groundstate leading to the same density. Hence assume that there is another groundstate $|\psi_0'\rangle$ with the same particle density

$$n_0(\boldsymbol{r}) = |\psi_0(\boldsymbol{r})|^2 = |\psi_0'(\boldsymbol{r})|^2 = n_0'(\boldsymbol{r}). \tag{2.21}$$

If $|\psi_0\rangle \neq |\psi_0'\rangle$ and there is no degeneracy then both groundstates belong to different Hamiltonians $\mathcal{H}$ and $\mathcal{H}'$. However, due to the constant number of electrons in the system the kinetic part and the exchange part of the Hamiltonians are equal, i.e., only the single-particle potentials V, V' are allowed to be different $V \neq V'$. From the variational principle of quantum mechanics it follows that

$$\begin{aligned} E_0 = \langle \psi_0 | \mathcal{H} | \psi_0 \rangle &< \langle \psi_0' | \mathcal{H} | \psi_0' \rangle \\ &= \langle \psi_0' | \mathcal{H}' - V' + V | \psi_0' \rangle \\ &= E_0' + \langle \psi_0' | V - V' | \psi_0' \rangle \\ &= E_0' + \int \mathrm{d}\boldsymbol{r} \, \big(V(\boldsymbol{r}) - V'(\boldsymbol{r}) \big) \, n_0'(\boldsymbol{r}). \end{aligned} \tag{2.22}$$

Changing $\mathcal{H}'$ with $\mathcal{H}$ gives

$$E_0' < E_0 + \int \mathrm{d}\boldsymbol{r} \, \big(V'(\boldsymbol{r}) - V(\boldsymbol{r}) \big) \, n_0(\boldsymbol{r}). \tag{2.23}$$

Adding equation (2.22) and (2.23) leads to the contradiction (note that $n_0 = n_0'$)

$$\begin{aligned} E_0 + E_0' &< E_0' + E_0 + \int \mathrm{d}\boldsymbol{r} \underbrace{\big(V(\boldsymbol{r}) - V'(\boldsymbol{r}) + V'(\boldsymbol{r}) - V(\boldsymbol{r}) \big)}_{=0} n_0(\boldsymbol{r}), \\ E_0 + E_0' &< E_0' + E_0, \end{aligned} \tag{2.24}$$

which proofs the theorem.

The second theorem is proven by using the variational principle. One starts by defining the functionals

$$F[n(\boldsymbol{r})] \equiv \langle\psi|T+U|\psi\rangle\,,$$
$$E[n(\boldsymbol{r})] \equiv F[n(\boldsymbol{r})] + \int \mathrm{d}\boldsymbol{r}\, V(\boldsymbol{r})n(\boldsymbol{r}).$$

Then is follows

$$\begin{aligned} E[n'(\boldsymbol{r})] &= \langle\psi'|T+U|\psi'\rangle + \langle\psi'|V|\psi'\rangle \\ &= F[n'(\boldsymbol{r})] + \int \mathrm{d}\boldsymbol{r}\, V(\boldsymbol{r})n'(\boldsymbol{r}) \end{aligned}$$

using the variational principle

$$\begin{aligned} F[n'(\boldsymbol{r})] + \int \mathrm{d}\boldsymbol{r}\, V(\boldsymbol{r})n'(\boldsymbol{r}) &> \langle\psi_0|T+U|\psi_0\rangle + \langle\psi_0|V|\psi_0\rangle \\ &= F[n_0(\boldsymbol{r})] + \int \mathrm{d}\boldsymbol{r}\, V(\boldsymbol{r})n_0(\boldsymbol{r}), \end{aligned}$$

which implies

$$E[n'(\boldsymbol{r})] > F[n_0(\boldsymbol{r})] + \int \mathrm{d}\boldsymbol{r}\, V(\boldsymbol{r})n_0(\boldsymbol{r}) = E[n_0(\boldsymbol{r})].$$

Hence

$$E_0 = E[n_0(\boldsymbol{r})] = \min E[n(\boldsymbol{r})], \qquad \left.\frac{\delta E[n(\boldsymbol{r})]}{\delta n(\boldsymbol{r})}\right|_{n(\boldsymbol{r})=n_0(\boldsymbol{r})} = 0,$$

which proofs the theorem.

Armed with this, the whole density functional $E[n(\boldsymbol{r})]$ can be seperated into three parts

$$E[n(\boldsymbol{r})] = T[n(\boldsymbol{r})] + V[n(\boldsymbol{r})] + U[n(\boldsymbol{r})], \tag{2.25}$$

with

$$T[n(\boldsymbol{r})] = \langle\psi|T|\psi\rangle\,, \tag{2.26a}$$
$$V[n(\boldsymbol{r})] = \langle\psi|V|\psi\rangle = \int \mathrm{d}\boldsymbol{r}\, V(\boldsymbol{r})n(\boldsymbol{r}), \tag{2.26b}$$
$$U[n(\boldsymbol{r})] = \langle\psi|U|\psi\rangle\,. \tag{2.26c}$$

Although only trivial functionals such as in equation (2.26b) are known one might think that

$$U[n(\boldsymbol{r})] = \frac{e^2}{4\pi\varepsilon_0}\int \mathrm{d}\boldsymbol{r}\int \mathrm{d}\boldsymbol{r}'\,\frac{n(\boldsymbol{r})n(\boldsymbol{r}')}{|\boldsymbol{r}-\boldsymbol{r}'|}, \tag{2.27}$$

which is just the Hartree part (known from classical electrodynamics), i.e., electron-electron interaction. Exchange interactions and further correlations are still missing. Insead we use for equation (2.26c) the ansatz

$$\begin{aligned} U[n(\boldsymbol{r})] &= \frac{e^2}{4\pi\varepsilon_0}\int \mathrm{d}\boldsymbol{r}\int \mathrm{d}\boldsymbol{r}'\,\frac{n(\boldsymbol{r})n(\boldsymbol{r}')}{|\boldsymbol{r}-\boldsymbol{r}'|} + E_{\mathrm{XC}}[(n(\boldsymbol{r})] \\ &= V_{\mathrm{ee}}[n(\boldsymbol{r})] + E_{\mathrm{XC}}[(n(\boldsymbol{r})], \end{aligned} \tag{2.28}$$

where $E_{\mathrm{XC}}[(n(\boldsymbol{r})]$ is the exchange and correlation energy. Hence the whole DFT functional is

$$E[n(\boldsymbol{r})] = \underbrace{T[n(\boldsymbol{r})] + E_{\mathrm{XC}}[n(\boldsymbol{r})]}_{\text{still unknown}} + \underbrace{V_{\mathrm{ee}}[n(\boldsymbol{r})] + V[n(\boldsymbol{r})]}_{\text{known}}. \tag{2.29}$$

2.2.2 Kohn-Sham equations

The remaining task is now to find an expression for the functional

$$F[n(\boldsymbol{r})] \equiv \langle\psi|T+U|\psi\rangle\,, \tag{2.30}$$

which remains till today a challenging task.

In order to derive the important equations we here to follow the work of Kohn and Sham [28] and [26] to approximate the kinetic part of the functional.

1. We start with the introduction of an alternative noninteracting many-body system of the form

$$\mathcal{H} = \sum_{i=1}^{N}\frac{\hat{p}_i^2}{2m} + \sum_{i=1}^{N} V'(\boldsymbol{r}_i). \tag{2.31}$$

The wavefunctions, given by Slater determinants are

$$\psi(\boldsymbol{r}_1,\ldots,\boldsymbol{r}_N) = \frac{1}{\sqrt{N!}}\det(\psi_i(\boldsymbol{r}_j)), \tag{2.32}$$

with the single-particle wavefunctions $\psi_i(\boldsymbol{r}_j)$. Each single-particle wavefunction should fulfill the Schrödinger equation

$$\left[-\frac{\hbar^2}{2m}\boldsymbol{\nabla}^2 + V'(\boldsymbol{r})\right]\psi_i = \varepsilon_i\psi_i \tag{2.33}$$

under the constraint $\langle\psi_i|\psi_j\rangle = \delta_{i,j}$. The particle density of the system is then given by

$$n(\boldsymbol{r}) = \sum_{i=1}^{N}|\psi_i(\boldsymbol{r})|^2. \tag{2.34}$$

The corresponding energy functional is

$$E[n(\boldsymbol{r})] = \sum_{i=1}^{N}\int \mathrm{d}\boldsymbol{r}\,\psi_i^*(\boldsymbol{r})\left[-\frac{\hbar^2}{2m}\boldsymbol{\nabla}^2\right]\psi_i(\boldsymbol{r}) + \sum_{i=1}^{N}\int \mathrm{d}\boldsymbol{r}\,V'(\boldsymbol{r})|\psi_i(\boldsymbol{r})|^2. \tag{2.35}$$

Note that in this non-interacting system the kinetic functional is also just known implicitly.

2. This should also be true for the interacting system, i.e., the ansatz for the kinetic-energy-functional is

$$T[n(\boldsymbol{r})] = \sum_{i=1}^{N}\int \mathrm{d}\boldsymbol{r}\,\psi_i^*(\boldsymbol{r})\left[-\frac{\hbar^2}{2m}\boldsymbol{\nabla}^2\right]\psi_i(\boldsymbol{r}), \tag{2.36}$$

if it is possible to express the particle density in the form

$$n(\boldsymbol{r}) = \sum_{i=1}^{N}|\psi_i(\boldsymbol{r})|^2 = \sum_{i=1}^{N} n_i(\boldsymbol{r}). \tag{2.37}$$

Since this is just an approximation, further corrections of the kinetic functional are imprinted into the exchange-correlation functional. Hence the whole DFT functional is

$$E[n(\boldsymbol{r})] = T[n(\boldsymbol{r})] + V[n(\boldsymbol{r})] + V_{\mathrm{ee}}[n(\boldsymbol{r})] + E_{\mathrm{XC}}[n(\boldsymbol{r})], \tag{2.38}$$

with

$$T[n(\boldsymbol{r})] = \sum_{i=1}^{N}\int \mathrm{d}\boldsymbol{r}\,\psi_i^*(\boldsymbol{r})\left[-\frac{\hbar^2}{2m}\boldsymbol{\nabla}^2\right]\psi_i(\boldsymbol{r}), \tag{2.39a}$$

$$V[n(\boldsymbol{r})] = \int \mathrm{d}\boldsymbol{r}\,V(\boldsymbol{r})n(\boldsymbol{r}), \tag{2.39b}$$

$$V_{\mathrm{ee}}[n(\boldsymbol{r})] = \frac{1}{2}\frac{e^2}{4\pi\varepsilon_0}\int \mathrm{d}\boldsymbol{r}\int \mathrm{d}\boldsymbol{r}'\,\frac{n(\boldsymbol{r})n(\boldsymbol{r}')}{|\boldsymbol{r}-\boldsymbol{r}'|}. \tag{2.39c}$$

This representation of the density functional is sometimes called Kohn-Sham expression of the energy. The functional should be minimal for the ground-state, which is also true for the unknown single-particle wavefunctions $\psi_i(\boldsymbol{r})$. The variational principle under the constraint of normalized $\psi_i(\boldsymbol{r})$ leads to

$$\frac{\delta}{\delta\psi_i}\left\{E[n(\boldsymbol{r})] - \sum_{j=1}^{N}\varepsilon_j \underbrace{\left(\int \mathrm{d}\boldsymbol{r}\,|\psi_j(\boldsymbol{r})|^2 - 1\right)}_{\text{constraint}}\right\} = 0, \tag{2.40}$$

where ε_j is a Lagrangian multiplier. This will result in the Kohn-Sham equations

$$\left[-\frac{\hbar^2}{2m}\boldsymbol{\nabla}^2 + V_{\text{eff}}(\boldsymbol{r})\right]\psi_i(\boldsymbol{r}) = \varepsilon_i\psi_i(\boldsymbol{r}), \tag{2.41}$$

with the effective potential

$$V_{\text{eff}}(\boldsymbol{r}) = V(\boldsymbol{r}) + \frac{e^2}{4\pi\varepsilon_0}\int \mathrm{d}\boldsymbol{r}'\,\frac{n(\boldsymbol{r}')}{|\boldsymbol{r}-\boldsymbol{r}'|} + \frac{\delta E_{\text{XC}}[(n(\boldsymbol{r}))]}{\delta n(\boldsymbol{r})}. \tag{2.42}$$

The Kohn-Sham equation are of the same form as equation (2.33), i.e., these are Schrödinger equations for every single-particle wavefunction $\psi_i(\boldsymbol{r})$.

3. Solving the Kohn-Sham equations (2.41). Since the effective potential depends on $n(\boldsymbol{r})$ or $\psi_i(\boldsymbol{r})$ the Kohn-Sham equations are selfconsistent equations which are typically solved iteratively. The selfconsistent cycle follows the steps:

   (i) Start with an appropriate choice of $n(\boldsymbol{r})$.

   (ii) Calculate $V_{\text{eff}}(\boldsymbol{r})$ (single-particle potential).

   (iii) Solving the KS equations (2.41) (effective single-particle Schrödinger equation) for the $\psi_i(\boldsymbol{r})$.

   (iv) Calculate the new density $n'(\boldsymbol{r})$ from the $\psi_i(\boldsymbol{r})$ via equation (2.37).

   (v) Compare $n'(\boldsymbol{r})$ and $n(\boldsymbol{r})$ if:

   - $n'(\boldsymbol{r}) = n(\boldsymbol{r})$ end the cycle because $n(\boldsymbol{r})$ is the ground state density.
   - $n'(\boldsymbol{r}) \neq n(\boldsymbol{r})$ set $n(\boldsymbol{r}) = n'(\boldsymbol{r})$ and repeat from the second step (ii).

Note the following:

- The here introduced selfconsistent problem is similar to Hartree-Fock equations. However, the KS-equations are simpler due to the effective local potential.
- The density functional of the kinetic energy is exact if all corrections are included in $E_{\mathrm{XC}}[n(\boldsymbol{r})]$.
- The wavefunction ψ_i and their corresponding eigenenergies ε_i have no physical meaning. They were just introduced for the calculations.

Although the whole Hamiltonian is expressed as a density functional the exchange-correlations functional $E_{\mathrm{XC}}[n(\boldsymbol{r})]$ is still unknown. Most approximation are performed on the level of this functional.

2.2.3 Local density approximation (LDA) and beyond

LDA uses a similar argumentation as the Thomas-Fermi approximation for the kinetic functional. In the case of a homogenous electron gas (Hartree-Fock approximation) one finds

$$E = -\frac{3e^2V}{4\pi}\left(3\pi^2\right)^{1/3} n_0^{4/3}. \tag{2.43}$$

Hence a possible ansatz for rewriting the exchange-correlation functional could be

$$E_{\mathrm{XC}}[n(\boldsymbol{r})] = -\frac{3e^2}{4\pi}\left(3\pi^2\right)^{1/3} \int \mathrm{d}\boldsymbol{r}\ \left(n(\boldsymbol{r})\right)^{4/3}. \tag{2.44}$$

With this ansatz it is at least possible to reproduce the Hartree-Fock results. The resulting exchange potential is then

$$V_{\mathrm{XC}}(\boldsymbol{r}) = \frac{\delta E_{\mathrm{XC}}[n(\boldsymbol{r})]}{\delta n(\boldsymbol{r})} = -e^2\left(\frac{3}{\pi}\right)^{1/3} n(\boldsymbol{r})^{1/3}. \tag{2.45}$$

Obviously the exchange potential at $\boldsymbol{r}$ just depends on the density at the same position $\boldsymbol{r}$, which is why we call it local density approximation [27].

Beyond LDA

In gerneral the density is not local, so better approximations are needed. For example GGA (generalized gradient approximation) which additionally includes the gradient $\nabla n(\boldsymbol{r})$ (expansion to first derivative) or meta-GGA (expansion to the second derivative, i.e., includes the Laplacian). Often one still sticks to LDA but allows additional variational parameters, e.g.

$$V_{\mathrm{XC}}(\boldsymbol{r}) = \beta(n(\boldsymbol{r}))n(\boldsymbol{r})^{1/3},$$

where $\beta(n(\boldsymbol{r}))$ is an empirical function. Further approximations are: Hybrid methods (LDA + Hartree-Fock), GW, LDA+U, etc.

Example: Thomas-Fermi

Let us assume a homogenous non-interacting electron gas. In this case the kinetic energy can be written as

$$E_{\mathrm{kin}} = 2\sum_{k<k_{\mathrm{F}}} \frac{\hbar^2 k^2}{2m} = \frac{3\hbar^2}{10m}\left(3\pi^2\right)^{2/3} V n_0^{5/3}, \tag{2.46}$$

with $n_0 = N/V$ and $N = Vk_{\mathrm{F}}^3/(3\pi^2)$ (constant density), then a generalization to a density-functional for the kinetic energy is

$$T[n(\boldsymbol{r})] = \frac{3\hbar^2}{10m}(3\pi^2)^{2/3}\int \mathrm{d}\boldsymbol{r}\ (n(\boldsymbol{r}))^{5/3}. \tag{2.47}$$

Hence the full density functional is

$$E[n(\boldsymbol{r})] = \frac{3\hbar^2}{10m}(3\pi^2)^{2/3}\int \mathrm{d}\boldsymbol{r}\ (n(\boldsymbol{r}))^{5/3} + \int \mathrm{d}\boldsymbol{r} V(\boldsymbol{r})n(\boldsymbol{r}) + \frac{1}{2}\frac{e^2}{4\pi\varepsilon_0}\int \mathrm{d}\boldsymbol{r}\int \mathrm{d}\boldsymbol{r}'\,\frac{n(\boldsymbol{r})n(\boldsymbol{r}')}{|\boldsymbol{r}-\boldsymbol{r}'|}, \tag{2.48}$$

where we just considered the electron-electron part of the interaction. Now variation of $E[n(\boldsymbol{r})]$, i.e., $\delta E[n(\boldsymbol{r})]_{\mathrm{min}} = \mu$ leads to

$$\frac{\hbar^2}{2m}\left(3\pi^2 n(\boldsymbol{r})\right)^{2/3} + V(\boldsymbol{r}) + \frac{1}{2}\frac{e^2}{4\pi\varepsilon_0}\int \mathrm{d}\boldsymbol{r}'\frac{n(\boldsymbol{r}')}{|\boldsymbol{r}-\boldsymbol{r}'|} = \mu. \tag{2.49}$$

Here μ is the chemical potential. Introducing the effective potential

$$V_{\text{eff}}(\boldsymbol{r}) \equiv V(\boldsymbol{r}) + \frac{1}{2}\frac{e^2}{4\pi\varepsilon_0}\int \mathrm{d}\boldsymbol{r}'\,\frac{n(\boldsymbol{r}')}{|\boldsymbol{r}-\boldsymbol{r}'|} \tag{2.50}$$

one achieves

$$\mu = \frac{\hbar^2}{2m}\left(3\pi^2 n(\boldsymbol{r})\right)^{2/3} + V_{\text{eff}}(\boldsymbol{r}), \tag{2.51a}$$

$$n(\boldsymbol{r}) = \frac{1}{3\pi^2}\left[\frac{2m}{\hbar}\left(\mu - V_{\text{eff}}(\boldsymbol{r})\right)\right]^{3/2}, \tag{2.51b}$$

which is consistent with the Thomas-Fermi approximation of screening [27].

2.2.4 Electronic structure calculations

Solving the Kohn-Sham equations (2.41) is possible by introducing a three-dimensional mesh. Unfortunately, this would require huge computational expenses because

- near the atomic center the diverging Coulomb potential dominates. Here the space mesh should be very fine.
- in the area between atoms the potential changes rather smoothly and hence the space mesh could be more coarsed.

Common calculations schemes for solving the Khon-Sham equations are based on variational approaches [29]. The wavefunctions $\psi_i(\boldsymbol{r})$ are then expressed as a series

$$|\psi_i\rangle = \sum_n a_n^i\,|\phi_n\rangle\,, \tag{2.52}$$

with the unknown coefficients a_n^i and a complete set of basis functions $|\phi_n\rangle$. Let's write the KS equations in the following form

$$\mathcal{H}\,|\psi_i\rangle = \varepsilon_i\,|\psi_i\rangle\,. \tag{2.53}$$

Multiplying from the left with the basis function $\langle\phi_{n'}|$ leads to an algebraic linear system of equations for the coefficients a_n^i

$$\sum_n \langle\phi_{n'}|\mathcal{H}|\phi_n\rangle = \varepsilon_i \sum_n \langle\phi_{n'}|\phi_n\rangle\, a_n^i, \tag{2.54}$$

where the left part is just the Hamiltonian matrix and the right part the overlap-matrix. Consequently we managed to reduce the general problem to the calculation of eigenvalues and eigenstates. Therefore the specific realization of the method is now defined via the choice of the basis functions $|\phi_n\rangle$. The exisiting DFT methods roughly can be divided into two major groups:

1. Atomic-like orbitals centered at the atoms a decaying with decreasing distance from the center. Probably one on of the most prominent set of functions are linearized muffin-tin orbitals (LMTO) with "muffin-tin orbitals" [30] as basis function

$$\phi_{lm}(\boldsymbol{r}) = \xi_l(|\boldsymbol{r}|)Y_{lm}(\theta,\phi), \tag{2.55a}$$

$$\xi_l(|\boldsymbol{r}|) = \begin{cases} R_l(|\boldsymbol{r}|), & |\boldsymbol{r}| < S \\ C|\boldsymbol{r}|^{-l-1}, & |\boldsymbol{r}| > S \end{cases} \tag{2.55b}$$

   where $Y_{lm}(\theta,\phi)$ are the spherical harmonics, R_l the radial part and S the atomic sphere radius. Here $|\boldsymbol{r}|^{-l-1}$ describes the decaying tail outside the sphere.

2. *Delocalized plane waves* (PW) of the form

$$|\boldsymbol{k}-\boldsymbol{g}\rangle = \mathrm{e}^{\mathrm{i}(\boldsymbol{k}-\boldsymbol{g})\cdot\boldsymbol{r}}, \tag{2.56}$$

   with the wavevector $\boldsymbol{k}$ and a reciprocal lattice vector $\boldsymbol{g}$. Although plane waves are a good approximation in the interatomic area, they are not suited in the diverging area. In this area atomic-like orbitals are much better. Again one has two choices

   a) *Linearized Augmented Plane Waves* (LAPW)

$$|\boldsymbol{k}-\boldsymbol{g}\rangle_{\mathrm{LAPW}} = \begin{cases} \sum_{lm} b_{lm} R_l(|\boldsymbol{r}|)Y_{lm}(\theta,\phi), & |\boldsymbol{r}| < S \\ C\mathrm{e}^{\mathrm{i}(\boldsymbol{k}-\boldsymbol{g})\cdot\boldsymbol{r}}, & |\boldsymbol{r}| > S \end{cases}. \tag{2.57}$$

   b) Pseudopotential method. Replace the Potential in the KS equations (2.41) with a pseudopotential which still allows plane waves.

More details can be found in [29].

2.3 Extracting minimal models – $SrVO_3$ as pardigma

2.3.1 Motivation

As mentioned before, the DFT approach allows numerical access to solids and typically supplies us with an approximated bandstructure and density of states for any compound or material of interest. It has become a standard tool for obtaining first glimpses of physical quantities which can be compared with experiments. Despite its huge success in describing lots of materials quite accurately, it fails for material classes with strong correlations, like most transition metal oxides. These strong correlations are a consequence of partially filled shells (often d shells) leading to many-body states which cannot represented in terms of a single-slater determinant and hence lie beyond the definition of DFT. This is particularly evident for Mott insulators, where the material should be in an insulating phase. DFT however predicts a metal. Nevertheless, it is an excellent starting point for many methods going beyond the single-particle description of DFT, like DMFT, when for example model parameter for real materials are needed. Hence DFT can help to identify the relevant degrees of freedom around the Fermi energy. So instead of sampling the parameter space of a specific model, e.g. tight-binding model, it is possible to extract this parameters directly from the DFT data, by projecting the relevant subspace – often known from experiments – onto a set of wavefunctions, here maximally-localized Wannier functions (MLWF). This projections scheme then leads to a minimal model Hamiltonian of the form

$$H_0 = \sum_{i,j} t_{ij}(\boldsymbol{R}) c_i^\dagger c_j, \tag{2.58}$$

where i,j are orbital indices, $\boldsymbol{R}$ the lattice vector and $t_{ij}(\boldsymbol{R})$ the corresponding hopping amplitudes. After a Fourier transformation and exact diagonalization

along a high symmetry point $\boldsymbol{k}$-path this model reproduces the bandstructure and density of states within the chosen energy window of the DFT calculation. Especially in cases where only few bands are present around the Fermi level and they are well separated from the other ones (e.g. see figure 2.2). Although correlation effects are not included in this model, crystal-field splitting and the size of the orbital hopping however is. In the subsequent chapters this scheme will be discussed in more detail for $SrVO_3$, which has often become the compound of choice for a first brief introduction.

2.3.2 Maximally-localized Wannier functions

Discussions of the electronic ground state and the formation of bands in solids often start with the free electron approximations in a periodic potential $V(\boldsymbol{r}) = V(\boldsymbol{R} + \boldsymbol{r})$. The Schrödinger equation then takes on the form

$$\left[-\frac{\hbar}{2m}\boldsymbol{\nabla}^2 + V(\boldsymbol{r})\right]\psi(\boldsymbol{r}) = E\psi(\boldsymbol{r}), \tag{2.59}$$

where $\psi(\boldsymbol{r})$ describes the wavefunction with energy E. From the Bloch theorem we can then find eigenfunctions of the above Hamiltonian and assign them to the quantum number $\boldsymbol{k}$ for the crystal momentum and a band index n. These so called Bloch states are then defined via

$$\psi_{n,\boldsymbol{k}}(\boldsymbol{r}) = \mathrm{e}^{-\mathrm{i}\boldsymbol{k}\boldsymbol{r}} u_{n,\boldsymbol{k}}(\boldsymbol{r}), \tag{2.60}$$

where $u_{n,\boldsymbol{k}}(\boldsymbol{r})$ is an $\boldsymbol{r}$ periodic function. The eigenvalues $E_{n,\boldsymbol{k}}$ of the Bloch functions are continuous, periodic in $\boldsymbol{k}$ and form the well known bands. Although this basis allows us to understand the formation of bands in solids and it is widely used in electronic structure calculations, the description of chemical bonds is not intuitive. On the other hand Wannier orbitals, which are technically an alternative representation, provide a natural extension of the concept of molecular orbitals into solids and are the real space picture of localized orbitals. They can be seen as solid-state equivalent of localized molecular orbitals [14, 31, 32]

The Wannier function of an isolated band n at any lattice vector $\boldsymbol{R}$ is defined by

$$w_n(r-\boldsymbol{R}) = \frac{V}{(2\pi)^3}\int_{\mathrm{BZ}} \mathrm{e}^{-\mathrm{i}\boldsymbol{k}\boldsymbol{R}}\psi_{n,\boldsymbol{k}}(\boldsymbol{r})\mathrm{d}\boldsymbol{k}, \tag{2.61}$$

where V denotes the real-space primitive cell volume and $\psi_{n,\boldsymbol{k}}(\boldsymbol{r})$ are the Bloch functions (2.60) corresponding to the nth band. On the other hand each Bloch function can be written in terms of Wannier functions by

$$\psi_{n,\boldsymbol{k}}(\boldsymbol{r}) = \sum_{\boldsymbol{R}} \mathrm{e}^{\mathrm{i}\boldsymbol{k}\boldsymbol{R}} w_n(\boldsymbol{r}-\boldsymbol{R}), \tag{2.62}$$

where the sum runs over each lattice vector $\boldsymbol{R}$. It can be shown that Wannier functions form an orthonormal set. Additionally two Wannier functions transform into each other with a translation of a lattice vector $\boldsymbol{R}-\boldsymbol{R}'$. Note that the definition of Wannier functions (2.61) is not unique due to the gauge freedom of the Bloch states $\psi_{n,\boldsymbol{k}}(\boldsymbol{r}) \to \exp(\mathrm{i}\phi(\boldsymbol{k}))\psi_{n,\boldsymbol{k}}(\boldsymbol{r})$, where $\phi(\boldsymbol{k})$ is a real valued function. While this not affects the Bloch states, the corresponding Wannier function however will be changed. In practice one uses this freedom to choose the phases of the Bloch states in order to give the most convenient maximally-localized set of Wannier function (MLWF), i.e. , a Wannier function which is mostly localized around $\boldsymbol{R}$ and rapidly decreases to zero elsewhere.

Numerically Wannier functions are constructed via a maximal-localization method, which aims to minimize the spread functional

$$\Omega = \sum_n \langle r^2\rangle_n - \langle \boldsymbol{r}\rangle_n^2\,, \tag{2.63}$$

where n is the Wannier function index, $\langle \boldsymbol{r}\rangle_n$ the position of its center and $\langle \boldsymbol{r}\rangle_n^2$ the corresponding matrix element. For isolated bands the Wannier functions are well defined and span the same Hilbert space as that of the isolated band. Wannier function can also be calculated numerically via a projection method. For more detail see [23, 31–33].

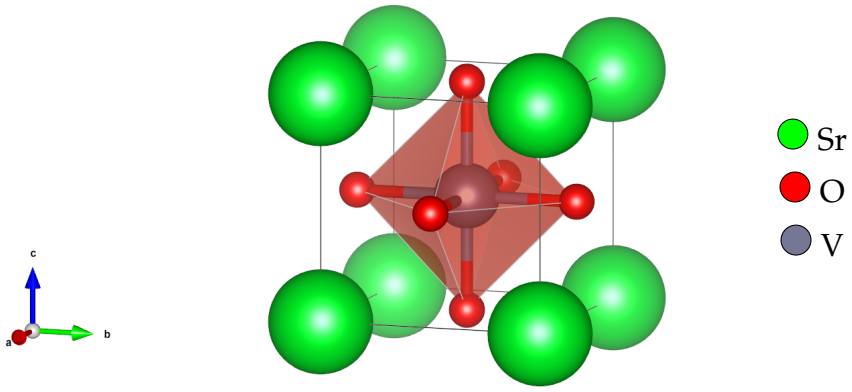

Figure 2.1.: Typical perovskite structure of $SrVO_3$. Within the cubic-symmetry structure the V cation is surrounded by an octahedron of O anions.

2.3.3 $SrVO_3$ as example

An archetypal TMO with perovskite structure is $SrVO_3$ as shown in figure 2.1. Per unit cell there is one Sr and one V atom surrounded by an octahedron of O anions, where only three of them are in one unit cell. Since it has cubic symmetry it is sufficient to give the side length of the cube, which within this chapter was chosen to be 3.777 06 Å. All DFT calculations were performed with VASP (The Vienna Ab initio Simulation Package) [34, 35] and the Wannier90 interface [23].

After a DFT calculation one calculates the bandstructure, total-, and partial-density of state, which is shown in figure 2.2 (a) and (b). To derive a minimal model the first step is to choose the region of interest. Experimental insight is at this step extremely helpful, so the relevant orbitals are chosen. Alternatively, since we are dealing with a transition metal oxide, a good start is to take into account the d-orbitals located around the Fermi energy, i.e. the partially filled shells which are correlated. Full or empty shells are not correlated, since they can be expressed as singe-slater determinant. This becomes evident, when comparing the partial density of states in figure 2.2 (b). As depicted around the Fermi level all the bands have a dominant t_{2g} (red line) character, while the e_g bands are shifted upwards. This clear separation of the t_{2g} bands is quite helpful, because it allows

us to decrease the complexity of the effective model to a pure t_{2g} model. Hence the red box indicates the region of interest on whom we want to project the Wannier orbitals onto.

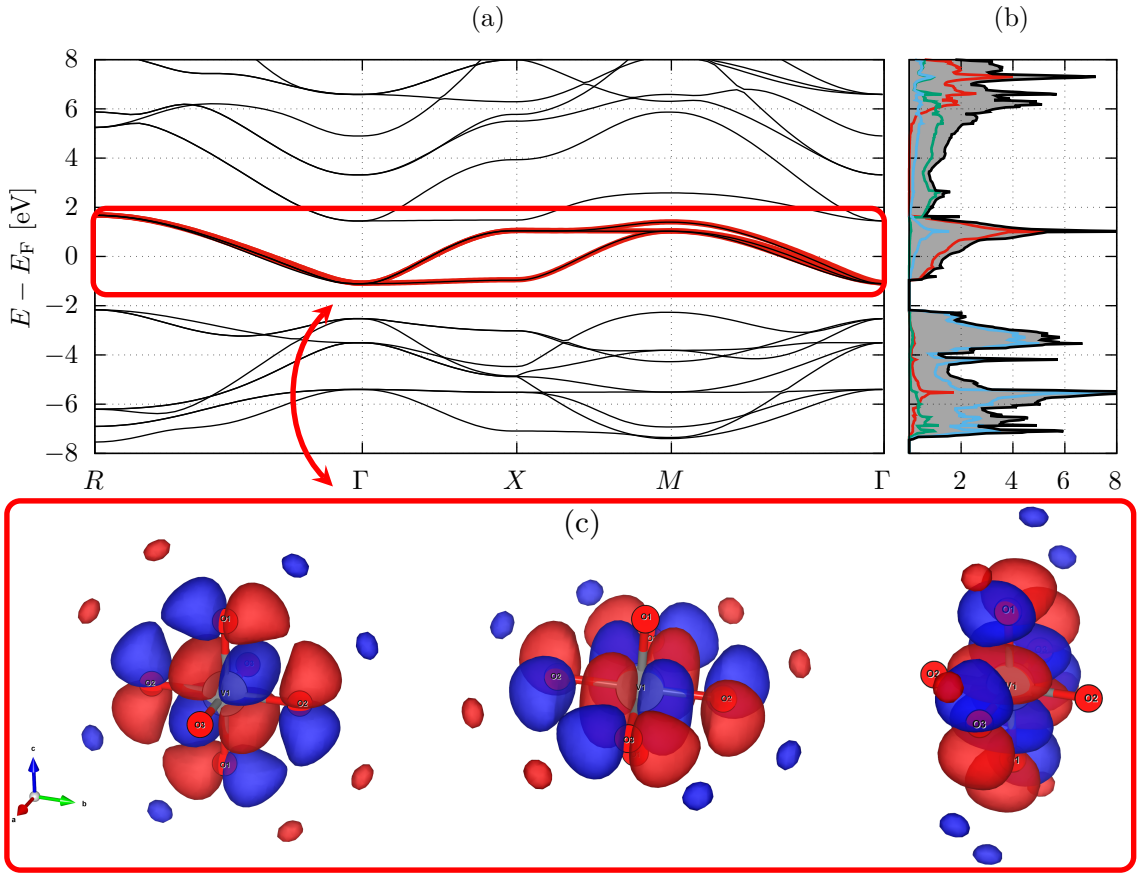

■ **Figure 2.2.:** Wannier projection scheme on $SrVO_3$. (a) Band structure from a DFT calculation (black). Red boxed inset shows the t_{2g} subspace on which the wannier orbitals are projected onto (red lines). (b) Total density of states (black) from DFT. The partial density of states are: red t_{2g}-orbitals of V, green e_g-orbitals of V, and blue are the p-orbitals of O. (c) Wannier orbitals, obtained from the projection scheme, from left to right: *xy*-, *xz*-, and *yz*-orbital.

The subsequent Wannier projection onto the t_{2g}-orbitals then leads to a tight-binding model, which contains besides nearest-neighbor hopping, also next nearest neighbors hopping and even further. They are visualized in figure 2.2 (c). One then truncates after a certain threshold, since the hopping amplitudes decrease quite

fast. From the Wannier projection as shown in figure 2.2 the leading hoppings are nearest-neighbor hoppings $t_{d\sigma}$ or $t_{d\pi}$, (depending on the orientation of the orbitals), and next-nearest neighbor hopping t_{NNN} with the values:

$$t_{d\sigma} = 0.2890\,\mathrm{eV}, \quad t_{d\pi} = 0.0342\,\mathrm{eV}, \quad t_{NNN} = 0.0951\,\mathrm{eV}. \tag{2.64}$$

The tight-binding Hamiltonian is then of the form

$$H_{\mathrm{TB}} = \sum_{\boldsymbol{k},\alpha,\beta,\sigma} \varepsilon^{\alpha\beta}(\boldsymbol{k}) c^{\dagger}_{\boldsymbol{k}\alpha\beta} c_{\boldsymbol{k}\alpha\beta} \tag{2.65}$$

with $\varepsilon^{\alpha\beta}(\boldsymbol{k})$ the dispersion relation and $c^{\dagger}_{\boldsymbol{k}\beta}$ ($c_{\boldsymbol{k}\beta}$) describing the creation (annihilation) of an electron with spin σ ($\sigma = \uparrow, \downarrow$), and orbital α ($\alpha = xy, xz, yz$) with the momentum $\boldsymbol{k}$. Note that Hamiltonian (2.65) technically describes the Fourier transformed Hamiltonian on a three-dimensional cubic lattice, so the leading hoppings lead to the following parts of the dispersion relation

$$\begin{aligned}
\varepsilon^{xy}(\boldsymbol{k}) &= -2(t_{d\sigma}\cos k_x + t_{d\pi}\cos k_y + t_{d\sigma}\cos k_z) - 4t_{\mathrm{NNN}}\cos k_x \cos k_z - \mu, \\
\varepsilon^{xz}(\boldsymbol{k}) &= -2(t_{d\pi}\cos k_x + t_{d\sigma}\cos k_y + t_{d\sigma}\cos k_z) - 4t_{\mathrm{NNN}}\cos k_y \cos k_z - \mu, \\
\varepsilon^{yz}(\boldsymbol{k}) &= -2(t_{d\sigma}\cos k_x + t_{d\sigma}\cos k_y + t_{d\pi}\cos k_z) - 4t_{\mathrm{NNN}}\cos k_x \cos k_y - \mu.
\end{aligned} \tag{2.66}$$

The μ is a result of the crystal-field splitting and the chemical potential calculated from the DFT calculation, which in this example is $\mu = 0.656\,\mathrm{eV}$. Without this factor the resulting bandstructures Fermi energy is not at $E_{\mathrm{F}} = 0$. All above shown details are in good agreement with the results shown in [36], where the authors go to even bigger models including p-orbitals and all d-orbitals.

At this point it is also worth mentioning, that the real space extension of the Wannier orbitals can change as e.g. shown in figure 2.2 (c) in the t_{2g}-model. This means that they highly depend on the chosen projection window. If we include for example the oxygen p-orbitals (all the bands below the red box in figure 2.2 (a)) the form of the projected t_{2g}-orbitals would change to the one shown in figure 2.3. Although the local character will mostly look like an atomic d-orbital the object itself is a molecular orbital inheriting all the hybrdizations neglected by the choice

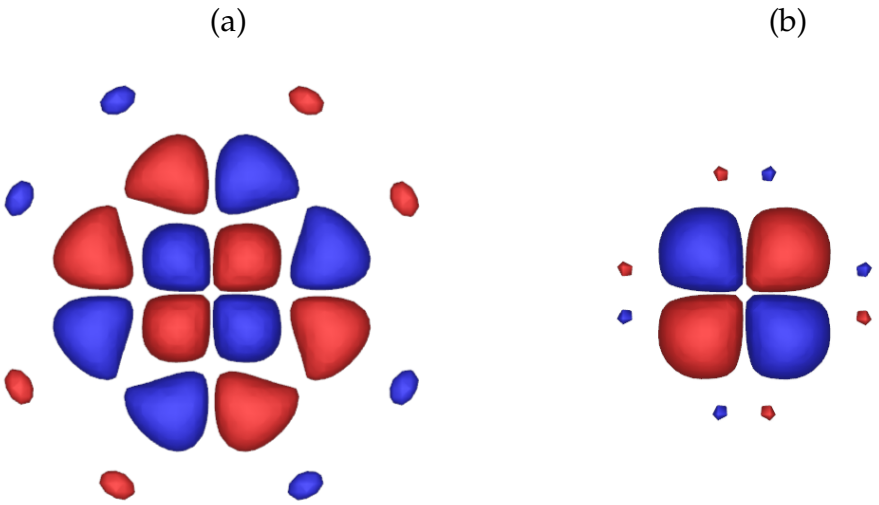

Figure 2.3.: Comparision of a wannier-projected d-Orbital. (a) d-model, where just the t_{2g} orbitals of V are considered. (b) dp-model, where the p orbitals of O are also included.

of the projection window. In this specific case the d-orbitals look more "atomic" like the broader the projection window. Typically one has to consider this because it is not always possible to reduce the whole model onto a simple t_{2g}-model, e.g. when working with charge transfer insulators or cuprates, where also p-orbitals, or even s-orbitals are important. Moreover within the projection window the electron-electron interaction will be of great importance, since it determines physical properties. However, within the chosen subspace it must be renormalized, due to the screening process, to an effective interaction. Hence the real space extension of the chosen Wannier basis will affect the strength of this effective interaction. For more detail on $SrVO_3$ see [36, 37].

Chapter 3 Green's functions

3.1 Green's function formalism

Before defining the Green's function it is helpful to first motivate them via linear response theory, where they naturally appear as response function, i.e., as answer to an external perturbation of the system. Moreover linear response theory relates models from many-body theory to experiments [14, 38–40].

3.1.1 Linear response theory

Linear response theory considers small perturbations to a system, hence the name of the theory. Let a system be described by the Hamiltonian [14]

$$H = H_0 + V_t, \tag{3.1}$$

where H_0 is the Hamiltonian of the unperturbed system and V_t the perturbation. In this notation V_t describes the interaction of the system with an external F_t and is of the form

$$V_t = \hat{V} F_t. \tag{3.2}$$

Here $\hat{V}$ is an operator and F_t a complex number. In addition let $\hat{A}$ be a not explicitly time dependent observable. The thermodynamic expectation value without external

field is then given by

$$\langle \hat{A} \rangle = \mathrm{tr}\left[\varrho_0 \hat{A}\right], \tag{3.3}$$

with the unperturbed single-particle density matrix

$$\varrho_0 = \frac{1}{\Xi_0} \mathrm{e}^{-\beta H_0}. \tag{3.4}$$

The important question is how the observable $\hat{A}$ reacts to the perturbation V_t. When using the grand canonical ensemble, the system Hamiltonian has to be extended by a chemical potential

$$\mathcal{H}_0 = H_0 - \mu \hat{N}, \tag{3.5}$$

where μ is the chemical potential and $\hat{N}$ the particle number operator. Also the density matrix will change when switching on the external field $\varrho_0 \to \varrho_t$, so the expectation value is

$$\langle \hat{A} \rangle_t = \mathrm{tr}\left[\varrho_t \hat{A}\right]. \tag{3.6}$$

In the Schrödinger picture the time dependent ϱ_t is then determined by the von Neumann equation

$$\mathrm{i}\hbar \partial_t \varrho_t = \left[\mathcal{H} + V_t, \varrho_t\right], \tag{3.7}$$

with the boundary condition

$$\lim_{t \to -\infty} \varrho_t = \varrho_0, \tag{3.8}$$

which means that at some point in time the perturbation was switched on. In the Dirac picture, which we achieve via the transformation

$$\varrho_t^{\mathrm{D}}(t) = \mathrm{e}^{\frac{\mathrm{i}}{\hbar}\mathcal{H}_0 t} \varrho_t \mathrm{e}^{-\frac{\mathrm{i}}{\hbar}\mathcal{H}_0 t}, \tag{3.9}$$

we find the following equation of motion

$$\varrho_t^{\mathrm{D}}(t) = \frac{\mathrm{i}}{\hbar}\left[\varrho_t^{\mathrm{D}}(t), V_t^{\mathrm{D}}(t)\right]_-. \tag{3.10}$$

Since the boundary condition from above needs to be fulfilled, the solution of this differential equation is achieved by a simple integration

$$\varrho_t^{\mathcal{D}}(t) = \varrho_0 - \frac{\mathrm{i}}{\hbar}\int_{-\infty}^{t}\left[V_t^{\mathrm{D}}(t'), \varrho_t^{\mathrm{D}}(t')\right]_- \mathrm{d}t. \tag{3.11}$$

Iteratively solving this equation leads to the Dyson like expression

$$\varrho_t^{\mathrm{D}}(t) = \varrho_0 + \sum_{n=1}^{\infty}\varrho_t^{\mathrm{D}(n)}(t), \tag{3.12a}$$

$$\varrho_t^{\mathrm{D}(n)}(t) = -\left(-\frac{\mathrm{i}}{\hbar}\right)^n \int_{-\infty}^{t}\mathrm{d}t_1 \ldots \int_{-\infty}^{t_{n-1}}\mathrm{d}t_n \left[V_{t_1}^{\mathrm{D}}(t_1), \left[\cdots, \left[V_{t_n}^{\mathrm{D}}(t_n), \varrho_0\right]_- \cdots\right]_-\right]_-. \tag{3.12b}$$

Although this equation is exact, it is rather useless. The restriction to sufficient small external perturbations, i.e., only linear terms and the transformation back to the Schrödinger picture gives

$$\varrho_t \approx \varrho_0 - \frac{\mathrm{i}}{\hbar}\int_{-\infty}^{t}\mathrm{e}^{-\frac{\mathrm{i}}{\hbar}\mathcal{H}_0 t}\left[V_{t'}^{\mathrm{D}}(t'), \varrho_0\right]\mathrm{e}^{\frac{\mathrm{i}}{\hbar}\mathcal{H}_0 t}\mathrm{d}t'. \tag{3.13}$$

This is the fundamental approximation of the linear response theory. Plugging this into equation (3.6) and exploiting the cyclic invariance of the trace

$$\langle\hat{A}\rangle_t = \langle\hat{A}\rangle_0 - \frac{\mathrm{i}}{\hbar}\int_{-\infty}^{t}F_{t'}\left\langle\left[\hat{A}^{\mathrm{D}}(t'), \hat{B}^{\mathrm{D}}(t')\right]_-\right\rangle_0 \mathrm{d}t'. \tag{3.14}$$

Hence we now have an explicit expression, which describes how the system responds to an external perturbation mediated by the observable $\hat{A}$

$$\Delta A_t = \langle\hat{A}\rangle_t - \langle\hat{A}\rangle_0 = -\frac{\mathrm{i}}{\hbar}\int_{-\infty}^{t}F_{t'}\left\langle\left[\hat{A}^{\mathrm{D}}(t'), \hat{B}^{\mathrm{D}}(t')\right]_-\right\rangle_0 \mathrm{d}t'. \tag{3.15}$$

Here it is worth to stress that the response is determined by an expectation value of the unperturbed system. Now we want to define the retarded two-times Greens function

$$G_{AB}^{\mathrm{ret}}(t,t') \equiv -\mathrm{i}\Theta(t,t')\left\langle\left[\hat{A}(t),\hat{B}(t')\right]_-\right\rangle_0, \tag{3.16}$$

where the operators $\hat{A}$ and $\hat{B}$ are taken in the Heisenberg picture of the nonperturbed system. This allows us to express equation 3.15 in the following form

$$\Delta A_t = -\frac{\mathrm{i}}{\hbar}\int_{-\infty}^{\infty}F_{t'}G_{AB}^{\mathrm{ret}}(t,t')\mathrm{d}t'. \tag{3.17}$$

Consequently the response of the system is represented by the retarded Green's function. The label retarded comes from the Heaviside function $\Theta(t,t')$ which only allows perturbations for $t < t'$. At this point it is also common to introduce the Kubo formula,

$$\Delta A_t = \frac{1}{2\pi\hbar^2}\int_{-\infty}^{\infty} F(\omega) G^{\mathrm{ret}}_{AB}(\omega + \mathrm{i}\delta)\mathrm{e}^{-\mathrm{i}(\omega+\mathrm{i}\delta)t/\hbar}\mathrm{d}\omega, \tag{3.18}$$

which we can derive by taking the Fourier transform

$$F_t = \frac{1}{2\pi}\int_{\infty}^{\infty} F(\omega)\mathrm{e}^{-\mathrm{i}(\omega+\mathrm{i}\delta)}\mathrm{d}\omega. \tag{3.19}$$

For not explicitly time dependent Hamiltonians the Green's function depends only on the difference $t - t'$. Here δ has to be chosen as $\delta > 0$, otherwise the boundary condition from above is not valid anymore [14].

3.1.2 Two time Green's functions

The single-particle Green's function (or single-particle propagator) is defined as

$$G_{\sigma\sigma'}(\boldsymbol{r},t,\boldsymbol{r}',t') = -\mathrm{i}\left\langle \mathrm{GS}\middle|\, \hat{T}\left(\hat{\psi}_\sigma(\boldsymbol{r},t)\hat{\psi}^\dagger_{\sigma'}(\boldsymbol{r}',t')\right)\middle|\,\mathrm{GS}\right\rangle, \tag{3.20}$$

where $\hat{\psi}_\sigma(\boldsymbol{r},t)$, $\hat{\psi}^\dagger_\sigma(\boldsymbol{r},t)$ are field operators in the Heisenberg picture, and $|\mathrm{GS}\rangle$ denotes the (many-body) ground state. Here $\hat{T}$ stands for the time-order operator, which gives a minus sign if $t < t'$ and for those Green's functions using the anti-commutator (Fermions) [14, 38–40]. This form of the Green's function is also called causal Green's function to discriminate from the retarded or advanced Green's function. In general the following holds

$$G_{\sigma\sigma'}(\boldsymbol{r},t,\boldsymbol{r}',t') = \begin{cases} -\mathrm{i}\left\langle \mathrm{GS}\middle|\, \hat{\psi}_\sigma(\boldsymbol{r},t)\hat{\psi}^\dagger_{\sigma\prime}(\boldsymbol{r}',t')\,\middle|\,\mathrm{GS}\right\rangle, & \text{for } t > t' \\ \mathrm{i}\left\langle \mathrm{GS}\middle|\, \hat{\psi}^\dagger_{\sigma'}(\boldsymbol{r}',t')\hat{\psi}_\sigma(\boldsymbol{r},t)\,\middle|\,\mathrm{GS}\right\rangle, & \text{for } t < t' \end{cases}. \tag{3.21}$$

Although this object looks quite complicated it is quite convenient, since a lot of physical quantities can be expressed through Green's functions, e.g. spectral functions. Formerly it can also be understood as a propagator, describing the

propagation of an electron created at t' and $\boldsymbol{r}'$ and later annihilated at t and $\boldsymbol{r}$. The Green's function in that sense then describes the probability amplitude of that process. Similarly, the interpretation also holds for a hole created at t and $\boldsymbol{r}$ and later annihilated at t' and $\boldsymbol{r}'$. Combining both process by the time ordering operator T then leads to the definition of (3.20). For general operators $\hat{A}$ and $\hat{B}$, the causal Green's function takes on the same forms as above, i.e.

$$G_{\sigma\sigma'}(\boldsymbol{r},t,\boldsymbol{r}',t') = -\mathrm{i}\left\langle \mathrm{GS}\middle|\, \hat{T}\left(\hat{A}_{\mathrm{H},\sigma}(t)\hat{B}_{\mathrm{H},\sigma'}(t')\right)\middle|\,\mathrm{GS}\right\rangle, \tag{3.22}$$

where the subscript H denotes the Heisenberg picture [38].

The particle density operator $n(\boldsymbol{r})$ of a system can then be calculated via

$$n(\boldsymbol{r}) = -2\mathrm{i}\lim_{t'\to t} G(\boldsymbol{r},t,\boldsymbol{r},t'), \tag{3.23}$$

when both spins are considered. For homogeneous and isotropic system, the Green's function depends only on the difference of coordinates

$$G_{\sigma\sigma'}(\boldsymbol{r},t,\boldsymbol{r}',t') = G_{\sigma\sigma'}(\boldsymbol{r}-\boldsymbol{r}',t-t'). \tag{3.24}$$

Furthermore if the system does not include a spin dependent term, e.g. a magnetic field, the Green's function reduces to $G_{\sigma,\sigma'} = \delta_{\sigma,\sigma'}G$. The above results also hold when a Fourier transformation is applied leading to

$$G_{\sigma\sigma'}(\boldsymbol{r}-\boldsymbol{r}',t-t') = \int \frac{\mathrm{d}^3\boldsymbol{k}\mathrm{d}\omega}{(2\pi)^4} G(\boldsymbol{k},\omega)\mathrm{e}^{\mathrm{i}[\boldsymbol{k}\cdot(\boldsymbol{r}-\boldsymbol{r}')-\omega(t-t')]}, \tag{3.25}$$

which allows us to express thermodynamic properties, such as the thermodynamic potential Ω, in terms of Green's functions. At $T = 0$, where $\mathrm{d}\Omega = -\mu\mathrm{d}N$ one finds

$$\Omega(\mu) = 2\mathrm{i}V\int_0^{\mu}\mathrm{d}\mu' \lim_{t\to-\infty}\int G(\boldsymbol{p},\omega)\mathrm{e}^{-\mathrm{i}\omega t}\frac{\mathrm{d}\omega\mathrm{d}^3\boldsymbol{k}}{(2\pi)^4}. \tag{3.26}$$

Note that for simplicity the Planck constant $\hbar$ was assumed to be 1, otherwise it would appear in the denominator in definition (3.20) [38–40].

Green's function for non-interacting particles

In the case of non-interacting particles (here fermions) an explicit form of the Green's function can be derived by expressing the field operators in terms of plane waves

$$\hat{\psi}_\sigma(\boldsymbol{r},t) = \frac{1}{\sqrt{V}} \sum_{\boldsymbol{k}} \mathrm{e}^{\mathrm{i}(\boldsymbol{k}\cdot\boldsymbol{r}-\varepsilon_0(\boldsymbol{k})t)} a_{\boldsymbol{k}\sigma}, \tag{3.27}$$

where $a_{\boldsymbol{k},\sigma}$ is an annihilation operator of a electron of spin σ, V the system volume and $\varepsilon_0(\boldsymbol{k})$ is the bare spectrum of the non-interacting particles. Using definition (3.20) gives the free fermion Green's function

$$\begin{aligned} G_0(\boldsymbol{r},t) &= -\mathrm{i}\left\langle \hat{T}\left(\hat{\psi}_\sigma(\boldsymbol{r},t), \hat{\psi}^\dagger_{\sigma'}(0,0)\right)\right\rangle \\ &= -\frac{\mathrm{i}}{V}\sum_{\boldsymbol{k},\boldsymbol{k}'} \mathrm{e}^{\mathrm{i}(\boldsymbol{k}\cdot\boldsymbol{r}-(\varepsilon_0(\boldsymbol{k})-\mu)t)} \left\langle \hat{T}\left(\hat{a}_{\boldsymbol{k}}\hat{a}^\dagger_{\boldsymbol{k}'}\right)\right\rangle \\ &= -\frac{\mathrm{i}}{V}\sum_{\boldsymbol{k}} \mathrm{e}^{\mathrm{i}(\boldsymbol{k}\cdot\boldsymbol{r}-(\varepsilon_0(\boldsymbol{k})-\mu)t)} \times \begin{cases} 1-f_{\boldsymbol{k}}, & t>0 \\ -f_{\boldsymbol{k}}, & t<0, \end{cases} \end{aligned}$$

where $f_{\boldsymbol{k}} = \langle c^\dagger_{\boldsymbol{k}} c_{\boldsymbol{k}}\rangle = \Theta(\varepsilon_0(\boldsymbol{k})-\mu)$ is the Fermi distribution function, which for $T=0$ takes on the values 1 if $|\boldsymbol{k}|<k_\mathrm{F}$, and 0 for $|\boldsymbol{k}|>k_\mathrm{F}$, leading to

$$= -\frac{\mathrm{i}}{V}\sum_{\boldsymbol{k}} \mathrm{e}^{\mathrm{i}(\boldsymbol{k}\cdot\boldsymbol{r}-(\varepsilon_0(\boldsymbol{k})-\mu)t)} \left(\Theta(t)(1-f_{\boldsymbol{k}}) - \Theta(-t)f_{\boldsymbol{k}}\right)$$

and applying a Fourier transformation

$$G_0(\boldsymbol{k},t) = \frac{1}{\omega - (\varepsilon_0(\boldsymbol{k})-\mu) + i\,\delta\,\mathrm{sign}(\varepsilon_0(\boldsymbol{k})-\mu)}, \tag{3.28}$$

where the term $\mathrm{i}\delta$ is an infinitesimal number indicating in what half-plane of complex frequency the integrals converge [38–41].

The non-interacting Green's function (3.28), coincides with the mathematical definition of a Green's function from the theory of linear differential equation, since it obey the (differential) equation

$$(\mathrm{i}\partial_t - \varepsilon_0(\boldsymbol{k}))\, G_0(\boldsymbol{k},t) = \delta(t). \tag{3.29}$$

In the interacting case the equation is in general nonlinear, so the framing would not be accurate. Nevertheless within solid state physics or field theory it is common to still speak of Green's functions [41].

From equation (3.28) it can be seen that the poles of the Green's function describe excitations, so called quasi particle excitations, which is also true for interacting Green's function. Hereby the real part of the poles gives then energy and the imaginary part the the lifetime of a quasi particle. While for the non-interacting case this lifetime would be infinite, due to a delta peak of width $\to 0$, in the interacting one it is finite (due to the finite peak width). Here the quasi particle picture holds, if the lifetime of these particles is not to long. In general close to pole the following holds

$$G(\boldsymbol{k},\omega) \simeq \frac{Z_{\boldsymbol{k}}}{\omega - \varepsilon(\boldsymbol{k}) + \mathrm{i}\gamma}, \tag{3.30}$$

where $\varepsilon(\boldsymbol{k})$ can be interpreted as the quasi particle dispersion (energy), γ its lifetime, and $Z_{\boldsymbol{k}} \leq 1$ the weight of the real electron in the quasi particle. In interacting systems the excitations are then called quasi particles, which can be interpreted as renormalized, electron excitations [14, 38–41].

Lehmann representation and spectral density

On can show that the Green's function $G(\boldsymbol{k},\omega)$ and the spectral function $A(\boldsymbol{k},\omega)$ are connected via

$$G(\boldsymbol{k},\omega) = \int_{-\infty}^{\infty} \frac{A(\boldsymbol{k},\omega)}{\omega - \omega' + \mathrm{i}\,\omega'\,\delta}\,\mathrm{d}\omega', \tag{3.31}$$

which is also known as spectral representation. For an ideal Fermi gas, i.e. see Green's function (3.28), the spectral function is

$$A(\boldsymbol{k},\omega) = \delta(\omega - (\varepsilon_0(\boldsymbol{k}) - \mu)). \tag{3.32}$$

Essentially this is a delta function at the position of the pole, i.e. quasi particle excitation. Of course for non-interacting systems the $A(\boldsymbol{k},\omega)$ will differ from this

simple form. Nonetheless the spectral peak of finite width,can be interpreted as a quasi particle [38, 39].

One important form of the Green's function, which can be derived from its definition, is the Lehmann representation of the retarded Green's function

$$G^{\mathrm{ret}}(\boldsymbol{k},\omega) = \frac{1}{\Xi}\sum_{n,m}\frac{|\langle m|c_{\boldsymbol{k}}^{\dagger}|n\rangle|^2}{\omega + E_n - E_m + \mathrm{i}\,\delta}\left(\mathrm{e}^{-\beta E_n} + \mathrm{e}^{-\beta E_m}\right), \tag{3.33}$$

where $|n\rangle$ and $|m\rangle$ are the corresponding eigenstates of the systems Hamiltonian with eigenvalues E_n and E_m. The Lehmann representation allows us to connect the spectral representation of the Green's function with the spectral function via

$$A(\boldsymbol{k},\omega) = \frac{1}{\Xi}\sum_{n,m}|\langle m|c_{\boldsymbol{k}}^{\dagger}|n\rangle|^2\left(\mathrm{e}^{-\beta E_n} + \mathrm{e}^{-\beta E_m}\right)\delta(\omega + E_n - E_m). \tag{3.34}$$

For a given ground state $|\mathrm{GS}\rangle$ containing N particles and $T = 0$, then the states $|m\rangle$ (or $|n\rangle$) are all from the $N \pm 1$ particle sector with corresponding energies $E^{N\pm1}$. Hence the spectral function can be expressed in a electron removal and addition part of the form

$$A(\boldsymbol{k},\omega) \propto \sum_{m}|\langle m|c_{\boldsymbol{k}}^{\dagger}|\mathrm{GS}\rangle|^2\delta(\omega - E_m^{N+1}) + |\langle m|c_{\boldsymbol{k}}|\mathrm{GS}\rangle|^2\delta(\omega - E_m^{N-1}). \tag{3.35}$$

Here the positive part of A ($\omega > A$) the creation (addition) of an electron to the system , while the right part $\omega < 0$ an annihilation (removal) of the electron. This representation is especially helpful, when compared to the experimental spectral function. Lets first consider first the positive frequency part of $A(\boldsymbol{k},\omega)$. The probability of finding the system in the state with energy ω is

$$P_{\omega}(\boldsymbol{k})\mathrm{d}\omega = \int_{\omega}^{\omega+\mathrm{d}\omega} A(\boldsymbol{k},\omega')\mathrm{d}\omega', \tag{3.36}$$

and this gives the intensity of the spectrum of angle-resolved inverse photoemission (IPES) spectroscopy. The negative frequency $A(\boldsymbol{k},\omega)$ on the other hand gives then the angle-resolved photoemission (ARPES) spectrum [38].

3.2 Matsubara Theory

The single-particle Matsubara function, as defined vide infra, is a key part in the quantum field theoretical representation of solid states physics, precisely because of its powerful diagrammatic representation. Despite its abstract shape it is often not the quantity of interest, it can rather be seen as an extremely useful tool from whom we can easily determine physical quantities, like the spectral density or thermodynamic expectation values. This section follows the textbooks [14, 39–41].

3.2.1 Definition

The single-particle Matsubara function or temperature Green's function is defined as

$$G_{\alpha\beta}(\tau) \equiv -\left\langle T_\tau \left(c_\alpha(\tau) c_\beta^\dagger(0) \right) \right\rangle, \tag{3.37}$$

where T_τ is the time ordering operator and τ is called complex time (although $\tau \in \mathbb{R}$) and $-\beta < \tau < \beta = 1/k_\mathrm{B}T$. For a system of bosons or fermions the time ordering operator is defined as

$$T_\tau \left(c_{\alpha_1}^\dagger(\tau_1) c_{\alpha_2}^\dagger(\tau_2) \dots \right) \equiv \varepsilon^P c_{\alpha_{P(1)}}^\dagger(\tau_{P(1)}) c_{\alpha_{P(2)}}^\dagger(\tau_{P(2)}) \dots, \tag{3.38}$$

where is $\varepsilon = \pm 1$ (1 for bosons and -1 for fermions), P the number of permutation, and $P(\bullet)$ indicates the permutation operator. It enforces time ordering onto the creation or annihilation operators in the following manner

$$\tau_{P(1)} > \tau_{P(2)} > \dots. \tag{3.39}$$

Roughly speaking it ensures that operators of earlier time act earlier. The creation and annihilation operators are represented in the Heisenberg picture which is given in the imaginary time τ notation via

$$A(\tau) = \mathrm{e}^{\mathcal{H}\tau} A \mathrm{e}^{-\mathcal{H}\tau}, \tag{3.40}$$

and $A = c, c^\dagger$. In this modified Heisenberg picture a quantity $A(\tau)$ fulfills a Bloch equation

$$-\partial_\tau A(\tau) = [A(\tau), \mathcal{H}]_- . \tag{3.41}$$

It should be noted that the correlation function in the imaginary time expression is in principal achieved with a Wick-Rotation. This will be important since it is then easily possible to express a time dependent correlation function of the form $\langle A(\tau)B(0)\rangle$ as series expansion of the interaction part of a Hamiltonian $\mathcal{H}$. Furthermore it will be easy to develop a diagrammatic expansion.

Furthermore it can be shown that the single-particle Matsubara function fulfills the subsequent properties:

- $G_{\alpha\beta}(\tau)$ is unsteady at zero temperature, i.e. $G_{\alpha\beta}(0^+) - G_{\alpha\beta}(0^-) = -\delta_{\alpha\beta}$.
- Since

$$\begin{aligned}\Xi \left\langle c_\alpha \tau_1 c_\beta^\dagger(\tau_2)\right\rangle &= \Xi \,\mathrm{tr}\left[\mathrm{e}^{-\beta\mathcal{H}}\mathrm{e}^{\mathcal{H}\tau_1} c_\alpha \mathrm{e}^{-\mathcal{H}\tau_1}\mathrm{e}^{\mathcal{H}\tau_2} c_\beta^\dagger \mathrm{e}^{-\mathcal{H}\tau_2}\right] \\ &= \Xi \left\langle c_\alpha(\tau_1 - \tau_2) c_\beta^\dagger\right\rangle\end{aligned}$$

  we find

$$G_{\alpha\beta}(\tau_1 - \tau_2) = -\left\langle T_\tau(c_\alpha(\tau_1) c_\beta^\dagger(\tau_2))\right\rangle , \tag{3.42}$$

  for $-\beta < \tau_1 - \tau_2 < \beta$, which shows the homogeneity of the Matsubara function for an explicitly time independent Hamiltonian $\mathcal{H}$.

For a diagrammatic representation it is common to introduce an energy dependent expression of the Matsubara function. Since this can be found in standard text books, such as [14, 41], we will restrict ourselves just on the results. These are

$$G_{\alpha\beta}(\tau) = \frac{1}{\beta}\sum_{n=-\infty}^{\infty} \mathrm{e}^{-\mathrm{i}E_n\tau} G_{\alpha\beta}(\mathrm{i}E_n), \tag{3.43a}$$

$$G_{\alpha\beta}(\mathrm{i}E_n) = \int_0^\beta G_{\alpha\beta}(\tau)\mathrm{e}^{\mathrm{i}E_n\tau}\mathrm{d}\tau, \tag{3.43b}$$

with the Masubara energies

$$\mathrm{i}E_n = \begin{cases} \mathrm{i}(2n+1)\frac{\pi}{\beta}, & \text{Fermions} \\ \mathrm{i}2n\frac{\pi}{\beta}, & \text{Bosons} \end{cases} \tag{3.44}$$

and $n \in \mathbb{Z}$. Here $G_{\alpha\beta} \equiv a^{(n)}_{\alpha\beta}$ are the Fourier coefficients.

3.2.2 Spectral representation

The spectral representation of the Matsubara function (3.37) will show a direct correspondence to the energy dependent expressions (3.43). Assume that E_r and E_s are eigenenergies of a Hamiltonian $\mathcal{H}$. Then $|r\rangle$ and $|s\rangle$ are the corresponding eigenstates. We find

$$\begin{aligned} G_{\alpha\beta}(\mathrm{i}E_n) &= \int_0^\beta G_{\alpha\beta}(\tau)\mathrm{e}^{\mathrm{i}E_n\tau}\mathrm{d}\tau \\ &= -\sum_{r,s}\int_0^\beta \mathrm{e}^{(\mathrm{i}E_n+E_r-E_s)\tau}\mathrm{d}\tau\frac{1}{\Xi}\langle r|c_\alpha|s\rangle\langle s|c^\dagger_\beta|r\rangle \end{aligned}$$

with $\mathrm{e}^{\mathrm{i}\beta E_n} = \varepsilon$ and explicitly solving the integral leads to

$$\begin{aligned} &= -\frac{1}{\Xi}\sum_{r,s}\frac{\left(\mathrm{e}^{-\beta(E_s-E_r)}\varepsilon - 1\right)}{\mathrm{i}E_n - (E_s-E_r)}\langle r|c_\alpha|s\rangle\langle s|c^\dagger_\beta|r\rangle \\ &= \frac{1}{\Xi}\sum_{r,s}\mathrm{e}^{-\beta E_r}\left(1-\varepsilon\mathrm{e}^{-\beta(E_s-E_r)}\right)\frac{\langle r|c_\alpha|s\rangle\langle s|c^\dagger_\beta|r\rangle}{\mathrm{i}E_n-(E_s-E_r)}. \end{aligned} \tag{3.45}$$

Compared with the single-particle spectral function

$$A_{\alpha\beta}(E) = \frac{1}{\Xi}\sum_{r,s}\mathrm{e}^{-\beta E_r}\left(1-\varepsilon\mathrm{e}^{-\beta(E_s-E_r)}\right)\langle r|c_\alpha|s\rangle\langle s|c^\dagger_\beta|r\rangle\,\delta(E-(E_s-E_r)). \tag{3.46}$$

it is straightforward to find the spectral representation of (3.37) as

$$G_{\alpha\beta}(\mathrm{i}E_n) = \int_{-\infty}^{\infty}\frac{A_{\alpha\beta}(E')}{\mathrm{i}E_n - E'}\mathrm{d}E'. \tag{3.47}$$

From a given Matsubara function we can directly get the spectral density via the substitution $\mathrm{i}E_n \to E + \mathrm{i}0^+$

$$A_{\alpha\beta}(E) = \mp\frac{1}{\pi}\mathrm{Im}\left[G_{\alpha\beta}(E\pm\mathrm{i}0^+)\right]. \tag{3.48}$$

Moreover we can define the retarded Green's function as

$$G^{\text{ret}}_{\alpha\beta}(E) \equiv G_{\alpha\beta}(E + \mathrm{i}0^+) \tag{3.49}$$

and the advanced Green's function

$$G^{\text{a}}_{\alpha\beta}(E) \equiv G_{\alpha\beta}(E - \mathrm{i}0^+). \tag{3.50}$$

In both cases is $E \in \mathbb{R}$ and one finds

$$A_{\alpha\beta}(E) = -\frac{1}{\pi}\text{Im}\left[G^{\text{ret}}_{\alpha\beta}(E)\right] = \frac{1}{\pi}\text{Im}\left[G^{\text{a}}_{\alpha\beta}(E)\right]. \tag{3.51}$$

3.3 Dyson equation and self-energy

So far we concentrate on non-interacting systems, leading to a Green's function of the form (3.28). This however will change when interaction, e.g Coulomb interaction is included. When treated via perturbation theory, where the interaction is treated a small perturbation upon the system, the corresponding terms can be interpreted in the framework of Feynman diagrams. Therefore the Hamiltonian is assumed to be $\mathcal{H} = \mathcal{H}_0 + \mathcal{H}_{\text{int}}$, where H_0 is the non-interaction (single-particle) part and the second term is the small perturbation. Note that for the actual expansion the field operators are expressed in the interaction representation, i.e. $\hat{\psi}_{\text{H}}(t) = \mathrm{e}^{\mathrm{i}\mathcal{H}_0 t}\hat{\psi}(0)\mathrm{e}^{-\mathrm{i}\mathcal{H}_0 t}$. A rigorous derivation and corresponding expansion rules can be found in [14, 39–41]. From the diagrammatic expansion of electron Green's function for the electron-electron interaction the following lowest order diagrams

can be found

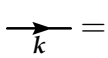

$$= G_0(\boldsymbol{k}) \tag{3.52a}$$

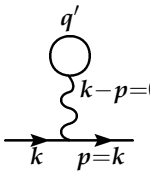

$$= (-2\mathrm{i})G_0(\boldsymbol{k}) \int V(0)G_0(\boldsymbol{q})\frac{\mathrm{d}^4\boldsymbol{q}}{(2\pi)^4}G_0(\boldsymbol{k}) \tag{3.52b}$$

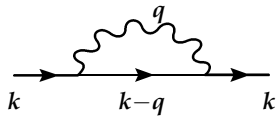

$$= \mathrm{i}G_0(\boldsymbol{k}) \int G_0(\boldsymbol{p}-\boldsymbol{q})V(q)\frac{\mathrm{d}^4\boldsymbol{q}}{(2\pi)^4}G_0(\boldsymbol{k}) \tag{3.52c}$$

Here the diagram ⟶ denotes the single-particle Green's function $G_0(\boldsymbol{k})$, the second term (3.52b) the Hartree term of the Coulomb interaction, and term (3.52c) the Fock term. The full Green's function $G(\boldsymbol{k})$ will be indicated by ⟹, so the full expansion looks like

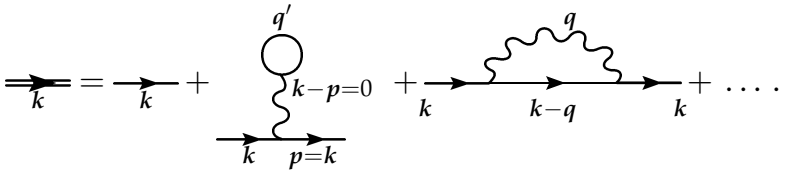

(3.53)

Although here only the lowest order diagrams are shown, often a summation over an infinite number of diagrams (of a certain class) is necessary. A convenient way of doing so is via Dyson equations

$$G = G_0 + G_0\Sigma_0 G_0 + G_0\Sigma_0 G_0\Sigma_0 G_0 + \dots\,, \tag{3.54}$$

where we introduced a new quantity, the self-energy $\Sigma_0(\boldsymbol{k},\omega)$, which is of the form

$$\Sigma_0(\boldsymbol{k},\omega) = \frac{1}{(2\pi)^4}\int V(\boldsymbol{q},\omega)G_0(\boldsymbol{k}-\boldsymbol{q},\omega-\omega')\mathrm{d}^3\boldsymbol{q}\mathrm{d}\omega'. \tag{3.55}$$

In terms of Feynman diagrams the self-energy will be illustrated as ◯ = Σ, leading to a representation of equation (3.54) as

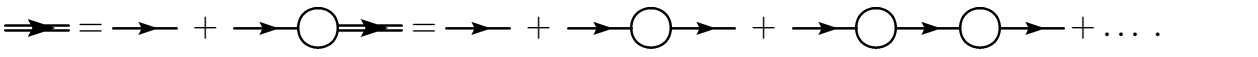

(3.56)

So far the summation is was only considered over the lowest order diagram. Hence also Σ_0 is only the lowest contribution of the self energy. When summed over all diagrams the notation changes as follows

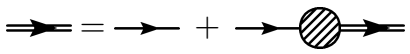

$$= + , \tag{3.57a}$$

$$G(\boldsymbol{k},\omega) = G_0(\boldsymbol{k},\omega) + G_0(\boldsymbol{k},\omega)\,\Sigma(\boldsymbol{k},\omega)\,G(\boldsymbol{k},\omega), \tag{3.57b}$$

where $\Sigma =$  is now the full self-energy. The Dyson equation (3.57b) can then be solved by

$$G(\boldsymbol{k},\omega) = \frac{1}{\omega - \varepsilon(\boldsymbol{k}) - \Sigma(\boldsymbol{k},\omega) + \mathrm{i}\delta}. \tag{3.58}$$

The introduction of the self-energy has some important consequences, concerning its interpretation. When compared to the non-interacting case where we interpreted the poles as quasi particle excitations, the self-energy in the interacting case, can be understood as a fudge factor taking into account correlation arising from the interaction. In that sense the electronic features are still present, however changed by $\Sigma(\boldsymbol{k},\omega)$ due to additional interactions. When expressed as real- and imaginary part $\Sigma(\boldsymbol{k},\omega) = R(\boldsymbol{k},\omega) + \mathrm{i}I(\boldsymbol{k},\omega)$, it can be shown that the following relations holds for small ω values

$$R(\boldsymbol{k},\omega) = \alpha_{\boldsymbol{k}} + \beta_{\boldsymbol{k}}\omega + \mathcal{O}(\omega^2), \qquad I(\boldsymbol{k},\omega) = \gamma_{\boldsymbol{k}}\omega^2 + \mathcal{O}(\omega^3), \tag{3.59}$$

where α, β, and γ are some $\boldsymbol{k}$ dependent expansion coefficients. Nonetheless we obtain the important Fermi liquid like features, a linear real part and quadratic imaginary part for small energies. Moreover the self-energy connects the life time and effective mass of a quasi particle. A nice introduction into this can be found in [14, 38].

Chapter 4 Transition metal oxides

Transition metal oxides (TMOs) are a wide class of compounds, where transition metal ions are embedded in a network of oxygen atoms. These compounds present a unique class of solids which show a plethora of physical phenomena mostly derived from their partially filled d shells. One of the most prominent examples are probably the metal-to-insulator transition [20] and high-temperature superconductivity, which triggered a huge amount of research activity within the last decades.

4.1 Transition metal ions in a solid – cubic symmetry (O_h)

When a transition metal ion is put into a crystal, where it is surrounded by ligands, e.g. oxygens, the electronic states will be modified. The resulting crystal-field, stemming from the ligands, breaks the spherical symmetry and splits the *d*-orbitals of the transition metal ions via Δ_{CF}. Within this section we only focus on a d^1 configuration, since it is conceptually easier to treat.

4.1.1 Cubic Symmetry O_h

For perovskites or double perovskites the transition metal ions are surrounded by an octahedral cage of oxygen anions resulting in a splitting of the *d*-orbital (see

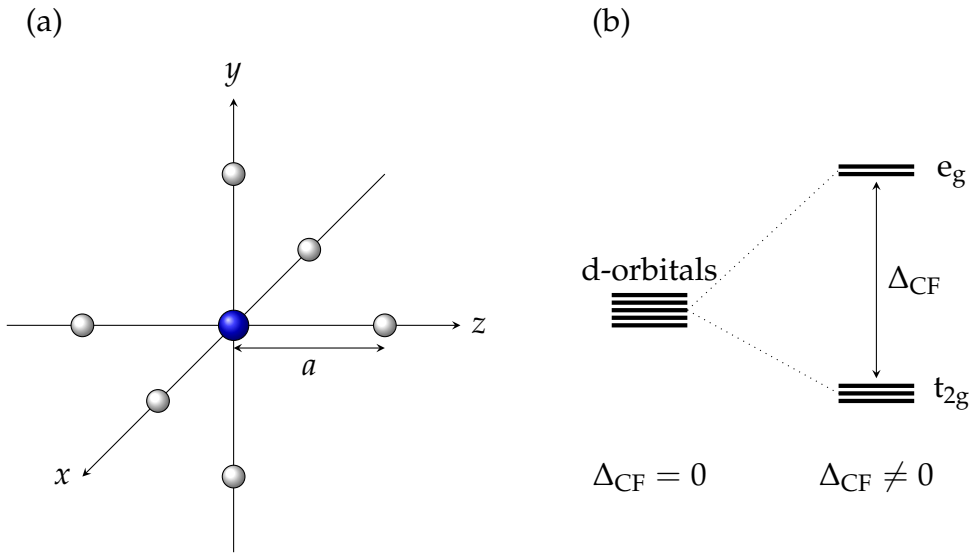

■ **Figure 4.1.:** (a) A single *d*-electron in a cubic crystal-field. The Ligands are white and the hydrogen atom is blue. (b) *d*-orbitals with and without cubic crystal-filed splitting. As depicted the resulting e_g level is four-fold degenerate and the t_{2g} level is six-fold degenerate. The blue box is the remaining system of interest (see text).

figure 4.1 (b)) into a four-fold degenerate e_g-manifold and six-fold t_{2g} manifold.

Assume a single *d*-electron in a cubic crystal-field as shown in figure 4.1 (a). The blue electron (hydrogen atom) is surrounded by six ligands or charges from which the crystal-field arises. It should be noted that $\boldsymbol{R}_i$ are the vectors pointing to the six ligands

$$\begin{aligned}
\boldsymbol{R}_1 &= \begin{pmatrix} a & 0 & 0 \end{pmatrix}^T = -\boldsymbol{R}_4, \\
\boldsymbol{R}_2 &= \begin{pmatrix} 0 & a & 0 \end{pmatrix}^T = -\boldsymbol{R}_5, \\
\boldsymbol{R}_3 &= \begin{pmatrix} 0 & 0 & a \end{pmatrix}^T = -\boldsymbol{R}_6,
\end{aligned}$$

and Z obeys the convention

$$Z = \begin{cases} > 0, & \text{negative charge}, \\ < 0, & \text{positive charge}. \end{cases} \tag{4.1}$$

The stationary Schrödinger equation of the sketched problem is given via

$$\left[-\frac{\hbar^2}{2m}\boldsymbol{\nabla}^2 + U(r) + V_C(\boldsymbol{r})\right]\phi(\boldsymbol{r}) = E\phi(\boldsymbol{r}), \tag{4.2}$$

where $U(r)$ is the potential energy due to the field of the hydrogen nucleus, $\phi(\boldsymbol{r})$ the wavefunction, and E the corresponding energy eigenvalue. In order to solve the Schrödinger equation, perturbation theory is used,. The crystal-field is assumed to be small perturbation of the hydrogen atom. An explicit form of the crystal-field V_C can be derived when expanded in terms of Legendre-polynomials

$$V_C(\boldsymbol{r}) = Ze^2 \sum_{i=1}^{6}\sum_{k=0}^{\infty}\left(\frac{r_<^k}{r_>^{k+1}}\right) P_k(\cos\omega_i), \tag{4.3}$$

where $P_k(\bullet)$ are the Legendre-polynomial. A simplification of this equation is achievable when we assume that a is much larger than the radius of the hydrogen atom, so the replacement $r_< \to r$ and $r_> \to a$ holds. This leads to the expression

$$V_C(\boldsymbol{r}) = \frac{Ze^2}{a}\sum_{i=1}^{6}\sum_{k=0}^{\infty}\left(\frac{r}{a}\right)^k P_k(\cos\omega_i), \tag{4.4}$$

Further we will use the addition theorem

$$P_k(\cos\omega_i) = \frac{4\pi}{2k+1}\sum_{m=-k}^{k} Y_m^{(k)}(\theta,\phi)Y^{*(k)}_m(\theta_i,\phi_i),$$

where $Y_{km}(\theta,\phi)$ are the spherical harmonics fulfilling the relation

$$Y^{*(k)}_m(\theta,\phi) = (-1)^m Y^{(k)}_{-m}(\theta,\phi).$$

A short calculations shows

$$V_C(\boldsymbol{r}) = \sum_{k=0}^{\infty}\sum_{m=-k}^{k} r^k \underbrace{\sqrt{\frac{4\pi}{2k+1}}\frac{Ze^2}{a^{k+1}}\left(\sum_{i=1}^{6} Y^{*(k)}_m(\theta_i,\phi_i)\right)}_{\equiv q_{km}} \underbrace{\sqrt{\frac{4\pi}{2k+1}}Y_m^{(k)}(\theta,\phi)}_{\equiv C_m^{(k)}(\theta,\phi)} \tag{4.5}$$

$$= \sum_{k=0}^{\infty}\sum_{k=-k}^{k} r^k q_{km} C_m^{(k)}(\theta,\phi) \tag{4.6}$$

Expressed in spherical coordinates, the six Ligands are given by

$$\begin{aligned}(\theta_1,\phi_1) &= (\pi/2,0), & (\theta_2,\phi_2) &= (\pi/2,\pi),\\ (\theta_3,\phi_3) &= (\pi/2,\pi/2), & (\theta_4,\phi_4) &= (\pi/2,-\pi/2),\\ (\theta_5,\phi_5) &= (0,0), & (\theta_6,\phi_6) &= (\pi,0).\end{aligned}$$

Using the definition of the spherical harmonics shows that

$$q_{km} = \begin{cases} 0, & m \text{ odd} \\ \neq 0, & m \text{ even} \end{cases} \tag{4.7}$$

A rather cumbersome calculation leads to the crystal-field potential

$$V_C(\boldsymbol{r}) = \frac{6Ze^2}{a}\left[1 + \frac{7r^4}{12a^4}\left\{C_0^{(4)} + \sqrt{\frac{5}{14}}\left[C_4^{(4)} + C_{-4}^{(4)}\right]\right\} + \frac{r^6}{8a^6}\{\ldots\} + \ldots\right], \tag{4.8}$$

where the brackets $\{\ldots\}$ contain combinations of the $C_m^{(k)}(\theta,\phi)$ terms with $m \in \{4,0,-4\}$ and $k \in \{\pm 6\}$, i.e. higher orders which will be neglected for the further calculation. Since the first term is just an energy shift a modified potential can defined as

$$V_C^0 = V_C - \frac{6Ze^2}{a}. \tag{4.9}$$

Expressed in Cartesian coordinates the crystal-field potential is of the form

$$V_C^0 = \frac{35Ze^2}{4a^5}\left[x^4 + y^4 + z^4 - \frac{3}{5}r^4\right]. \tag{4.10}$$

Subsequently we treat this potential as a small perturbation of the well known hydrogen atom with the known solutions

$$\phi_{nlm}(\boldsymbol{r}) = R_{nl}(\boldsymbol{r})Y_m^{(l)}(\theta,\phi). \tag{4.11}$$

Hence we can calculate the matrix elements of V_C^0 via

$$\langle nlm|V_C^0|n'l'm'\rangle = \int \mathrm{d}\boldsymbol{r}\, \phi_{nlm}^*(\boldsymbol{r})V_C^0(\boldsymbol{r})\phi_{n'l'm'}(\boldsymbol{r}). \tag{4.12}$$

For the calculation it is useful to know that terms of the form

$$c^k(l'm';l''m'') = \int \mathrm{d}\phi\mathrm{d}\theta\, Y^{*(l')}_{m'}(\theta,\phi) C^{(k)}_m(\theta,\phi) Y^{(l')}_{m''}(\theta,\phi)\sin\theta \tag{4.13}$$

are not vanishing if

- from ϕ-integration: $m = m' - m''$,
- $k + l + l'$ = even and $|l - l'| \le k \le l + l'$.

As a consequence there are no contributions by the p-state and from the d-states proportional to r^k ($k > 4$). Non-vanishing matrixelements with $l = l' = 2$ and $n = n'$ are

$$\langle n,2,\pm 2|V_C^0|n,2,\pm 2\rangle = Dq, \qquad \langle n,2,\pm 1|V_C^0|n,2,\pm 1\rangle = -4Dq,$$
$$\langle n,2,0|V_C^0|n,2,0\rangle = 6Dq, \qquad \langle n,2,\pm 2|V_C^0|n,2,\mp 2\rangle = 5Dq,$$

with $D = 35Ze^2/4a^5$, $q = (2/105)\langle r^4\rangle_{n,2}$, and

$$\langle r^m\rangle_{n,2} = \int \mathrm{d}r\, r^{2+m}|R_{n,2}(\boldsymbol{r})|^2.$$

The energy levels are obtained from the resulting perturbation matrix

$$\langle nlm|V_C^0|n'l'm'\rangle = \begin{vmatrix} Dq & 0 & 0 & 0 & 5Dq \\ 0 & -4Dq & 0 & 0 & 0 \\ 0 & 0 & 6Dq & 0 & 0 \\ 0 & 0 & 0 & -4Dq & 0 \\ 5Dq & 0 & 0 & 0 & Dq \end{vmatrix}.$$

Considering the energy shift one finds $E_3^{(0)} = E_3 + 6Ze^2/a$. The eigenvalues are then given by

$$E_1 = E_3^{(0)} + 6Dq, \quad E_2 = E_3^{(0)} - 4Dq, \tag{4.14}$$

where E_1 is doubly-, and E_2 triply degenerate. It is common to call the triply degenerate states t_{2g}-orbitals and the doubly degenerate states e_g-orbitals. The

corresponding eigenstates are then

$$e_g\text{-states:} \quad \phi_{3,2,0}(\boldsymbol{r}), \quad \frac{\phi_{3,2,2}(\boldsymbol{r}) + \phi_{3,2,-2}(\boldsymbol{r})}{\sqrt{2}}, \tag{4.15a}$$

$$t_{2g}\text{-states:} \quad \phi_{3,2,1}(\boldsymbol{r}), \quad \phi_{3,2,-1}(\boldsymbol{r}), \quad \frac{\phi_{3,2,2}(\boldsymbol{r}) - \phi_{3,2,-2}(\boldsymbol{r})}{\sqrt{2}}. \tag{4.15b}$$

Instead of working with complex eigenstates of the t_{2g}-orbitals it is convenient to apply a unitary transformation U within this subspace to find real eigenstates. The unitary transformation reads

$$\phi_\gamma = \sum_i U_{i\gamma}\phi_i \tag{4.16}$$

with

$$U = \frac{1}{\sqrt{2}} \begin{pmatrix} \mathrm{i} & -1 & 0 \\ \mathrm{i} & 1 & 0 \\ 0 & 0 & -\sqrt{2}\mathrm{i} \end{pmatrix}. \tag{4.17}$$

The matrix is sorted in the way it is presented in equation (4.15b). The real forms

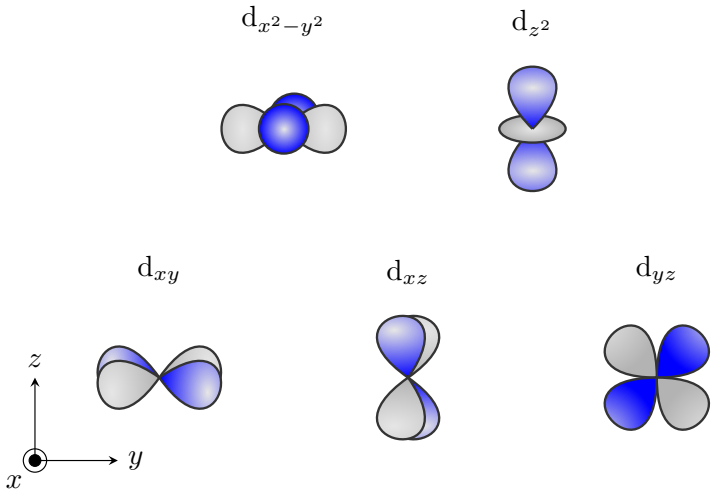

Figure 4.2.: Visualization of the d orbitals as given in equation (4.15b) and (4.15a). In presence of a cubic crystal field, the upper two orbitals are the e_g orbitals and the lower three the t_{2g} orbitals.

are then

$$\begin{aligned}\phi_{yz} &= \frac{\mathrm{i}}{\sqrt{2}}(\phi_{3,2,1} + \phi_{3,2-1}) \\ &= \sqrt{\frac{15}{4\pi}}\sin(\theta)\cos(\theta)\sin(\phi)R_{32}(r) = \sqrt{\frac{15}{4\pi}}\frac{zy}{r^2}R_{32}(r), \qquad (4.18a)\\ \phi_{xz} &= -\frac{1}{\sqrt{2}}(\phi_{3,2,1} - \phi_{3,2-1}) \\ &= \sqrt{\frac{15}{4\pi}}\sin(\theta)\cos(\theta)\cos(\phi)R_{32}(r) = \sqrt{\frac{15}{4\pi}}\frac{zx}{r^2}R_{32}(r), \qquad (4.18b)\\ \phi_{xy} &= -\frac{\mathrm{i}}{\sqrt{2}}(\phi_{3,2,2} - \phi_{3,2-2}) \\ &= \sqrt{\frac{15}{4\pi}}\sin^2(\theta)\cos(\phi)\sin(\phi)R_{32}(r) = \sqrt{\frac{15}{4\pi}}\frac{xy}{r^2}R_{32}(r). \qquad (4.18c)\end{aligned}$$

From the last term of each line it is self-explanatory why the subscript is chosen the way it is. Similarly, we can proceed with the e_g-states, which are already real functions

$$\begin{aligned}\phi_{3z^2-r^2} &= \phi_{3,2,0} \\ &= \sqrt{\frac{5}{16\pi}}(3\cos^2(\theta) - 1)R_{32}(r) = \sqrt{\frac{5}{16\pi}}\frac{(3z^2 - r^2)}{r^2}R_{32}(r), \qquad (4.19a)\\ \phi_{x^2-y^2} &= \frac{1}{\sqrt{2}}\left(\phi_{3,2,2}(\boldsymbol{r}) + \phi_{3,2,-2}(\boldsymbol{r})\right) \\ &= \sqrt{\frac{15}{16\pi}}\sin^2(\theta)\cos(2\phi)R_{32}(r) = \sqrt{\frac{15}{16\pi}}\frac{(x^2 - y^2)}{r^2}R_{32}(r). \qquad (4.19b)\end{aligned}$$

Plotting the angular part leads the well known plots of the $d-$orbitals as visualized in figure 4.2.

4.1.2 Group theoretical details

Using the symmetries of a crystal-field often helps us to find out whether orbital levels, such as the d-orbitals, are split into subspaces or not. As we will see below in the case of a cubic field the d-levels are split in a triply- and doubly degenerate level. However, by symmetry arguments alone, it is not possible to predict the magnitude of this splitting. This is for example done by using degenerate perturbation theory as in the previous section.

To find the irreducible representation one starts with the transformation of a function $f(\boldsymbol{r})$ by a symmetry operation R. The function $f(\boldsymbol{r})$ for example is an electron contribution or the crystal-field. The symmetry operation R could be a rotation. Via the symmetry operation R, a point P whose coordinate is $\boldsymbol{r}$ is transformed to the point P' whose coordinates are given by $\boldsymbol{r}'$

$$\boldsymbol{r}' = R\boldsymbol{r}.$$

In the case of the cubic crystal-field typical symmetry operations R are given by rotation around the x-, y-, or z- axes by angles of $n \cdot \pi/2$ and $n \in \{1,2,3,4\}$. A rotation around the z-axis by $\pi/2$ is denoted as $C_4(z)$, where the subscript 4 denotes the amount of rotation needed till the starting point is reached again. Rotations by π or $3\pi/2$ are in this sense denoted as $C_4^2(z)$ or $C_4^3(z)$. Including also rotation around other axis such as $[1,1,1]$ by C_3, ... there are 24 possible symmetry operations, also including the identity operation. The corresponding point group is called O-group, or octahedral group. The generating elements of this group are $C_4(z)$ and $C_4(y)$, since successive use of these elements generate all other possible symmetry elements.

Using the symmetry operation $C_4(z)$ on a function $f(\boldsymbol{r})$ one has to keep in mind, that the symmetry operation operates on the functions x, y and z instead of the coordinate. So a point P on a solid contour is transformed to point P' via

$$Rf(\boldsymbol{r}') = f(\boldsymbol{r}). \tag{4.20}$$

Since $\boldsymbol{r}' = R\boldsymbol{r}$ it is

$$Rf(\boldsymbol{r}) = f(R^{-1}\boldsymbol{r}) \tag{4.21}$$

For example if we transform $C_4(z)$ on the wavefunction ϕ_{zy} we end up with

$$C_4(z)\phi_{zy} = -\phi_{xz}. \tag{4.22}$$

This is clear, since for $C_4(z)$ the following substitution is true

$$C_4(z) = \begin{bmatrix} x \to y \\ y \to -x \\ z \to z \end{bmatrix}_{\text{funct}},$$

where the subscript "funct" refers to the operation of the transformation on the functions $\boldsymbol{r}$. Considering the vector

$$\boldsymbol{v} = \begin{pmatrix} \phi_{yz} & \phi_{xz} & \phi_{xy} & \phi_{3z^2-r^2} & \phi_{x^2-y^2} \end{pmatrix}^T, \tag{4.23}$$

then we can express the transformation $C_4(z)$ as

$$C_4(z)\boldsymbol{v} = \boldsymbol{v}D(C_4(z)), \tag{4.24}$$

where

$$D(C_4(z)) = \left[\begin{array}{ccc|cc} 0 & 1 & 0 & & \\ -1 & 0 & 0 & \multicolumn{2}{c}{0} \\ 0 & 0 & -1 & & \\ \hline & & & 1 & 0 \\ \multicolumn{3}{c|}{0} & 0 & -1 \end{array}\right]. \tag{4.25}$$

Similarly, we find for the symmetry operation $C_4(y)$ the matrix

$$D(C_4(y)) = \left[\begin{array}{ccc|cc} 0 & 0 & -1 & & \\ 0 & -1 & 0 & \multicolumn{2}{c}{0} \\ 1 & 0 & 0 & & \\ \hline & & & -\frac{1}{2} & \frac{\sqrt{3}}{2} \\ \multicolumn{3}{c|}{0} & \frac{\sqrt{3}}{2} & \frac{1}{2} \end{array}\right]. \tag{4.26}$$

In that sense the matrices $D(R)$ are called representation D of the O-group. Moreover in both cases, the t_{2g} states and e_g states are not coupled, i.e. the matrices are

of block diagonal form. More generally, $D(R)$ for any element R of the O-group can be shown to have block diagonal form with separated t_{2g} and e_g blocks. Since $C_4(z)$ and $C_4(y)$ are the generating elements of the octahedral group the representation D may be reduced to two representation of smaller dimensions

$$D = D^{T_2} + D^E. \tag{4.27}$$

From that point it should be clear that the superscript T_2 refers to the t_{2g} subspace and E to the e_g subspace. Each representation D which may be reduced to the representation of smaller dimensions is called reducible representation otherwise it is an irreducible representation. Hence D^{T_2} and D^E are irreducible representations [42, 43].

4.1.3 Spin-orbit coupling

The spin-orbit interaction has its origin in the relativistic theory. For a single electron the spin-orbit Hamiltonian part arises from the Dirac equation as

$$\mathcal{H}_{\mathrm{SOC}} = f(r)\boldsymbol{l}\cdot\boldsymbol{s}, \tag{4.28}$$

where $f(r)$ contains constants and the derivative of the spherical potential for the electron. From a semiclassical perspective this interaction can be interpreted as interaction of the magnetic moment of an electron spin with the magnetic field induced by the motion of the nucleus around the electron. Consequently spin-orbit coupling is responsible for the fine structure for multiplets. Subsequently we express the orbital momentum operator in the t_{2g}-basis. We know

$$l_z\phi_{lm}(\boldsymbol{r}) = m\phi_{lm}(\boldsymbol{r}), \quad l_\pm\phi_{lm}(\boldsymbol{r}) = \sqrt{l(l\pm1) - m(m\pm1)}\phi_{lm\pm1}(\boldsymbol{r}), \tag{4.29}$$

where

$$l_\pm = l_x \pm \mathrm{i}l_y.$$

It is then straightforward to calculate the matrices via

$$(l_\kappa)_{ij} = \langle v_i|l_\kappa|v_j\rangle\,, \quad \kappa\in\{x,y,z\},$$

and v_i is a state within the state-vector $\boldsymbol{v}$ defined as

$$\boldsymbol{v} = \begin{pmatrix} \phi_{zy} & \phi_{xz} & \phi_{xy} & \phi_{3z^2-r^2} & \phi_{x^2-y^2} \end{pmatrix}^T, \tag{4.30}$$

Some calculations gives

$$l_x = \begin{bmatrix} 0 & 0 & 0 & -\sqrt{3}\mathrm{i} & -\mathrm{i} \\ 0 & 0 & \mathrm{i} & 0 & 0 \\ 0 & -\mathrm{i} & 0 & 0 & 0 \\ \sqrt{3}\mathrm{i} & 0 & 0 & 0 & 0 \\ \mathrm{i} & 0 & 0 & 0 & 0 \end{bmatrix} \quad \overset{t_{2g}}{\Longrightarrow} \quad l_x^{t_{2g}} = \begin{bmatrix} 0 & 0 & 0 \\ 0 & 0 & \mathrm{i} \\ 0 & -\mathrm{i} & 0 \end{bmatrix}, \tag{4.31a}$$

$$l_y = \begin{bmatrix} 0 & 0 & -\mathrm{i} & 0 & 0 \\ 0 & 0 & 0 & -\sqrt{3}\mathrm{i} & -\mathrm{i} \\ \mathrm{i} & 0 & 0 & 0 & 0 \\ 0 & \sqrt{3}\mathrm{i} & 0 & 0 & 0 \\ 0 & \mathrm{i} & 0 & 0 & 0 \end{bmatrix} \quad \overset{t_{2g}}{\Longrightarrow} \quad l_y^{t_{2g}} = \begin{bmatrix} 0 & 0 & -\mathrm{i} \\ 0 & 0 & 0 \\ \mathrm{i} & 0 & 0 \end{bmatrix}, \tag{4.31b}$$

$$l_z = \begin{bmatrix} 0 & \mathrm{i} & 0 & 0 & 0 \\ -\mathrm{i} & 0 & 0 & 0 & 0 \\ 0 & 0 & 0 & 0 & -2\mathrm{i} \\ 0 & 0 & 0 & 0 & 0 \\ 0 & 0 & 2\mathrm{i} & 0 & 0 \end{bmatrix} \quad \overset{t_{2g}}{\Longrightarrow} \quad l_z^{t_{2g}} = \begin{bmatrix} 0 & \mathrm{i} & 0 \\ -\mathrm{i} & 0 & 0 \\ 0 & 0 & 0 \end{bmatrix}. \tag{4.31c}$$

From this we see that all matrix elements of l_κ in the e_g-states are zero, i.e. completely quenched. A further interesting peculiarity is the *T-P* equivalence, i.e. the t_{2g}-subspace is equivalent to the matrix elements to those of the *p*-states (except of a sign). The following relation holds

$$\boldsymbol{l}^{(t_{2g})} = -\boldsymbol{l}^{(p)}. \tag{4.32}$$

As a consequence one can treat the t_{2g} manifold as having an effective orbital momentum $\tilde{l} = 1$.

The spin momentum operators $\boldsymbol{s}$ of the spin-orbit Hamiltonian are given by the

Pauli matrices σ_κ. One finds

$$\boldsymbol{s} = \frac{1}{2}\boldsymbol{\sigma}. \tag{4.33}$$

Hence the spin-orbit Hamiltonian is

$$\begin{aligned}\mathcal{H}_{\mathrm{SOC}} &= f(r)\left[l_x \otimes s_x + l_y \otimes s_y + l_z \otimes s_z\right] \\ &= \frac{f(r)}{2}\begin{pmatrix} 0 & \mathrm{i}\sigma_z & -\mathrm{i}\sigma_y \\ -\mathrm{i}\sigma_z & 0 & \mathrm{i}\sigma_x \\ \mathrm{i}\sigma_y & -\mathrm{i}\sigma_x & 0 \end{pmatrix}.\end{aligned} \tag{4.34}$$

4.2 Further crystal-fields

In nature there are many transition metal compounds whose symmetry is reduced compared to cubic symmetry. Mainly due to the distortions of the ligand octahedra. Often these distortions can be interpreted as a small deviation from the cubic symmetry. Typical example, which will be discussed within this chapter are trigonal D_{3d}, tetragonal D_{4h}, and orthorombic D_{2h} distortions. Figure 4.3 summarizes the very essence of this. The subsequent discussion follows [17, 42–45].

4.2.1 Tetragonal symmetry (D_{4h})

Consider first teragonal D_{4h} distortions of the cubic symmetry, which can be imagined by squeezing or stretching the O_6-octahedron shown in figure 4.1 (a) along the z axis and compression or elongation along the x and y axis. As a result the e_g degeneracy will be lifted by creating a lower a_{1g} states and higher b_{1g} state. The t_{2g} manifold will be split into a doublet e_g state and singlet b_{2g} state. The explicit level splitting, i.e. which state is higher or lower in energy depends on the teragonal distortion. The case shown in figure 4.3 corresponds to a elongation along the z axis (axis and sometimes compression in x and y). Note, that the cubic harmonic basis remains the eigenbasis. In order to find an explicit form of the

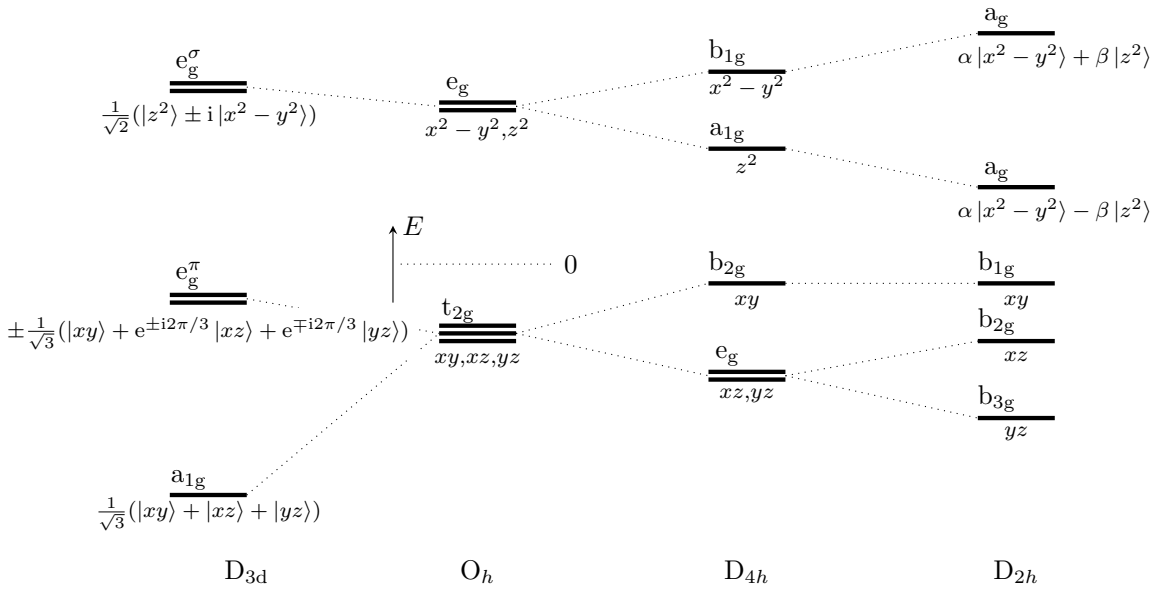

■ **Figure 4.3.:** Energy level splitting diagram for d^1 configuration under the trigonal D_{3d}, cubic O_h, tetragonal D_{4h}, and orthorombic D_{2h} symmetries.

tetragonal crystal field a similar procedure as for the cubic crystal field is performed. The difference is that the tetragonal distortion additionally can be treated as small perturbation upon the cubic field, i.e.

$$V_{\text{tetr.}}(\boldsymbol{r}) = V_{\text{C}}^0 + V_{\text{pert}}. \tag{4.35}$$

Here V_{C}^0 is the cubic field (4.9) and V_{pert} the tetragonal distortion. Considering a tetragonal distortion along $z \to a + \varepsilon$ and only terms up to order $\mathcal{O}(\varepsilon)$. This leads to a perturbation part of the form

$$V_{\text{pert}} = -\varepsilon \left(\frac{Ze^2}{a^6} \left[r^2 a^2 \sqrt{\frac{3\pi}{4}} Y_0^{(2)} - r^4 20 \sqrt{\frac{\pi}{9}} Y_0^{(4)} \right] + \frac{2Ze^2}{a^2} \right). \tag{4.36}$$

4.2.2 Trigonal symmetry (D_{3d})

In the trigonal symmetry D_{3d} the t_{2g} levels further split into a singlet a_{1g} and doublet e_g^π. The former e_g are not affected but now labeled e_g^σ. Since within a trigonal crystal field the C_3 axis is now the new symmetry axis, also the states

corresponding to the different energy levels are now linear combinations of the former cubic d orbitals. One finds

$$|e^{\pi}_{g\pm}\rangle = \pm\frac{1}{\sqrt{3}}(|xy\rangle + e^{\pm i2\pi/3}|xz\rangle + e^{\mp i2\pi/3}|yz\rangle), \tag{4.37a}$$

$$|e^{\sigma}_{g}\rangle = \frac{1}{\sqrt{2}}(|z^2\rangle \pm i|x^2-y^2\rangle), \tag{4.37b}$$

$$|a_{1g}\rangle = \frac{1}{\sqrt{3}}(|xy\rangle + |xz\rangle + |yz\rangle). \tag{4.37c}$$

When the z axis is rotated along the [111] (C_3) axis, so $z \to z'$, the a_{1g} takes on the form

$$|a_{1g}\rangle = |z'^2\rangle\,. \tag{4.38}$$

The remaining two t_{2g} orbitals $|e^{\pi}_{g\pm}\rangle$ under the rotation take on the form

$$|e^{\pi}_{g,1}\rangle = \frac{1}{\sqrt{3}}\left(\sqrt{2}\,|x'^2-y'^2\rangle - |x'z'\rangle\right), \tag{4.39a}$$

$$|e^{\pi}_{g,2}\rangle = \frac{1}{\sqrt{3}}\left(\sqrt{2}\,|x'y'\rangle + |y'z'\rangle\right), \tag{4.39b}$$

with orbital momentum $\ell_{z'} = \pm 1$, when quantized along the z' axis.

4.2.3 Orthorombic symmetry (D_{2h})

Consider figure 4.1 (a) and a distortion of the form $x \to x+\delta$, $y \to y+\delta$, and $z \to z$, which is an example of orthormbic D_{2d} symmetry. When compared to the cubic one, the t_{2g} and e_g manifolds are split into three $b_{1/2/3g}$ and two a_g energy levels, respectively. For the above mentioned distortion the level scheme is shown in figure 4.3. As a consequence of the splitting the originally chosen $|z^2\rangle$ and $|x^2-y^2\rangle$ orbitals are not the eigenbasis of the levels anymore, but their linear combination

$$|a^{\pm}_{g}\rangle = \frac{1}{2}\left(|z^2\rangle \pm |x^2-y^2\rangle\right). \tag{4.40}$$

Similarly, the t_{2g} levels are spit into three singlets.

4.3 Coulomb interaction and Slater integrals

The Coulomb interaction between electrons is typically given as

$$\mathcal{H}_{\text{int}} = \sum_{i\neq j} \frac{1}{2} \frac{e^2}{|\boldsymbol{r}_i - \boldsymbol{r}_j|}, \tag{4.41}$$

where e is the electron charge. In a second quantized form the Coulomb interaction takes on the form

$$\mathcal{H}_{\text{int}} = \sum_{ijul} \sum_{aa'bb'} U_{ijul}^{aa'bb'} c_{ia}^\dagger c_{ja'}^\dagger c_{lb'} c_{ub}, \tag{4.42}$$

where the indices $a = \{\alpha, \sigma\}$ labels spin ($\sigma = \uparrow, \downarrow$) and orbital ($\alpha$) degrees of freedom. The matrix elements of the Coulomb tensor $U_{ijul}^{aa'bb'}$, when expressed in Wannier orbitals $\phi_{ai}(\boldsymbol{r})$, are

$$U_{ijul}^{aa'bb'} = \int \phi_{ai}^*(\boldsymbol{r}) \phi_{a'i}^*(\boldsymbol{r}') V_{\text{ee}}(\boldsymbol{r} - \boldsymbol{r}') \phi_{b'l}(\boldsymbol{r}') \phi_{bu}(\boldsymbol{r}) \mathrm{d}^3 r \mathrm{d}^3 r'. \tag{4.43}$$

In order to find an explicit expression for the Coulomb tensor, the Coulomb potential $\frac{1}{|\boldsymbol{r}_i - \boldsymbol{r}_j|}$ is expanded in spherical harmonics $Y_m^{(k)}(\theta_i, \phi_i)$ leading to [46]

$$\sum_{i\neq j} \frac{1}{2} \frac{e^2}{|r_i - r_j|} = \sum_{i\neq j} \frac{1}{2} \sum_{k=0}^{\infty} \frac{r_<^k}{r_>^{k+1}} \sum_{m=-k}^{k} \frac{4\pi}{2k+1} Y_m^{(k)}(\theta_i, \phi_i) Y_m^{(k)}(\theta_j, \phi_j)^*, \tag{4.44}$$

with $r_< = \text{Min}[r_i, r_j]$ and $r_> = \text{Max}[r_i, r_j]$. Using the this expansion in equation (4.43) and the fact that angular- and radial part can be separated, gives

$$\begin{aligned} U_{ijul} = \langle \alpha_i \alpha_j | V_{\text{ee}} | \alpha_l \alpha_u \rangle = \delta_{\sigma_i, \sigma_u} \delta_{\sigma_j, \sigma_l} \sum_{k=0}^{\infty} R_{ijul}^{(k)} \\ \times \sum_{q=-k}^{k} (-1)^q \delta_{q, m_u - m_i} \delta_{q, m_j - m_l} \left\langle \ell_i m_i | C_{-q}^{(k)} | \ell_u m_u \right\rangle \left\langle \ell_j m_j | C_q^{(k)} | \ell_l m_l \right\rangle, \end{aligned} \tag{4.45}$$

where $\alpha_i = \{n_i, \ell_i, m_i, \sigma_i\}$ collects all quantum numbers, and

$$R_{ijul}^{(k)} \equiv \int_0^\infty \mathrm{d}r\, r^2 \int_0^\infty \mathrm{d}r'\, r'^2 \frac{r_<^k}{r_>^{k+1}} R_{n_i,\ell_i}(r) R_{n_j,\ell_j}(r') R_{n_u,\ell_u}(r) R_{n_l,\ell_l}(r'), \tag{4.46a}$$

$$C_q^{(k)}(\theta_i, \phi_i) \equiv \sqrt{\frac{4\pi}{2k+1}} Y_m^{(k)}(\theta_i, \phi_i). \tag{4.46b}$$

From this we can define Slater- and exchange integrals (F^k and $G^{(k)}$) as

$$F^{(k)} = R^{(k)}_{ijij}, \quad \text{and} \quad G^{(k)} = R^{(k)}_{iuui}, \tag{4.47}$$

leading to the contributions

$$U_{ijij} = \sum_{k=0}^{\infty} F^{(k)} \langle \ell_i,m_i|C^{(k)}_0|\ell_i,m_i\rangle \langle \ell_j,m_j|C^{(k)}_0|\ell_j,m_j\rangle , \tag{4.48a}$$

$$U_{iuui} = \delta_{\sigma_i,\sigma_i'} \sum_{k=0}^{\infty} G^{(k)} \left[\langle \ell_i,m_i|C^{(k)}_0|\ell_u,m_u\rangle\right]^2. \tag{4.48b}$$

Both integrals, $F^{(k)}$ and $G^{(k)}$ are known as Slater integrals in literature [46–48]. For the $F^{(k)}$ the k takes on the values $k = 0,2,\ldots,2\cdot \mathrm{Min}[\ell_i,\ell_j]$, where as for the $G^{(k)}$ it is $k = |\ell_i - \ell_u|, |\ell_i - \ell_u| + 2, \ldots, \ell_i + \ell_u$. For electrons in the same shell $F^{(k)} \equiv G^{(k)}$.

Considering two electrons in the same shell $n\ell = n'\ell'$ the U value can be expressed in Slater integrals via

$$U_{ss} = F^{(0)}, \tag{4.49a}$$

$$U_{pp} = F^{(0)} - \frac{2}{25}F^{(2)}, \tag{4.49b}$$

$$U_{dd} = F^{(0)} - \frac{2}{63}F^{(2)} - \frac{2}{63}F^{(4)}, \tag{4.49c}$$

or in different shells $n\ell \neq n'\ell'$

$$U_{ss'} = F^{(0)} - \frac{1}{2}G^{(0)}, \tag{4.50a}$$

$$U_{sp'} = F^{(0)} - \frac{1}{6}G^{(1)}, \tag{4.50b}$$

$$U_{sd'} = F^{(0)} - \frac{1}{10}G^{(2)}, \tag{4.50c}$$

$$U_{pp'} = F^{(0)} - \frac{1}{6}G^{(2)} - \frac{1}{15}G^{(2)}, \tag{4.50d}$$

$$U_{pd'} = F^{(0)} - \frac{1}{15}G^{(1)} - \frac{3}{70}G^{(3)}. \tag{4.50e}$$

The actual values of $F^{(k)}$ or $G^{(k)}$ are typically calculated numerically by approximation schemes, like the Hartree-Fock approximation [46, 47], or directly calculated by using localized Wannier orbitals as basis functions [49]. Compared to experiments these values are however subject to renormalizations resulting from the screening

effect of solids. For higher-order multipole-parts, e.g. d electrons, an empirical scaling factor of 0.8 is often enough to reproduce the experimental spectra [50].

4.4 Kanamori-Interaction

When concentrating only on a d electron system, especially with cubic symmetry, often the Kanamori interaction Hamiltonian [51], which subsequently will be derived, is used. The idea is to simplify the Coulomb interaction

$$\mathcal{H}^{\text{el-el}} = \sum_{\sigma,\sigma'} \sum_{ijkl} \sum_{\alpha\beta\gamma\delta} U_{ijk\ell}^{\alpha\beta\gamma\delta} c_{\alpha i\sigma}^{\dagger} c_{\beta i\sigma'}^{\dagger} c_{\delta i\sigma'} c_{\gamma i\sigma}, \tag{4.51}$$

first by only considering a local d system, i.e. the atomic limit, where the atoms are well separated, by applying $i = j = k = l$ and defining the new U value

$$U_{iiii}^{\alpha\beta\gamma\delta} = U^{\alpha\beta\gamma\delta}. \tag{4.52}$$

As a consequence this allows to define new "Kanamori" parameter [51] of the form

$$U \equiv U^{\alpha\alpha\alpha\alpha} \tag{4.53a}$$

$$U' \equiv U^{\alpha\beta\alpha\beta} \tag{4.53b}$$

$$J \equiv U^{\alpha\beta\beta\alpha} = U^{\alpha\alpha\beta\beta}. \tag{4.53c}$$

The parameter U is the already known on-site Coulomb interaction within one band (intra-band interaction), U' the inter-band interaction, and J the parameter of the Hund's coupling. An explicit form can then be derived by considering the following four cases:

1. Starting with the simplest case $\alpha = \beta = \gamma = \delta$ leads to

$$\begin{aligned} \mathcal{H}_U &\equiv \sum_{\sigma,\sigma'} \sum_{i} \sum_{\alpha} U^{\alpha\alpha\alpha\alpha} c_{\alpha i\sigma}^{\dagger} c_{\alpha i\sigma'}^{\dagger} c_{\alpha i\sigma'} c_{\alpha i\sigma} \\ &= U \sum_{i,\alpha} n_{i\uparrow}^{(\alpha)} n_{i\downarrow}^{(\alpha)}, \end{aligned} \tag{4.54}$$

   which is the intra-band Coulomb interaction, or densit-density interaction on each orbital.

2. The second case is $\alpha = \gamma$, $\beta = \delta$, and $\alpha \neq \beta$, leading to

$$\begin{aligned}\tilde{\mathcal{H}}_{U'} &\equiv \sum_{\sigma,\sigma'}\sum_{i}\sum_{\alpha\beta} U^{\alpha\beta\alpha\beta} c^{\dagger}_{\alpha i\sigma} c^{\dagger}_{\beta i\sigma'} c_{\beta i\sigma'} c_{\alpha i\sigma} \\ &= \frac{U'}{2} \sum_{i,\alpha,\beta,\sigma} \left(n^{(\alpha)}_{i\sigma} n^{(\beta)}_{i\bar{\sigma}} + n^{(\alpha)}_{i\sigma} n^{(\beta)}_{i\sigma} \right), \end{aligned} \tag{4.55}$$

which is the inter-band Coulomb interaction or the density-density interaction between different orbitals.

3. For $U^{\alpha\beta\alpha\beta}$ and $\alpha \neq \beta$ we find the term

$$\begin{aligned}\tilde{\mathcal{H}}_{\text{pair}} &\equiv \sum_{\sigma,\sigma'}\sum_{i}\sum_{\alpha\beta} U^{\alpha\alpha\beta\beta} c^{\dagger}_{\alpha i\sigma} c^{\dagger}_{\alpha i\sigma'} c_{\beta i\sigma'} c_{\beta i\sigma} \\ &= -J \sum_{i,\alpha,\beta} c^{\dagger}_{i\alpha\uparrow} c^{\dagger}_{i\alpha\downarrow} c_{i\beta\uparrow} c_{i\beta\downarrow}, \end{aligned} \tag{4.56}$$

which is the pair-hopping part of Hund's coupling.

4. For $\alpha = \delta$, $\beta = \gamma$, and $\alpha \neq \beta$ a short calculation shows

$$\begin{aligned}\tilde{\mathcal{H}}_{J} &\equiv \sum_{\sigma,\sigma'}\sum_{i}\sum_{\alpha\beta} U^{\alpha\beta\beta\alpha} c^{\dagger}_{\alpha i\sigma} c^{\dagger}_{\beta i\sigma'} c_{\alpha i\sigma'} c_{\beta i\sigma} \\ &= -\frac{J}{2} \sum_{i,\alpha,\beta,\sigma} n^{(\alpha)}_{i\sigma} n^{(\beta)}_{i\sigma} - \frac{1}{2}\sum_{i\alpha\beta} \left(c^{\dagger}_{i\alpha\uparrow} c_{i\alpha\downarrow} c^{\dagger}_{i\beta\downarrow} c_{i\beta\uparrow} + c^{\dagger}_{i\alpha\downarrow} c_{i\alpha\uparrow} c^{\dagger}_{i\beta\uparrow} c_{i\beta\downarrow} \right), \end{aligned} \tag{4.57}$$

where the last part in this equation are the spin-flip parts of the Hund's interaction.

Other contributions, not mentioned in the above cases, vanish by symmetry. Hence the simplified electron-electron interaction can be expressed as

$$\begin{aligned}\mathcal{H}^{\text{el-el}} = U \sum_{i,\alpha} n^{(\alpha)}_{i\uparrow} n^{(\alpha)}_{i\downarrow} + \frac{U'}{2} \sum_{i,\alpha,\beta,\sigma} n^{(\alpha)}_{i\sigma} n^{(\beta)}_{i\bar{\sigma}} + \frac{1}{2}\left(U' - J\right) \sum_{i,\sigma}\sum_{\alpha,\beta\neq\alpha} n^{(\alpha)}_{i\sigma} n^{(\beta)}_{i\sigma} \\ - J \sum_{i,\alpha,\beta\neq\alpha} c^{\dagger}_{i\alpha\uparrow} c^{\dagger}_{i\alpha\downarrow} c_{i\beta\uparrow} c_{i\beta\downarrow} - \frac{J}{2} \sum_{i,\sigma}\sum_{\alpha,\beta\neq\alpha} c^{\dagger}_{i\alpha\sigma} c_{i\alpha\bar{\sigma}} c^{\dagger}_{i\beta\bar{\sigma}} c_{i\beta\sigma}. \end{aligned} \tag{4.58}$$

When defining the different parts of the Hamiltonian via

$$\mathcal{H}_{U'} = \frac{U'}{2} \sum_{i,\alpha,\beta,\sigma} n_{i\sigma}^{(\alpha)} n_{i\bar{\sigma}}^{(\alpha)}, \tag{4.59a}$$

$$\mathcal{H}_{U'-J} = \frac{1}{2}\left(U' - J\right) \sum_{i,\sigma} \sum_{\alpha,\beta\neq\alpha} n_{i\sigma}^{(\alpha)} n_{i\sigma}^{(\beta)}, \tag{4.59b}$$

$$\mathcal{H}_{J} = -J \sum_{i,\alpha,\beta\neq\alpha} c_{i\alpha\uparrow}^{\dagger} c_{i\alpha\downarrow}^{\dagger} c_{i\beta\uparrow} c_{i\beta\downarrow} - \frac{J}{2} \sum_{i,\sigma} \sum_{\alpha,\beta\neq\alpha} c_{i\alpha\sigma}^{\dagger} c_{i\alpha\bar{\sigma}} c_{i\beta\bar{\sigma}}^{\dagger} c_{i\beta\sigma}, \tag{4.59c}$$

reduces Hamiltonian (6.3) to

$$\mathcal{H}^{\text{el-el}} = \mathcal{H}_{U} + \mathcal{H}_{U'} + \mathcal{H}_{U'-J} + \mathcal{H}_{J}, \tag{4.60}$$

where $\mathcal{H}_{U'}$ and $\mathcal{H}_{U'-J}$ describe the inter-band Coulomb interaction containing only density-density terms. $\mathcal{H}_J$ describes Hund's coupling and part (4.59b) includes the z-component of Hund's coupling and is known as the Ising component. This can be seen if the Hamiltonian is expressed via the spin operators

$$S_{i\alpha}^{(\kappa)} = \frac{1}{2} \sum_{\mu\nu} a_{i\alpha\mu}^{\dagger} \sigma_{\mu\nu}^{(\kappa)} a_{i\alpha\nu}, \tag{4.61}$$

where $\kappa \in \{x,y,z\}$ and $\sigma^{(\kappa)}$ the corresponding Pauli matrix. Thus

$$S_{i\alpha}^{(z)} = \frac{1}{2}\left(n_{i\uparrow}^{(\alpha)} - n_{i\downarrow}^{(\alpha)}\right), \tag{4.62a}$$

$$S_{i\alpha}^{(z)} S_{i\beta}^{(z)} = \frac{1}{4} \sum_{\sigma} \left(n_{i\sigma}^{(\alpha)} n_{i\sigma}^{(\beta)} - n_{i\sigma}^{(\alpha)} n_{i\bar{\sigma}}^{(\beta)}\right). \tag{4.62b}$$

Note that the Kanamori interaction is only valid if spherical symmetry is guaranteed, so that $U = U' - 2J$ holds. In terms of the Slater integrals this leads to the following terminology

$$U = F^{(0)} + \frac{4}{49}\left(F^{(2)} + F^{(4)}\right), \tag{4.63a}$$

$$U' = F^{(0)} - \frac{4}{49} F^{(2)} - \frac{4}{441} F^{(4)}, \tag{4.63b}$$

$$J = \frac{3}{49} F^{(2)} + \frac{20}{441} F^{(4)}, \tag{4.63c}$$

or if inverted and using $U = U' - 2J$

$$F^{(0)} = U - \frac{8}{5}J, \quad F^{(2)} = 7J, \quad F^{(4)} = \frac{9}{5} F^{(2)}. \tag{4.64}$$

Further detail can be found in [38, 48, 51, 52].

Part II.

DFT+DMFT and beyond

Chapter 5 Dynamical mean-field theory

Studying electronic correlations plays a crucial role in modern condensed matter physics. Typically strong correlations manifest in "the breakdown of single-particle approaches" (e.g. Hartree-Fock approximations, DFT, ...) since the nature of many-body physics itself becomes important. In other words strong electronic correlations refer to electronic interactions which can not easily described by factorization approximations such as mean-field approximations. An example is the expectation value of the charge density $n(\boldsymbol{r})$ of an electronic system at two different points $\boldsymbol{r}_i$ and $\boldsymbol{r}_j$. In general in an interacting system the expectation value can not be factorized, i.e.

$$\langle n(\boldsymbol{r}_i) n(\boldsymbol{r}_j) \rangle \neq \langle n(\boldsymbol{r}_i) \rangle \langle n(\boldsymbol{r}_j) \rangle , \tag{5.1}$$

which is a direct consequence the Coulomb interaction of the electrons and the Pauli principle, causing a small $n(\boldsymbol{r}_i)$ if $n(\boldsymbol{r}_j)$ is large and $\boldsymbol{r}_i - \boldsymbol{r}_j$ becomes small. The equality of both sites would only hold if the system is purely non-interaction.

The correlations effects are particularly strong in transition metal compounds with partially filled d and f electron shells [17, 20]. The phenomena resulting from electronic correlations are enormous, including heavy fermion behavior [53], high temperature superconductivity [54], colossal magnetoresistance [55], Mott metal-to-insulator transitions [20], and to the breakdown of the Fermi liquid regime [56].

One of the simplest lattice models including Coulomb interaction is probably

the Hubbard model [18], which is only solvable in two cases despite its simplicity: (i) analytically for one dimension $d = 1$, which is known as the Bethe-Ansatz [57] and (ii) in the case of infinite dimensions $d \to \infty$, which is know as dynamical mean-field theory (DMFT) [21] leading to an exact solution. Subsequently the Hubbard Hamiltonian and especially the DMFT approach will be discussed in more detail.

5.1 The Hubbard model

From a microscopic model point of view the single-band Hubbard model [18] is the simplest model describing interacting electrons on a lattice. The Hamiltonian reads

$$\mathcal{H} = -t \sum_{\langle i,j \rangle,\sigma} c^{\dagger}_{i\sigma} c_{j\sigma} + \frac{U}{2} \sum_{i,\sigma} n_{i\sigma} n_{i\bar{\sigma}}, \tag{5.2}$$

where $c^{\dagger}_{i\sigma}$ ($c_{i\sigma}$) creates (annihilates) an electron of spin σ at lattice site i, t is the hopping strength, U the Coulomb strength, and $\langle i,j \rangle$ denotes the summation over nearest neighbors. In the Hubbard model the Coulomb interaction is assumed to be strongly screened leading to a purely local interaction on a lattice site i. A schematic picture of the Hubbard model on a square lattice is shown in figure 5.1. Basically every type of lattice can be applied to the Hubbard model since the Coulomb interaction is independent of the lattice. Only the hopping amplitudes need to be adjusted, typically via $t \to t_{ij}$. All derived physical phenomena arise from the competition between kinetic (hopping) energy and Coulomb interaction.

Considering the limit $U/t \to 0$, which is the easiest case, leads to a Hamiltonian of non-interacting electrons on a lattice with dispersion relation (for the square lattice)

$$\varepsilon(k_x, k_y) = -2t \left(\cos(k_x a) + \cos(k_y a) \right), \tag{5.3}$$

where a is the lattice constant. This follows directly by applying the Fourier

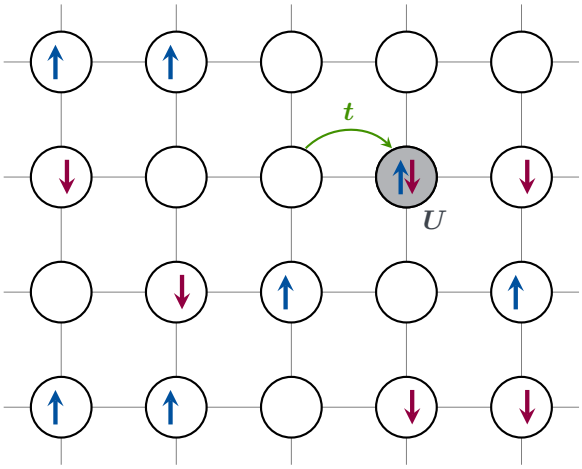

■ **Figure 5.1.:** Schematic illustration of the Hubbard Hamiltonian in the case of a square lattice. The electrons with negative charge and spin ↑ or ↓ move from lattice site to lattice site with hopping amplitude t. When two electrons of opposite spin – due to the Pauli principle – meet at the same lattice site i they encounter the local Coulomb interaction U.

transformation to the creation and annihilation operators

$$c_{i\sigma}^{\dagger} = \frac{1}{\sqrt{N}} \sum_{\boldsymbol{k}} \mathrm{e}^{-\mathrm{i}\boldsymbol{k}\boldsymbol{r}_i} c_{\boldsymbol{k}\sigma}^{\dagger}, \quad c_{i\sigma} = \frac{1}{\sqrt{N}} \sum_{\boldsymbol{p}} \mathrm{e}^{\mathrm{i}\boldsymbol{p}\boldsymbol{r}_i} c_{\boldsymbol{p}\sigma}, \tag{5.4}$$

where N is the total number of electrons and $\boldsymbol{k}$ (or $\boldsymbol{p}$) are wave vectors in the reciprocal space. Without interaction this simple tight-binding Hamiltonian always leads to a metallic solution, regardless of the hopping strength t or site to site distance a. This however, cannot be correct since t describes the tunneling of electrons from one site to a neighboring, which is exponentially small when increasing the site distance [17]. The other limit, which is $U/t \to \infty$ leaves the Hubbard Hamiltonian only with the Coulomb interaction $U \sum_i n_{i\uparrow} n_{i\downarrow}$. At half-filling all electrons are localized on one atom site with zero probability at all other sites. The resulting state would be insulating, despite being metallic in the conventional band picture. This insulating behavior occurs not only if t vanishes, it is enough if the hopping is small compared to U, i.e. $U \gg t$. This is known as the Mott-Hubbard insulator [20]. Furthermore it can be shown that the insulating phase can be expected for U values fulfilling

$$U \geqslant W = 2zt, \tag{5.5}$$

where z is the coordination number of the lattice and W the total bandwidth [17]. The nature of the insulating state is quite different from the band picture interpretation, since it is a direct consequence of the electron-electron interaction, hence giving rise to strong electron correlations.

Another interesting phenomena in the half-filled case and $U \gg t$ is the emergence of antiferromagnetism due to superexchange. Applying the strong U perturbation theory (treat the hopping as perturbation instead of the interaction) shows that the alignment of antiparallel spins gives an energy gain of $-2t^2/U$, indeed favoring an antiferromagnetic state. When carrying out this calculation it can be shown that the magnetic state can be described by an effective Heisenberg Hamiltonian

$$\mathcal{H}_{\text{eff}} = J \sum_{\langle i,j \rangle} \boldsymbol{S}_i \cdot \boldsymbol{S}_j, \quad J = \frac{2t^2}{U}, \tag{5.6}$$

where $\boldsymbol{S}_i$ are the spin operators and J the Heisenberg coupling constant. For more details see [17].

5.2 Weiss mean-field theory for the Ising model

Although mean-field theories, based on the factorization of correlations functions, fail to describe electronic systems like the Hubbard model, they often give a rough, overall description of the properties of it. Typically the route to mean-field approximations make use of simplifications resulting when some parameters are taken to be large, e.g. the length of the spin S, or the coordination number z of the lattice. For regular lattices, like Bravais-lattices, it is always possible to define a dimension and coordination number so either z or d can be used. However, there are lattices for whom a physical dimension cannot be defined, but a coordination number z. An example for such a lattice is the Bethe lattice.

One of the most prominent mean-field theories is probably the Weiss mean-field

theory for the Ising model, which is defined by

$$\mathcal{H} = -\frac{J}{2}\sum_{\langle i,j\rangle} S_i^z S_j^z, \tag{5.7}$$

and becomes exact for the limit of infinite coordination number $z \to \infty$ or spatial dimension $d \to \infty$. Here S_i^z corresponds to the z-component of the spin on site i. Furthermore we assume the coupling to be ferromagnetic $J > 0$. The basic idea of the mean-field treatment is to map the whole lattice problem onto an effective single-site problem with an effective mean-field magnetization. The magnetization is chosen to reproduce the original lattice magnetization, leading to a self-consistency condition.

First the two-spin interaction above is replace by the mean-field Hamiltonian

$$\mathcal{H}_{\mathrm{MF}} = -h\sum_i S_i^z + E_{\mathrm{shift}}, \tag{5.8}$$

where a single spin S_i interacts only with the global averaged fields of its neighbors

$$h = J\sum_j \langle S_j\rangle = Jz\,\langle S^z\rangle\,. \tag{5.9}$$

Here $\langle\bullet\rangle$ denotes the thermal average. The constant energy shift turns out to be $E_{\mathrm{shift}} = NJz\,\langle S^z\rangle^2/2$, where N is the number lattice sites. In terms of a factorization this corresponds to the decoupling of the form

$$S_i^z S_j^z \to -\langle S_i^z\rangle\langle S_j^z\rangle + \langle S_i^z\rangle S_j^z + \langle S_j^z\rangle S_i^z. \tag{5.10}$$

Note that in general the thermal average $\langle S^z\rangle$ is not the true mean value of the distribution since the sum runs only over z neighboring sites. However in the limit of infinite coordination number $z \to \infty$ this is true, due to the central limit theorem. Hence the replacement of $\langle h\rangle$ by $Jz\,\langle S^z\rangle$ becomes exact [58–60]. In order to keep $\langle h\rangle$ finite the coupling constant J is rescaled by

$$J \to \frac{J^*}{z}, \quad J^* = \text{const.} \tag{5.11}$$

In conclusion this means, that $\langle h \rangle = J^* \langle S^z \rangle$ is independent of the lattice site, so the effective Hamiltonian becomes purely local

$$\mathcal{H}_{\mathrm{MF}} = -h \sum_i S_i^z + \frac{1}{2} L J^* \langle S^z \rangle . \tag{5.12}$$

Since the effective field h depends on the spin configuration the mean-field Hamiltonian needs to be solved via the self-consistent equation

$$\langle S \rangle = \tanh(\beta J^* \langle S^z \rangle), \tag{5.13}$$

where $\beta = 1/(k_{\mathrm{B}} T)$. Defining the magnetization as $m = \langle S^z \rangle$ leads to the formulation used in standard textbook [60]. As we will see later in this chapter, the treatment of lattice quantum models with DMFT is similar to the classical Weiss mean-field theory for the Ising model.

5.3 Lattice fermions in high dimensions

Following $z \to \infty$ in the Ising model, this limit will be subsequently applied to lattice models particularly Hubbard models. The discussion follows [21], where first the kinetic energy term in equation (5.2) is generalized to d dimensions. Considering only nearest neighbor hopping the dispersion $\varepsilon(\boldsymbol{k})$ of a d dimensional hypercubic lattice (with $z = 2d$) is given by

$$\varepsilon(\boldsymbol{k}) = -2t \sum_i^d \cos(k_i), \tag{5.14}$$

so the corresponding density of states $\varrho(\omega)$ when L lattice sites are considered is

$$\varrho(\omega) = \frac{1}{L} \sum_{\boldsymbol{k}} \delta(\omega - \varepsilon(\boldsymbol{k})). \tag{5.15}$$

In order to use the central limit theorem the sum over the dimension d in dispersion relation (5.2) can be interpreted as a summation of d random variables $X_i = \sqrt{2}\cos(k_i)$. The random variables X_i are drawn from the same distribution as the k_i, which are independently and uniformly distributed in the interval $[-\pi,\pi]$.

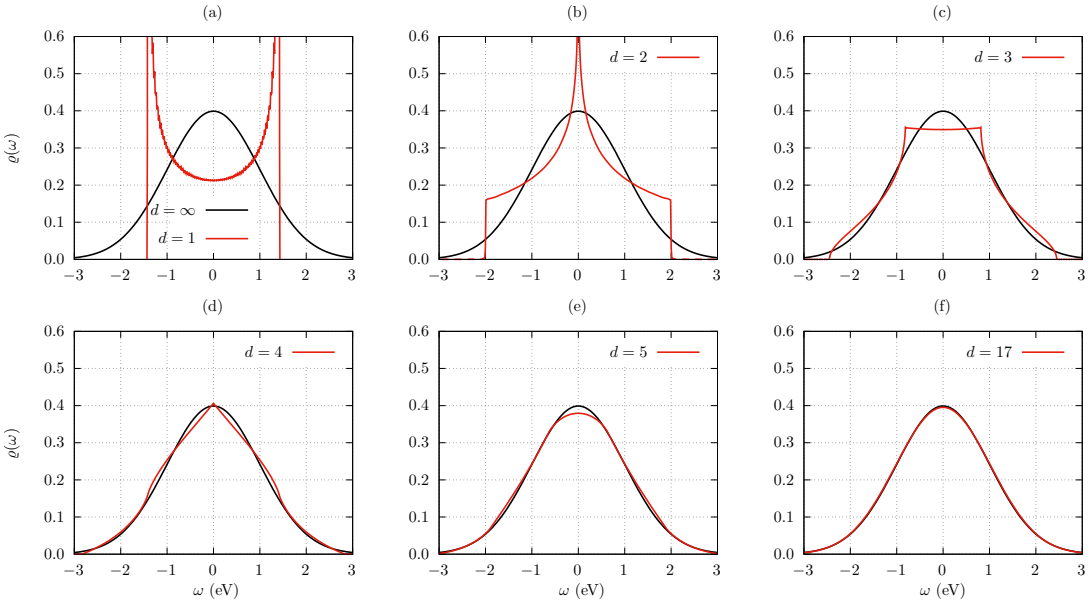

■ **Figure 5.2.:** Density of states $\varrho(\omega)$ of the hypercubic lattice for dimensions $d \in \{1,2,3,4,5,17,\infty\}$. The hopping is rescaled according to $t \to t^*/\sqrt{2d}$ with $t^* = 1.0$. The black line in the background corresponds to the $d = \infty$ case.

Mathematically speaking the X_i are random variables $X : \Omega \to E$ with Ω being the probability space given as set off all $\boldsymbol{k}$ vectors and E the measurable space (set of events) $[-2t,2t]$. The central limit theorem then implies that in the limit $d \to \infty$ the density of states is given by Gaussian distribution

$$\varrho_d(\omega) = \frac{1}{2t\sqrt{\pi d}} \exp\left[-\left(\frac{\omega}{t\sqrt{2d}}\right)^2\right]. \tag{5.16}$$

Note that as in the case of J in the Ising model the hopping t needs to be rescaled by

$$t \to \frac{t}{\sqrt{d}}, \quad t^* = \text{const}, \tag{5.17}$$

otherwise the gaussian becomes arbitrarily broad and featureless. The $d = \infty$ density of states is hence given via

$$\varrho_\infty(\omega) = \frac{1}{t^*\sqrt{2\pi}} \exp\left[-\frac{1}{2}\left(\frac{\omega}{t^*}\right)^2\right]. \tag{5.18}$$

For different dimensions the density of states $\varrho(\omega)$ is shown in figure 5.2, indicating that already for lower dimensions, e.g. $d = 5$ the overall $\varrho(\omega)$ becomes close to the $d = \infty$ (black line) case. Note that for a hypercubic lattice in $d = 5$ the coordination number is $z = 10$. Comparing this for example with the three dimensional fcc-lattice the coordination would already be $z = 12$.

5.3.1 Simplifications in infinite dimensions

The above scaling (5.17) comes with a great simplification in the investigation of Hubbard-type models [21, 61–65]. One of them is that in the $d \to \infty$ certain terms in perturbative expansion scaling with t^* are expected to vanish. This can be seen when applying a perturbation theory in terms of U. In order to see which terms are affected, one starts with the kinetic energy in the case of $T = 0$ and $U = 0$, which is given by the non-interacting Green's function (see chapter 3)

$$\langle T_{\text{kin}} \rangle = -t \sum_{\langle i,j \rangle,\sigma} G^0_{ij,\sigma}(\tau \to 0^-), \tag{5.19}$$

where the one-particle density matrix $G^0_{ij,\sigma}(\tau \to 0) = \langle c^\dagger_{i\sigma} c_{j\sigma} \rangle$ describes the probability amplitude for a hopping from site i to j. The square of its absolute value is then proportional to the probability of this process, especially, i.e. $|G^0_{ij,\sigma}(\tau \to 0)|^2 \propto 1/d$. Given a site i, the summation over all neighboring sites j, and i itself must be consistent to a probability of one. Thus for z neighboring sites this leads to

$$1 = |G^0_{ii,\sigma}(0^-)|^2 + \underbrace{\sum_{\text{NN of } i} |G^0_{ij,\sigma}(0^-)|^2}_{\sim \mathcal{O}(d)}, \tag{5.20}$$

indicating that the NN hopping amplitude t must be scaled via $t \to t^*/\sqrt{d}$, so $\langle T_{\text{kin}} \rangle$ remains finite in infinite dimensions. Hence for each term we find

$$G^0_{ij,\sigma}(0^-) \sim \mathcal{O}\left(\frac{1}{\sqrt{d}}\right), \tag{5.21}$$

leading to a normalized probability. Note that the diagonal term is allowed to stay finite, since it scales with $\mathcal{O}(d^0)$. The discussed scaling behavior also holds for

$\tau \neq 0^-$ or its Fourier transformation $G^0_{ij,\sigma}(\mathrm{i}\omega_n)$. In fact this whole argument is also valid for the real frequency Green's function

$$G^0_{ij,\sigma}(\omega) = -\left\langle T c_{i\sigma}(t) c^\dagger_{j\sigma}(0)\right\rangle, \tag{5.22}$$

where T is the time ordering operator. The time evolution of the annihilation/creation operator is given in the Heisenberg picture. The one-particle density matrix is then obtained via $\langle c^\dagger_{i\sigma} c_{j\sigma}\rangle = \lim_{t\to 0^-} G^0_{ij,\sigma}(t)$. This however also means that the scaling properties do not depend on time evolution or quantum mechanical representations.

So far it was shown that $G^0_{ij,\sigma} \sim 1/\sqrt{d}$ vanishes in the limit $d \to \infty$. However, this does not imply that the particles become localized, since the hopping of a particle to z nearest neighbors still contributes with $t^*/\sqrt{2d}$, although this probability is small. For general sites it was shown in [62, 66] that

$$G^0_{ij,\sigma} \sim \mathcal{O}\left(d^{-\frac{1}{2}\|\boldsymbol{R}_i - \boldsymbol{R}_j\|}\right), \tag{5.23}$$

where $\|\boldsymbol{R}\| = \sum_{n=1}^{d} |R_n|$ describing the hopping of particles along horizontal and vertical lines (also called New York metric). Equation (5.23) is actually the origin of all simplifications in the $d \to \infty$ limit, which can be seen on the level of Feynman diagrams. Namely, all connected, irreducible perturbation theory diagrams in position space will collapse [21, 61, 62], resulting in a purely local irreducible self-energy [21, 61] of the form

$$\lim_{d\to\infty} \Sigma_{ij,\sigma}(\omega) = \Sigma_{ii,\sigma}(\omega)\delta_{ij}. \tag{5.24}$$

Writing $\Sigma_{ii,\sigma}(\omega) = \Sigma(\omega)$ in the paramagnetic regime, and applying a Fourier transformation, which is then momentum independent, gives

$$\lim_{d\to\infty} \Sigma_\sigma(\boldsymbol{k},\omega) = \Sigma_\sigma(\omega). \tag{5.25}$$

Considering all Hubbard or related model, this results is a severe simplification, since it allows us to relate the local Green's function directly to the self-energy via

$$G_\sigma(\omega) = \int \frac{\mathrm{d}^d k}{(2\pi)} \frac{1}{\omega + \mu - \varepsilon(\boldsymbol{k}) - \Sigma_\sigma(\omega)}. \tag{5.26}$$

5.4 Dynamical mean-field theory

Although the collapse of all connected diagrams into local ones is already a tremendous simplification, the solution of the Hubbard model is still challenging. For example the self-energy, which is self-consistently connected to the local Green's function via equation (5.26), can still not be calculated analytically. The major breakthrough came 1992 by Georges and Kotliar [67], who showed that the Hubbard model can be mapped onto an Anderson impurity model [68] with an effective bath which is self-consistently determined. Later they showed in [22] that an extension from the classical Weiss mean-field theory to the dynamical quantum case can be made, by embedding a single lattice site into a dynamical quantum bath. However in contrast to the classical case the effective mean-field of the impurity model remains time dependent, or as the name indicates "dynamical". Other methods leading to the same results are given in [67, 69–71]. Subsequently a brief derivation of the relevant dynamical mean-field theory equations, as shown in [22], will be given.

5.4.1 Mapping onto effective impurity models

With all the previous simplifications based on the $d \to \infty$ limit, the last step is to actually construct the functional $\Sigma_\sigma[G_\sigma]$ [22, 65, 67, 71, 72]. Starting point of this procedure is the path integral representation of Green's functions [73]. Especially the partition function Ξ and the action S if the Hubbard model can be written in terms of functionals over Grassmann variables

$$\Xi = \int \prod_i D c^+_{i\sigma} D c_{i\sigma} \mathrm{e}^{-S}, \tag{5.27a}$$

$$S = \int_0^\beta \mathrm{d}\tau \left[\sum_{i\sigma} c^+_{i\sigma}(\partial_\tau - \mu) c_{i\sigma} + \sum_{ij,\sigma} t_{ij} c^+_{i\sigma} c_{j\sigma} + U \sum_i n_{i\uparrow} n_{i\downarrow} \right]. \tag{5.27b}$$

Note that the Grassmann fields are actually τ dependent, i.e. $c^+_{i\sigma}(\tau)$. The fundamental idea to map the Hubbard model to the Anderson impurity model uses the

"cavity" method, which imposes a certain form onto the action S. Basically this means one proceeds by focusing on a certain site i of the lattice, usually labeled by the variable 0, and integrating out all other sites in order to define an effective dynamics for the selected site i. This is done by spitting the action into three parts $S = S^{(0)} + S_0 + \Delta S$, where S_0 is the lattice action containing only variables at site 0, ΔS contains hoppings between site 0 and other sites $i \neq 0$, and $S^{(0)}$ is the part of the action, where the site 0 and its bonds are removed. Explicit terms can be found in [72]. Rewriting the partition function by using the ensemble average with respect to $S^{(0)}$, where $\Xi^{(0)}$ is the corresponding partition functions, reads

$$\Xi = \Xi^{(0)} \int \prod_{i\neq 0,\sigma} Dc^+_{i\sigma} Dc_{i\sigma} \mathrm{e}^{-S^{(0)}} \left\langle \mathrm{e}^{-\Delta S} \right\rangle_{(0)} . \tag{5.28}$$

Expanding the second exponent with respect to the action ΔS and rescaling of the hopping amplitudes t_{ij} for the $d \to \infty$ limit again leads to simplifications in the Green's function without lattice site 0

$$G^{(0)}_{ik,\sigma}(\tau_1 - \tau_2) = - \left\langle T_\tau c_{j\sigma}(\tau_1) c^+_{k\sigma}(\tau_2) \right\rangle_{(0)} . \tag{5.29}$$

Furthermore it leads to the effective local DMFT action

$$S_{\mathrm{loc}} = \int_0^\beta \mathrm{d}\tau \left[\sum_\sigma c^+_{0\sigma}(\partial_\tau - \mu) c_{0\sigma} + U n_{0\uparrow} n_{0\downarrow} \right] + \int_0^\beta \mathrm{d}\tau_1 \int_0^\beta \mathrm{d}\tau_2 \, \Delta_\sigma(\tau_1 - \tau_2) c^+_{0\sigma}(\tau_1) c_{0\sigma}(\tau_2), \tag{5.30}$$

with Δ_σ being the hybridization function

$$\Delta_\sigma(\tau_1 - \tau_2) = \sum_{jk\neq 0} t^*_{j0} t^*_{k0} G^{(0)}_{jk,\sigma}(\tau_1 - \tau_2). \tag{5.31}$$

allowing us to define the effective Weiss field propagator $\mathcal{G}_\sigma$ via

$$\mathcal{G}^{-1}_\sigma(\tau_1 - \tau_2) = -(\partial_{\tau_1} - \mu)\delta(\tau_1 - \tau_2) - \Delta_\sigma(\tau_1 - \tau_2). \tag{5.32}$$

This is quite an important results since it shows, that in the $d \to \infty$ limit the action of the Hubbard model becomes identical to that of a single-site with local Coulomb

interaction embedded in an effective field $\mathcal{G}_\sigma$. The relation between the Green's function $G^{(0)}(\tau_1 - \tau_2)$ where site 0 is removed an the full lattice Green's function is then

$$G^{(0)}_{jk,\sigma} = G_{jk,\sigma} - G_{j0,\sigma} G^{-1}_{00,\sigma} G_{0k,\sigma}. \tag{5.33}$$

Here $G_{jk,\sigma}$ is the Green's function of the full lattice. Moreover the Fourier transformation of the Weiss field gives the important relation

$$\mathcal{G}^{-1}_\sigma(\mathrm{i}\omega_n) = \mathrm{i}\omega_n + \mu - \Delta_\sigma(\mathrm{i}\omega_n), \tag{5.34}$$

which together with equation (5.33) leads to a Dyson like equation relating local Green's function $G_\sigma = G_{00,\sigma}$ and Weiss field

$$G^{-1}_\sigma(\mathrm{i}\omega_n) = \mathcal{G}^{-1}(\mathrm{i}\omega_n) - \Sigma_\sigma(\mathrm{i}\omega_n), \tag{5.35a}$$

$$\mathcal{G}^{-1}_\sigma(\mathrm{i}\omega_n) = \mathrm{i}\omega_n + \mu - \left(\Delta_\sigma(\mathrm{i}\omega_n) + \Sigma_\sigma(\mathrm{i}\omega_n)\right). \tag{5.35b}$$

5.4.2 DMFT equations

From this point the derivation is technically done, since we are now able to write down the important DMFT equations. These are

$$G_\sigma(\mathrm{i}\omega_n) = \int \mathrm{d}\boldsymbol{k} \frac{1}{\mathrm{i}\omega_n + \mu - \varepsilon(\boldsymbol{k}) - \Sigma(\mathrm{i}\omega_n)}, \tag{5.36}$$

$$G_\sigma(\mathrm{i}\omega_n) = \left[\mathcal{G}^{-1}_\sigma(\mathrm{i}\omega_n) - \Sigma_\sigma(\mathrm{i}\omega_n)\right]^{-1}, \tag{5.37}$$

where $\varepsilon(\boldsymbol{k})$ is the non-interacting dispersion relation of the original lattice. The remaining task is now to finally relate the DMFT equations to the Anderson impurity problem, which is given by Hamiltonian

$$\mathcal{H}_{\mathrm{AIM}} = \sum_{\ell,\sigma} \varepsilon^{(b)}_\ell c^\dagger_{\ell\sigma} c_{\ell\sigma} + V_\ell (c^\dagger_{\ell\sigma} d_\sigma + \mathrm{h.c.}) + U n_\uparrow n_\downarrow - \tilde{\mu} \sum_\sigma n_\sigma. \tag{5.38}$$

It consists of a single impurity site, given by the operators d, which interacts with a non-interacting bath via the hoppings V_ℓ and bath energies $\varepsilon^{(b)}_\ell$, labeled via operators c_i. The Coulomb interaction is only present on the impurity site. $\tilde{\mu}$

corresponds to the chemical potential of the impurity. The bath can be integrated out from the Hubbard local action S_{loc} resulting in a Weiss field of the form

$$\mathcal{G}_\sigma^{-1}(\mathrm{i}\omega_n) = \mathrm{i}\omega_n - \tilde{\mu} - \int_{-\infty}^{\infty} \mathrm{d}\omega \frac{\Delta(\omega)}{\mathrm{i}\omega_n - \omega}, \tag{5.39}$$

and the hybrdization function

$$\Delta(\omega) = \sum_\ell V_\ell^2 \delta(\omega - \varepsilon_\ell^{(b)}). \tag{5.40}$$

For more detail see [22, 72].

5.4.3 DMFT self-consistency

As every relation and formula is now established, it is possible to solve the Hubbard model self-consistently. The actual problem which is numerically demanding is solving the Anderson impurity model defined by the Weiss field $\mathcal{G}$. This can be done in many ways, typically exact diagonalization [74–76], numerical renomalization group [77], density-matrix renormalization group [78], or with quantum Monte Carlo (QMC) [71, 79, 80]. The actual consistency loop is schematically shown in figure 5.3. As shown, in the first step from a Hubbard like model with non-interacting Hamiltonian $\mathcal{H}(\boldsymbol{k})$ the local lattice Green's function is constructed via equation (5.36) for the filling μ. In the first loop the self-energy is typically set $\Sigma = 0$. In step two the Weiss field is calculated using equation (5.37). As shown above, the Weiss field defines the Anderson impurity model (5.38), which is then solved numerically in step three, giving the impurity Green's function $G_{\text{imp}}(\mathrm{i}\omega_n)$. From impurity Green's function and former Weiss field the Σ can be calculated in step four by explicitly using the DMFT relation that the Σ are equivalent for the lattice system and impurity system. The convergence criterion of DMFT loop n is hence

$$\Sigma^{(n)}(\mathrm{i}\omega_n) = \Sigma^{(n-1)}(\mathrm{i}\omega_n). \tag{5.41}$$

When converged also impurity and local Green's function are equivalent. If convergence is not reached, one restarts in step one with the extracted Σ, adjusting μ to

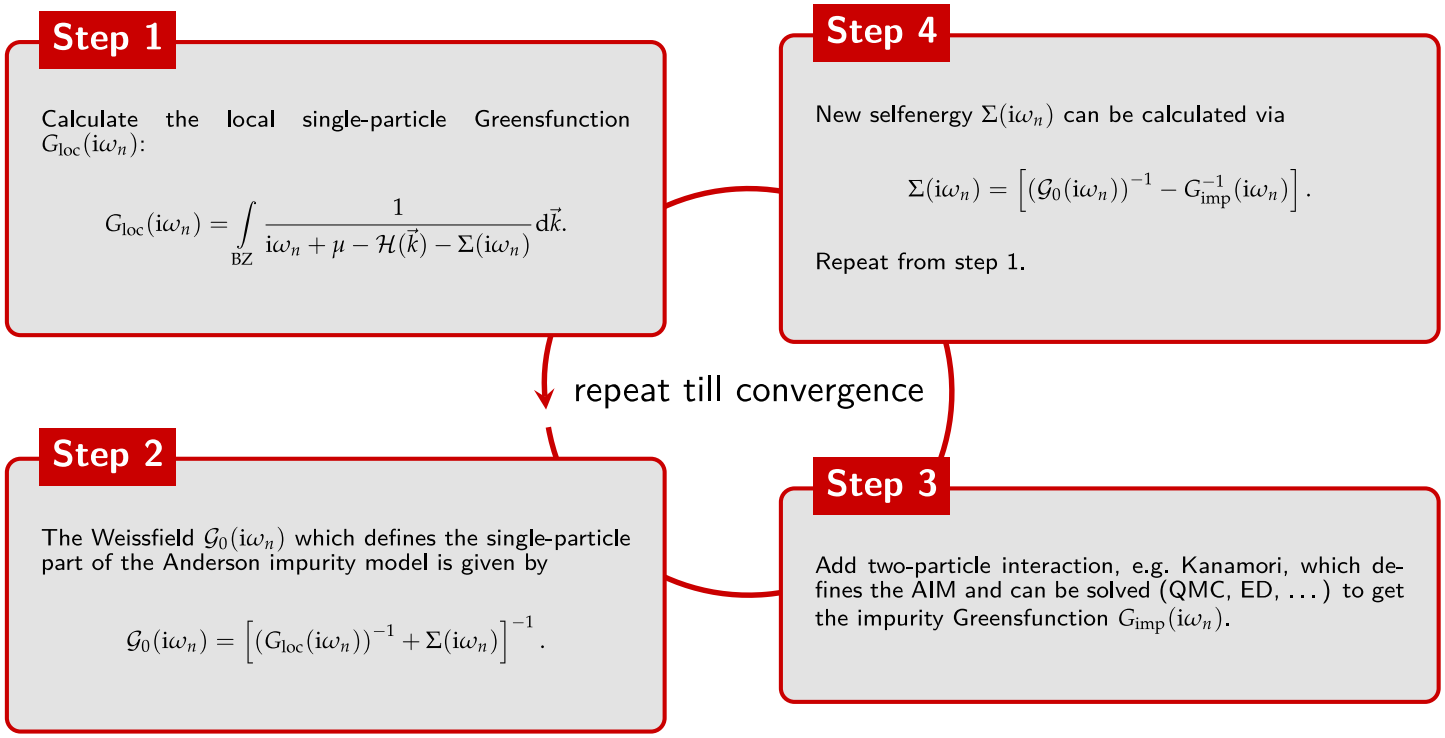

Figure 5.3.: Schematic visualization of the DMFT self-consistency loop

the correct filling and, the loop is repeated till convergence or a specific amount of loops is reached.

5.5 DFT+DMFT approach

Although with all the previous derived conclusions on how to solve the Hubbard model, it cannot describe the physics of real materials in any detail. This can easily be understand since realistic models must take into account the material specific electronic- and lattice structures and symmetries. The first step for treating real materials is to extend the DMFT, which so far was formulated for the single-band Hubbard model, to multi-orbital/band systems, which is luckily straightforward. The multi-orbital Hubbard model is

$$\mathcal{H} = -\sum_{ii'}\sum_{\sigma,\sigma'}\sum_{mm'} t^{ii'}_{m\sigma,m'\sigma} c^{\dagger}_{im\sigma} c_{i'm'\sigma'} + \frac{1}{2}\sum_{i}\sum_{\sigma,\sigma'}\sum_{mm'}\sum_{pp'} U_{mpm'p'} c^{\dagger}_{im\sigma} c^{\dagger}_{ip\sigma'} c_{ip'\sigma'} c_{im'\sigma}, \tag{5.42}$$

where m, m' and p,p' are different orbitals and the Coulomb interaction tensor is local. The DMFT approach is then extended to solve models of this form by mapping them onto multi-orbital quantum impurity models. When compared to the previously introduced formalism the following substitution is performed on the DMFT equations

$$\varepsilon(\boldsymbol{k}) \to H_{m\sigma,m'\sigma'}(\boldsymbol{k}), \qquad t_{ij} \to t^{ii'}_{m\sigma,m'\sigma},$$

also affecting the Green's function and self-energies in the following form

$$\mathcal{G}_{\sigma}(\mathrm{i}\omega_n) \to \mathcal{G}^{\sigma\sigma'}_{mm'}(\mathrm{i}\omega_n), \quad G_{\sigma}(\mathrm{i}\omega_n) \to G^{\sigma\sigma'}_{mm'}(\mathrm{i}\omega_n), \quad \Sigma_{\sigma}(\mathrm{i}\omega_n) \to \Sigma^{\sigma\sigma'}_{mm'}(\mathrm{i}\omega_n).$$

In general the local Coulomb interaction tensor $U_{mpm'p'}$ and its resulting terms go beyond density-density terms. See therefore chapter 4.3. Nonetheless, when describing real materials the actual question remains, how the material relevant parameters like $U_{mpm'p'}$ and $t^{ii'}_{m\sigma,m'\sigma}$ can be estimated.

Within the last decades one method has proven to provide qualitatively good results in describing real materials, namely DFT+DMFT [81–83]. The DFT+DMFT approach merges ab initio electronic band structure calculations with DMFT. The basic idea is to use DFT calculations to extract the material specific properties, i.e. the Wannier projections scheme discussed in chapter 2.3 for extracting the material hoppings $t^{ii'}_{m\sigma,m'\sigma}$ and cRPA (constrained random phase approximation) [32, 84, 85] calculations to estimate values for $U_{mpm'p'}$. With these parameters the DMFT calculations is then performed as discussed in the previous section. Note that this method is typically known as single-shot DFT+DMFT or DFT+DMFT in its single-shot procedure, which already leads to accurate results for a wide range of transition metal oxides. This is also the method of choice within this thesis.

Another variation of the DFT+DMFT approach goes even a bit further by "feeding" back the DMFT self-energy to the DFT code itself, so a second self-consistency run is performed. This method is commonly known as charge self-consistency DFT+DMFT and is extensively discussed for example in [37].

5.6 Analytical continuation

The analytical continuation of the Matsubara Green's function is needed when spectral functions such as $A(\omega)$ or $A(\omega, \boldsymbol{k})$ are investigated (see schematic figure 5.4). Although, there are well established methods such as MaxEnt [86, 87] (maximum entropy method) or SOM (stochastic optimization method) [88], both have the same technical problem, namely to deal with an ill-posed task, i.e. the kernel is ill-conditioned. Since MaxEnt is mostly used within this thesis it will be briefly discussed below. Instead of deriving the $\boldsymbol{k}$-resolved spectral function $A(\omega, \boldsymbol{k})$ from a Green's function, getting the self-energy $\Sigma(\omega)$ directly on the real axis allows easy and direct access to lots of quantities and is therefore desirable, however more unstable. Subsequently this will be discussed in more detail.

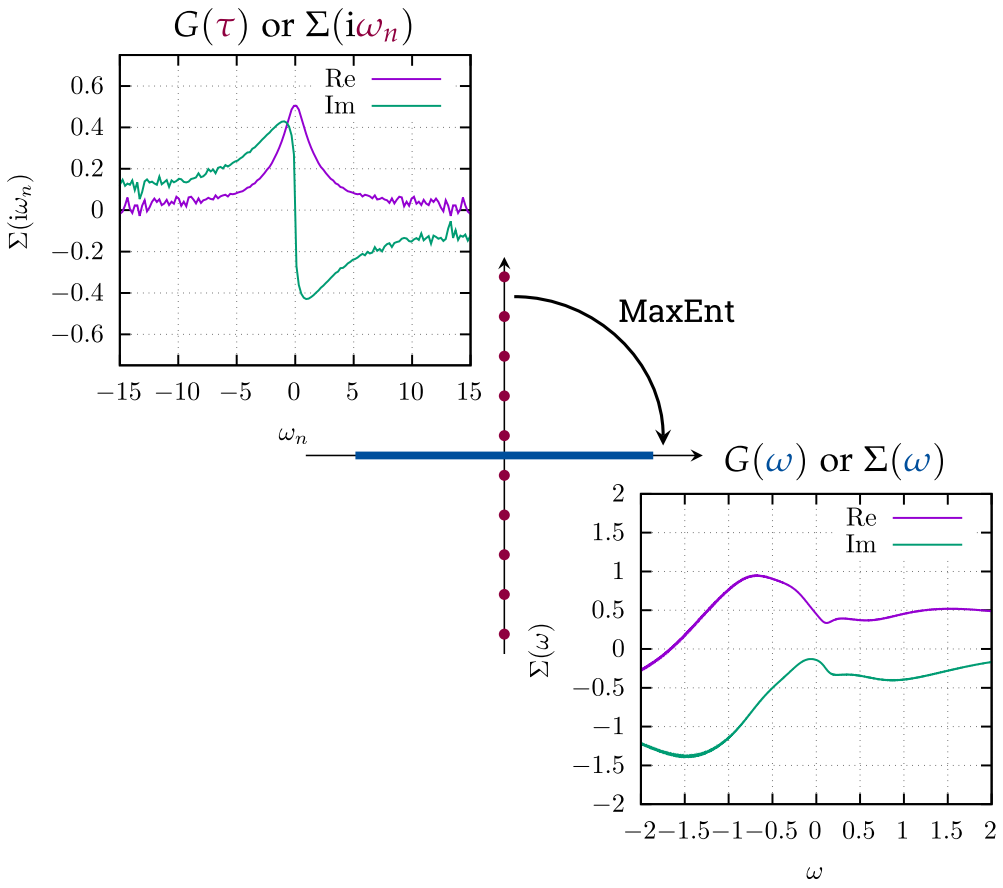

■ **Figure 5.4.:** Analytical continuation scheme. From Matsubara axis $i\omega_n$ to real axis ω. Exemplary shown for a test self-energy $\Sigma(i\omega_n)$.

5.6.1 Why so serious?

While the transformation from the real axis to the Matsubara axis is an easy task, the way back is not. The nature of the problem arises from the formulation of the problem itself, i.e. when writing down the Matsubara Green's function $G(z)$ in terms of the spectral function

$$G_{ij}(z) = \int \frac{A_{ij}(\omega)}{z-\omega} \mathrm{d}\omega, \tag{5.43}$$

where $A_{ij}(\omega)$ is the spectral function and z a complex number. In general $G_{ij}(z)$ and $A_{ij}(\omega)$ are matrix-valued, the above equation holds however for each matrix element. Since equation (5.43) couples the real and imaginary parts of Green's function and spectral function this can be avoided by Fourier transforming $G(z =$

iω_n), leading to

$$G_{ij}(\tau) = \int \frac{\mathrm{e}^{-\omega\tau}}{1+\mathrm{e}^{-\beta\omega}} A_{ij}(\omega)\mathrm{d}\omega. \tag{5.44}$$

In order to solve such an integral numerically, the functions $G(\tau)$ and $A(\omega)$ are discretized to vectors $G_n = G(\tau_n)$ and $A_m = A(\omega_m)$ resulting in a reformulation of the above integral of the form

$$\boldsymbol{G} = K\boldsymbol{A}, \tag{5.45}$$

where the matrix

$$K_{nm} = \frac{\mathrm{e}^{-\omega_m\tau_n}}{1+\mathrm{e}^{-\beta\omega_m}}\Delta\omega_m \tag{5.46}$$

is the kernel of the transformation. The ill-posed problem arises when trying to extract the $A(\omega)$ by inverting K, i.e. $\boldsymbol{A} = K^{-1}\boldsymbol{G}$. Rigorously this manifests in a large condition number of K, due to the exponential decay with ω_m and τ_n, leading to an inversion problem of K [87].

5.6.2 The maximum entropy method in a nutshell

Ongoing from equation (5.46) the task of the analytical continuation is now to approximate the spectral function $\boldsymbol{A}_{\text{approx}}$ in manner that $\boldsymbol{G}_{\text{rep}} = K\boldsymbol{A}_{\text{approx}}$ reproduces the main features of the given data set $\boldsymbol{G}$ but does not follow the noise. Note that typically $\boldsymbol{G}$ are data obtained by QMC solvers containing in the worst case very noisy data. Methods which simply try to minimize the bare misfit

$$\chi^2(\boldsymbol{A}) = (K\boldsymbol{A}-\boldsymbol{G})^T C^{-1}(K\boldsymbol{A}-\boldsymbol{G}), \tag{5.47}$$

where is the covariance matrix, are doomed to fail. This can be spectacularly seen when for example trying to use least-squares (see [37]). However, instead of trying to minimize χ^2, one tries to minimize

$$Q_\alpha(A) = \frac{1}{2}\chi^2(A) - \alpha S(A), \tag{5.48}$$

where $S(A)$ is an entropic term and α a hyperparameter. This is known as maximum entropy method (short: MaxEnt). Note that α is introduced ad hoc and needs to be specified later. Here the entropic term $S(A)$ coincides with the well known Shannon entropy [89], which can be interpreted as the average information or entropy produced by a stochastic information source. Without going into much detail it is important to mention that by choosing the hyperparameter α differently new flavors of the maximum entropy approach are achieved (see e.g. [86, 87, 90, 91]. Nonetheless it was shown by Skilling in 1989, by using a Baysian method [92], that the only consistent choice of $S(A)$ to achieve a non-negative spectral function $A(\omega)$ is

$$S(A) = \int \left[A(\omega) - D(\omega) - A(\omega) \log \frac{A(\omega))}{D(\omega)} \right] \mathrm{d}\omega. \tag{5.49}$$

The quantity $D(\omega)$ is a default model, based on the choice of assumptions made about its behavior. This dependence on the other hand is also the main drawback of the method. Nonetheless, it has become the standard tool within the DMFT community, since often the obtained spectral functions are remarkably stable under the choice of α. Additionally its extension to matrix valued functions and hence to the non-diagonal can be found in [87].

5.6.3 Analytical continuation of the self-energy

Instead of the analytical continuation of the imaginary time Green's function $G(\tau)$, where typically only the diagonal elements are needed, the self-energy $\Sigma(\mathrm{i}\omega_n)$ can be analytically continued. This will be especially helpful in chapter 6, where $\boldsymbol{k}$ resolved spectral functions $A(\omega, \boldsymbol{k})$ are of interest, or in chapter 7, where a real ω axis expression for the hybrdization function $\Delta(\omega)$ is needed to construct the underlying Anderson impurity model. Technically, imaginary time axis objects are still the input of the analytical continuation, so in the end spectral functions can be

extracted via

$$A(\omega) = -\frac{1}{\pi}\mathrm{Im}\left[G(\omega)\right], \tag{5.50a}$$

$$A(\omega, \boldsymbol{k}) = -\frac{1}{\pi}\mathrm{Im}\left[G(\omega, \boldsymbol{k})\right]. \tag{5.50b}$$

Depending on the overall shape of the self-energy, i.e. if non-diagonals elements are of importance or not, there are two choices:

1. Create an auxiliary Green's function by subtraction of the Hartree part of the real-part of $\Sigma(\mathrm{i}\infty)$, namely

   $$\tilde{\Sigma}(\mathrm{i}\omega_n) = \Sigma(\mathrm{i}\omega_n) - \Sigma(\mathrm{i}\infty). \tag{5.51}$$

   The analytical continuation then gives the real frequency self-energy on which the subtracted offset $\Sigma(\mathrm{i}\infty)$ is added again. This choice directly gives access to the self-energy, however only to the diagonal elements, since the non-diagonal elements do not fulfill the same relations as the diagonal elements.

2. Create an auxiliary Green's function

   $$G_{\mathrm{aux}}(\mathrm{i}\omega_n) = \left(\mathrm{i}\omega_n + \mu - \Sigma(\mathrm{i}\omega_n)\right)^{-1}, \tag{5.52}$$

   where μ is an additional free parameter, which is often chosen to be $\mu = \mu_{\mathrm{DMFT}} - \Sigma(\mathrm{i}\infty)$, or as in most of the presented data within this thesis at half-filling. The analytical continuation then leads to the real axis object $G_{\mathrm{aux}}(\omega)$ from whom the self-energy can be extracted via

   $$\Sigma(\omega) = \omega + \mu - G^{-1}_{\mathrm{aux}}(\omega). \tag{5.53}$$

   This method allows access to the non-diagonal elements of the self-energy, e.g. by using the MaxEnt implementation in [87].

Within this thesis both methods are used. It should be noted that, when dealing with purely diagonal self-energies, both methods qualitatively give the same results.

Chapter 6 Ruthenates

6.1 Ca_2RuO_4

The subsequent chapter is an extensive discussion of the theoretical and numerical results published in [24]. Methods, especially of numerical nature, used within this letter are given in more detail to further enhance reproducibility. Since the focus is mainly on the theoretical details, experimental results are just briefly mentioned.

6.1.1 Classification $Ca_{2-x}Sr_xRuO_4$

The class of $Ca_{2-x}Sr_xRuO_4$, as depicted in figure 6.1, shows a rich phase diagram in dependence of Sr/Ca doping. One of the most prominent members within this class is Sr_2RuO_4, which has a paramagnetic metallic high-temperature phase and transitions to a conventional Fermi liquid at temperatures below $\sim$20 K. Sr_2RuO_4 consists of layered RuO_6 octahedra and is of perovskite structure with the space group $I4/mmm$ (tetragonal space group). At even lower temperatures 0.93 K [93, 94] a non-conventional superconducting phase emerges whose origin and pairing mechanism is still under heavy debate [95, 96]. When doping with Ca, especially for $x = 0$, the other site of the phase diagram, i.e. Ca_2RuO_4, is reached. Ca_2RuO_4 is an archetypal Mott insulator of double perovskite structure with Pbca (orthorombic) space group. At $T_{\mathrm{MIT}} = 357$ K it undergoes a metal-to-insulator transition from a

paramagnetic metallic (L-Pbca) into a paramagnetic Mott insulating phases (S-Pbca). The phase transition is accompanied by an additional structural phase transition manifesting in orthorombic distortions, tilting and rotation of the RuO_6 octahedra. Moreover a shrinking of the c-axis is observed, justifying the conventional framing as S-Pbca (S: short) phase or L-Pbca (L: long) phase for the insulating or metallic phase. In general the structure becomes more orthorombic for lower temperatures [97–99]. Additionally an antiferromagnetic insulating phase is observed for temperatures $T_N = 110\,K$. Note that Ca has a smaller ionic radius than Sr but the same valence.

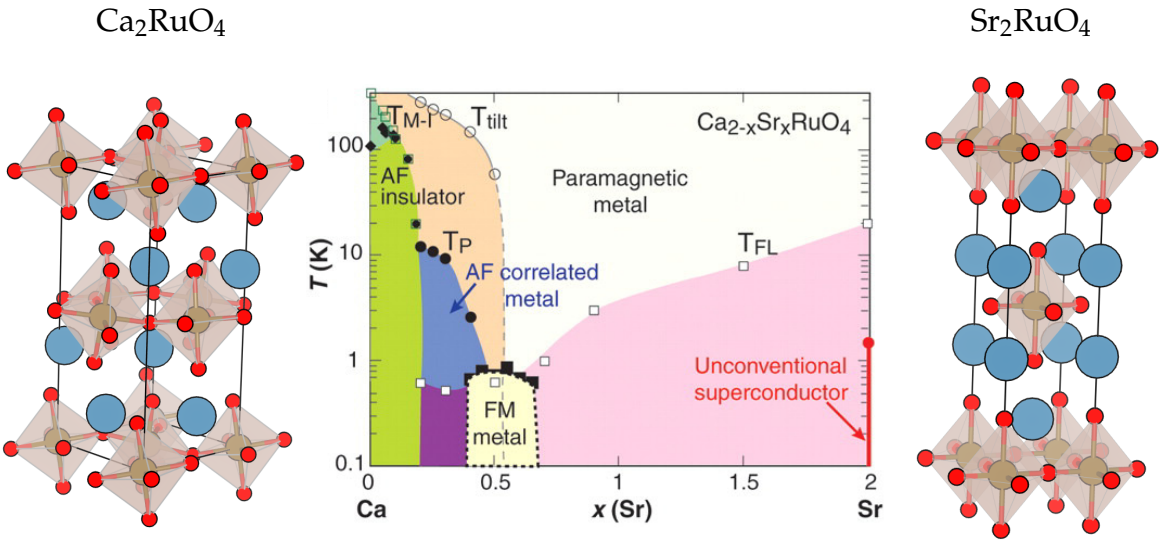

■ **Figure 6.1.:** Temperature phase diagramm of Ca_2RuO_4 (left structure) when doped with Sr_2RuO_4 (right structure). Taken from [100]. Red are the oxygen atoms, blue are Ca/Sr, and brown are the Ru atoms.

6.1.2 Ca_2RuO_4

In Ca_2RuO_4 the ruthenium is tetravalent, resulting in a $4d^4$ electron configuration. Since the t_{2g}-e_g cubic crystal field splitting is large, all four electrons are located within the t_{2g} subspace, thus forming a $S = 1$ spin state and total angular momentum of $L = 1$. The structural phase transition at T_{MIT} is accompanied by a large

rearrangement of orbital occupation, leading to strong d_{xy} orbital character below the Fermi level in the insulating phase (see next section). Recent experiments [101, 102] suggest that during the metal-to-insulator transition the structural changes lead to a fully occupied d_{xy} orbital and a orbital selective stabilization of a Mott insulator in the d_{xz} and d_{yz} orbitals (both filled with roughly one electron).

Below T_N calcium ruthenate is a quasi two dimensional antiferromagnetic insulator with magnetization in b direction. The origin of this behavior is currently debated, with the two prominent possible scenarios attributing it either to excitonic magnetism or simply as an emerging Heisenberg model with large single-ion anisotropy. Proponents of the former case argue that spin-orbit coupling could feasibly stabilize a non-magnetic ground state on a single site level. Superexchange of sufficient size could then drive condensation of excited spin-orbital multiplet states and facilitate a magnetic moment (and the emergence of a Higgs mode) [103]. Recent calculations [104] and experiments [102, 105] seems to validate the excitonic picture. However, an alternative explanation using a simple Heisenberg model with anisotropy would be a feasible scenario if the crystal field originating from orthorombic distortions overwhelms the spin-orbit coupling – a scenario suggested by some ab initio calculations [106–108] – leading to a more conventional $S = 1$ spin-order.

6.2 Current induced phases in Ca_2RuO_4

The following sections will follow the discussion from J. Bertinshaw et al., Phys. Rev. Lett. 123, 137204 (2019), Copyright 2019 American Physical Society (see [24]).

6.2.1 Experimental results

In [24] neutron and x-ray diffraction experiments were conducted on single-crystal samples of Ca_2RuO_4. Starting from the paramagnetic insulating S-phase small DC currents were applied stabilizing nonequilibrium crystal structures distinct

from those of the equilibrium phases realized by chemical doping, high pressure, or epitaxial strain [97, 109–112]. This is evident in the neutron diffraction data depicted in figure 6.2. When a small current is applied, two distinct peaks evolve (from (a) to (b)) which are referred to as S^*- and L^*-phase. When extracting the length of the c axis in dependence of temperature for both peaks (see (c)), the red data are always closer to c values of the equilibrium high temperature L-phase, vice verse the blue data are closer to the c lengths of the insulating S-phase. The assignment of the phases with an additional $*$ follows this trend. Further x-ray and resistivity measurements indicate that the S^*-phase evolves with

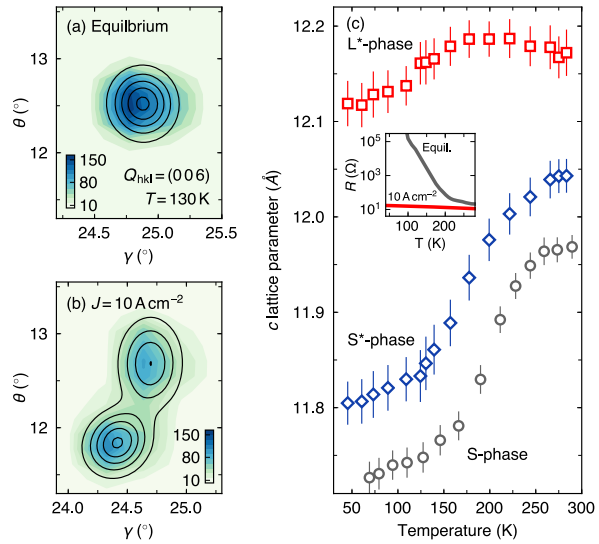

Figure 6.2.: (a) Single crystal neutron diffraction rocking scan at $T = 130\,\mathrm{K}$ in the S-phase, shown is the scattering angle θ over the horizontal detector axis γ. (b) Same measurement by applying a current parallel to the c-axis with $J = 10\,\mathrm{A\,cm^{-2}}$. (c) The fitted Q position of the reflections, shown as contour lines in (a) and (b), was used to calculate the temperature trend of the c-axis lattice parameters. The nonequilibrium S^*- and L^*-phases display a behavior distinct from the equilibrium S-phase, shown in gray. The inset plots the in situ resistance of the two states. Taken from J. Bertinshaw et al., Phys. Rev. Lett. 123, 137204 (2019), Copyright 2019 American Physical Society.

current density and persists as the whole system becomes semimetallic before the L^*-phase emerges. Moreover, the experiments show that the nonequilibrium

state does not become antiferromagnetic, as in the case of the equilibrium phase, when further lowering the temperature. From several measured reflections the crystallographic structure of both nonequilibrium phases were extracted using the FULLPORF software suite. The structural data are shown in table 6.1. As given in the table the refined data allow us to deduce some general behavior. By introducing the distance $b - a$, which is simply the difference of the crystal axis, it is possible to estimate orthorombic distortions. While in the nonequilibrium phases the orthorombic distortion become bigger in the paramagnetic insulating phase, the high temperature metallic structure is more tetragonal. Although rather small, this observation is also true in the nonequilibrium phases. Hence small deviations of the tetragonal crystal-field, resulting in small splittings of the d_{xz}- and d_{zy}-orbitals are expected. In the S-phase these distortions lead to c-axis flattening, tilting in the basal plane through the ab plane, and a rotation around the c-axis of the RuO_6 octahedra. In the establishment of the AFM phase orthormobicity and tetragonal compression are important [113]. Through perturbations, e.g. with temperature or Sr doping the equilibrium phase undergoes a first order transition to a metallic L-phase, where the c-axis increases while the unit cell volume will decrease. The difference to other perturbations is especially notable in the S*-phase, where orthorombicity and tetragonal compression are reduced, even as the c-axis lattice parameter is minor [24, 114].

6.2.2 Effective models for experimentally determined structures

Using the structural details in table 6.1 DFT calculations with a Wannier projection scheme (see chapter 2.3) is applied. All discussed DFT calculations were performed with VASP [34, 35], where the Perdew-Burke-Ernzerhof approximation for the universal exchange-correlation functional is implemented without spin-orbit coupling. For the L-phase we used the structural data published in [98].

Table 6.1.: Neutron diffraction structural refinement in the orthorhombic *Pbca* space group. Ru–O bonds and RuO_6 octahedral parameters at $T = 130\,K$ of the S-phase and S*- and L*-phases at $J = 10\,A\,cm^{-2}$. Θ–O(1) refers to the tilt angle between the basal plane and the *ab*-plane, Θ–O(2) is the angle between the Ru—O(2) bond and the *c*-axis, and Φ is rotation of the RuO_6 around the *c*-axis. The Ru–O ratio compares the apical and averaged in-plane Ru-O bond lengths, and is a measure of the tetragonal distortion. Taken from J. Bertinshaw et al., Phys. Rev. Lett. 123, 137204 (2019), Copyright 2019 American Physical Society.

Phase	S-phase	S*-phase	L*-phase
Temperature (K)	130	130	130
a (Å)	5.3842(8)	5.404(4)	5.341(5)
b (Å)	5.6158(9)	5.547(4)	5.436(6)
c (Å)	11.7461(11)	11.848(8)	12.153(9)
Volume ($Å^3$)	355.16(3)	355.2(2)	352.8(3)
Orthorhombicity ($b-a$)	0.23	0.14	0.10
Ru–O(1)a (Å)	2.0132(11)	2.001(4)	1.964(4)
Ru–O(1)b (Å)	2.0161(10)	2.005(3)	1.968(5)
Ru–O(2) (Å)	1.9683(11)	1.979(4)	2.021(4)
Ru–O avg (Å)	1.999	1.995	1.984
Ru–O ratio	1.023	1.012	0.972
Θ–O(1) (°)	12.79(1)	12.43(4)	10.69(4)
Θ–O(2) (°)	11.53(1)	10.65(4)	9.76(4)
Φ (°)	11.965(3)	11.874(10)	12.034(11)

Equilibrium Phases

For the equilibrium phases the crystal structure and DFT results are shown in figure 6.3, where (a) is the L-phase and (b) the S-phase. While a difference on the structural level is hard to identify, in the bandstructure and density of states (shown below) is. Although both bandstructures are of nearly similar shape, the S-phase bandstructure, especially for the bands with strong t_{2g} character (red curve in the DOS) are well separated from the lower lying bands with mainly oxygen character (blue curve in the DOS). In the L-phase this is not the case indicating a stronger oxygen hybridization with the t_{2g} orbitals. An additional difference is clearly visible in the DOS, while in the S-phase the whole DOS is uniform, in the L-phase a dip at roughly $-0.3\,\mathrm{eV}$ is apparent. It should be noted, that both structures lead to a metallic solution on the DFT level, due to the lack of correlations in DFT when dealing with Mott materials.

Nonequilibrium Phases

For the nonequilibrium phases the crystal structure, bandstructrue and density of state are shown in figure 6.4. Here column (a) shows the L*-phase and (b) the S*-phase. In general the behavior of these two phases on the DFT level is similar to the nonequilibrium phases, i.e. from simple DFT calculations it is not possible to see the physics describing a semimetallic state.

Nevertheless, DFT provides us – at least within the Wannier projection scheme – with the feasible crystal-fields and orbital hoppings. In figure 6.3 and 6.4 the red bands indicate the projection window ($-2\,\mathrm{eV}$ to $1\,\mathrm{eV}$) used to extract a low energy model of the form

$$\mathcal{H}_{\mathrm{hop}} = \sum_{i,j} t(\boldsymbol{R}) c_i^\dagger c_j, \tag{6.1}$$

where i,j are orbital indices and $\boldsymbol{R}$ a lattice vector. By Fourier transformation, e.g. for a specific $\boldsymbol{k}$ path, it is then possible to reproduce the bandstructure of the projection window. The red bands in both figures are actually the bands recalculated from the Wannier model and lie on top of the DFT bands. Note, that our basis is given by

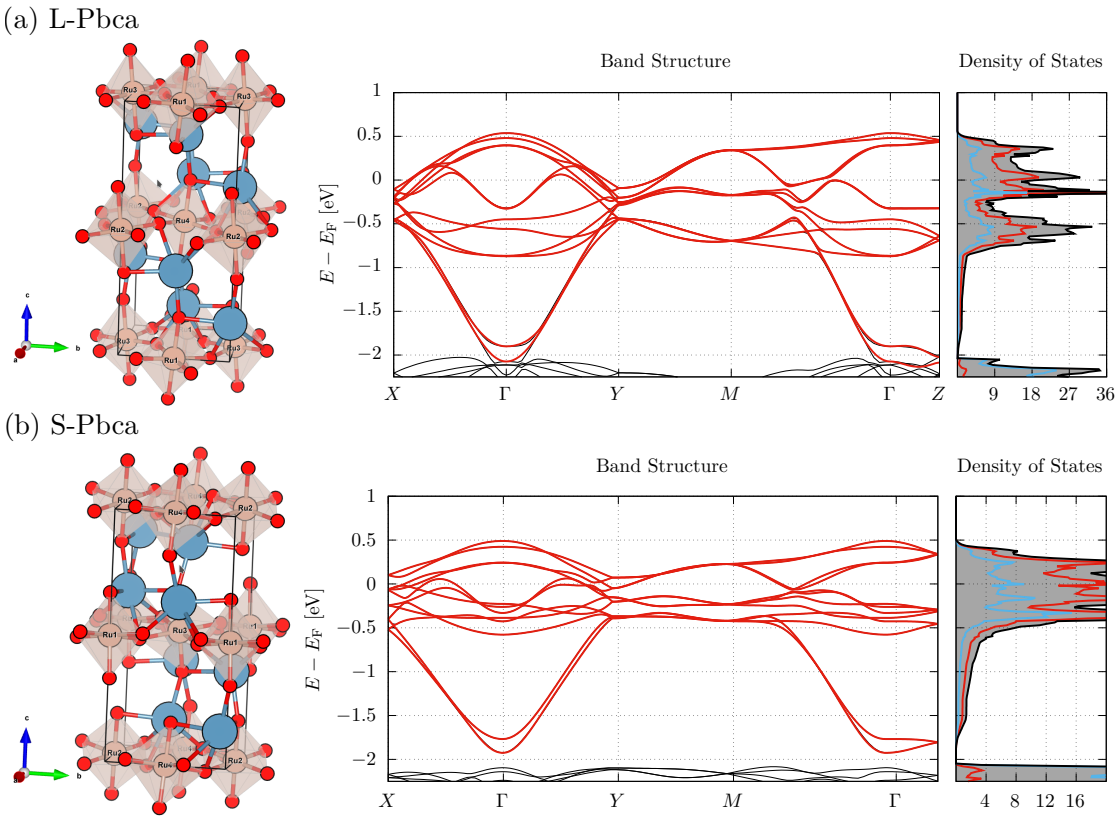

Figure 6.3.: Experimental structure, corresponding bandstructure, and density of states for the: (a) $T = 400\,\mathrm{K}$-phase (L-phase) and (b) S-phase of Ca_2RuO_4. Red bands correspond to the Wannier projection onto the t_{2g} orbitals, black are the DFT bands. DOS: DFT density of states and partial density of states for the t_{2g}- orbitals (red) of Ru and the p-orbitals of O.

tesseral harmonics (i.e. cubic harmonics) of a cubic t_{2g} subspace for each Ru atom, i.e. since four ruthenium atoms are in the primitive cell (two for each layer), each hopping matrix $t(\boldsymbol{R})$ is of the size 12×12.

6.2.3 Constructing the lattice Hamiltonian

From the above mentioned DFT calculations and Wannier projection a lattice Hamiltonian, containing spin-orbit coupling and Coulomb interaction, can be constructed via

$$\mathcal{H}_{\mathrm{lat}} = \mathcal{H}_{\mathrm{hop}} + \mathcal{H}_{\mathrm{SOC}} + \mathcal{H}_U, \tag{6.2}$$

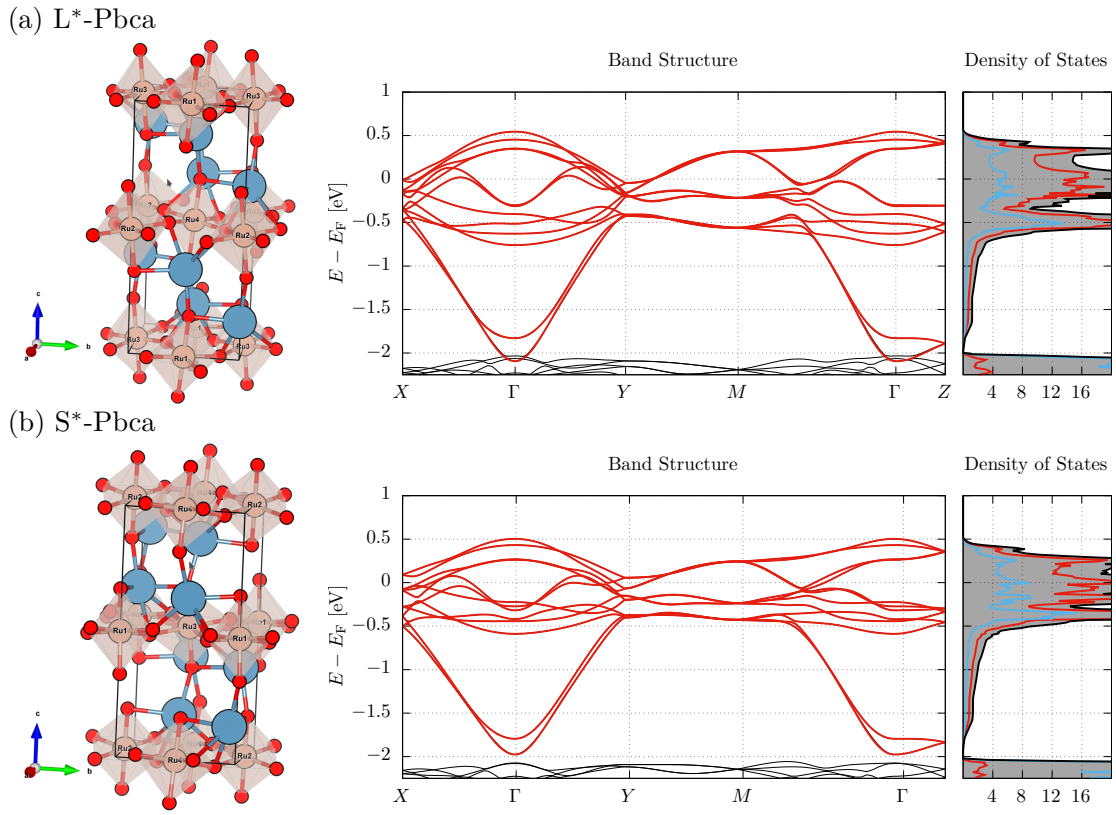

■ **Figure 6.4.:** Experimental structure, corresponding bandstructure, and density of states for the: (a) L*-phase and (b) S*-phase of Ca_2RuO_4. Red bands correspond to the Wannier projection onto the t_{2g} orbitals, black are the DFT bands. DOS: DFT density of states and partial density of states for the t_{2g}- orbitals (red) of Ru and the p-orbitals of O.

where for the Coulomb interaction we used the rotationally invariant Kanamori interaction operator of the form

$$\mathcal{H}_U = U\sum_{i,\alpha} n_{i\uparrow}^{(\alpha)} n_{i\downarrow}^{(\alpha)} + \frac{U'}{2}\sum_{i,\sigma}\sum_{\alpha\neq\beta} n_{i\sigma}^{(\alpha)} n_{i\bar{\sigma}}^{(\beta)} + \frac{(U'-J_H)}{2}\sum_{i,\sigma}\sum_{\alpha\neq\beta} n_{i\sigma}^{(\alpha)} n_{i\sigma}^{(\beta)} - J_H\sum_{i,\alpha\neq\beta}\left(c_{i\alpha\uparrow}^\dagger c_{i\alpha\downarrow} c_{i\beta\downarrow}^\dagger c_{i\beta\uparrow} - c_{i\alpha\uparrow}^\dagger c_{i\alpha\downarrow}^\dagger c_{i\beta\downarrow} c_{i\beta\uparrow}\right). \quad (6.3)$$

Here J_H describes Hund's coupling, U the Coulomb interaction strength, and $U' = U - 2J_H$. The spin-orbit coupling operator is added as a local operator for

each Ru site, by projecting only on the t_{2g} subspace, via

$$\mathcal{H}_{\mathrm{SOC}} = \zeta \sum_{i}^{N_e} \boldsymbol{l}_i \cdot \boldsymbol{s}_i, \tag{6.4}$$

where the sum runs over all N_e electrons. The explicit matrix form is give by

$$\mathcal{H}_{\mathrm{SOC}} = \frac{\zeta}{2} \begin{pmatrix} 0 & -\mathrm{i} & 0 & 0 & 0 & \mathrm{i} \\ \mathrm{i} & 0 & 0 & 0 & 0 & -1 \\ 0 & 0 & 0 & -\mathrm{i} & 1 & 0 \\ 0 & 0 & \mathrm{i} & 0 & \mathrm{i} & 0 \\ 0 & 0 & 1 & -\mathrm{i} & 0 & 0 \\ -\mathrm{i} & -1 & 0 & 0 & 0 & 0 \end{pmatrix}. \tag{6.5}$$

The ordering follow $\{d^{\uparrow}_{xz}, d^{\uparrow}_{yz}, d^{\uparrow}_{xy}, d^{\downarrow}_{xz}, d^{\downarrow}_{yz}, d^{\downarrow}_{xy}\}$. Within all calculations the strength of spin-orbit coupling is approximated by its Hartree-Fock value of $\zeta = 0.16\,\mathrm{eV}$ [106, 107, 115]. Note that Hamiltonian (6.2) actually describes a model with four different ruthenium sites, so spin-orbit coupling is always added on the corresponding subspace. During the subsequent DMFT calculations, Ru atoms related to the same layer are treated as equal, i.e. instead of solving four independent impurity problems only two are actually solved. Within our calculations Hund's coupling is chosen to be $J_{\mathrm{H}} = 0.4\,\mathrm{eV}$ and Coulomb interaction around $U \sim 2.0\,\mathrm{eV}$. The chosen values are consistent to cRPA calculations [107] and other publications [106].

6.2.4 DMFT results

With the help of the aforementioned lattice Hamiltonian, DMFT calculations for all four compounds were performed by using the triqs library [116] for $\beta = 30\,\mathrm{eV}$, which corresponds to a temperature of 387 K. Although this temperature does not fit to the experimental one, DMFT calculations using a CT-HYB QMC solver are limited by the fermionic sign-problem, restricting the calculations to higher temperatures. However, higher temperatures still lead to qualitatively correct physical phenomena, since the underlying Mott physics is still apparent. Of course,

this typically depends on the system of interest and does not hold for every DMFT calculation. From a numerical point of view the choice of this temperature is necessary, since DMFT calculations with spin-orbit coupling and the resulting off-diagonal elements within the hybridization function lead to a severe sign problem of CT-QMC solvers and hence to very noisy and qualitatively bad data.

In figure 6.5 single-particle spectral functions for all four phases, obtained from a fully converged DMFT calculation with U values ranging from 1.5 eV to 2.5 eV, are shown. The analytical continuation to obtain the $A(\omega)$ was done with a stochastic optimization method as presented and implemented in [88]. There is one trend clearly visible within the matrix plot. When going from left to right and to bigger U values the metal-to-insulator transition is shifted to smaller U values. When comparing the L-phase and the S- or S*-phase this behavior can be seen at $U = 2.0$ eV. Although the nonequilibrium phases and the equilibrium phases seem to share similar behavior, there are minor difference. First of all, except of the high temperature phase all other phases for $U = 2.5$ eV are purely insulating, where the equilibrium low temperature phase has the largest band gap. Since we are interested in studying all four phases on the brink of the metal-to-insulator transition, and also to compare the different phases with each other, a U value of 1.9 eV was chosen for subsequent calculations. As can be seen later (and also indicated for $U = 2.0$ eV), at this value the S*-phase is already more on the metallic side, with minor spectral weight at the Fermi level, suggesting a semimetal. The S-phase is still insulating. It should also be stressed, that the strength of the screened Coulomb interaction highly depends on the spreading of the derived Wannier function, i.e. the same U values for two different Wannier models is only justified if the spreading is equal. In the case of the S- and S*-phase this spreading is of the size $46.9(5)$ Å^2, indicating that the screened Coulomb interaction, if calculated via cRPA, is expected to be similar.

Similar calculations without spin-orbit coupling are presented in appendix B in figure B.1. Although the overall behavior is consistent with the discussion above,

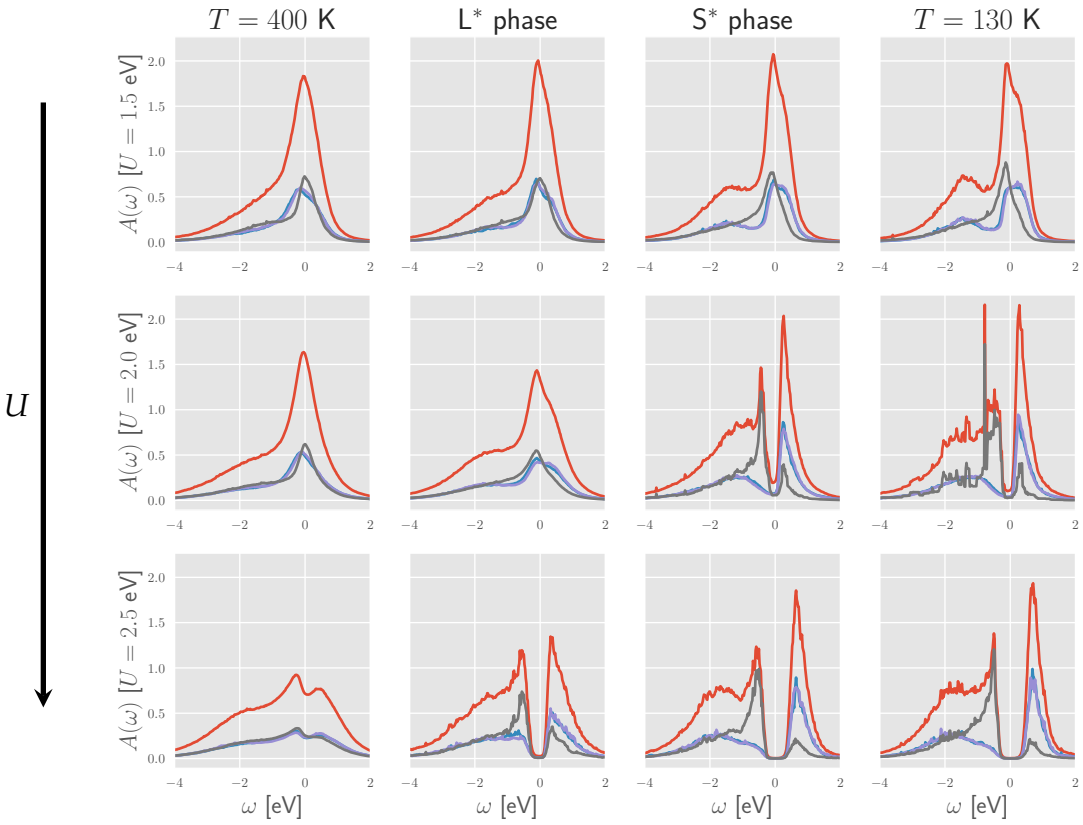

■ **Figure 6.5.:** Parameter search of all four phases (from left to right: L-phase, L*-phase, S*-phase, S-phase), with $J_{\mathrm{H}} = 0.4\,\mathrm{eV}$, $\lambda = 0.16\,\mathrm{eV}$, and U =1.5 eV to 2.5 eV, where the metal-to-insulator transition is expected. Shown are the single-particle spectral function for: xy-orbital (gray), xz/yz- orbital (blue/purple), and the total spectral function (red).

spin-orbit coupling seems to push the metal-to-insulator transition to smaller U values. When comparing the gaps in the insulating phases, e.g. for $U = 2.5\,\text{eV}$ this manifests in somewhat narrower gaps.

For $U = 1.9\,\text{eV}$ the $\boldsymbol{k}$-resolved spectral function $A(\omega, \boldsymbol{k})$ and the single-particle spectra $A(\omega)$ are shown for all four phases in figure 6.6 within a small energy range around the Fermi level. Following the observations discussed above, the current induced structural changes affect the metal-to-insulator transition quite severely. While the S-phase (a) is found to be Mott insulating with gap of $\sim 0.2\,\text{eV}$ between the upper and lower Hubbard bands, the features below the Fermi energy are predominantly of d_{xy} orbital character while the d_{xz}/d_{yz}-orbital character is forming the upper Hubbard band. In the nonequilibrium S*- and L*-phase ((b) and (c)) this behavior changes. Since the bands are broadened and overlap, releasing electron and hole charge carriers. Nonetheless, the semimetallic phase (b) is suggested by the suppression of spectral weight at the Fermi level, forming electron and hole pockets, emerging from the d_{xy} and d_{xy}/d_{zy} orbitals. Since spin-orbit coupling and small low-symmetry distortion mix the orbital character a clear distinction of the content of these pockets is quite difficult. The L-phase (d) and L*-phase (c), in both tetragonal and orthorombic distortions are further reduced, resembling similar features. There is no distinct orbital selective dominance around the Fermi level. All orbitals contribute nearly equally forming a metallic state. The average orbital occupation of all four phases are listed in table 6.2.

Comparing the orbital occupation of the metallic phases L and L* further exemplifies the similarity of both phases. This is up to some point also true for the S- and S*-phase, indicating a stronger tetragonal splitting than in the other phases. Of course, the S-phase has the strongest tetragonal filling leading to an average filling of 1.76 for the d_{xy} orbital. Considering the calculations done for U values of 2.0 eV to 2.5 eV shown in figure 6.5 (right column) this filling changes to $n_{xy} = 1.83$ and the rest of the electrons are nearly equally distributed to the d_{xz}/d_{yz} orbitals, supporting the orbital selective Mott transition picture of Ca_2RuO_4.

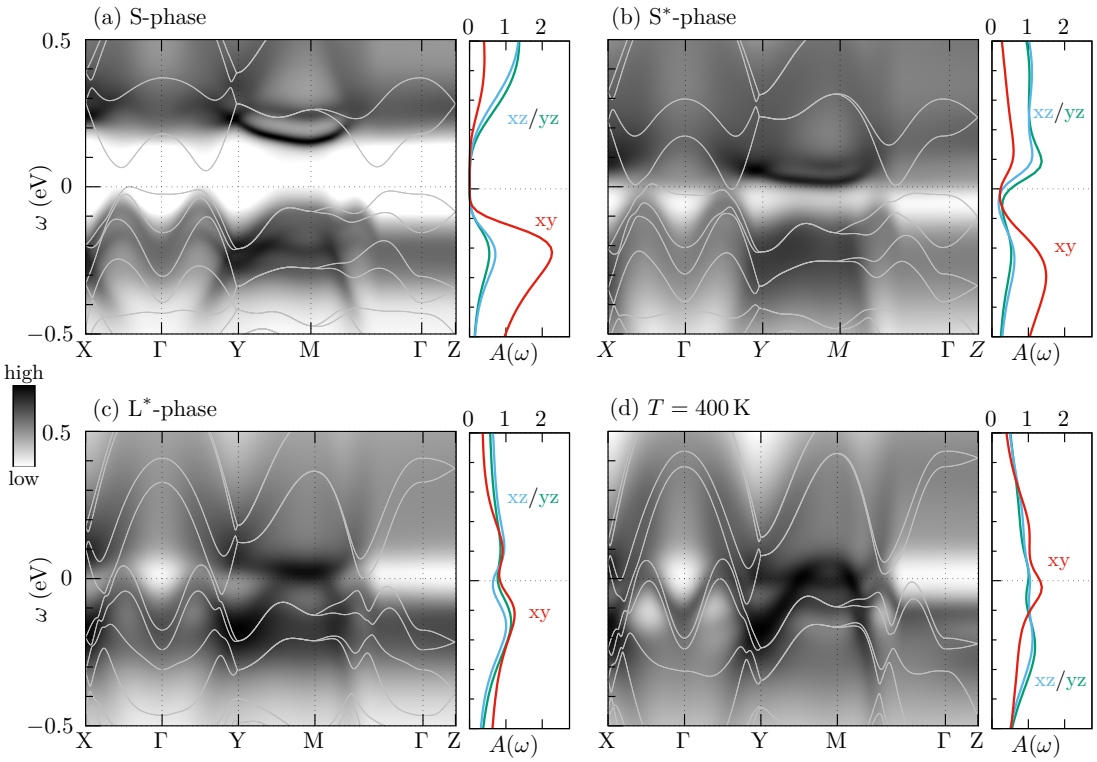

■ **Figure 6.6.:** DMFT-calculated intensity map for electron spectral function $A(\omega,\mathbf{k})$ (in arbitrary units, dark color implies high intensity) as a function of energy ω (counted from chemical potential) and momentum $\mathbf{k}$ along high-symmetry directions in the orthorhombic Brillouin zone. Orbitally resolved local spectra $A(\omega)$ (in units of 1/eV) are shown on the right of each panel. Light gray lines show DFT+U mean-field bands. Calculations are based on the $T = 130\,\mathrm{K}$ structure of the (a) equilibrium S-phase, non-equilibrium (b) S*- and (c) L*-phases, and on the (d) $T = 400\,\mathrm{K}$ structure from [109]. In the current-induced phases (b) and (c), the insulating gap is closed and electron and hole pockets are formed, indicating semi-metallic behavior. Reproduced from J. Bertinshaw et al., Phys. Rev. Lett. 123, 137204 (2019), Copyright 2019 American Physical Society.

Table 6.2.: Occupation numbers of three t_{2g} orbitals from DMFT calculations. The structural similarity is reflected in similar occupation numbers between the S- and S*-phases, and between the L*- and 400 K phases.

	S	S*	L*	$T = 400\,\mathrm{K}$
n_{xz}	1.11	1.16	1.28	1.34
n_{yz}	1.13	1.14	1.25	1.32
n_{xy}	1.76	1.70	1.47	1.34
n_{tot}	4.00	4.00	4.00	4.00

6.2.5 Analytic continuation of the self-energy

Subsequently, the quality of the analytic continuation of the self-energy $\Sigma(i\omega_n)$, as introduced in chapter 5.6, will be discussed in more detail. As mentioned earlier, when performing DMFT calculations with a CT-QMC solver, or generally on the Matsubara axis one always needs to go back to the real ω axis. Typically this analytic continuation is performed only on the diagonal elements of the converged impurity or lattice (local) Green's function. It only leads to the single-particle spectral function $A(\omega)$. For all four phases of Ca_2RuO_4 the result is depicted in figure 6.7 (upper row). All calculations were performed with a MaxEnt method as provided by [87]. As shown all four phases correspond and agree with the discussion from the previous section.

However, when the object of interest is the $\boldsymbol{k}$-resolved spectral function $A(\omega, \boldsymbol{k})$, which is the case for ARPES spectra, one is left with two choices: (i) Analytical continuation of local Green's function for one specific $\boldsymbol{k}$ point, i.e. to obtain the full $A(\omega, \boldsymbol{k})$ multiple Green's functions for different $\boldsymbol{k}$ points must be analytically continued, or (ii) analytic continuation of the $\Sigma(i\omega)$ itself (see chapter 5.6). While the first method is known to work most of the time, the spectral features are often washed out, especially in calculation where the sign problem becomes severe.

On the other hand the second method, although leading to qualitatively better $A(\omega, \boldsymbol{k})$, is known to be difficult for systems with big off-diagonal elements in the hybridization function. The latter concept was used to obtain the spectral function for all four phases of Ca_2RuO_4 and is shown in figure 6.7 (bottom row).

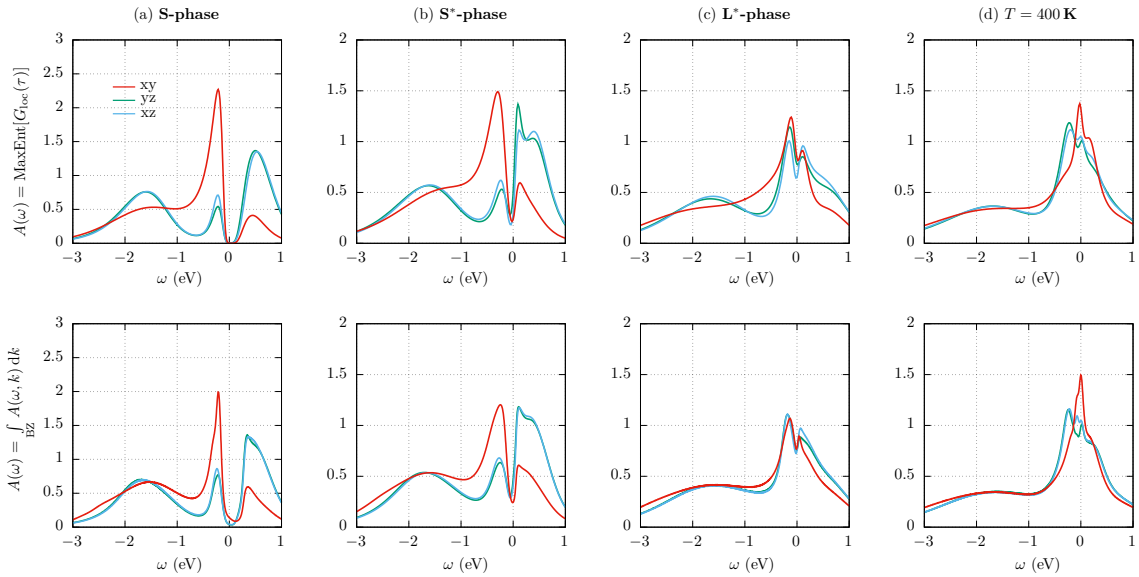

■ **Figure 6.7.:** Local spectral functions $A(\omega)$ for all studied structures, as obtained from two different procedures: (upper panels) Direct analytical continuation of the local Green's function, $G_{\text{loc}}(i\omega_n)$. (lower panels) Analytical continuation of the self-energy, $\Sigma(i\omega_n)$, and integration of the resulting k-resolved spectral function over the 1st Brillouin zone. Reproduced from J. Bertinshaw et al., Phys. Rev. Lett. 123, 137204 (2019), Copyright 2019 American Physical Society.

Within this thesis we tried to enhance the quality of the analytic continued self-energies by performing a rotation onto the self-energy so it becomes diagonal, which of course is in general not possible. Instead we performed a rotation into a basis where the diagonal elements of $\Sigma(i\omega_n)$ are absolutely dominant compared to the off-diagonals. The off-diagonals are then neglect for the analytical continuation itself. A good candidate for the rotation $\mathcal{R}$ – at least in our case – seems to be the

rotation into the density basis of the half-filled $G_{\text{aux}}(i\omega_n)$, which is given by

$$G_{\text{aux}}(i\omega_n) = \frac{1}{i\omega_n + \mu - \Sigma(i\omega_n)}. \tag{6.6}$$

Extracting the density matrix ϱ_{aux} and diagonalizing gives $d = \mathcal{R}^\dagger \varrho_{\text{aux}} \mathcal{R}$, where d is a diagonal matrix. The rotated self-energy is then $\tilde{\Sigma}(i\omega_n) = \mathcal{R}^\dagger \Sigma(i\omega_n)\mathcal{R}$, from whom we can construct a diagonal auxiliary Green's function $\tilde{G}_{\text{aux}}(i\omega_n)$. After the analytic continuation the self-energy on the real axis is then

$$\Sigma(\omega) = \mathcal{R}\left[\omega + \mu - \tilde{G}^{-1}_{\text{aux}}(\omega)\right]\mathcal{R}^\dagger. \tag{6.7}$$

When comparing both rows in figure 6.7 the general agreement is satisfying. Nonetheless there are some minor differences. These are probably best indicated in (a), where the insulating gap is decreasing, due to a "wandering" tail of the low energy features below the Fermi energy. Nevertheless, it should be stressed that our rotation procedure leads to good results when compared to the overall $\boldsymbol{k}$ resolved spectral functions $A(\omega, \boldsymbol{k})$ (e.g. figures 6.11, 6.10, 6.9, 6.8) and experiments performed in the S-phase (see ARPES spectra in [106]).

The DMFT self-energies $\Sigma(i\omega_n)$ and its analytic continuations $\Sigma(\omega)$ are explicitly shown in appendix B in figure B.3 and figure B.4, respectively. Within both plots all diagonal elements and the dominating off-diagonal elements are plotted in a ω window of $-1.5\,\text{eV}$ to $1.5\,\text{eV}$. Other off-diagonal elements were neglected, since their contributions were rather small. Considering only the diagonal elements of the analytic continued self-energy in figure B.3 and comparing the phase L to S (from bottom to top) a remarkable Fermi-liquid like behavior, i.e. a linear real and a quadratic imaginary self-energy for small ω is observed even up to the S*-phase. The Fermi-liquid like behavior in the metallic phases can be extracted from the power expansion of the imaginary part of $\Sigma(i\omega_n)$. For small $i\omega_n$ one finds

$$\text{Im}\left[\Sigma(i\omega_n)\right] \approx \omega^\alpha. \tag{6.8}$$

In the Fermi-liquid case the exponent is $\alpha = 1.0$. For values $0 < \alpha < 1$ metals are also called Hund's metals [117–119]. The parameter α can be extracted from $\Sigma(i\omega_n)$

by fitting around the lowest Matsubara frequencies. Comparing only d_{xy} elements of the L- and L*-phase, in the presented results, α is of the size 0.82 and 0.59. This indicates that these phases of Ca_2RuO_4 are indeed Hund's metals. It should be noted that framing metals as Hund's metals is not rigorously defined, the phrase should rather emphasize the importance of Hund's coupling, typically resulting in bad metallic behavior, in various compounds. For further insight see [117, 118].

6.2.6 Further DMFT single-particle spectra

Since figure 6.6 provides better insight into details within a small energy window around the Fermi energy, subsequently the same data in a broader energy window are shown. This allows a better comparison with experiments such as [106, 120]. In this section spectral functions $A(\omega)$ and $A(\omega, \boldsymbol{k})$ for all four phases in a energy window ranging from $-3\,\mathrm{eV}$ to $1\,\mathrm{eV}$ are provided.

In figure 6.8 the equilibrium S-phase is shown. As mentioned earlier it is fully insulating with gap of $\sim 0.2\,\mathrm{eV}$, where the lower Hubbard band is dominated by the d_{xy} orbital. The upper Hubbard band is mostly of d_{yz}/d_{xz} character. It should be stressed that the experimentally observed gap is roughly $0.5\,\mathrm{eV}$ and hence a bit bigger than the numerical one. In the past a couple of measurements were performed on this phase (see [106, 120]) providing us with the opportunity to compare our DMFT spectra. Overall the agreement is satisfactory. As confirmed by the experiments there is a dispersive band around $-2\,\mathrm{eV}$ to $-1\,\mathrm{eV}$ of mainly d_{xy} character. Additionally in our data there are minor d_{xz}/d_{yz} features around $0.3\,\mathrm{eV}$.

Applying a small current to the S-phase stabilizes the S*-phase, as shown in figure 6.9, making it semimetallic by redistributing spectral weight from the Hubbard bands towards the Fermi level. Most of the spectral weight around and especially below the Fermi energy is of d_{xy} character and originates from quasi-particle bands crossing E_F between Γ and X/Y. The hole pockets are hence mostly derived from the d_{xy} orbital. However, it should be noted that this assignment is a bit flawed, because the resolution of the spectra highly depends on the calculation temperature,

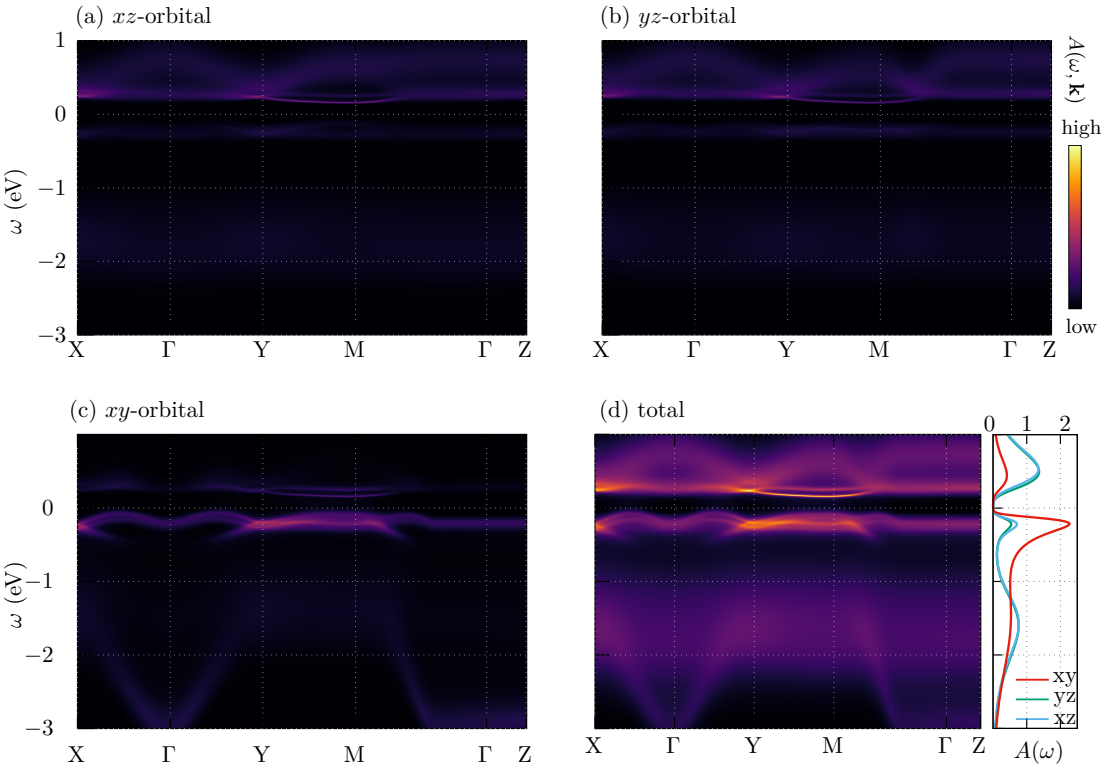

■ **Figure 6.8.:** $T = 130\,\mathrm{K}$ equilibrium S-phase: DMFT intensity map of the single particle spectral function $A(\omega,\mathbf{k})$ (in arbitrary units, dark color implies high intensity) as a function of energy ω and momentum $\mathbf{k}$ along high-symmetry directions in the orthorhombic Brillouin zone, projected on the (a) xz-orbital, (b) yz-orbital and (c) xy-orbital. Panel (d) shows the total spectral function $A(\omega,\mathbf{k})$ (left) and orbital resolved local spectra $A(\omega)$ (right, in units of $1/\mathrm{eV}$). Reproduced from J. Bertinshaw et al., Phys. Rev. Lett. 123, 137204 (2019), Copyright 2019 American Physical Society.

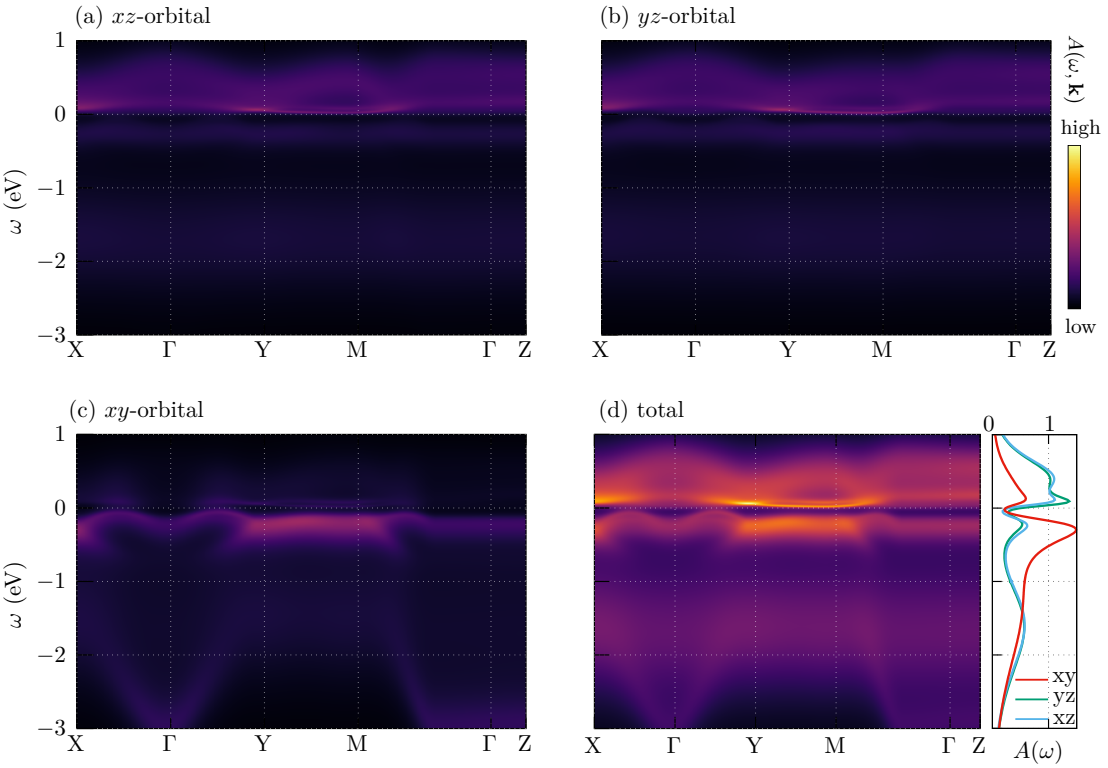

■ **Figure 6.9.:** Non-equilibrium S*-phase: DMFT intensity map of the single particle spectral function $A(\omega,\mathbf{k})$ (in arbitrary units, dark color implies high intensity) as a function of energy ω and momentum $\mathbf{k}$ along high-symmetry directions in the orthorhombic Brillouin zone, projected on the (a) xz-orbital, (b) yz-orbital and (c) xy-orbital. Panel (d) shows the total spectral function $A(\omega,\mathbf{k})$ (left) and orbital resolved local spectra $A(\omega)$ (right, in units of 1/eV). Reproduced from J. Bertinshaw et al., Phys. Rev. Lett. 123, 137204 (2019), Copyright 2019 American Physical Society.

which in our case was rather high. Additionally, the low symmetry distortions and spin-orbit coupling mix the orbital character in the quasi-particle bands.

Increasing the current even more leads to the stabilization of the L^*-phase, as shown in figure 6.10. More spectral weight is transferred towards the Fermi energy and smaller tetragonal distortions pushing the phase into the metallic regime. Although structurally different from the high temperature L-phase (depicted in figure 6.11) the features are quite similar. Nonetheless, all calculations show an extreme sensitivity of the electronic structure to minor structural changes caused by applying small DC currents. Models describing these non-equilibrium phases hence must include such distortions.

6.2.7 Numerical details

All calculations were performed with DFT+DMFT in its single-shot procedure. While for the DFT part we used the VASP [34, 35] package and its interface to wannier90 [23], the DMFT calculations were done with the triqs [116] library with the hybridization expansion solver as provided from [121] as additional module to the triqs library. For the analytic continuation mainly a maximum entropy method (MaxEnt) implemented by [87], and sometimes a stochastic optimization method as implemented in [88] was used. In order to achieve qualitatively good data (especially for the delicate analytical continuation) for each aforementioned phase of Ca_2RuO_4 a statistical ensemble of about 100 to 200 independent solutions (measurements) – each containing $\sim 10^6$ QMC cycles – of the converged impurity model was accumulated. The quantities of interest are hence extracted form the averaged single-particle propagator $G_{\text{loc}}(i\omega_n)$ and self-energy $\Sigma(i\omega_n)$.

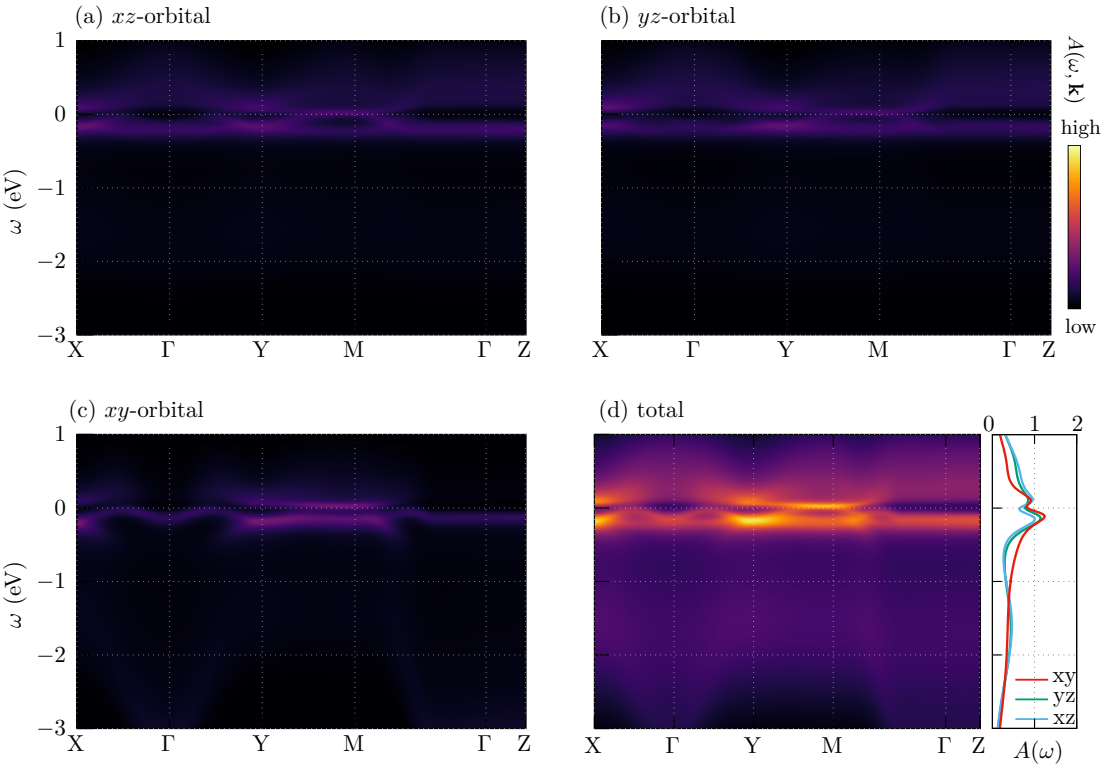

■ **Figure 6.10.:** Non-equilibrium L*-phase: DMFT intensity map of the single particle spectral function $A(\omega,\mathbf{k})$ (in arbitrary units, dark color implies high intensity) as a function of energy ω and momentum $\mathbf{k}$ along high-symmetry directions in the orthorhombic Brillouin zone, projected on the (a) xz-orbital, (b) yz-orbital and (c) xy-orbital. Panel (d) shows the total spectral function $A(\omega,\mathbf{k})$ (left) and orbital resolved local spectra $A(\omega)$ (right, in units of 1/eV). Reproduced from J. Bertinshaw et al., Phys. Rev. Lett. 123, 137204 (2019), Copyright 2019 American Physical Society.

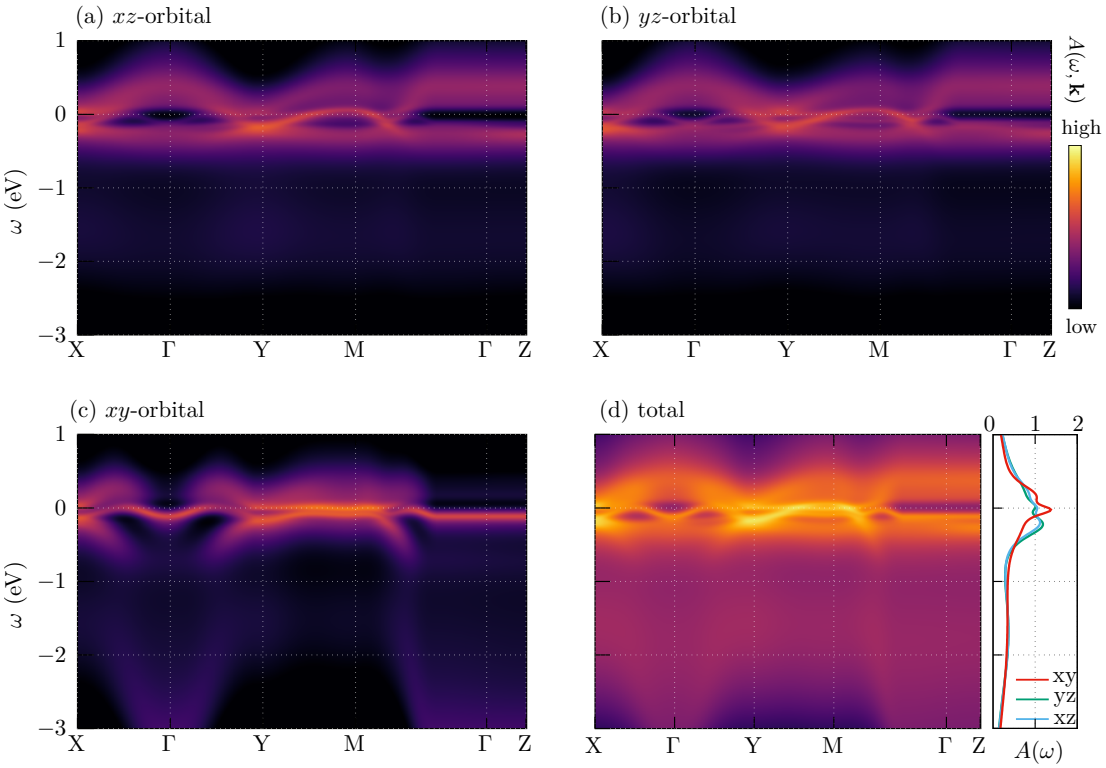

■ **Figure 6.11.:** Equilibrium L-phase: DMFT intensity map of the single particle spectral function $A(\omega,\boldsymbol{k})$ (in arbitrary units, dark color implies high intensity) as a function of energy ω and momentum $\boldsymbol{k}$ along high-symmetry directions in the orthorhombic Brillouin zone, projected on the (a) xz-orbital, (b) yz-orbital and (c) xy-orbital. Panel (d) shows the total spectral function $A(\omega,\boldsymbol{k})$ (left) and orbital resolved local spectra $A(\omega)$ (right, in units of 1/eV). Reproduced from J. Bertinshaw et al., Phys. Rev. Lett. 123, 137204 (2019), Copyright 2019 American Physical Society.

Chapter 7 From DMFT to core-level spectroscopy

So far all the DMFT calculations were restricted to calculating local quantities, such as the single-particle spectral function $A(\omega)$ or $A(\omega, \boldsymbol{k})$. Although in principal static susceptibilities and other thermodynamic quantities are accessible, due to steadily increasing resolution of core-spectroscopic methods such as XAS or RIXS also core-level spectroscopy has become a more and more popular tool in studying materials within the last decades. Especially, RIXS enables the observation of low-energy spin, orbital, and charge excitations ($\sim 100\,\text{meV}$) [122–124] together with high-energy excitations (1 eV to 10 eV), like atomic multiplets or charge-transfer excitations [50, 125].

RIXS spectra are traditionally calculated within a configuration-interaction cluster calculation scheme. However, these calculations are limited when fine spectral features become crucial, which is the case in high-resolution experiments. Especially in the case of L-edge RIXS experiments of numerous TMOs this becomes evident. To overcome this obstacle it was recently proposed in [126] to use converged LDA+DMFT calculations to extract XAS and RIXS spectra. Of course DMFT alone was not constructed to solve core-level problems, since the core states are not part of the DMFT scheme. However as we will see below there is possibility to extend the DFT+DMFT scheme. Subsequently, this will be explained in more detail and then tested for LiV_2O_4.

7.1 Extracting the Anderson impurity model

7.1.1 Idea

Following [25, 126] the fundamental idea of extracting XAS or RIXS spectra is to discretize the DMFT converged hybridization function $\Delta(\omega)$, so one can construct the underlying Anderson impurity model for a discrete number of bath sites. The Anderson impurity model is typically written in the form

$$\mathcal{H}_{\mathrm{AIM}} = \sum_{\sigma} \varepsilon_{\sigma}^{(i)} d_{\sigma}^{\dagger} d_{\sigma} + \sum_{i,\sigma} \varepsilon_{i}^{(b)} c_{i\sigma}^{\dagger} c_{i\sigma} + V_i (c_{i\sigma}^{\dagger} d_{\sigma} + \mathrm{h.c.}) + \mathcal{H}_{\mathrm{int}}, \tag{7.1}$$

where $d/d^{\dagger}$ ($c/c^{\dagger}$) are the annihilation and creation operators of an electron with spin σ on the impurity (bath). While the first term of the Hamiltonian describes the impurity with impurity energy $\varepsilon_{\sigma}^{(i)}$, the second and third term describe the bath energies $\varepsilon_{i\sigma}^{(b)}$ and the impurity-to-bath hopping V_i. The sum over i runs over the number of bath sites. The last term $\mathcal{H}_{\mathrm{int}}$ describes a local interaction on the impurity. In order to construct the Hamiltonian one needs to know the hopping parameter V_i and the bath energies $\varepsilon_{i\sigma}^{(b)}$. The local impurity values are typically given by the model Hamiltonian of the DMFT calculation. This step is consistent with DMFT methods using an exact diagonalization solver, such as the Lanczos method [127] for solving the Anderson impurity model [32], where the bath Green's function

$$G_{\mathrm{bath}}^{-1}(\omega) = \omega + \mu - \int_{-\infty}^{\infty} \frac{\Delta(\omega)}{\omega - \omega'} \mathrm{d}\omega' \tag{7.2}$$

is approximated by the discretized version

$$G_{\mathrm{And}}^{-1}(\omega) = \omega + \mu - \sum_{\ell=1}^{N_b} \frac{V_{\ell}^2}{\omega - \varepsilon_{\ell}^{(b)}} \tag{7.3}$$

corresponding to the Anderson impurity model $\mathcal{H}_{\mathrm{AIM}}$. Here N_b denotes the number of bath sites.

Writing $\mathcal{H}_{\mathrm{AIM}}$ on the single-particle level as a matrix of the form

$$\mathcal{H}_{\mathrm{AIM}} = \begin{pmatrix} \varepsilon^{(i)} & V_1 & V_2 & V_3 & \dots \\ V_1 & \varepsilon_1^{(b)} & 0 & 0 & \\ V_2 & 0 & \varepsilon_2^{(b)} & 0 & \\ V_3 & 0 & 0 & \varepsilon_3^{(b)} & \\ \vdots & & & & \ddots \end{pmatrix} \tag{7.4}$$

shows, that the baths do not "talk" to each other. For simplicity only the one band case is discussed and the spin index is suppressed. However since so far no spin mixing term is included it should be clear that when the spin index is included, the $\mathcal{H}_{\mathrm{AIM}}$ can be written in block form. Moreover, this representation shows the "star geometry" of the Anderson impurity model, which will be important later. From here on there are two possibilities to extract the V_ℓ and $\varepsilon_\ell^{(b)}$:

1. Fitting of the hybridization function $\Delta(\mathrm{i}\omega_n)$ on the Matsubara axis via the function

$$\Delta_{\mathrm{Fit}}(\mathrm{i}\omega_n) = \sum_\ell \frac{V_\ell^2}{\mathrm{i}\omega_n - \varepsilon_\ell}. \tag{7.5}$$

The hybridization function can be calculated from the converged DMFT loop as

$$\Delta_{\mathrm{DMFT}}(\mathrm{i}\omega_n) = \mathrm{i}\omega_n + \mu - h^{(0)} - \mathcal{G}_0^{-1}(\mathrm{i}\omega_n), \tag{7.6}$$

where μ is the DMFT chemical potential, h^0 the local part of the model Hamiltonian, and $\mathcal{G}_0^{-1}(\mathrm{i}\omega_n) = (\Sigma(\mathrm{i}\omega_n) + G_{\mathrm{loc}}^{-1}(\mathrm{i}\omega_n))$. The cost function which is then minimized is typically given by

$$\chi = \frac{1}{n_{\max}+1} \sum_{n=0}^{n_{\max}} |\Delta_{\mathrm{DMFT}}(\mathrm{i}\omega_n) - \Delta_{\mathrm{Fit}}(\mathrm{i}\omega_n)|^2, \tag{7.7}$$

where $n_{\max}$ is the Matsubara cut-off. This can be minimized by standard methods like conjugate gradient. Historically this is also the method of choice when using an exact diagonalization solver [22, 74].

2. Construct the hybridization function on the real axis by analytical continuation of the self-energy $\Sigma(\mathrm{i}\omega_n)$. When applying this method one assumes a diagonal hybridization and self-energy, which is in the case of non-diagonal $\Sigma(\mathrm{i}\omega)$, a further approximation.

In the ideal case both methods should give equivalent results – at least when assuming infinite bath sites – however the first method turns our to be more unstable. This typically manifests when only a few number of bath sites are considered, in differences between the numerical and physical values of V_ℓ and $\varepsilon_\ell^{(b)}$, which of course fulfill the χ^2 minimization, compared to $\Delta(\omega)$ directly. However the second method, as subsequently discussed, leads to a more consistent way in sampling $\Delta(\omega)$.

7.1.2 Discretization of the hybridization function

Within this section the discretization using the second method (see above) will be discussed. To do so, one first has to analytically continue the self-energy $\Sigma(\mathrm{i}\omega_n)$ of the converged DMFT calculations. The procedure is described in chapter 5.6. It should be noted, that in the case of a purely diagonal self-energy, this procedure is not an approximation so far. In general however, one sticks to the approximation of only concentrating on the diagonal elements [126], since otherwise also the non-diagonal elements need to be discretized and included into $\mathcal{H}_{\mathrm{AIM}}$. For simplicity the here presented work only uses the diagonal parts. The analytical continuation leads to a self-energy of the form shown in figure 7.1. Here a maximum entropy method as implemented in [87] was used. With the help of the real frequency self-energy we can easily calculated the local Greens function and extract the hybridization function $\Delta(\omega)$ via

$$\Delta(\omega) = \omega + \mu - h^{(0)} - (\Sigma(\omega) + G_{\mathrm{loc}}^{-1}(\omega)). \tag{7.8}$$

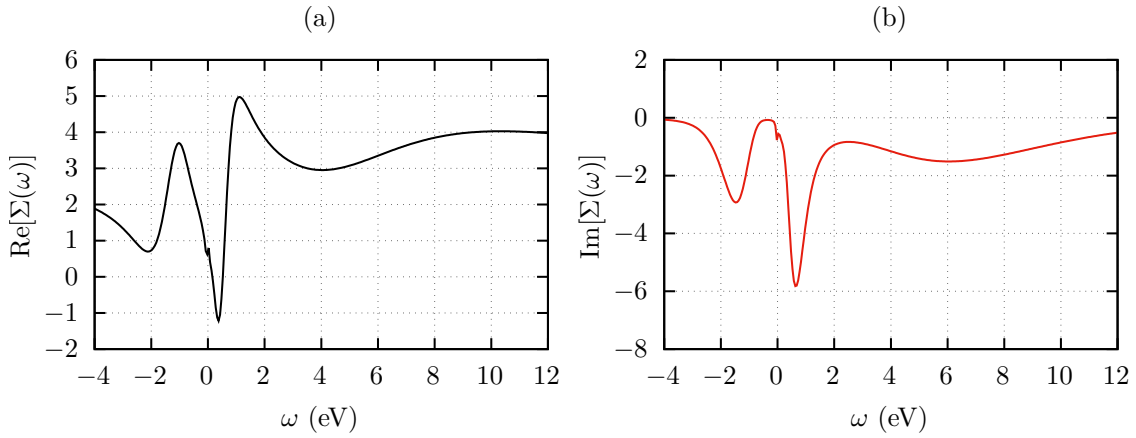

■ **Figure 7.1.:** Self-energy on the real axis from a converged DMFT calculation of a test orbital taken from LiV_2O_4: (a) Imaginary part, (b) real part.

The spin- and orbital-diagonal hybridization density $V(\omega)$, from whom we will extract the bath hopping and energies, on the real axis is then given by

$$V^2_{\gamma\sigma}(\omega) = -\frac{1}{\pi}\mathrm{Im}\left[\Delta_{\gamma\sigma}(\omega)\right], \tag{7.9}$$

where γ is the orbital index [25]. From those functions we can derive the bath hoppings V_ℓ and energies ε_ℓ by calculating

$$V^2_\ell = \int_{I_\ell} V^2_{\gamma\sigma}(\omega)\mathrm{d}\omega, \tag{7.10a}$$

$$\varepsilon_\ell = \frac{1}{V^2_\ell}\int_{I_\ell} \omega V^2_{\gamma\sigma}(\omega)\mathrm{d}\omega. \tag{7.10b}$$

Each interval $I_\ell \in [\omega_\ell, \omega_{\ell+1}]$ corresponds to a bath site. This discretization can be interpreted as representing each interval I_ℓ as a delta peak at position ε_ℓ and weight V^2_ℓ [128, 129]. In the discretization, we have employed a uniform energy mesh in the intervals with sizable hybridization intensity (here defined as larger than 1% of the peak value). The results for 15 bath sites for the one test orbital is shown in figure 7.2 (a). We note here that the hybridization strength V^2_ℓ represented by the vertical bars should be distinguished from the hybridization intensities $V^2_{\gamma\sigma}(\omega)$

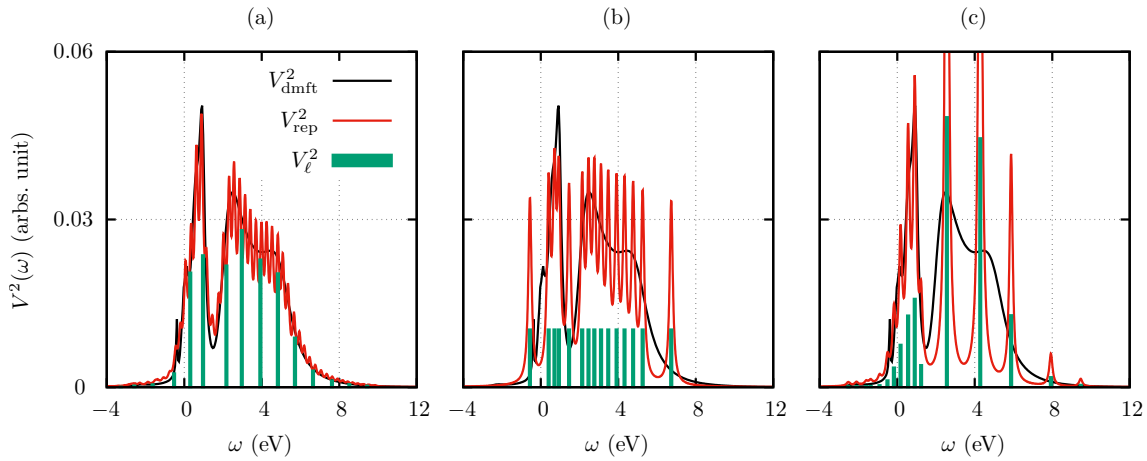

Figure 7.2.: Hybridization density $V^2(\omega)$ (black) from the DMFT calculations, discretized bath hopping V^2_ℓ (green bars), and reproduced hybridization density for a test orbital of LiV_2O_4 with different methods: (a) Discretization by 15 bath sites when ω axis is divided by equidistant ranges (linear discretization), (b) Nonlinear discretization which results in equidistant hoppings weights V^2_ℓ, and (c) linear scaling of 17 bath sites but by splitting the hybridization density into an less sampled high energy part and lower energy part with finer sampling. For all reproduced hybridization densities (red) a smearing of $\delta = 0.1$ was applied.

because V_ℓ and (diagonal element of) $V^2_{\gamma\sigma}(\omega)$ are related by (from [25])

$$V^2_{\gamma\sigma}(\omega) = -\frac{1}{\pi}\mathrm{Im}\left[\sum_\ell \frac{V^2_\ell}{\omega - \varepsilon_\ell + \mathrm{i}\delta}\right]. \tag{7.11}$$

In figure 7.2 this is shown for a smearing of $\delta = 0.1$ in the red curves.

Instead of using a uniform mesh one can create a non-uniform one by dividing the total weight of the function by the number of bath sites, i.e.

$$W_{\mathrm{tot}} = \int V^2_{\gamma\sigma}(\omega)\mathrm{d}\omega, \tag{7.12}$$

$$V^2_\ell = \int_{I_\ell} V^2_{\gamma\sigma}(\omega)\mathrm{d}\omega = \frac{W_{\mathrm{tot}}}{N_b}. \tag{7.13}$$

Within this scheme the bath-hoppings V_ℓ are equivalent. An example for various bath sites is shown in figure 7.2 (b).

Instead of sampling the whole hybridization density figure 7.2 (b) by one of the above mentioned features it is also common to split into high energy and low energy part of $V^2(\omega)$, so a different kind of bath sampling becomes possible. This might be helpful if, e.g. a good separation of weight within $V^2(\omega)$ is clearly visible or as shown in figure 7.2 (c) (linear discretization) the low energy part need a finer sampling.

7.1.3 Natural orbital basis

With the aforementioned discretization scheme the Anderson impurity model can be extracted for an arbitrary amount of bath sites. Unfortunately, this still faces the problem of an exponentially growing Hilbert space, so exact diagonalization is still very challenging. Luckily, in 2014 Haverkort et al [130] have demonstrated, that exact diagonalization for a one-band impurity model with a few hundred (301!) bath sites can be efficiently solved when represented in a convenient basis, namely the natural orbital basis. In a follow up paper [131] they extended this to density-matrix renormalization group calculations. The schematic visualization of the idea is depicted in figure 7.3. As already discussed earlier the Anderson impurity model as presented in equation (7.1) can be understood as an impurity surrounded by N_b bath sites, where the bath is non-interacting, i.e. no bath interaction terms are included, giving rise to the star geometry (left part), when represented on single-particle level. The transformation $\mathcal{U}$ into the natural orbital basis then leads a to geometry as shown on the right site. The advantage of this single-particle basis lies in the discrimination of impurity i, active bath site b, valence bath sites v_i, and conduction bath sites c_i. When calculating the density matrix the naming becomes clear. Technically the bath sites were separated into fully occupied valence and empty conduction sites, except of one bath with filling $1 - n_{\mathrm{imp}}$, i.e., $n_{\mathrm{imp}} + n_{\mathrm{b}} = 1$, the active bath site. Note within this geometry hopping between valence and conduction bath sites is always mediated over the impurity or active bath sites, while during the basis change the impurity is left untouched. Following [131] the

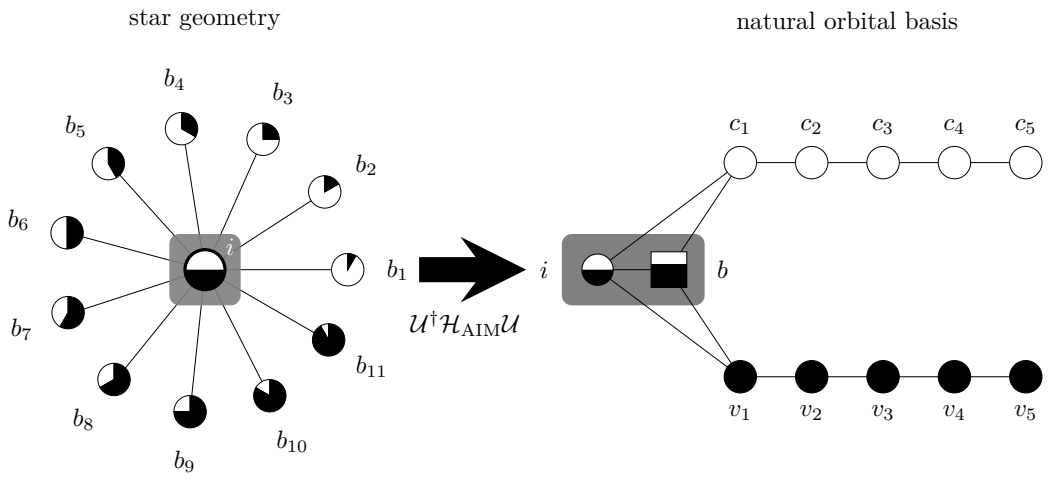

Figure 7.3.: Schematic idea of the basis change from the star geometry (left) of the Anderson impurity model into the natural orbital basis (right). The impurity site is always marked as i and stays invariant under the transformation $\mathcal{U}$. Explanation see text.

transformation $\mathcal{U}$ can be achieved in the following way:

1. Solving Hamiltonian $\mathcal{H}_{\mathrm{AIM}}$ in the form presented in equation (7.4) leads to a list of eigenvalues λ_i and a matrix $\mathcal{D}$ with the corresponding eigenvectors into the columns, mediating the basis change into the eigenbasis of the Hamiltonian. When calculating the density matrix ϱ only the occupied eigenstates are relevant. Hence only the columns of $\mathcal{D}$ are considered, which correspond to occupied states, leading to a matrix $\tilde{\mathcal{D}}$ with many columns as there are occupied states. The density matrix is then given by

$$\varrho = \tilde{\mathcal{D}}\tilde{\mathcal{D}}^\dagger = \begin{pmatrix} \varrho_i & \varrho_{i\ell} \\ \varrho_{i\ell} & \varrho_\ell \end{pmatrix}, \tag{7.14}$$

   where i denotes the impurity and ℓ the bath part.

2. Diagonalization of the bath density matrix $\varrho_\ell = A^\dagger d A$ leads to a new set of orbitals of occupation 0 or 1, except of m values fulfilling $0 < m < 1$. Here d denotes the diagonal matrix and m is the number of impurity spin-orbitals, e.g. in the one-band case there are two values (one for spin up and one for spin down). As shown in figure 7.3, orbitals with value 1 are assigned as valence

baths, the orbitals with 0 to the conduction baths. The remaining m orbitals are the active bath sites. Impurity and active bath site density matrix then fulfill the relation $\operatorname{tr}\varrho_b = m - \operatorname{tr}\varrho_i$. We should stress that the transformation matrix A is ordered according to $[m, 0, \ldots, 1, \ldots]$. When adding an additional 1 at the missing impurity the Hamiltonian $\mathcal{H}_{\mathrm{AIM}}$ can then be rotated into the basis of fully, empty and fractional occupied bath sites, i.e.

$$\tilde{\mathcal{H}}_{\mathrm{AIM}} = A^\dagger \mathcal{H}_{\mathrm{AIM}} A. \tag{7.15}$$

3. Now impurity sites i and active bath site b are linearly combined into bonding and anti-bonding site with occupation m and 0. Technically this means only the subspace of impurity and active bath of $\tilde{\mathcal{H}}_{\mathrm{AIM}}$ is diagonalized leading to an additional transformation matrix S. When extended to the full Hamiltonian dimension we end up with the transformation $\mathcal{S} = \operatorname{diag}(S, \mathbb{1})$, so the Hamiltonian takes on the form

$$\tilde{\tilde{\mathcal{H}}}_{\mathrm{AIM}} = \mathcal{S}^\dagger \tilde{\mathcal{H}}_{\mathrm{AIM}} \mathcal{S}. \tag{7.16}$$

4. Now a Lanczos tridiagonalization is performed separately on the subspace of empty and occupied bath sites of $\tilde{\tilde{\mathcal{H}}}_{\mathrm{AIM}}$. This will lead to the empty and filled chain structure of figure 7.3 starting with the bonding and anti-bonding sites, respectively. This Hamiltonian will be denoted as $\mathcal{H}^{\mathrm{tri}}_{\mathrm{AIM}}$ and the Lanczos transformation as $\mathcal{L}$, where a unity matrix is extended for the missing impurity and active bath.

5. In the last step the transformation of $\mathcal{S}$ on impurity and active bath is reversed via $\mathcal{H}^{\mathrm{NOB}}_{\mathrm{AIM}} = \mathcal{S}\mathcal{H}^{\mathrm{tri}}_{\mathrm{AIM}}\mathcal{S}^\dagger$, leading to geometry of the natural orbital basis.

Since every transformation is unitary the whole procedure basically describes a basis change in various steps. The full transformation is than given via

$$\mathcal{H}^{\mathrm{NOB}}_{\mathrm{AIM}} = \mathcal{S}\mathcal{L}^\dagger\mathcal{S}^\dagger A^\dagger \mathcal{H}_{\mathrm{AIM}} \underbrace{A\mathcal{S}\mathcal{L}\mathcal{S}^\dagger}_{\equiv \mathcal{U}} = \mathcal{U}^\dagger \mathcal{H}_{\mathrm{AIM}} \mathcal{U}. \tag{7.17}$$

Note that within this thesis the mapping onto the natural orbital basis is exact, since it is always done on the single-particle level (mean-field level), where U is not included. For more details see [131].

Historically the idea of the natural orbital basis comes from the quantum chemistry community and is motivated by a Schmidt decomposition of a Hamiltonian. During this decomposition the Hamiltonian is divided into two subspaces, e.g. impurity and bath, so that the original Hamiltonian can be written as $\mathcal{H} = \mathcal{H}_i \oplus \mathcal{H}_b$ [132, 133]. Technically till step (2) of the above numeration this transformation is used for methods like density matrix embedding theory [134], where the complexity of the entire many-body system is reduced by an embedding system and the empty and full bath sites are neglected, since impurity and active bath are considered to form a (quantum chemical) active space [135].

7.2 Easy tests

The advantage of the natural orbital basis is especially of numerical nature, since it allows to set additional restrictions during an exact diagonalization scheme. This means instead of solving the whole Hamiltonian with all full and empty bath sites, it is sufficient to only focus on the subspace of impurity and active bath. The remaining bath sites are considered to be fully occupied or empty. This restricts the configuration space quite severely, however, as will be shown for two simple examples below, this often leads to sufficient results. For the subsequent exact diagonalization scheme the Quanty package [49, 130, 136] was used.

7.2.1 The Bethe lattice

The above discretization scheme is first tested on the Bethe lattice, which is due to its simplicity an excellent benchmark case. The Bethe lattice in general in not a regular Bravais lattice, from a graph theory point of view it is an infinite cycle-free graph, where each node is connected to z neighbors. When visually shown one

node is chosen as the root in the middle and all other nodes are arranged in shells around. The number of nodes that can be reached from a given center (only next nearest neighbor hopping) then is $z(z-1)^{k-1}$, where k is the shell index. The ideal DMFT benchmark case is the $z \to \infty$ limit, where DMFT gives the exact solution. Furthermore it can be shown that the density of states on the Bethe lattice is semicircular

$$\varrho(\omega) = \frac{2\sqrt{D^2 - \omega^2}}{\pi D^2}\Theta(D - |\omega|), \tag{7.18}$$

where D describes the bandwidth. The DMFT self-consistency condition can then be written as

$$\mathcal{G}_0^{-1}(\mathrm{i}\omega_n) = \mathrm{i}\omega_n + \mu - t^2 G(\mathrm{i}\omega_n), \tag{7.19}$$

where t is hopping strength [137]. For the Coulomb interaction the Hubbard term is used

$$\mathcal{H}_{\text{int}} = U n_\uparrow n_\downarrow. \tag{7.20}$$

Given the density of states and self-consistency condition a DMFT calculation for $D = 1.0\,\text{eV}$, $t = 0.5\,\text{eV}$, $U = 1.7\,\text{eV}$, and $\beta = 100\,\text{eV}^{-1}$ was performed, followed by analytical continuation with MaxEnt to extract the spectral function $A(\omega)$ and hybridization function $\Delta(\omega)$. The Bethe lattice was solved in the half-filled case $n_{\text{imp}} = 1.0$. The spectral function from DMFT is shown in figure 7.4 (purple lines), giving rise to the well known three peak structure for DMFT calculations. Then the above mentioned discretization scheme was used to construct an Anderson

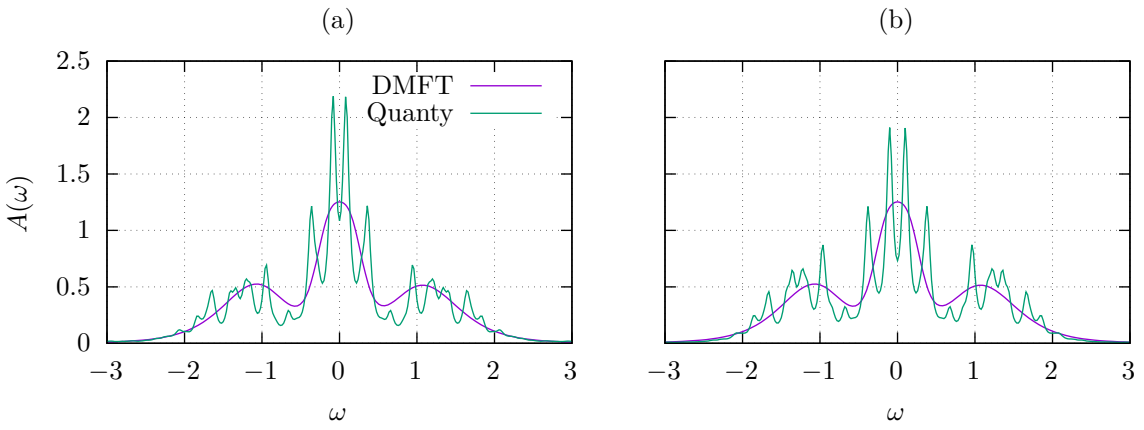

Figure 7.4.: Comparison of the spectral functions $A(\omega)$ between the analytical continued converged DMFT local Green's function (purple) vs. the reproduced spectral function from the discretized DMFT hybridization function (green) for the half-filled Bethe lattice with $U = 1.7\,\text{eV}$ and $D = 1.0\,\text{eV}$: (a) Only the subspace of impurity and active bath is diagonalized. (b) Full diagonalization of the total AIM with all baths.

impurity model for 7 bath sites leading to

$$\mathcal{H}^{\text{NOB}}_{\text{AIM},\sigma} = \begin{pmatrix} 0.0000 & 0.3824 & 0.2283 & 0.0000 & 0.0000 & -0.2282 & 0.0000 & 0.0000 \\ 0.3824 & -0.0003 & 0.2282 & 0.0000 & 0.0000 & 0.2283 & 0.0000 & 0.0000 \\ 0.2283 & 0.2282 & 1.0756 & 0.5263 & 0.0000 & 0.0000 & 0.0000 & 0.0000 \\ 0.0000 & 0.0000 & 0.5263 & 0.9028 & 0.4087 & 0.0000 & 0.0000 & 0.0000 \\ 0.0000 & 0.0000 & 0.0000 & 0.4087 & 0.7319 & 0.0000 & 0.0000 & 0.0000 \\ -0.2282 & 0.2283 & 0.0000 & 0.0000 & 0.0000 & -1.0759 & 0.5266 & 0.0000 \\ 0.0000 & 0.0000 & 0.0000 & 0.0000 & 0.0000 & 0.5266 & -0.9033 & 0.4086 \\ 0.0000 & 0.0000 & 0.0000 & 0.0000 & 0.0000 & 0.0000 & 0.4086 & -0.7306 \end{pmatrix}, \tag{7.21}$$

when expressed in single-particle natural orbital basis. Armed with this, an exact diagonalization was performed to extract the spectral function $A(\omega)$ to compare it with the DMFT results. In order to study the restrictions on the configuration space the following calculations were performed:

1. Only the subspace of impurity and active bath site is diagonalized, while the configuration on the remaining bath orbitals is restricted to be full or empty.

The obtained spectral function is shown in figure 7.4 (a) (green lines).

2. The full Hamiltonian without restricting the configuration space is diagonalized leading to the spectral function shown in figure 7.4 (b) (green line).

Already by comparing both obtained spectral functions $A(\omega)$ it is evident that up to some minor details the general behavior is similar, suggesting that restrictions of the configurations space, when the Hamiltonian is expressed in the natural orbital basis, can speed up the exact diagonalization process and produce satisfactory results.

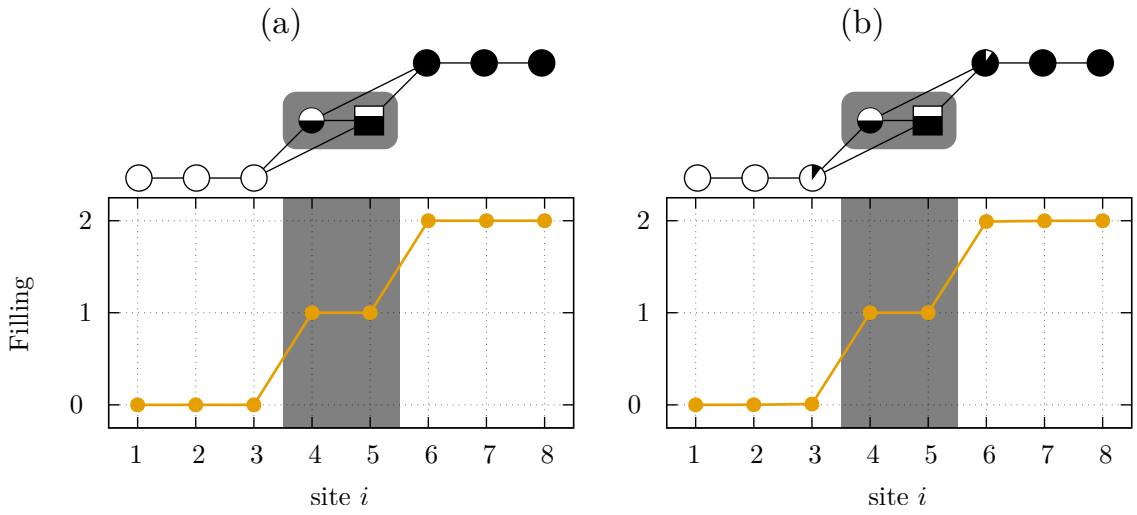

■ **Figure 7.5.:** Filling over site index of the Bethe lattice with $U = 1.7$ at half-filling discretized with 7 bath sites. (Upper cartoon) Visualization of the natural orbital basis, where the half-filled circle depicts the impurity site and the partially filled square the active bath site. (a) Restrictions are chosen only on the impurity and active bath site (gray box in the upper panel). (b) Full diagonalization of the problem. Although the whole Hamiltonian is diagonalized in (b), the restriction to a smaller subspace (impurity plus active bath) (a) leads to similar results.

Additionally, during both calculations the filling of each site (impurity, active bath, and remaining bath sites) was measured. The results are shown in figure 7.5 for (a) the restricted impurity-active bath system, and (b) the system without restrictions. Here site $i = 4$ refers to the impurity site and $i = 5$ to the active bath.

When comparing (a) and (b) there is nearly no difference of the site fillings. This can especially seen on site $i = 6$ (valence bath site) and $i = 3$ (conduction bath site), since the electron filling difference is of the order of magnitude 10^{-3}.

7.2.2 The 2d Hubbard model

A further benchmark of the discretization scheme was performed on the two dimensional Hubbard model, which can be described by the Hamiltonian

$$\mathcal{H} = -t \sum_{\langle i,j \rangle} \left(c_i^\dagger c_j + \text{h.c.} \right) + \frac{U}{2} \sum_i n_{i\uparrow} n_\downarrow, \tag{7.22}$$

where $\langle i,j \rangle$ only considers the sum over nearest neighbors, t is the hopping strength, and U the Coulomb interaction. In the non-interacting case the Hubbard model has the well known dispersion relation

$$\varepsilon(k_x,k_y) = -2t \left(\cos(k_x) + \cos(k_y) \right). \tag{7.23}$$

DMFT calculations were performed for $t = 0.5\,\text{eV}$, $U = 3.8\,\text{eV}$, and $\beta = 100\,\text{eV}^{-1}$ and filling of $n = 0.8$. The resulting spectral function $A(\omega)$ is shown in figure 7.6 (purple line). Again from the analytical continued $\Delta(\omega)$ an Anderson impurity model for 7 bath sites was extracted, leading to the Hamiltonian

$$\mathcal{H}^{\text{NOB}} = \begin{pmatrix} 0.0000 & -0.3755 & -0.2953 & 0.0000 & 0.0000 & 0.0000 & -0.1754 & 0.0000 \\ -0.3755 & -0.1385 & 0.2459 & 0.0000 & 0.0000 & 0.0000 & -0.2106 & 0.0000 \\ -0.2953 & 0.2459 & 1.3191 & 0.8976 & 0.0000 & 0.0000 & 0.0000 & 0.0000 \\ 0.0000 & 0.0000 & 0.8976 & 1.4261 & -0.6271 & 0.0000 & 0.0000 & 0.0000 \\ 0.0000 & 0.0000 & 0.0000 & -0.6271 & 1.1237 & 0.3569 & 0.0000 & 0.0000 \\ 0.0000 & 0.0000 & 0.0000 & 0.0000 & 0.3569 & 0.5040 & 0.0000 & 0.0000 \\ -0.1754 & -0.2106 & 0.0000 & 0.0000 & 0.0000 & 0.0000 & -0.9434 & 0.3525 \\ 0.0000 & 0.0000 & 0.0000 & 0.0000 & 0.0000 & 0.0000 & 0.3525 & -0.7693 \end{pmatrix} \tag{7.24}$$

in the single-particle natural orbital basis. For the discretization of the hybridization function the method given in equation (7.13) was used. Again the DMFT

spectral function is compared to the spectral function under the restrictions (i) only impurity and active bath sites are diagonalized, and (ii) no restrictions of the configuration space. The resulting spectral functions are shown in figure 7.6 (a) and (b), respectively. Again the agreement of both spectral function, despite the huge difference in the number of states in the configuration space, are excellent.

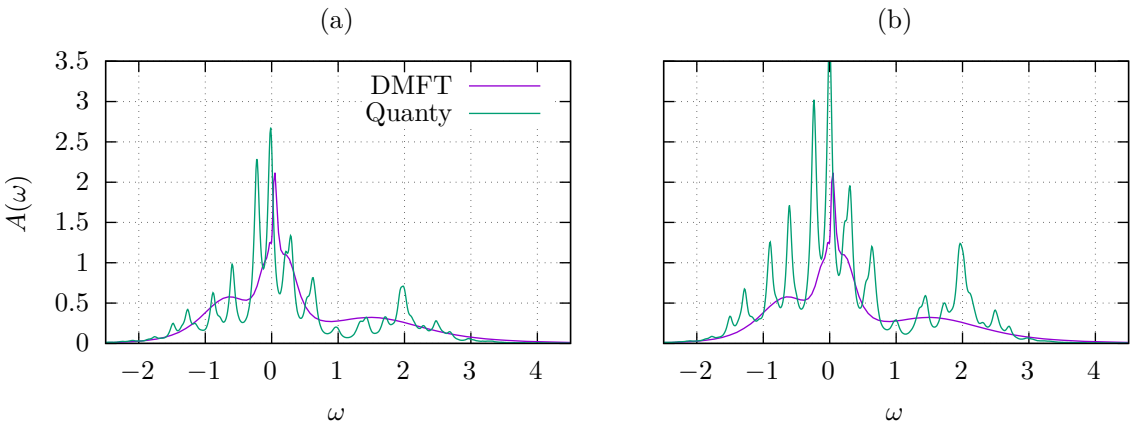

■ **Figure 7.6.:** Comparison of the spectral functions $A(\omega)$ between the analytical continued converged DMFT local Green's function (purple) vs. the reproduced spectral function from the discretized DMFT hybridization function (green) for the 2d Hubbard model at a filling of $n = 0.8$ and $U = 3.8$: (a) Only the subspace of impurity and active bath is diagonalized. (b) Full diagonalization of the total AIM with all baths.

The site resolved filling in both cases is shown in figure 7.7 (a) and (b), respectively. As in the case of the half-filled Bethe lattice the fillings of valence bath sites and conduction bath sites is nearly left unchanged. The differences between (a) and (b) is also of the order 10^{-3} indicating the advantages of the natural orbital basis discussed above.

As in both benchmark tests shown, the natural orbital basis allows the treatment of Anderson impurity model with many bath sites, although using a simple exact diagonalization method. It should however be noted, that the qualitative outcome of the spectral function highly depends on the problem. While here only one-band systems were investigated, multi-orbital systems – as shown later – are still challenging. Additionally, it should be stressed that up to some point the amount

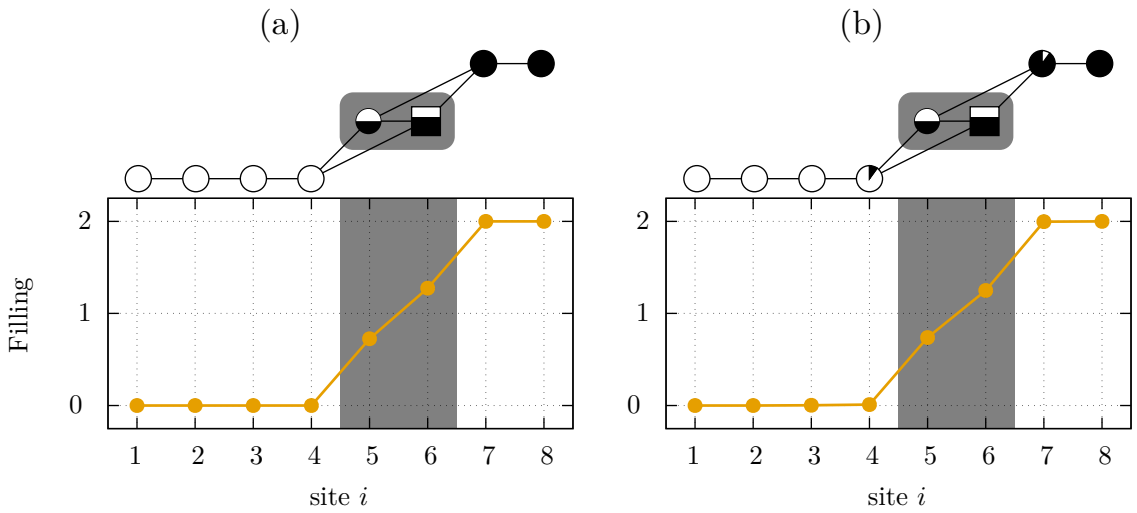

Figure 7.7.: Filling over site index of the 2d Hubbard model with $U = 3.8\,\text{eV}$ and a chosen filling of $n = 0.8$ discretized with 7 bath sites. (Upper cartoon) Visualization of the natural orbital basis, where the half-filled circle depicts the impurity site and the partially filled square the active bath site. (a) Restrictions are chosen only on the impurity and active bath site (gray box in the upper panel). (b) Full diagonalization of the problem. Although the whole Hamiltonian is diagonalized in (b), the restriction to a smaller subspace (impurity plus active bath) (a) leads to similar results.

of bath sites one wants to discretize are important. While it is easy to see at least three baths are needed in order to construct the natural orbital basis. This, however, can change when there is far less spectral weight below the Fermi energy than above (see Hubbard case above). In such cases it sometimes helps to sample with more bath sites below the Fermi energy than above to get better results [25].

7.3 Extension to core-level spectroscopy

After finding the discretization of the hybridization function $\Delta(\omega)$ into a finite number of bath sites the core levels need to be augmented into the model. In the case of a d orbital model (as in Ca_2RuO_4 or later in LiV_2O_4) one therefore extends the model by core p orbitals. In agreement with configuration interaction cluster

approaches then additional interactions important for describing XAS or RIXS are included. The extended model must then augmented by the spin-orbit coupling of the core-levels and the core-valence interaction, given by the Coulomb repulsion operator between two shells. Hence the Hamiltonian needed for XAS and RIXS spectra takes on the form

$$\mathcal{H} = \mathcal{H}_{\mathrm{AIM}} + \mathcal{H}_{\mathrm{C}}^{\mathrm{SOC}} + \mathcal{H}_{\mathrm{CV}}, \tag{7.25}$$

where the spin-orbit coupling operator is given by

$$\mathcal{H}_{\mathrm{C}}^{\mathrm{SOC}} = \xi_{\mathrm{C}} \sum_i \ell_i \cdot s_i, \tag{7.26}$$

where ℓ_i and s_i are the one electron orbital and spin operators. The core-valence interaction operator is

$$\mathcal{H}_{\mathrm{CV}} = \sum_{\tau_1\tau_2\tau_3\tau_4} U_{\tau_1\tau_2\tau_3\tau_4} a^\dagger_{\tau_1} a^\dagger_{\tau_2} a_{\tau_3} a_{\tau_4}, \tag{7.27}$$

where the subscript τ_i contains spin- and orbital information. The object $U_{\tau_1\tau_2\tau_3\tau_4}$ is quite cumbersome to calculate and can be found in chapter 4.3. Since this is now the Coulomb interaction between two shells one typically needs to calculated the Slater integrals F^k and exchange integrals G^k given in equation 4.47. The general Hamiltonian can also be expressed in the form

$$\begin{aligned}\mathcal{H} = &\sum_{\gamma,\sigma} \varepsilon_d^{(i)}(\gamma) \hat{d}^\dagger_{\gamma\sigma} \hat{d}_{\gamma\sigma} + \sum_{\alpha,\gamma,\sigma} \varepsilon^{(b)}_{\alpha,\gamma,\sigma} \hat{v}^\dagger_{\alpha\gamma\sigma} \hat{v}_{\alpha\gamma\sigma} \\ &+ \sum_{\alpha,\gamma,\sigma} V_{\alpha\gamma,\sigma} (\hat{d}^\dagger_{\gamma\sigma} \hat{v}_{\alpha\gamma\sigma} + \hat{v}^\dagger_{\alpha\gamma\sigma} \hat{d}_{\gamma\sigma} + U_{dd} \sum_{\gamma\sigma > \gamma'\sigma'} \hat{d}^\dagger_{\gamma\sigma} \hat{d}_{\gamma\sigma} \hat{d}^\dagger_{\gamma'\sigma'} \hat{d}_{\gamma'\sigma'} \\ &- U_{dc} \sum_{\gamma,\sigma,\zeta,\eta} \hat{d}^\dagger_{\gamma\sigma} \hat{d}_{\gamma\sigma} (1 - \hat{c}^\dagger_{\zeta\eta} \hat{c}_{\zeta\eta}) + \mathcal{H}_{\mathrm{C}}^{\mathrm{SOC}} + \mathcal{H}_{\mathrm{multiplet}}. \end{aligned} \tag{7.28}$$

This expression is equivalent to the version above, however it allows a bit more insight into the important terms. Here the term U_{dd} denotes the isotropic part of the Coulomb interaction acting only on the impurity, i.e. the d orbitals. U_{dc} is the isotropic part of the 2p-3d interaction and $\varepsilon_d(\gamma)$ are the energies of the Wannier

states. Furthermore $\mathcal{H}_{\text{multiplet}}$ contains the higher order Slater and exchange integrals, $V_{\alpha\gamma,\sigma}$ the impurity bath hopping amplitudes from the discretization scheme, d or $d^\dagger$ are the annihilation and creation operators belonging to the impurity (d orbitals) sites, $v/v^\dagger$ the operators belonging to the bath sites, and $c/c^\dagger$ the operators belonging to the core states. The values for U_{dc} and spin-orbit coupling of the core states are typically chosen by the corresponding Hartree-Fock values. The Slater and exchange integrals $F^{(k)}$ and $G^{(k)}$ are then downscaled to 80% of their original value to simulate the effect of intraatomic-configuration neglected by not including higher order configurations. First this sounds a bit strange, however this has shown to be a good empirical treatment [46, 50, 138, 139].

Within this thesis all ED calculations were performed with Quanty [49, 130, 136], where most of the routines needed for calculating the XAS and RIXS spectra are already efficiently included. The relevant formula for extracting RIXS or XAS spectra can be found in chapter C.

7.4 XAS and RIXS spectra for LiV_2O_4

Within this chapter the aforementioned discretization scheme to obtain XAS and RIXS spectra from DFT+DMFT calculations is tested on a multi-orbital system, namely LiV_2O_4.

7.4.1 LiV_2O_4

Strongly correlated $3d$ transition metal oxides [20] and $4f$ rare earth heavy fermion compounds are archetypal examples for material families beyond the reach of effective single particle theories. While there are some exciting emergent phenomena common for both cases – like unconventional high-T_c superconductivity in close vicinity to magnetic order – TMO and heavy fermion compounds are generally considered to be very different in terms of their relevant degrees of freedom at low energies/temperature. LiV_2O_4, characterized as a TMO and heavy fermion

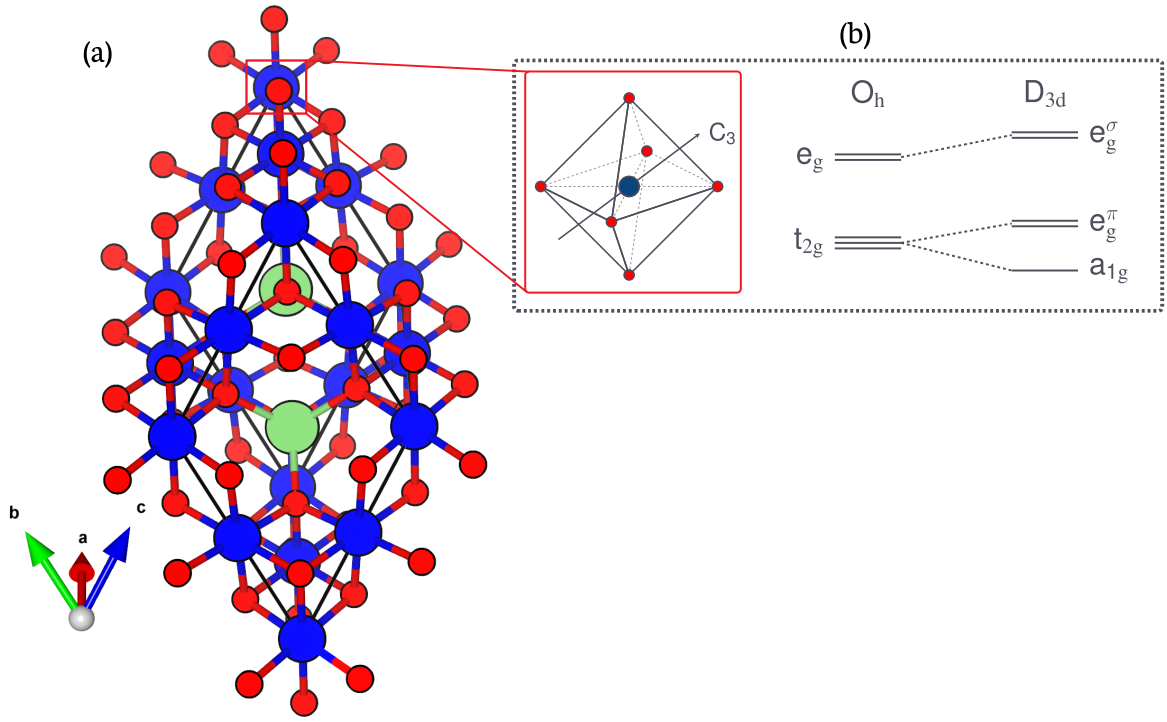

■ **Figure 7.8.:** (a) Crystal structure of LiV_2O_4, where V are blue, O are red, and Li is green. (b) Symmetry and crystal-field splitting due to the trigonal symmetry. Trigonal field splitting results in further splitting of the t_{2g} subspace into an additional a_{1g} and e_g^π subspace. Note that intra e_g mixing is possible.

compound therefore is a fascinating link between the two material classes. The heavy fermion behavior in LiV_2O_4 was first observed in [140] and emerges at temperatures below $\sim 25\,\mathrm{K}$ resulting in a linear specific heat coefficient γ, leading to an effective mass enhancement of $\frac{m^*}{m} \sim 25$ [141, 142]. Moreover experiments revealed that Grüneisen parameter [140] and quadratic resistivity coefficient [143] are of the magnitude expected for heavy fermion compounds and hence are much larger than in other TMOs. Within a temperature range of 50 K to 1000 K the existence of local magnetic moments was observed [141, 144], corresponding to the Curie-Weiss susceptibility measured in [140].

From a crystallographic point LiV_2O_4 is a 3d TMO of spinel structure, formed by edge-sharing oxygen octahedra with V atoms in the center. The total space group is

cubic, however the local point group is of different symmetry, namely trigonal D_{3d} symmetry. Expressed in trigonal symmetry the structure takes on the form shown in figure 7.8 (a). The symmetry leads to a splitting of the t_{2g} orbitals into an a_{1g} state and a twofold degenerate e_g^π state (see (b), where intra e_g mixing is possible. The vanadium formal oxidation is +3.5 leading to a filling of 1.5 electrons per vanadium. LiV_2O_4 exhibits a metallic phase even down to the lowest temperatures without undergoing any structural phase transition [142, 145].

During the last decades describing the heavy fermion behavior in LiV_2O_4 has been challenging and various mechanisms have been suggested. While early DFT calculations suggested that the heavy fermion behavior stems from the a_{1g} electrons acting like the f electrons in conventional heavy fermion compounds [141, 146–148], also geometrical frustration originating from the spinel structure [149–152] was considered for describing the mass enhancement. Since for geometrical frustration any kind of long-range order is suppressed, i.e. spin or orbital fluctuations should be dominant, DMFT calculations were performed in [152, 153]. These early DMFT calculations however either neglect a_{1g}-e_g^π hybridization, simplify it to a simple two band model, or were restricted to very high temperatures. They concluded that the heavy fermion physics is not caused by the a_{1g}-e_g^π hybridization, rather only the a_{1g} orbital is responsible by being close to a Mott-Hubbard transition. Nonetheless LiV_2O_4 seems to remain a curiosity within the TMO family.

7.4.2 DFT+DMFT results

Using the structure file from [145] a simple DFT bandstructure calculation was performed. Bandstructure and density of states are shown in figure 7.9 (a) and (b). As shown, the bands with dominant d orbital of vanadium character (red in (b)) are well separated from the lower lying p orbitals of the oxygen atoms (blue curve in (b)). For the following Wannier projection an energy window of $-1.5\,\mathrm{eV}$ to $3.5\,\mathrm{eV}$ was chosen (red box in (a)) including all five d orbitals. It should be stressed that a pure t_{2g} model would have also been sufficient, since the upper lying bands in

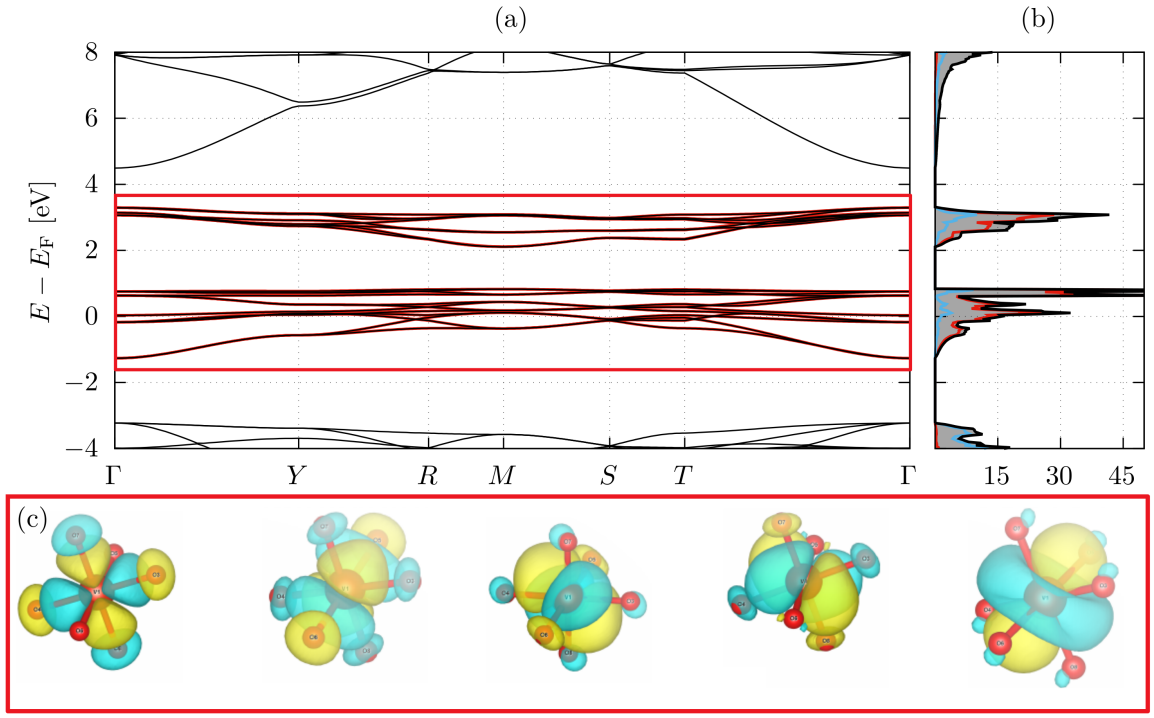

Figure 7.9.: (a) Simple DFT bandstructure of LiV_2O_4 where the red box defines the low-energy window for the Wannier projection. (b) Density of states for the oxygen p-orbitals (blue) and vanadium d-orbitals (red). (c) Wannier projection onto the low energy window (red box) for all d orbitals.

the projection (red) window are clearly separated to the bands around the Fermi energy. These bands belong to the e_g^σ states visualized in figure 7.8 (b). Since in the RIXS and XAS spectrum all d-d interactions are included, these states are kept in our Wannier model. The crystal structure shown in figure 7.8 (a) contains four independent vanadium atoms for which the wannier projection was performed, leading to a model Hamiltonian of size 20×20. Although hybridization terms exist, the local subspaces are numerically equivalent suggesting an equivalent treatment when the DMFT impurity model is solved. The local Hamiltonian $\mathcal{H}(\boldsymbol{R} = (0,0,0))$

for the vanadium subspace is

$$\mathcal{H}_{V_1}\left(\boldsymbol{R}=(0,0,0)^T\right)=\begin{pmatrix} 0.1948 & 0 & 0 & 0 & 0 \\ 0 & 0.3968 & 0 & 0 & 0 \\ 0 & 0 & 0.3968 & 0 & 0 \\ 0 & 0 & 0 & 2.8028 & 0 \\ 0 & 0 & 0 & 0 & 2.8028 \end{pmatrix}, \tag{7.29}$$

where the subscript denotes the vanadium atom assigned to number one. The part for the remaining three vanadium atoms is numerically the same. From this the crystal-field splitting of the trigonal field is extracted, suggesting a splitting a_{1g}-e_g^π of magnitude 0.202 eV and a_{1g}-e_g^σ of magnitude 2.608 eV. A pure DFT calculation hence leads to a level splitting as sketched in figure 7.8 (b).

The shape of the Wannier orbitals is depicted in figure 7.9, where the a_{1g} orbital is on the right end. The first four orbitals are the remaining e_g orbitals. Note that the shown orbitals are not the orbitals belonging to the eigenbasis of the trigonal symmetry. The Wannier projection was performed in the cubic harmonic expression of the d orbitals where the z-axis was rotated to the symmetry axis of the trigonal symmetry. With other words to obtain the orbitals corresponding to trigonal symmetry one needs to rotate the Wannier Hamiltonian into its eigenbasis. Hence two different kind of DMFT calculations were performed: (i) Using the Wannier basis (not the eigenbasis), and (ii) using the eigenbasis. In both cases the Kanamori interaction given in equation (6.3) was used with $U = 4.0\,\text{eV}$ and $J = 0.6\,\text{eV}$. Hund's coupling and Coulomb strength are in agreement with common DMFT calculations of this compound [152, 153]. For all calculations the vanadium subspaces were treated equally, i.e. only one impurity problem was solved from whom the self-energy $\Sigma(\mathrm{i}\omega_n)$ was extracted. Again for the DMFT calculations the triqs package was used with a CT-HYB impurity solver. The DMFT self-consistency loop was performed at an inverse temperature of $\beta = 70\,\text{eV}^{-1}$ ($T \sim 165\,\text{K}$). The self-energy from the converged DMFT loop was then analytically continued by using the MaxEnt method discussed in chapter 5.6. The real ω axis single-particle

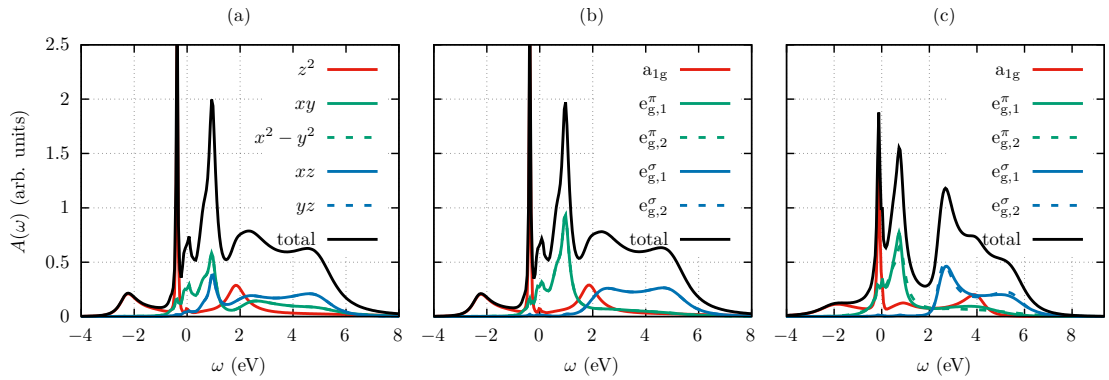

■ **Figure 7.10.:** Single-particle spectral function $A(\omega)$ for LiV_2O_4, obtained from the analytical continuation of the self-energy $\Sigma(i\omega_n)$ from DMFT. (a) $A(\omega)$ in the Wannier orbital basis, i.e. all d-orbitals rotated into the local coordination system for trigonal symmetry. (b) $A(\omega)$ when rotated into the eigenbasis of trigonal symmetry. (c) Spectral function obtained from a DMFT calculation, when vanadium subspaces are already rotated into the eigenbasis on the level of the model Hamiltonian.

spectral functions $A(\omega)$ are shown in figure 7.10 for (a) in the Wannier- and (c) eigenbasis. Figure (b) are the orbitals projected in the Wannier basis (same as (a)) but rotated after the DMFT run into the trigonal basis. Note that the general features in (b) and (c) are nearly similar. However, the advantage of performing a DMFT calculation in the trigonal basis comes, when the hybridization function $\Delta(\omega)$ is calculated. Here the whole object is purely diagonal, i.e. the discretization scheme does not lose information by neglecting off-diagonal elements. All DMFT calculations lead to orbital fillings of

$$n_{a_{1g}} \sim 0.9, \quad n_{e_g^{\pi}} \sim 0.3, \quad n_{e_g^{\sigma}} \sim 0.0, \tag{7.30}$$

which are consistent with already performed DMFT calculations. We should also stress, that the general features of the a_{1g} and e_g^{π} orbitals, like the high spectral peak of the a_{1g} orbital near the Fermi energy, are also in good agreement. For all following calculations the DMFT data from figure 7.10 (c) were used.

7.4.3 Discretization

In order to calculate the hybridization function $V^2(\omega)$ to derive an Anderson impurity model for a discrete number of bath sites, the self-energy is analytically continued to the real axis. As shown in figure 7.11, while the a_{1g} orbital and e_g^π orbitals indicate Fermi liquid behavior (a quadratic imaginary part and linear real part at low frequencies) and a metallic phase, the e_g^σ orbitals on the other hand are not. However, this should be expected, since they are technically empty as noted above. Next the hybridization function $\Delta(\omega)$ is calculated according to

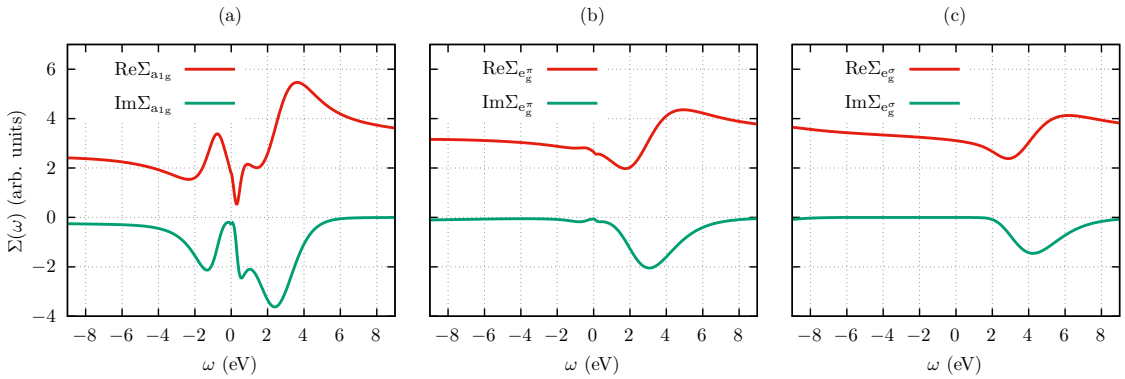

Figure 7.11.: Analytically continued self-energy $\Sigma(\omega)$. (a) a_{1g} orbital, (b) e_g^π orbital (c) e_g^σ orbital.

equation (7.11), from whom its spectral function $V^2(\omega)$ is extracted via

$$V^2(\omega) = -\frac{1}{\pi}\mathrm{Im}\left[\Delta(\omega)\right]. \tag{7.31}$$

The result is shown for the three species of orbitals in figure 7.12 (first row). Then the hybridization was discretized for different number of bath sites. When increasing the bath sites from 3 to 30 and recalculating the hybridization $V^2_{\mathrm{rep}}(\omega)$ (red curves) via equation (7.11) the overall mixing becomes more and more similar to the DMFT hybridization function. The explicit values of the impurity bath hopping V_i and bath energies $\varepsilon_i^{(b)}$ defining the bath part of the Anderson impurity model are shown as green bars. For the discretization scheme itself an equidistant sampling of bath sites along ω was used. Additionally, due to the rather smaller spectral weight

below $\omega = 0$ (position of the first peak) the negative energy regime and first peak was sampled with roughly 2/3 of the total number of bath sites. Hence the low energy hybridization part is better reproduced when $V^2_{\mathrm{rep}}(\omega)$ is calculated. From a numerical point of view this was necessary, otherwise when using few numbers of baths sites the natural orbital scheme can not find fully occupied orbitals.

7.4.4 XAS and RIXS spectra

In order to calculate XAS or RIXS spectra, equation (C.1) and (C.5) are evaluated with Quanty. Before computing the XAS or RIXS spectra, the spectral function $A(\omega)$ is obtained in order to judge the quality of the discretization procedure. These spectral functions are then compared to the original DMFT spectra. The results are shown in figure 7.13. As depicted, the overall agreement is satisfactory even when only the subsystem of impurity and active bath site is considered. The found ground state is then used to calculate XAS spectra.

XAS

The XAS spectra are shown in figure 7.14. For the spreading of the peaks we chose $\Gamma = 0.2$. Note that here we actually compared the XAS spectra for two types of core-valence interactions: (i) the full interaction as given in equation (7.28) (labeled by $\mathcal{H}_{\mathrm{full}}$), and (ii) a simplified core-valence interaction containing only density-density terms of the form $\mathcal{H}_{\mathrm{U}} = U_{\mathrm{dc}}\hat{N}_{\mathrm{imp}}\hat{N}_{\mathrm{core}}$, where U_{dc} is the Hartree-Fock value. The second approximation is actually not needed if the number of bath sites is small or the restrictions on the configuration space are quite strong. However, from a numerical point – at least in our case – the simplified core-valence interaction speeds up the calculations quite drastically. Moreover it allows us to investigate the different contributions and effects within the core-valence interaction more systematically. Note that for all calculations we used the Hartree-Fock values

$$U_{\mathrm{dc}} = 8.5\,\mathrm{eV} \quad \text{and} \quad \xi_{\mathrm{C}} = 4.65\,\mathrm{eV}, \tag{7.32}$$

which can be found in [47].

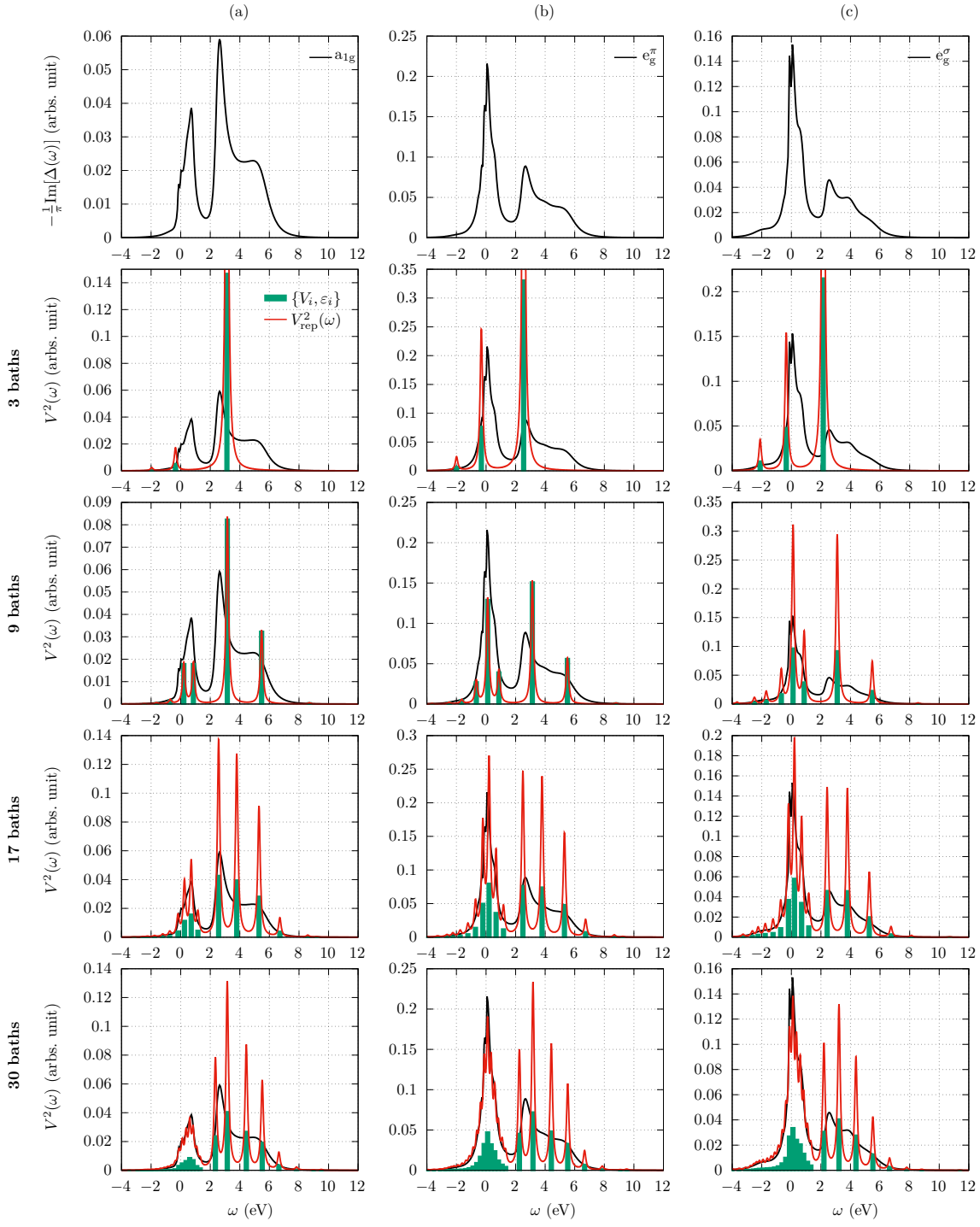

Figure 7.12.: Imaginary part of the hybridization function $V^2(\omega)$ from the analytical continued $\Sigma(\omega)$. Column wise: (a) a_{1g} orbital part from DMFT (top row). From second row till bottom: discretization of of $V^2(\omega)$ for increasing number of bath sites {3,9,17,30} plotted are the pairs $\{V_i, \varepsilon\}$ as green bars and in red the reproduced hybridization function $V^2_{\mathrm{rep}}(\omega)$. The same for (b) the e_g^π orbitals and (c) the e_g^σ orbitals.

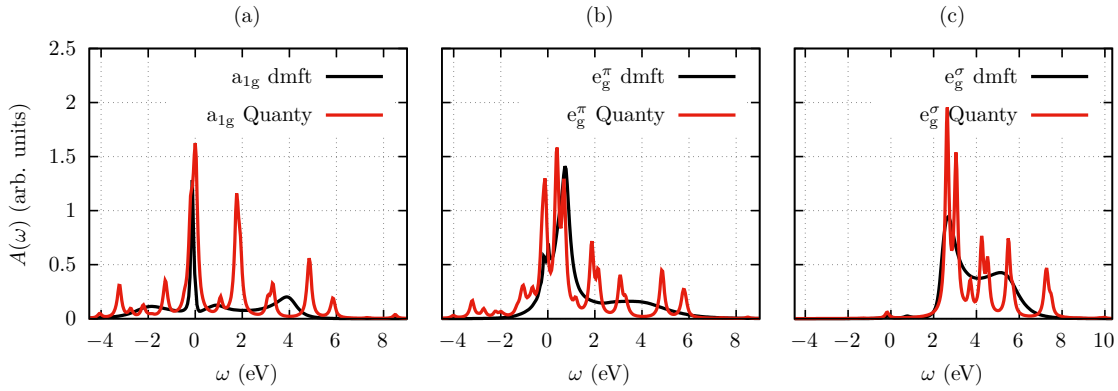

Figure 7.13.: Comparison of the spectral function $A(\omega)$ between the DMFT result (black lines) and the discretized model (red lines). (a) a_{1g} orbital, (b) e_g^π orbitals , (c) e_g^σ orbitals.

When comparing the different core-valence types in figure 7.14, we find that the overall XAS intensity is of the same form, however the neglected terms introduce new features to the spectra in the form of more peaks and a slight broadening of the overall structure. This is for example observable when (a) is compared to (c). Here the full calculation was purely restricted on the t_g subspace, i.e. the e_g orbitals were neglected. While the overall shape of the three dominant peaks in the L_3 or L_2 edge in (a) is clearly visible, the full interaction somehow broadens the peaks while shifting the spectral weight to minor new peaks in (c). The same is observed when focusing on the full d shell in (b) and (c), respectively.

RIXS

The same procedure described above for the XAS spectra is now used to obtain some RIXS spectra. The discussion however will be restricted to the simplified core-valence interaction and a three bath site model. Again when only the t_{2g} subspace is considered one obtains the RIXS spectra shown in figure 7.15. The full d orbital model is shown in figure 7.16. The label "geometry" takes into account the polarization of the incoming light, i.e. xx would refer to x polarized light. A label xy takes into account that equation C.5 actually allows two transition operators with different polarization. Comparing both figures shows that the inclusion of

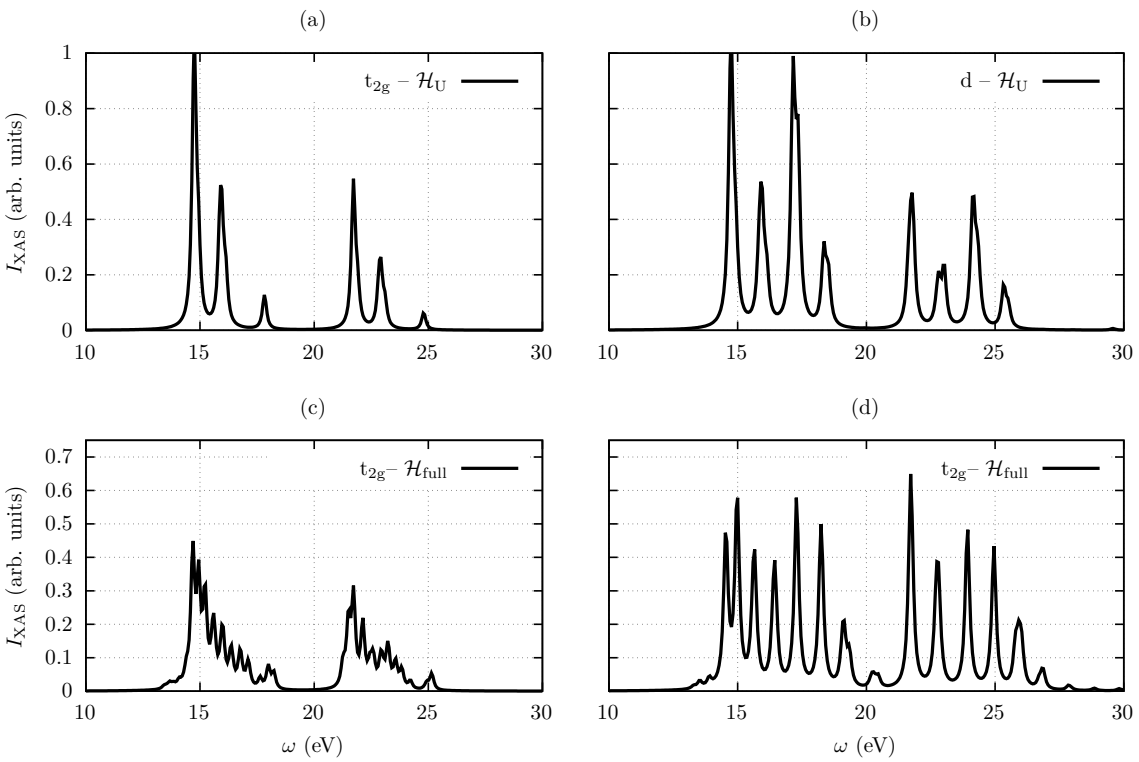

Figure 7.14.: Comparison of XAS spectra for different core-valence interaction. (a) Only t_{2g}-subspace considered in the model and the core-valence interaction is simplified by $\mathcal{H}_U$. (b) Same for all d-orbitals. (c) Only t_{2g}-subspace considered in the model and the core-valence interaction $\mathcal{H}_{full}$ is fully taken into account. (d) Same for all d-orbitals.

the full core-valence interaction, leads to a change of RIXS features. These are for example the emergence, disappearance, or simply some shifts of peaks. However, so far no fluorescence lines are observed in all our spectra.

When only one bath site is considered the corresponding RIXS spectra are shown in chapter D. Since in this case the configuration space is quite small, the numerical accessibility is quite easy. Hence the full core-valence interaction can be included. When comparing figure D.1 and D.3, where only the t_{2g} subspace is considered, the features in the RIXS spectra change quite drastically. While for the simplified core-valence interaction there are only three main RIXS "lines" visible, for the full interaction there are roughly seven or eight, depending on their intensity. Also here no fluorescence lines are observed.

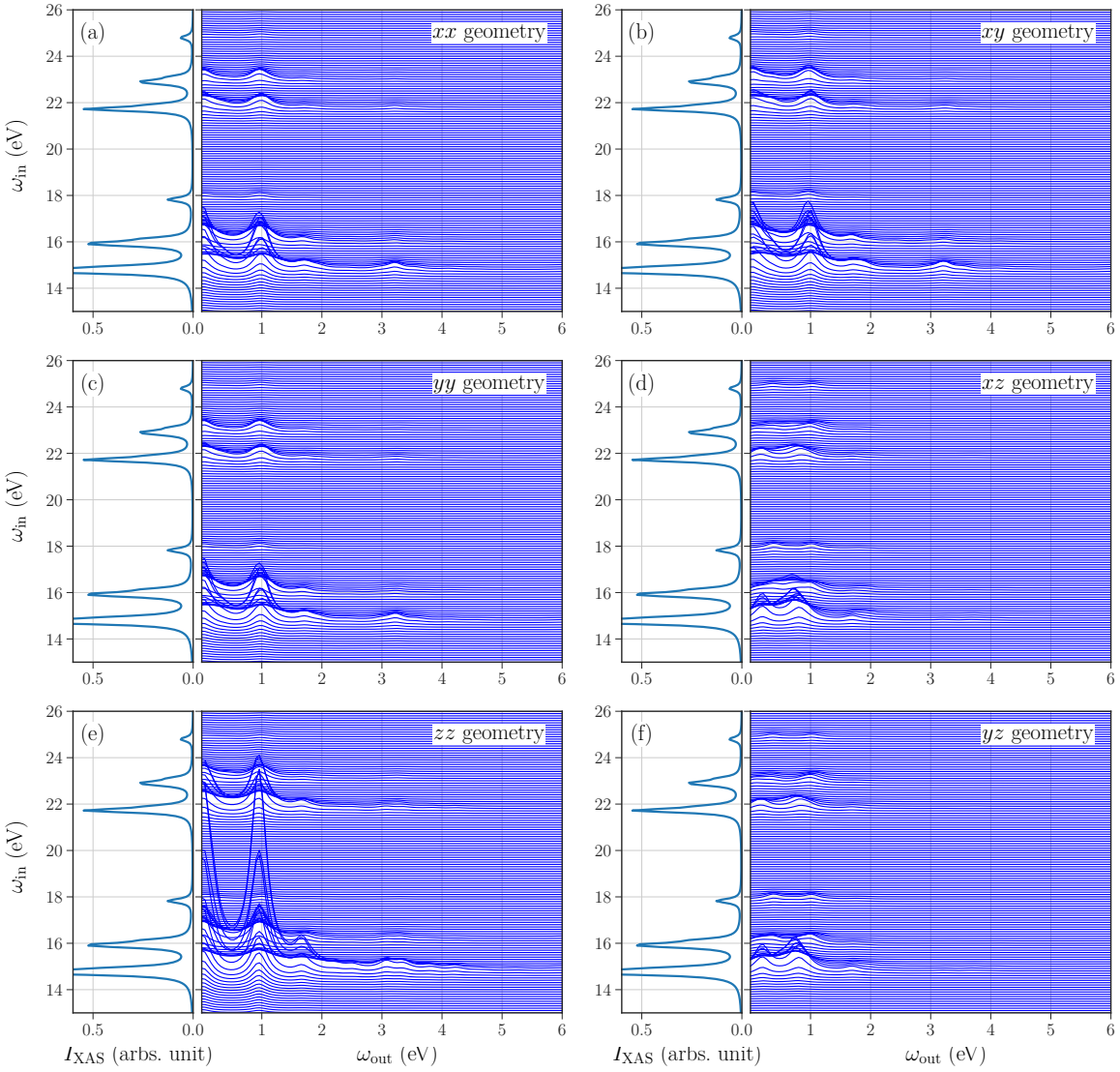

Figure 7.15.: XAS intensity (always left panel) and RIXS intensity (always right panel) for different geometries for a discretized model with 3 baths sites. All calculations were restricted to the t_{2g} subspace and a simplified core-valence interaction, including only density-density terms. (a) xx-, (b) xy-, (c) yy-, (d) xz-, (e) zz-, (f) yz-geometry. For all figures a spreading of $\Gamma = 0.3$ was used.

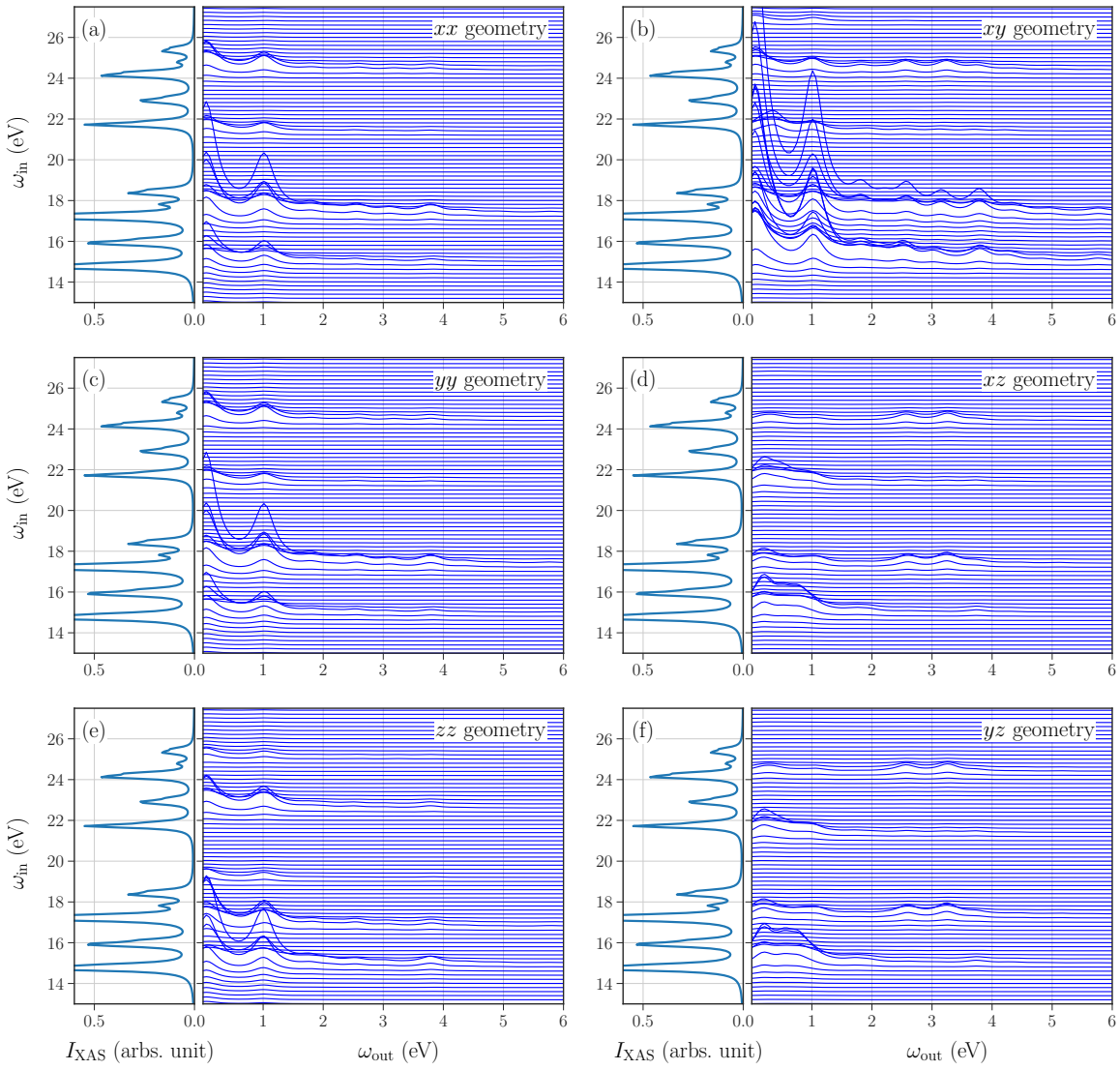

Figure 7.16.: XAS intensity (always left panel) and RIXS intensity (always right panel) for different geometries for a discretized model with 3 baths sites. All calculations were restricted to the simplified core-valence interaction, including only density-density terms, and $\Gamma = 0.4$. (a) xx-, (b) xy-, (c) yy-, (d) xz-, (e) zz-, (f) yz-geometry. For all figures a spreading of $\Gamma = 0.3$ was used.

The absence of fluorescence like features, as calculated in [25], is understandable, since for the most calculations done in this thesis we had to restrict either the dimension of our model (less bath sites) or the allowed configurations in the ED run. Essentially, the goal is to find a model with a sufficient number of bath sites, which still allows a numerical treatment with an ED solver, where nearly no further restrictions on the configuration space is needed.

Chapter 8 Summary

This thesis presented a state-of-the-art approach for real materials and how they can be treated numerically within the so called DFT+DMFT scheme in its single shot variant. Within the last decade this method has established itself by describing a range of physical phenomena in good agreement with experiments. Due to its wide variation reaching from the low temperature regime to high temperatures, especially when taken into account the enormous amount of well established solvers, it allows a wide range of treating electronic phenomena. In its original formulation it is, however, restricted to local electronic problems, i.e. solving a single-impurity problem. Nonetheless extension to clusters, which of course scale the numerical effort needed to solve problems, are available and successfully used nowadays. In times where physical problems often cannot be described by single-particle approximations, e.g. bandstructure calculations, DMFT and its extensions present a possibility to tackle electronic physics. From a numerical point of view the bottleneck is the dependence on efficient or intelligent solvers, since often the interesting physics sits on the brink of their accessibility. Subsequently I briefly want to summarize the main results and ideas presented in this thesis.

The richness of physical phenomena in TMOs and the resulting complex phase diagrams offer a fertile playground for experimenters and theorist, equally. Ca_2RuO_4 is no exception, since as an archetypal Mott insulator its equilibrium phases reach from a high temperature paramagnetic metallic phase, to a lower in temperature

paramagnetic Mott insulating phase, and for even lower temperatures to an antiferromagnetic insulating phase. As in many TMOs this is a result of the partially filled d orbitals and the absence of a hierarchy of energy scales, e.g. strong spin-orbit coupling, Hund's coupling, and crystal-field splitting, making theoretical predictions particularly cumbersome. The richness in phases even persists in nonequilibrium experiments, where it was shown that a small DC current can stabilize new phases. Although these phases are often similar to their equilibrium counterparts they are unique and distinct in their crystal structure. Based on these experimentally refined structures, DFT calculations were performed to extract a tight binding model by projecting the correlated t_{2g}-subspace onto maximally localized Wannier orbitals. Within our DMFT calculations SOC and the spherical invariant Coulomb interaction were added to compute spectral functions. The results indicate a semimetallic state with partially gapped Fermi surface in the nonequilibrium phases with elongated RuO_6 octahedra. Additionally, the calculations show that electronic band structure calculations are sensitive to the electric current and the induced structural changes. Hence structural details are crucial for the physical behavior and must be included in minimal models to describe the phenomena correctly.

Although the DFT+DMFT approach often successfully describes local electronic features in spectral functions, it is – at least in its original formulation – not suited to explain for example core-level spectroscopic methods. However, since the resolution of current beamlines has increased over the past years, alternative numerical approaches which can describe the high resolution spectra are needed. Resonant inelastic x-ray scattering spectra are traditionally calculated within a configuration-interaction cluster calculation scheme. Unfortunately these calculations are limited when fine spectral features become crucial, which is the case in high-resolution experiments. In the case of L-edge RIXS experiments of numerous TMOs this becomes evident. To overcome this obstacle it was recently proposed to use converged DFT+DMFT calculations to extract XAS and RIXS spectra. To do so the hybridization function is discretized with a sufficiently large number of baths sites

to construct the underlying Anderson impurity model, which can then be solved via exact diagonalization. In order to extract RIXS or XAS spectra the Anderson impurity model is augmented by core levels and a core-valence interaction. In principal the idea of the configuration-interaction cluster calculation is kept, since still Hartree-Fock approximated values for core spin-orbit coupling or core-valence interaction are used. However, the explicit inclusion of the DMFT hybridization function takes into account the local electronic features. These features are crucial if fluorescence line features, want to be observed or explained. Within this thesis we extended this idea by applying it to the natural-orbital basis. This basis allows quite strong restrictions on the configuration space of possible states and is hence important if an exact diagonalization solver is used. We showed this in a comparison between DMFT and ED spectra of the half-filled Bethe lattice and the two dimensional Hubbard model on square lattice for noninteger filling. By restricting the configuration space to an effective two side problem (impurity and active bath), the one-particle spectral functions are compared to those obtained by no restrictions. The qualitative agreement is satisfactory. Additionally, we performed DFT+DMFT calculations for LiV_2O_4 and applied the above mentioned discretization to extract XAS and RIXS spectra. Although, the shown results for a model with few bath sites are promising, an actual application to numerous bath sites, and the observation of fluorescence line like features is still pending and will be part of future projects.

Appendix A Spherical harmonics and Legendre-polynomials

The following chapter follows the textbooks [42, 43, 45, 154]. The spherical harmonics are the solution of the angular part of the Laplace's equation in spherical coordinates. In quantum mechanics the spherical harmonics appear as part of the solution of the Schrödinger equation of a particle within a spherically symmetric potential, e.g. the hydrogen atom, or as eigenfunctions of the square of the orbital angular momentum operator $\boldsymbol{L}^2$. The spherical harmonics are defined as

$$Y_m^{(\ell)}(\theta,\phi) = \sqrt{\frac{(2\ell+1)}{4\pi}\frac{(\ell-m)!}{(\ell+m)!}} P_m^{(\ell)}(\cos\theta) \mathrm{e}^{\mathrm{i}m\phi}, \tag{A.1}$$

where the associate Legendre-polynomials are given via

$$P_m^{(\ell)}(\cos\theta) = (-1)^m \sin^m(\theta) \frac{\mathrm{d}^m}{\mathrm{d}(\cos\theta)^m} P_\ell(\cos\theta). \tag{A.2}$$

And for negative m

$$P_{-m}^{(\ell)} = (-1)^m \frac{(\ell-m)!}{(\ell+m)} P_m^{(\ell)} \tag{A.3}$$

Here the P_ℓ are the ℓth Legendre polynomial defined by

$$P_\ell(x) = \frac{1}{2^\ell \ell!} \frac{\mathrm{d}^\ell}{\mathrm{d}x^\ell} \left(x^2-1\right)^\ell. \tag{A.4}$$

The first few associated Legendre polynomials, when $\cos\theta$ is substitute, and the corresponding spherical harmonics are:

ℓ	m	$P_m^{(\ell)}$	$Y_m^{(\ell)}$
0	0	1.0	$\sqrt{\frac{1}{4\pi}}$
1	-1	$\frac{1}{2}\sin\theta$	$\sqrt{\frac{3}{8\pi}}e^{-i\phi}\sin\theta$
	0	$\cos\theta$	$\sqrt{\frac{3}{4\pi}}\cos\theta$
	1	$-\sin\theta$	$-\sqrt{\frac{3}{8\pi}}e^{i\phi}\sin\theta$
2	-2	$\frac{1}{8}\sin^2\theta$	$\sqrt{\frac{15}{32\pi}}e^{-2i\phi}\sin^2\theta$
	-1	$\frac{1}{2}\sin\theta\cos\theta$	$\sqrt{\frac{15}{8\pi}}e^{-i\phi}\sin\theta\cos\theta$
	0	$\frac{3\cos^2\theta-1}{2}$	$\sqrt{\frac{5}{16\pi}}(3\cos^2\theta-1)$
	1	$-3\sin\theta\cos\theta$	$-\sqrt{\frac{15}{8\pi}}e^{i\phi}\sin\theta\cos\theta$
	2	$3\sin^2\theta$	$\sqrt{\frac{15}{32\pi}}e^{2i\phi}\sin^2\theta$
4	0	$\frac{1}{8}\left(35\cos^4\theta-30\cos^2\theta+3\right)$	$\sqrt{\frac{9}{256\pi}}\left(35\cos^4\theta-30\cos^2\theta+3\right)$

When studying solids it is convenient to express the basis in real harmonics. The construction follows the rules

$$\mathcal{Y}_m^{(\ell)} = \begin{cases} \frac{i}{\sqrt{2}}\left(Y_m^{(\ell)} - (-1)^m Y_{-m}^{(\ell)}\right), & \text{for } m < 0 \\ Y_0^{(\ell)}, & \text{for } m = 0 \\ \frac{1}{\sqrt{2}}\left(Y_{-m}^{(\ell)} + (-1)^m Y_m^{(\ell)}\right), & \text{for } m < 0 \end{cases}. \tag{A.5}$$

The real harmonics are sometimes known as *tesseral harmonics*. Yet another combination scheme leading to a real basis set are *cubic harmonics*, which are for s, p, and d orbitals identical to the tesseral harmonics beside a different order. For higher angular momentum they are different, however not listed here. The above spherical harmonics expressed in real harmonics are:

	ℓ	m	combination	$\mathcal{Y}_m^{(\ell)}$
s	0	0	$Y_0^{(0)}$	$\sqrt{\frac{1}{4\pi}}$
p_y	1	-1	$\frac{\mathrm{i}}{\sqrt{2}}\left(Y_1^{(1)}+Y_{-1}^{(1)}\right)$	$\sqrt{\frac{3}{4\pi}}\frac{y}{r}$
p_z		0	$Y_0^{(1)}$	$\sqrt{\frac{3}{4\pi}}\frac{z}{r}$
p_x		1	$\frac{1}{\sqrt{2}}\left(Y_1^{(1)}-Y_1^{(1)}\right)$	$\sqrt{\frac{3}{4\pi}}\frac{x}{r}$
d_{xy}	2	-2	$\frac{\mathrm{i}}{\sqrt{2}}\left(Y_2^{(2)}-Y_{-2}^{(2)}\right)$	$\sqrt{\frac{15}{4\pi}}\frac{xy}{r^2}$
d_{yz}		-1	$\frac{\mathrm{i}}{\sqrt{2}}\left(Y_1^{(1)}+Y_{-1}^{(1)}\right)$	$\sqrt{\frac{15}{4\pi}}\frac{yz}{r^2}$
d_{z^2}		0	$Y_2^{(0)}$	$\sqrt{\frac{5}{16\pi}}\frac{3z^2-r^2}{r^2}$
d_{xz}		1	$\frac{1}{\sqrt{2}}\left(Y_1^{(1)}-Y_{-1}^{(1)}\right)$	$\sqrt{\frac{15}{4\pi}}\frac{xz}{r^2}$
$d_{x^2-y^2}$		2	$\frac{1}{\sqrt{2}}\left(Y_2^{(2)}+Y_{-2}^{(2)}\right)$	$\sqrt{\frac{15}{16\pi}}\frac{x^2-y^2}{r^2}$
	4	0	$Y_0^{(4)}$	$\sqrt{\frac{9}{256\pi}}\frac{35z^4-30z^2r^2+3r^4}{r^4}$

Consider the Rotation $\mathcal{R}$ about the origin, which rotates the unit vector $\boldsymbol{r}$ to $\boldsymbol{r}'$. A spherical harmonics under the rotation $\mathcal{R}$ is then a linear combination of spherical harmonics of the same degree. One typically writes this as

$$Y_m^{(\ell)}(\boldsymbol{r}') = \sum_{m'=-\ell}^{\ell} \left[D_{mm'}^{(\ell)}(\mathcal{R})\right]^* Y_{m'}^{(\ell)}(\boldsymbol{r}), \tag{A.6}$$

where $\left[D_{mm'}^{(\ell)}(\mathcal{R})\right]^*$ is the complex conjugate of an element of the Wigner-D-matrix. When the rotation $\mathcal{R}$ is expressed in Euler angles (zyz convention) and using the ket notation of the spherical harmonics ($|\ell,m\rangle$), the Wigner-D-matrix is given by

$$\left[D_{mm'}^{(\ell)}(\alpha,\beta,\gamma)\right] = \langle \ell,m'|\mathcal{R}(\alpha,\beta,\gamma)|\ell,m\rangle = \mathrm{e}^{-\mathrm{i}m'\alpha}\,\langle \ell,m'|\mathrm{e}^{-\mathrm{i}\beta J_y}|\ell,m\rangle\,\mathrm{e}^{-\mathrm{i}m\gamma}, \tag{A.7}$$

and is of order $2\ell+1$. Here α, β, γ are the Euler angles, and J_y the y axis generator of the Lie algebra SO(3). Note that in general the matrix $\mathcal{R}$ can written in the form

$$\mathcal{R}(\alpha,\beta,\gamma) = \mathrm{e}^{-\mathrm{i}\alpha J_z}\mathrm{e}^{-\mathrm{i}\beta J_y}\mathrm{e}^{-\mathrm{i}\gamma J_z}. \tag{A.8}$$

For the case $\beta = 0$ and $\gamma = 0$ one then finds

$$D_{m'm}^{(\ell)}(\alpha,0,0) = \mathrm{e}^{-\mathrm{i}m'\alpha}\delta_{m,m'}, \tag{A.9}$$

leading to the identity

$$Y_m^{(\ell)}(\boldsymbol{r}') = \mathrm{e}^{\mathrm{i}m\phi} Y_m^{(\ell)}(\boldsymbol{r}), \tag{A.10}$$

where ϕ is the azimuth angle. Moreover the Wigner-D-matrix manifest in the calculation of the character, e.g. for a rotation α around the z axis, as

$$\chi^{(\ell)}(\mathcal{R}_z(\alpha)) = \sum_m D_{mm}^{(\ell)}(\alpha) = \frac{\sin[(\ell + 1/2)\alpha]}{\sin[(1/2)\alpha]}. \tag{A.11}$$

Appendix B Self-energies of Ca_2RuO_4

This chapter provides additional data to section 6.2. Besides a matrix plot for all four phases in the absence of spin-orbit coupling within the DMFT calculation (see figure B.1) also the self-energies on the Matsubara axis and the corresponding analytical continuated real ω object are supplied here (see figure B.3 and B.4). Note that the self-energy plots belong to the calculations done in section 6.2.

For the analytical continuation of the local propagator to obtain the single-particle spectral functions $A(\omega)$ shown in figure B.1, a stochastic optimization method as implanted in [88] was used. Since these calculations were performed in the absence of spin-orbit coupling the fermionic sign-problem, inherent in CT-QMC solvers such as CT-HYB, is not very severe here. Of course due to less off-diagonal elements in the hybrdization function. Nonetheless, the quality of the analytical continuation in this specific case depends highly on the accumulated statistics of the analytical continuation method used here.

In table B.2 the fillings corresponding to figure B.1 are given. When no spin-orbit coupling is present the d_{xy} orbital becomes nearly fully field resulting in a orbital selective metal-to-insulator transition. In comparison with figure 6.5, where spin-orbit coupling is present an (discussion in section 6.2) this picture becomes a bit distorted, since spin-orbit-coupling mixes the orbital character a bit.

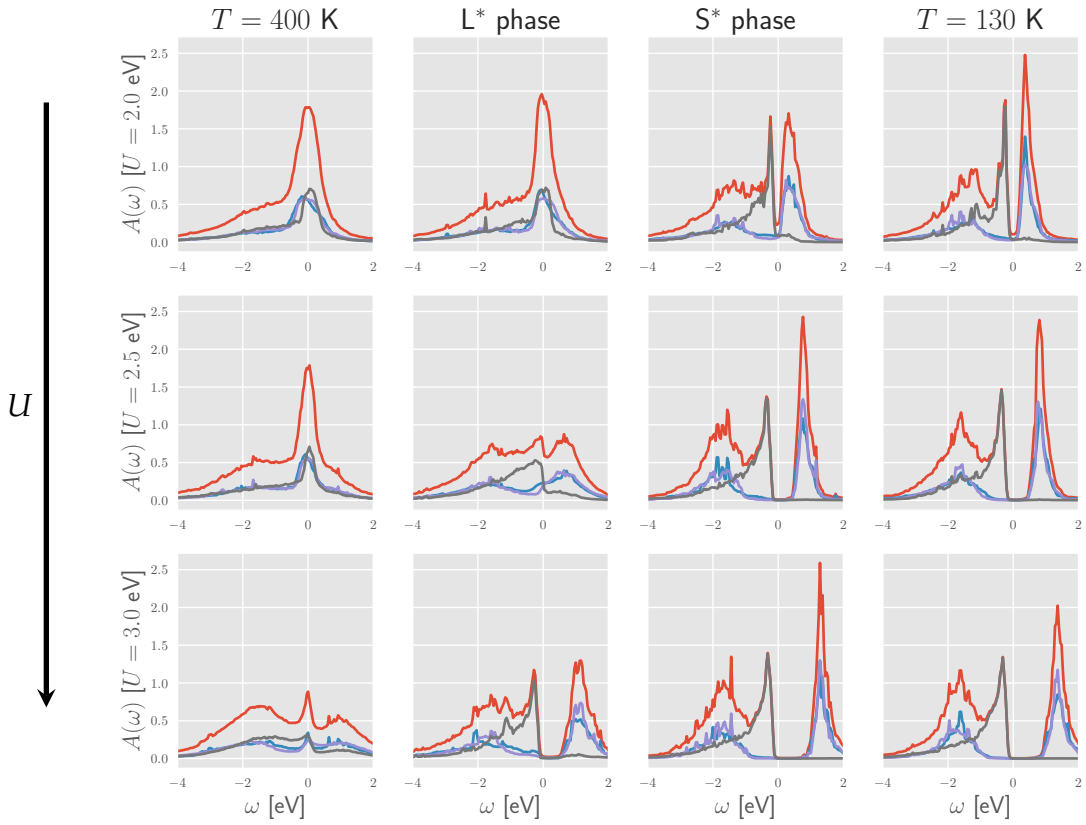

■ **Figure B.1.:** Parameter search of all four phases (from left to right: L-phase, L*-phase, S*-phase, S-phase), with $J_H = 0.4$ eV, $\lambda = 0$ eV, and U =2.0 eV to 3.0 eV, where the metal-to-insulator transition is expected. Shown are the single-particle spectral function for: xy-orbital (gray), xz/yz- orbital (blue/purple), and the total spectral function (red).

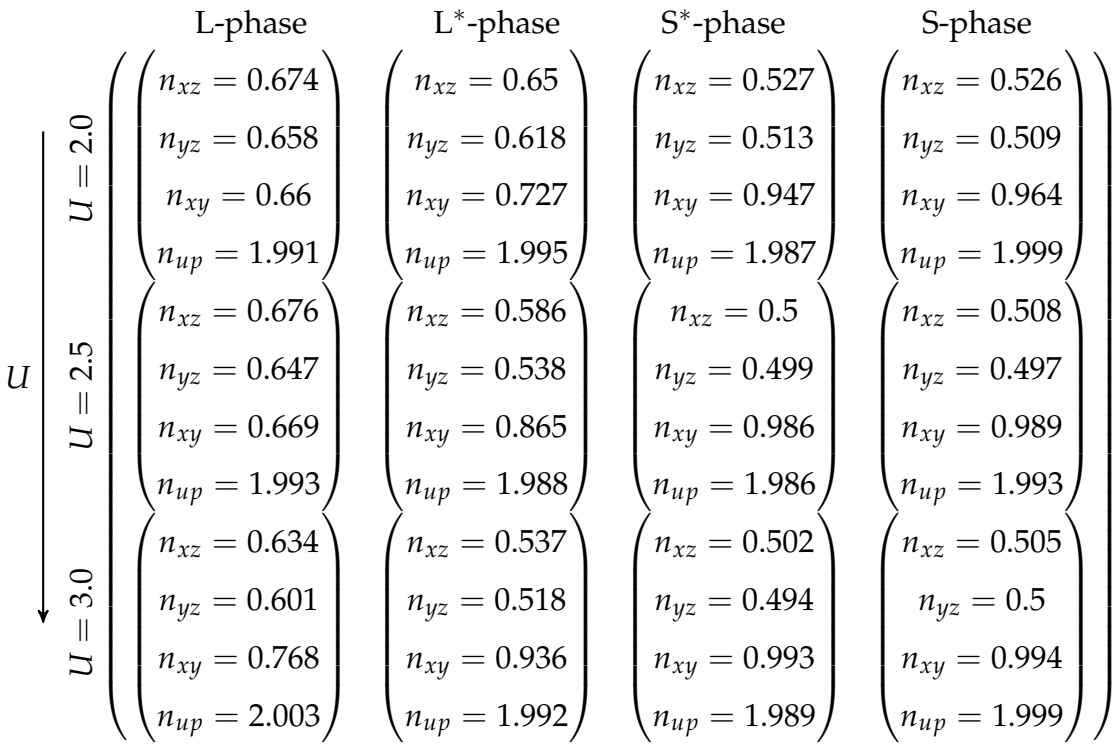

Figure B.2.: Orbital resolved fillings corresponding to the spectral function as shown in figure B.1. Since all solutions are paramagnetic only the spin up part is given.

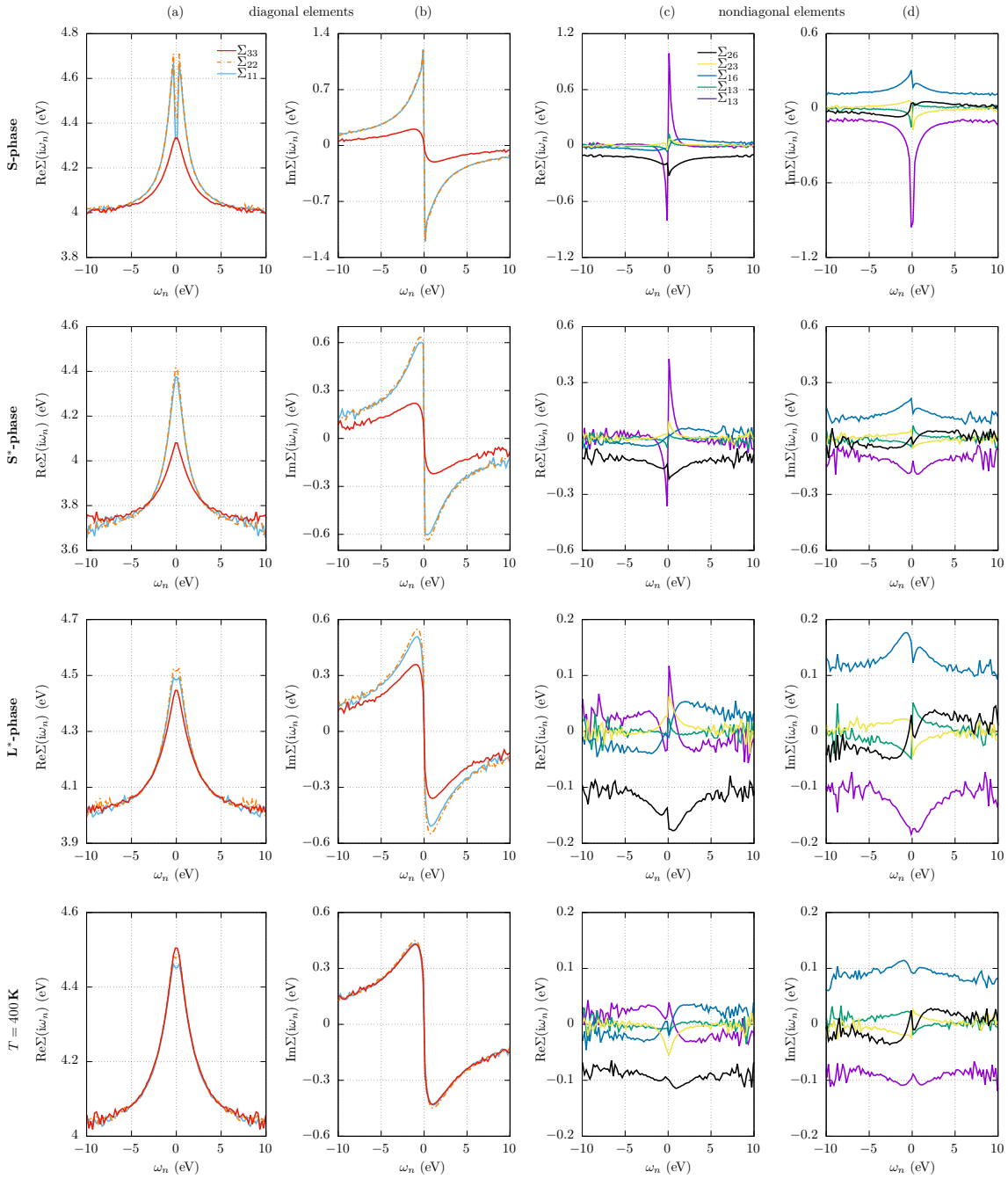

Figure B.3.: Self-energy $\Sigma(i\omega_n)$ on the Matsubara axis $i\omega_n$ for all phases. (a),(b) Real and imaginary part of the diagonal elements. (c),(d) Real and imaginary part of the off-diagonal elements. The notation Σ_{ij} corresponds to the basis convention $i,j \in \{d_{xz,\uparrow}, d_{yz,\uparrow}, d_{xy,\uparrow}, d_{xz,\downarrow}, d_{yz,\downarrow}, d_{xy,\downarrow}\}$. For better illustration of the diagonal elements only the spin up block is shown. Taken from [24]. Reproduced from J. Bertinshaw et al., Phys. Rev. Lett. 123, 137204 (2019), Copyright 2019 American Physical Society.

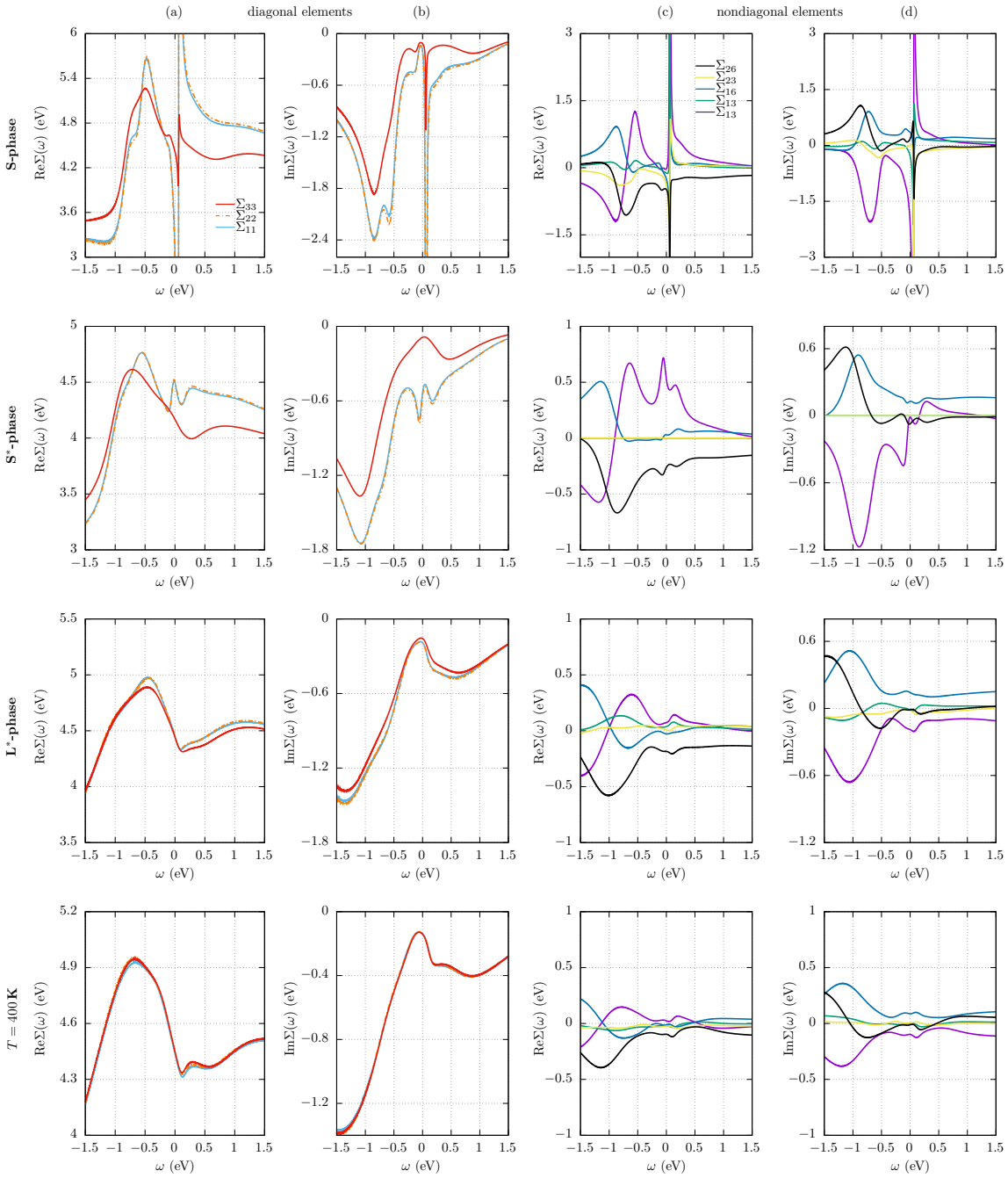

■ **Figure B.4.:** Analytically-continued self-energy $\Sigma(\omega)$ on the real axis ω for all phases. (a),(b) Real and imaginary part of the diagonal elements. (c),(d) Real and imaginary part of the off-diagonal elements. The notation Σ_{ij} corresponds to the basis convention $i,j \in \{d_{xz,\uparrow}, d_{yz,\uparrow}, d_{xy,\uparrow}, d_{xz,\downarrow}, d_{yz,\downarrow}, d_{xy,\downarrow}\}$. For better illustration of the diagonal elements only the spin-up block is shown. Reproduced from J. Bertinshaw et al., Phys. Rev. Lett. 123, 137204 (2019), Copyright 2019 American Physical Society.

Appendix C Core level spectroscopy

Core level spectroscopy covers a wide range of spectroscopic techniques probing properties of a system by exciting a core electron of a specific atom by applying high energy x-ray photons. Is the excited core electron high enough in energy to reach the continuum it can be detected as photoelectron. This method is generally known as photoemission spectroscopy. If the photon energy however matches the energy difference between core and certain conduction states, the excitations can also follow these states. The excitations of a core level leaves an unstable core hole which itself will interact with other core- or valence states. After a certain lifetime these states will decay by emitting an electron or photon. In order to excite core states, the incident photon must overcome their binding energy. For 3d transition metals, where on can either excite $2s/p$ states or $1s$ states, energies ranges 400–1000 eV or 4–10 keV are necessary [46, 155]. Note that the energy range of x-rays is $\sim 10^{2-5}$ eV. The core excitations are conventionally labeled after the core states, i.e. K, L, M for $n = 1,2,3$, where n is the principal quantum number. The different angular momenta are taken into account by giving an additional subscript 1,2,3,..., e.g. L_1 for the $2s$ state, L_2 for the $2p_{1/2}$ state, and L_3 for the $2p_{3/2}$ state. Probably two of the most common methods based on core-level excitations are XAS (x-ray absorption spectroscopy) and RIXS (resonant inelastic x-ray scattering), which differ mainly by the number of involved process steps. Both methods are sketched in figure C.1.

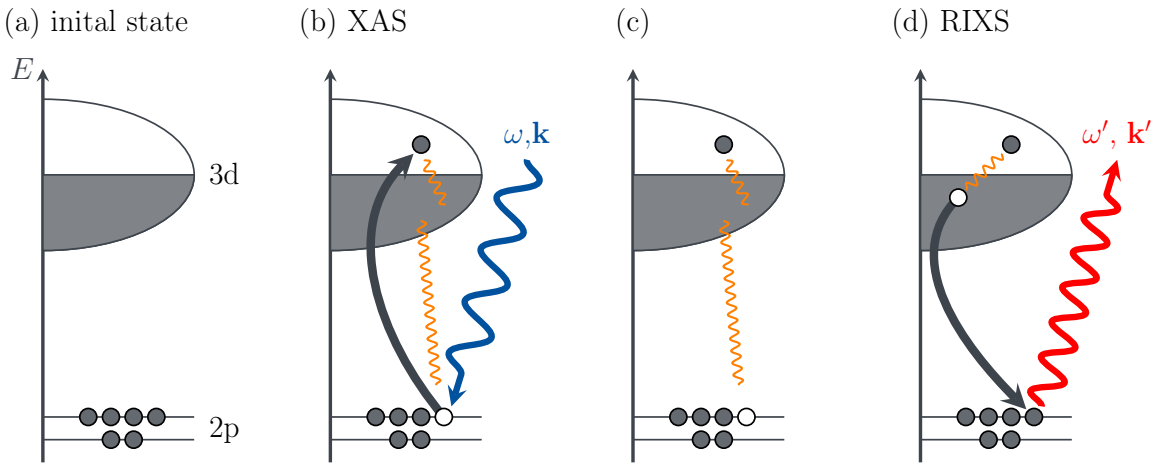

■ **Figure C.1.:** Schematic visualization of XAS (a)-(b) and RIXS (a)-(d). If the final state in (d) remains the same as the initial state (a), the scattering process is elastic. The emitted photon then obeys $\omega' = \omega$. For the inelastic case $\omega' \neq \omega$ the final states low energy excitations, like electron-hole pairs (see (d)).

XAS

The XAS process follow the sketched steps figure C.1 (a)-(b). A core electron (here $2s$) in the ground state is excited into the conduction band (here $2p$) of an atom by absorbing a photon of energy and momentum $(\omega,\boldsymbol{k})$ (see (b)). The system is left in a highly excited state, due to the strong interaction in the 3d bands and 2p core hole (see (c)). This excitation will propagate for a specific lifetime till another electron fills the core hole. There are two channels how the energy can be released. Either by emitting an Auger electron, or by emitting a photon (see (d)). Hence the experimental framing as electron yield or fluorescence yield. The absorption intensity can explicitly be calculated via a Green's function

$$I_{\mathrm{XAS}} \propto -\frac{1}{\pi}\mathrm{Im}\langle\psi_i|T^{\dagger}\frac{1}{(\omega + \mathrm{i}\Gamma/2 + E_i - \mathcal{H})}T|\psi_i\rangle, \tag{C.1}$$

where Γ a finite inverse core-hole lifetime, $|\psi_i\rangle$ is the ground state of the Hamiltonian $\mathcal{H}$, and T is an dipole transition operator. Note that the obtained XAS intensity describes a first order process given by Fermi's golden rule [155–157] leading to

$$I_{\mathrm{XAS}}(\omega) \propto |\langle f|T|i\rangle|^2\delta(E_f - E_i - \hbar\omega), \tag{C.2}$$

where the label f refers to the final state. Both formulas for the XAS intensity are equivalent, however the first one is used in all calculations within this thesis.

RIXS

The RIXS process is visualized in figure C.1 (a)-(d). It is called resonant because the energy of the incident photon coincides with the one of a atomic x-ray absorption edge. Although RIXS shares some similarities with XAS, the main difference is that RIXS is a two-particle process, where the scattered electron has a different energy than the incident electron (inelastic). In this case the system is left with low-energy excitations (phonon, magnons, ...) whose energy and momentum is deduced from the measured emitted photon. The RIXS intensity can be derived from the transition rate expanded to the second order term [155–157]

$$w = \frac{2\pi}{\hbar} \sum_f \left| \langle f|\mathcal{H}|i\rangle + \sum_n \frac{\langle f|\mathcal{H}|n\rangle \langle n|\mathcal{H}|i\rangle}{E_f - E_i} \right|^2 \delta(E_f - E_i). \tag{C.3}$$

It further can be shown [46] that the RIXS intensity is then

$$I_{\mathrm{RIXS}}(\omega, \omega') \propto \sum_f \left| \langle f|T' \frac{1}{\omega + E_n - \mathcal{H} + \mathrm{i}\Gamma} T|i\rangle \right|^2 \delta(\omega - \omega' + E_i - E_f), \tag{C.4}$$

where ω is the energy of the incoming photon and ω' of the emitted one. This formula is also known as Kramers-Heisenberg formula [156–158]. Expressed as Green's function we get

$$\begin{aligned} &I_{\mathrm{RIXS}}(\omega_1,\omega_2) = \\ &-\frac{1}{\pi}\mathrm{Im}\left\langle \psi_i \middle| T_1^\dagger \frac{1}{\omega_1 - \mathcal{H}_1 - \mathrm{i}\Gamma/2} T_2^\dagger \frac{1}{\omega_2 - \mathcal{H}_2 + \mathrm{i}\Gamma/2} T_2 \frac{1}{\omega_1 - \mathcal{H}_1 + \mathrm{i}\Gamma/2} T_1 \middle| \psi_i \right\rangle. \end{aligned} \tag{C.5}$$

Note that here $\mathcal{H}_1$ is Hamiltonian describing p and d orbitals and the core-valence interaction, while $\mathcal{H}_2$ can be any model describing low-energy excitations, e.g. only a d shell with inner shell interactions.

Appendix D Further XAS and RIXS spectra for LiV_2O_4

In this chapter additional XAS and RIXS spectra for LiV_2O_4 are shown. The parametrization follows the description of the main chapter. Again spectra are shown for the full core-valence interaction and a simplified one including only density-density terms as described in the main chapter. Subsequently the following cases are considered:

- 1 bath site, simplified core-valence interaction, with restriction to the t_{2g} subspace shown in figure D.1.
- 1 bath site, full core-valence interaction, with no restriction to the t_{2g} subspace shown in figure D.2.
- 1 bath site, simplified core-valence interaction, no restriction shown in figure D.3.
- 1 bath site, full core-valence interaction, with no restriction shown in figure D.4.

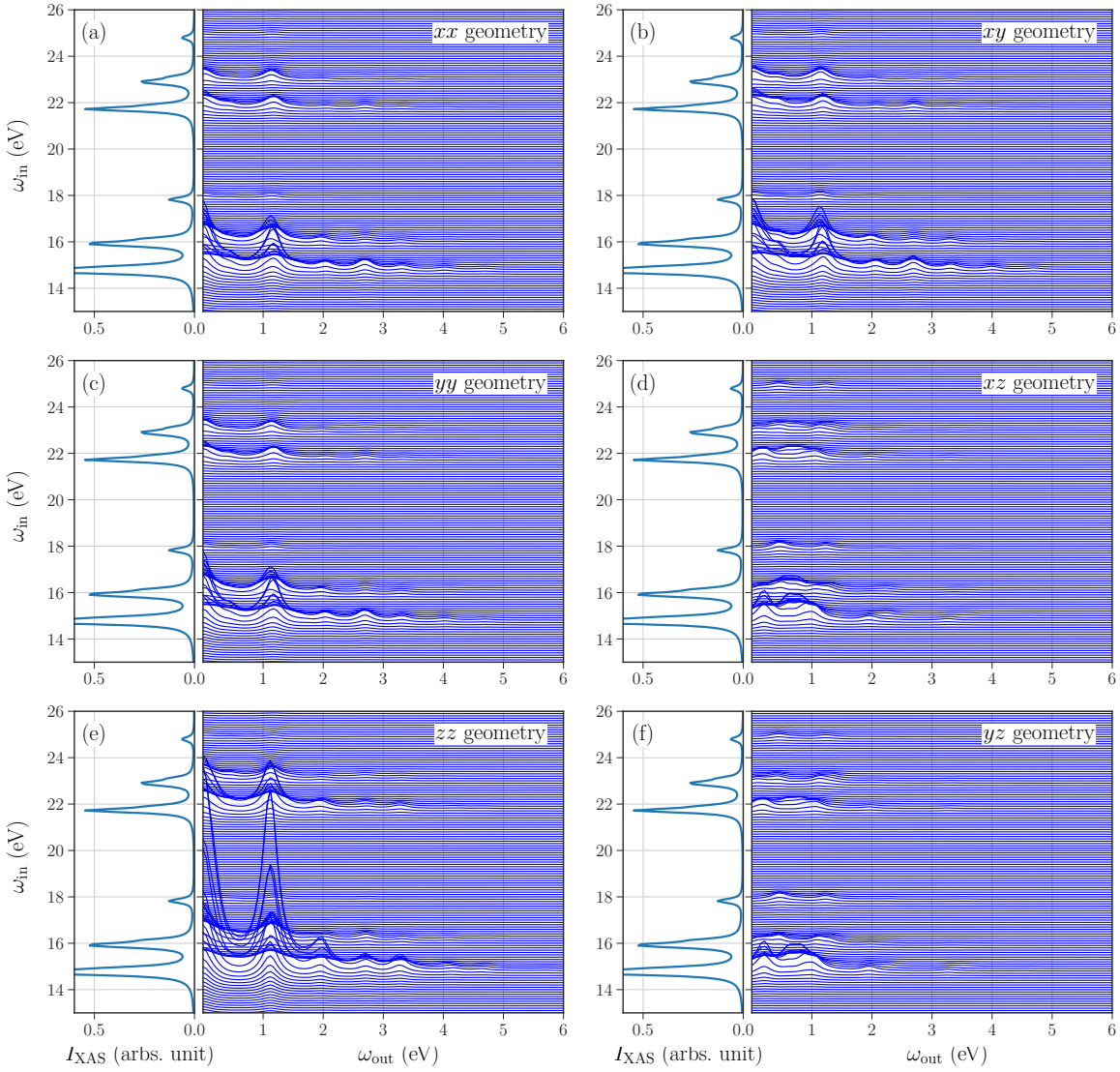

Figure D.1.: XAS intensity (always left panel) and RIXS intensity (always right panel) for different geometries for a discretized model with 1 bath site. All calculations were restricted to the t_{2g} subspace and a simplified core-valence interaction, including only density-density terms. (a) xx-, (b) xy-, (c) yy-, (d) xz-, (e) zz-, (f) yz-geometry. For all figures a spreading of $\Gamma = 0.3$ was used.

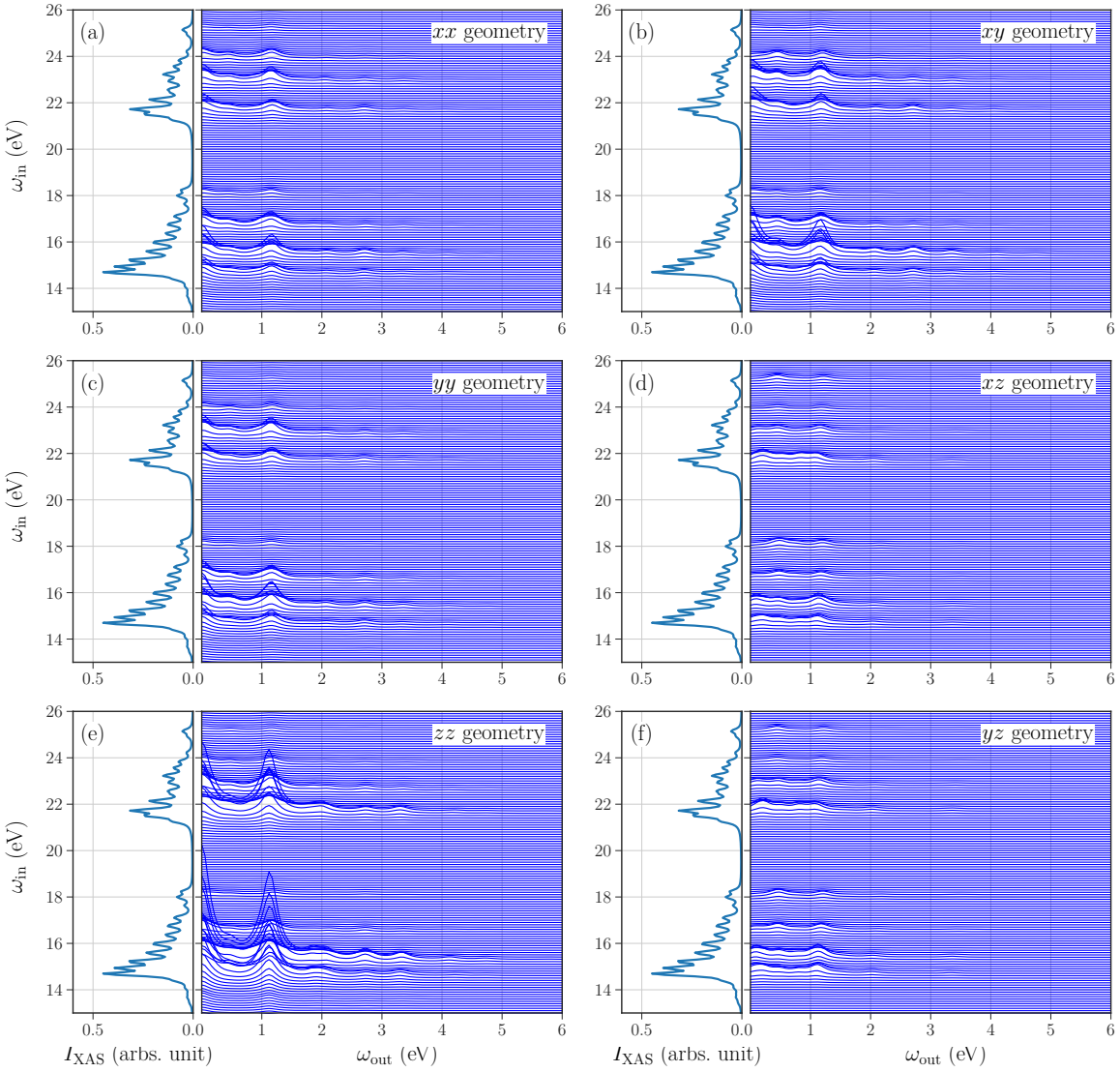

Figure D.2.: XAS intensity (always left panel) and RIXS intensity (always right panel) for different geometries for a discretized model with 1 bath site. All calculations were restricted to the t_{2g} subspace and the full core-valence interaction. (a) xx-, (b) xy-, (c) yy-, (d) xz-, (e) zz-, (f) yz-geometry. For all figures a spreading of $\Gamma = 0.3$ was used.

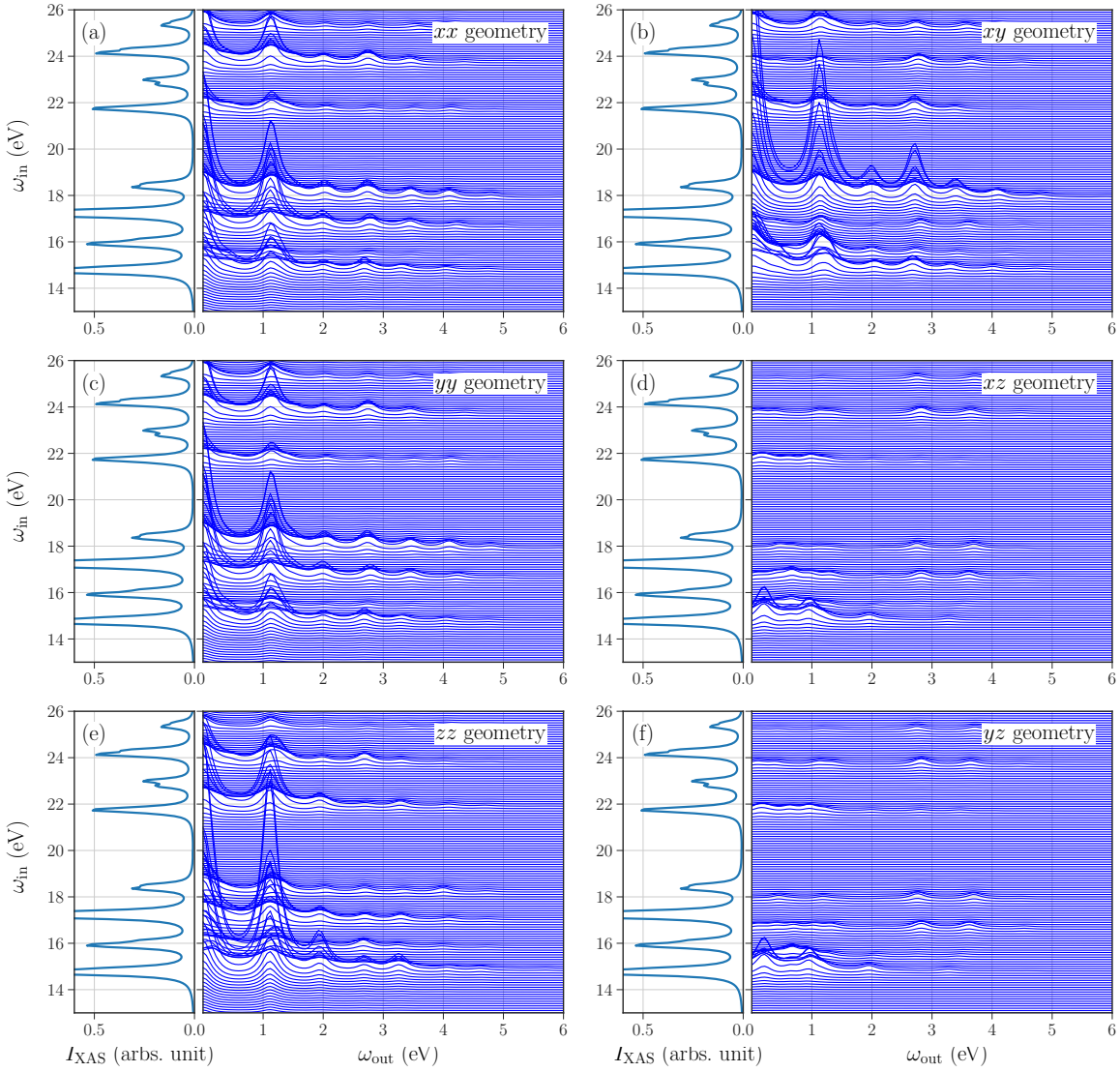

Figure D.3.: XAS intensity (always left panel) and RIXS intensity (always right panel) for different geometries for discretized a model with 1 bath site. All calculations were restricted to a simplified core-valence interaction, including only density-density terms. (a) xx-, (b) xy-, (c) yy-, (d) xz-, (e) zz-, (f) yz-geometry. For all figures a spreading of $\Gamma = 0.3$ was used.

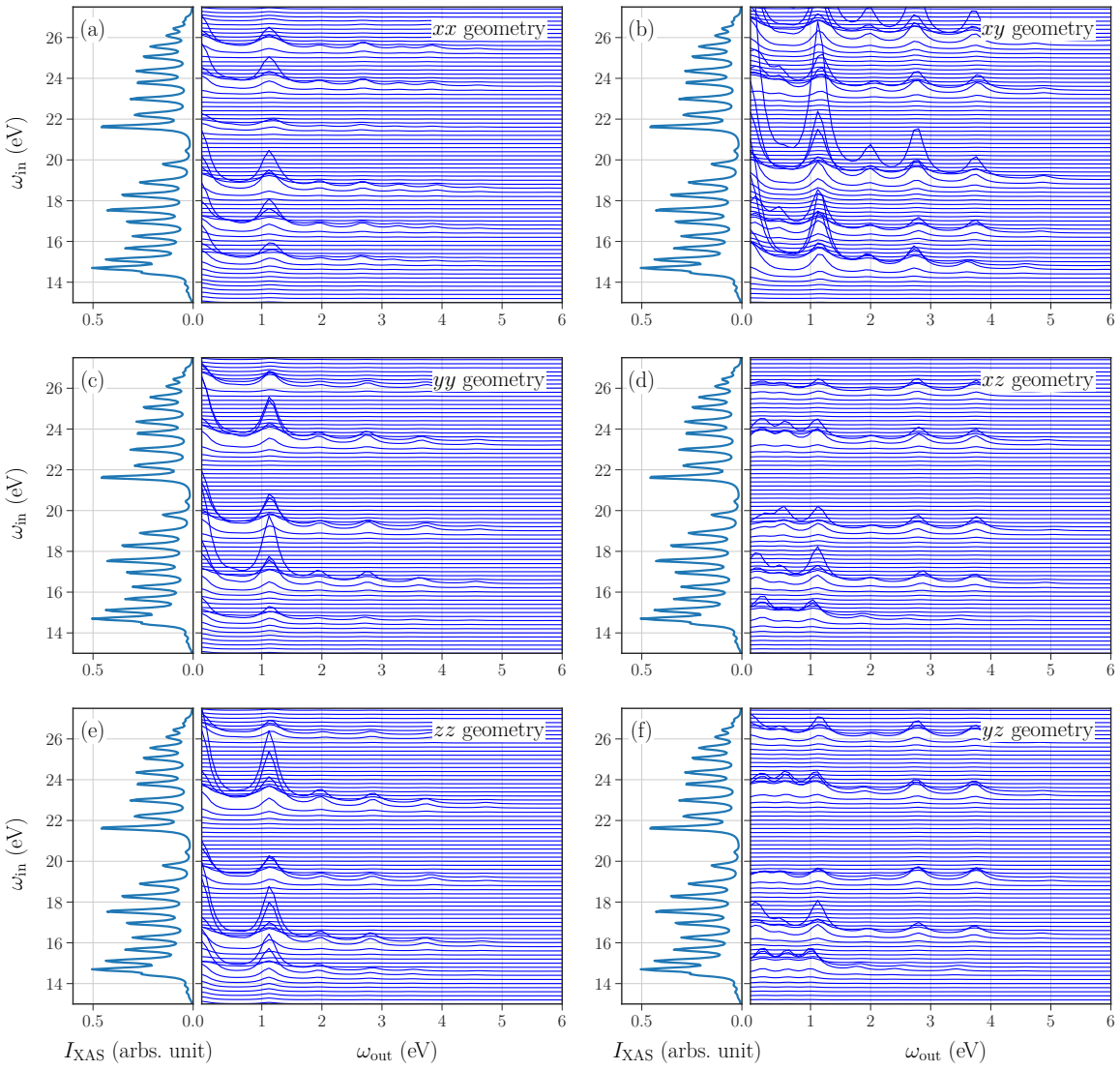

■ **Figure D.4.:** XAS intensity (always left panel) and RIXS intensity (always right panel) for different geometries for a discretized model with 1 bath site. All calculations were performed with full core-valence interaction. (a) *xx*-, (b) *xy*-, (c) *yy*-, (d) *xz*-, (e) *zz*-, (f) *yz*-geometry. For all figures a spreading of $\Gamma = 0.3$ was used.

List of Figures

List of Tables

Zusammenfassung

In der vorliegenden Arbeit wurde eine zeitgenössische numerische Methode, nämlich DFT+DMFT, zur Beschreibung echter Materialien verwendet. Die hier verwendete DFT+DMFT Methodik wird auch als "single shot" Variante bezeichnet, bei der einer Bandstrukturrechnung mit anschließender Wannierprojektion zur Erzeugung eine effektiven Modells eine normale DMFT Rechnung folgt. Innerhalb des letzten Jahrzehnts hat sich diese als eine Standardmethode herauskristallisiert, da ihre Beschreibung physikalischer Phänomen und Ergebnisse mit experimentellen Resultaten häufig übereinstimmt. Zudem eignet sie sich zur Beschreibung lokaler elektronischer Phänomene sowohl im Bereich niedriger als auch hoher Temperaturen. Dies ist der Vielzahl an möglichen Lösungsmethoden (ED, QMC, DMRG, NRG, ...) geschuldet. Es sei jedoch auch angemerkt, dass die ursprüngliche DMFT Formulierung, also das Lösen eines effektiven Störstellenproblems, auch nur lokale Phänomene Beschreiben kann. Nichtsdestotrotz existieren bereits Erweiterungen auf Gitterplatzsysteme mit mehreren Gitterplätzen, sogenannten Clustern, die erfolgreich angewendet werden. Diese Erweiterungen gehen jedoch meist mit einer deutlich erhöhten numerischen Rechenzeit einher. Die letzten Jahre haben gezeigt, dass simple Bandstrukturrechnungen der experimentellen Sachlage nicht mehr genügen, da diese an die Grenzen ihrer eigenen intrinsischen Approximation gelangen. Gerade im Fall von TMOs, in denen starke Korrelationen zu einer Vielzahl physikalischer Beobachtungen führen, kann dies demonstriert werden. DMFT und ihre Erweiterungen hingegen liefern jedoch gerade, zumindest für

elektronische Phänomene, die richtige Beschreibung. Im Folgenden sollen daher in kürze die Anwendungen und Resultate dieser Methode innerhalb dieser Arbeit zusammengefasst werden.

Übergangsmetalloxide sind aufgrund ihrer Reichhaltigkeit an physikalischen Phänomenen und damit einhergehenden komplexen Phasendiagrammen ein fruchtbarer Boden für viele Experimentatoren und Theoretiker. Ca_2RuO_4, ein Musterbeispiel eines Mottisolators, stellt dies geradezu unter Beweis. In der Gleichgewichtsphase besitzt es in Abhängigkeit von der Temperatur drei verschiedene Phasen. Eine metallische Hochtemperaturphase, die beim Abkühlen in eine paramagnetische mottisolierende Phase übergeht und eine antiferromagnetische mottisolierende Phase bei noch niedrigeren Temperaturen. Wie in vielen TMOs sind diese eine unmittelbare Konsequenz konkurrierender Energieskalen, bspw. Spin-Bahn Kopplung, Kopplung und Kristallfeldaufspaltung, was gerade eine theoretische Beschreibung deutlich erschwert. Zusätzlich wurde in den letzten Jahren gezeigt, dass durch Anlegen eines bereits kleinen Gleichstroms Nichtgleichgewichtsphasen stabilisiert werden können. Diese sind von ihren Verhalten ihren Gleichgewichtspartnern zwar ähnlich, führen jedoch zu unterschiedlichen Kristallstrukturen. Ausgehen von eben jenen Kristallstrukturen erfolgten DFT+DMFT Rechnungen, die zu verschiedenen metallischen und isolierenden Spektralfunktionen führten. Eine dieser Nichtgleichgewichtsphasen bevorzugt eine sogenannte semimetallische Phase, d.h. verschwindendes Spektralgewicht an der Fermienergie bei gleichzeitiger Leitfähigkeit. Es wurde gezeigt, dass die semimetalische Phase eine Femifläche mit partieller Bandlücke bevorzugt. Die Rechnungen der unterschiedlichen Phasen zeigen zudem, dass für eine akkurate Beschreibung, bzw, Erklärung der unterschiedlichen Phasen, die Kristallstruktur selbst wichtig ist, denn gerade Bandstruktur und Spektralfunktion reagieren extrem sensibel auf einen Gleichstrom und der damit einhergehenden Änderung der Kristallstruktur.

Obwohl der DFT+DMFT Ansatz erfolgreich zur Beschreibung lokaler elektronischer Phänomene herangezogen wurde, scheitert er – zumindest in seiner ur-

sprünglichen Formulierung – an der Beschreibung von röntgenspektroskopisches Messverfahren, wie etwas RIXS und XAS. Dies ist der einfachen Tatsache geschuldet, dass der DMFT Formalismus keine Kernniveaus beinhaltet, da sie für die Beschreibung elektronischer Phänomene um die Fermienergie irrelevant sind. Hochauflösende RIXS Experimente, besonders an der L-Kante, sind jedoch für viele TMOs wünschenswert da RIXS die unterschiedliche Anregungen besonders gut experimentell zugänglich macht. Die herkömmliche Methode, die im wesentlichen einen lokalen Cluster eines TMOs unter Berücksichtigung von Hartree-Fock ermittelten Werten mittels exakter Diagonalisierung beinhaltet, scheitert jedoch gerade an der Beschreibung eben jener Spektren. Gerade linienartige Fluoreszenzmerkmale können mit dieser nicht reproduziert werden. Durch die Zuhilfenahme von konvergierten DFT+DMFT Rechnungen wurde jedoch gezeigt, dass eben diese zugänglich werde. Hierzu wurde die DMFT Hybridisierungsfunktion diskretisiert um das darunterliegenden Anderson Störstellen Modell für eine endliche Anzahl an Bädern zu konstruieren. Anschließend wurden die Kernniveaus hinzugefügt, so wie die Kern-Valenz Wechselwirkung. Es folgt schließlich eine Rotation in die "natural orbital basis", da diese eine Einschränkung des Konfigurationsraumes erlaubt und damit die Rechenzeit verkürzt, bzw. erlaubt auf eine größerer Anzahl an Bädern zu gehen. Um die Qualität dieser Diskretisierung zu testen wurde gezeigt, dass für das halb gefühlte Bethe-Gitter und für das zweidimensionale Hubbardmodell auf einem Quadratgitter bei Füllungen abseits von Halbfüllung, DMFT und ED Spektralfunktionen im Einklang sind. Zudem wurde gezeigt, dass bereits bei großer Beschränkung des Konfigurationsraumes (Beschränkung auf eine effektives 2 Platz Problem), qualitativ gute Spektren reproduziert werden können. Anschließend wurden DFT+DMFT Rechungen mit anschließender Diskretisierung für LiV_2O_4 ausgeführt. Die Übertragung auf ein "reales" System und die Berechnungen von XAS und RIXS Spektren erfolgte hier lediglich für Modelle mit wenigen Bädern. Auch konnten wir bis dato noch keine Fluoreszenzlinien in den Spektren finden. Die kann jedoch als Konsequenz der wenigen Bädern gesehen werden. Modelle

mit großer Badanzahl sind somit noch ausstehend und Bestandteil zukünftiger Projekte.

List of publications

1. Excitonic Magnetism at the intersection of Spin-orbit coupling and crystal-field splitting, T. Feldmaier, P. Strobel, M. Schmid, P. Hansmann, M. Daghofer, arXiv:1910.13977

2. A Unique Crystal Structure of Ca_2RuO_4 in the Current Stabilized Semi-Metallic State, J. Bertinshaw, N. Gurung,P. Jorba, H. Liu, M. Schmid, D. T. Mantadakis, M. Daghofer, M. Krautloher, A. Jain, G. H. Ryu, O. Fabelo, P. Hansmann, G. Khaliullin, C. Pfleiderer, B. Keimer, and B. J. Kim, Phys. Rev. Lett. **123**, 137204, 2019

Acknowledgment

During the time at the FMQ (Institute for Functional Matter and Quantum technologies) and the Max Planck institute for solid state research in Stuttgart I meet many people which I am very grateful to work with, supported me throughout my whole time as PhD and became good friends in life. Therefore, I want to express my sincere gratitude to:

- Prof. Dr. Maria Daghofer for welcoming me at her institute, her supervision, the continuous support, her patience, motivation, and immense knowledge.
- Prof. Dr. Philipp Hansmann for being my daily advisor at the Max Planck institute, his patience, guidance, and valuable advice in general.
- Prof. Dr. Hidenori Takagi for accepting to be in my PhD examination committee, fruitful advice, and collaboration.
- Giniyat Khaliullin and Huimei Liu for the fruitful collaboration, encouragement, and interesting discussions.
- All members of the FMQ and Hansmann group at the MPI for the friendly and supporting working atmosphere. At the FMQ I especially want to thank Teresa Feldmaier who shared an office with me, Friedemann Aust and Jonas Heverhagen for proofreading this thesis and also Jan Lotze for thousands of discussions and explanations. On the MPI I meet Daniil Mantatadakis and Xiaodong Chao with whom I had the chance to spend time with. In particular I value their dinner and coffee discussions, support, and great sense of humor.

- My rommates Ulrike Niemann, Kai-Simon Guther, and Matthias Uhl for living with me, becoming close friends, going on vacations together, their spiritual and mental support, and patience, when I sometimes got lost in my mind.
- Stefan Käser, with whom I shared an office for a long time and becoming a valuable friend over the last three years.
- My family: my dad and to my brothers for supporting me spiritually throughout writing this thesis and my life in general.

Bibliography

[1] Max Karl Ernst Ludwig Planck. "Zur theorie des gesetzes der energieverteilung im normalspectrum". In: *Verhandl. Dtsc. Phys. Ges.* 2 (1900), p. 237.

[2] Heinrich Rubens and Ferdinand Kurlbaum. "Anwendung der Methode der Reststrahlen zur Prüfung des Strahlungsgesetzes". In: *Annalen der Physik* 309.4 (1901), pp. 649–666.

[3] Albert Einstein. "Über einen die Erzeugung und Verwandlung des Lichtes betreffenden heuristischen Gesichtspunkt". In: *Annalen der physik* 322.6 (1905), pp. 132–148.

[4] Walther Gerlach and Otto Stern. "Der experimentelle nachweis der richtungsquantelung im magnetfeld". In: *Zeitschrift für Physik* 9.1 (1922), pp. 349–352.

[5] Arthur H Compton. "A quantum theory of the scattering of X-rays by light elements". In: *Physical review* 21.5 (1923), p. 483.

[6] Werner Heisenberg. "Über quantentheoretische Umdeutung kinematischer und mechanischer Beziehungen." In: *Zeitschrift für Physik* 33 (1925), pp. 879–893.

[7] Werner Heisenberg. "Über den anschaulichen Inhalt der quantentheoretischen Kinematik und Mechanik". In: *Zeitschrift für Physik* 43 (1927), pp. 172–198.

[8] Erwin Schrödinger. "An undulatory theory of the mechanics of atoms and molecules". In: *Physical review* 28.6 (1926), p. 1049.

[9] Werner Heisenberg. *Quantentheorie und Philosophie*. 1979.

[10] Louis De Broglie. "Recherches sur la théorie des quanta". PhD thesis. Migration-université en cours d'affectation, 1924.

[11] Leonard I Schiff. *Quantum mechanics*. McGraw-Hill, 1968.

[12] Franz Schwabl. *Quantenmechanik (QM I): Eine Einführung*. Springer-Verlag, 2007.

[13] Michel Le Bellac. *Quantum physics*. Cambridge University Press, 2011.

[14] Wolfgang Nolting. *Grundkurs Theoretische Physik 7: Viel-Teilchen-Theorie*. Springer-Verlag, 2014.

[15] Wolfgang Pauli. "The connection between spin and statistics". In: *Physical Review* 58.8 (1940), p. 716.

[16] Charles Kittel et al. *Introduction to solid state physics*. Vol. 8. Wiley New York, 1976.

[17] Daniel Khomskii. *Transition metal compounds*. Cambridge University Press, 2014.

[18] John Hubbard. "Electron correlations in narrow energy bands". In: *Proceedings of the Royal Society of London. Series A. Mathematical and Physical Sciences* 276.1365 (1963), pp. 238–257.

[19] Pierre Hohenberg and Walter Kohn. "Inhomogeneous electron gas". In: *Physical review* 136.3B (1964), B864.

[20] Masatoshi Imada, Atsushi Fujimori, and Yoshinori Tokura. "Metal-Insulator Transitions". In: *Rev. Mod. Phys.* 70 (1998), pp. 1039–1263. DOI: 10.1103/RevModPhys.70.1039.

[21] Walter Metzner and Dieter Vollhardt. "Correlated lattice fermions in $d = \infty$ dimensions". In: *Physical review letters* 62.3 (1989), p. 324.

[22] Antoine Georges et al. "Dynamical mean-field theory of strongly correlated fermion systems and the limit of infinite dimensions". In: *Rev. Mod. Phys.* 68 (1 Jan. 1996), pp. 13–125. DOI: 10.1103/RevModPhys.68.13. URL: https://link.aps.org/doi/10.1103/RevModPhys.68.13.

[23] Arash A. Mostofi et al. "wannier90: A tool for obtaining maximally-localised Wannier functions". In: *Computer Physics Communications* 178.9 (2008), pp. 685–699. ISSN: 0010-4655. DOI: https://doi.org/10.1016/j.cpc.2007.11.016. URL: http://www.sciencedirect.com/science/article/pii/S0010465507004936.

[24] J. Bertinshaw et al. "Unique Crystal Structure of Ca_2RuO_4 in the Current Stabilized Semimetallic State". In: *Phys. Rev. Lett.* **123** (13 Sept. 2019), p. 137204.

[25] Atsushi Hariki, Takayuki Uozumi, and Jan Kuneš. "LDA+DMFT approach to core-level spectroscopy: Application to 3 d transition metal compounds". In: *Physical Review B* 96.4 (2017), p. 045111.

[26] Hermann Haken and Hans C Wolf. *Molekülphysik und Quantenchemie: Einführung in die experimentellen und theoretischen Grundlagen*. Springer-Verlag, 2013.

[27] Gerd Czycholl. *Theoretische Festkörperphysik: von den klassischen Modellen zu modernen Forschungsthemen*. Springer-Verlag, 2013.

[28] Walter Kohn. "Nobel Lecture: Electronic structure of matter—wave functions and density functionals". In: *Reviews of Modern Physics* 71.5 (1999), p. 1253.

[29] Anisimov Vladimir and Yuri Izumov. *Electronic Structure of Strongly Correlated Materials*. Springer-Verlag, 2010.

[30] O. Krogh Andersen. "Linear methods in band theory". In: *Phys. Rev. B* 12 (8 Oct. 1975), pp. 3060–3083. DOI: 10.1103/PhysRevB.12.3060. URL: https://link.aps.org/doi/10.1103/PhysRevB.12.3060.

[31] Nicola Marzari, Ivo Souza, and David Vanderbilt. "An introduction to maximally-localized Wannier functions". In: *Psi-K newsletter* 57 (2003), p. 129.

[32] Eva Pavarini et al. "The LDA+ DMFT approach to strongly correlated materials". In: *Reihe Modeling and Simulation* 1 (2011), pp. 2–13.

[33] Nicola Marzari and David Vanderbilt. "Maximally localized generalized Wannier functions for composite energy bands". In: *Physical review B* 56.20 (1997), p. 12847.

[34] G. Kresse and J. Furthmüller. "Efficient iterative schemes for ab initio total-energy calculations using a plane-wave basis set". In: *Phys. Rev. B* 54 (16 Oct. 1996), pp. 11169–11186. DOI: 10.1103/PhysRevB.54.11169. URL: https://link.aps.org/doi/10.1103/PhysRevB.54.11169.

[35] G. Kresse and D. Joubert. "From ultrasoft pseudopotentials to the projector augmented-wave method". In: *Phys. Rev. B* 59 (3 Jan. 1999), pp. 1758–1775. DOI: 10.1103/PhysRevB.59.1758. URL: https://link.aps.org/doi/10.1103/PhysRevB.59.1758.

[36] Masayuki Ochi and Kazuhiko Kuroki. "Effective interaction for vanadium oxyhydrides $Sr_{n+1}V_nO_{2n+1}H_n$ ($n = 1$ and $n \to \infty$): A constrained-RPA study". In: *Phys. Rev. B* 99 (15 Apr. 2019), p. 155143. DOI: 10.1103/PhysRevB.99.155143. URL: https://link.aps.org/doi/10.1103/PhysRevB.99.155143.

[37] Eva Pavarini et al. *DMFT: From Infinite Dimensions to Real Materials*. Tech. rep. Theoretische Nanoelektronik, 2018.

[38] Daniel I Khomskii. *Basic aspects of the quantum theory of solids: order and elementary excitations*. Cambridge University Press, 2010.

[39] Alexandre Zagoskin. *Quantum theory of many-body systems: techniques and applications*. Springer, 2014.

[40] Gerald D Mahan. *Many-particle physics*. Springer Science & Business Media, 2013.

[41] Alekseui Alekseevich Abrikosov, Lev Petrovich Gorkov, and Igor Ekhielevich Dzyaloshinski. *Methods of quantum field theory in statistical physics*. Courier Corporation, 2012.

[42] Satoru Sugano. *Multiplets of transition-metal ions in crystals*. Academic Press, 1970.

[43] Mildred S Dresselhaus, Gene Dresselhaus, and Ado Jorio. *Group theory: application to the physics of condensed matter*. Springer Science & Business Media, 2007.

[44] John Stanley Griffith. *The theory of transition-metal ions*. Cambridge University Press, 1964.

[45] Carl Johan Ballhausen. *Introduction to ligand field theory*. McGraw-Hill, 1962.

[46] Robert D Cowan. *The theory of atomic structure and spectra*. 3. Univ of California Press, 1981.

[47] Maurits W Haverkort. "Spin and orbital degrees of freedom in transition metal oxides and oxide thin films studied by soft x-ray absorption spectroscopy". In: *arXiv preprint cond-mat/0505214* (2005).

[48] T. Ribic et al. "Cubic interaction parameters for t_{2g} Wannier orbitals". In: *Phys. Rev. B* 90 (16 Oct. 2014), p. 165105. DOI: 10.1103/PhysRevB.90.165105. URL: https://link.aps.org/doi/10.1103/PhysRevB.90.165105.

[49] MW Haverkort, M Zwierzycki, and OK Andersen. "Multiplet ligand-field theory using Wannier orbitals". In: *Physical Review B* 85.16 (2012), p. 165113.

[50] Frank De Groot and Akio Kotani. *Core level spectroscopy of solids*. CRC press, 2008.

[51] Junjiro Kanamori. "Electron Correlation and Ferromagnetism of Transition Metals". In: *Prog. Theor. Phys.* 30 (1963), pp. 275–289. DOI: 10.1143/PTP.30.275.

[52] Shiro Sakai. "Theoretical study of multi-orbital correlated electron systems with Hund's coupling". PhD thesis. Ph. D. thesis, University of Tokyo, 2006.

[53] Norbert Grewe and Franck Steglich. "Handbook on the Physics and Chemistry of Rare Earths". In: *Elsevier, Amsterdam* 14 (1991), p. 343.

[54] John Robert Schrieffer and James S Brooks. *Handbook of high-temperature superconductivity: theory and experiment*. Springer, 2007.

[55] Elbio Dagotto. *Nanoscale phase separation and colossal magnetoresistance: the physics of manganites and related compounds*. Vol. 136. Springer Science & Business Media, 2013.

[56] Hilbert v Löhneysen et al. "Fermi-liquid instabilities at magnetic quantum phase transitions". In: *Reviews of Modern Physics* 79.3 (2007), p. 1015.

[57] Hans Bethe. "Zur theorie der metalle". In: *Zeitschrift für Physik* 71.3-4 (1931), pp. 205–226.

[58] R Brout. "Statistical mechanical theory of ferromagnetism. High density behavior". In: *Physical Review* 118.4 (1960), p. 1009.

[59] Colin J Thompson. "Ising model in the high density limit". In: *Communications in Mathematical Physics* 36.4 (1974), pp. 255–262.

[60] F. Schwabl. *Statistische Mechanik*. Springer-Lehrbuch. Springer, 2000. ISBN: 9783540671589.

[61] E Müller-Hartmann. "Correlated fermions on a lattice in high dimensions". In: *Zeitschrift für Physik B Condensed Matter* 74.4 (1989), pp. 507–512.

[62] Walter Metzner. "Variational theory for correlated lattice fermions in high dimensions". In: *Zeitschrift für Physik B Condensed Matter* 77.2 (1989), pp. 253–266.

[63] E Müller-Hartmann. "The Hubbard model at high dimensions: some exact results and weak coupling theory". In: *Zeitschrift für Physik B Condensed Matter* 76.2 (1989), pp. 211–217.

[64] H Schweitzer and G Czycholl. "Second order U-perturbation approach to the Anderson lattice model in high dimensions". In: *Solid state communications* 69.2 (1989), pp. 171–176.

[65] D Vollhardt. "Correlated Electron Systems". In: *Singapore: World Scienti* (1993).

[66] Peter GJ van Dongen, F Gebhard, and Dieter Vollhardt. "Variational evaluation of correlation functions for lattice electrons in high dimensions". In: *Zeitschrift für Physik B Condensed Matter* 76.2 (1989), pp. 199–210.

[67] Antoine Georges and Gabriel Kotliar. "Hubbard model in infinite dimensions". In: *Physical Review B* 45.12 (1992), p. 6479.

[68] Alexander Cyril Hewson. *The Kondo problem to heavy fermions*. Vol. 2. Cambridge university press, 1997.

[69] V Janiš. "A new construction of thermodynamic mean-field theories of itinerant fermions: application to the Falicov-Kimball model". In: *Zeitschrift für Physik B Condensed Matter* 83.2 (1991), pp. 227–235.

[70] V Janiš and D Vollhardt. "Comprehensive mean field theory for the Hubbard model". In: *International Journal of Modern Physics B* 6.05n06 (1992), pp. 731–747.

[71] M Jarrell. "Hubbard model in infinite dimensions: A quantum Monte Carlo study". In: *Physical review letters* 69.1 (1992), p. 168.

[72] Adolfo Avella, Ferdinando Mancini, et al. *Strongly Correlated Systems*. Springer, 2012.

[73] John W Negele and Henri Orland. *Quantum many-particle systems*. Westview Press, 1998.

[74] Michel Caffarel and Werner Krauth. "Exact diagonalization approach to correlated fermions in infinite dimensions: Mott transition and superconductivity". In: *Physical review letters* 72.10 (1994), p. 1545.

[75] Qimiao Si et al. "Correlation induced insulator to metal transitions". In: *Physical review letters* 72.17 (1994), p. 2761.

[76] Marcelo J Rozenberg, Goetz Moeller, and Gabriel Kotliar. "The metal–insulator transition in the hubbard model at zero temperature ii". In: *Modern Physics Letters B* 8.08n09 (1994), pp. 535–543.

[77] Ralf Bulla. "Zero temperature metal-insulator transition in the infinite-dimensional hubbard model". In: *Physical review letters* 83.1 (1999), p. 136.

[78] Michał Karski, Carsten Raas, and Götz S Uhrig. "Single-particle dynamics in the vicinity of the Mott-Hubbard metal-to-insulator transition". In: *Physical Review B* 77.7 (2008), p. 075116.

[79] Alexey N Rubtsov, Vladimir V Savkin, and Alexander I Lichtenstein. "Continuous-time quantum Monte Carlo method for fermions". In: *Physical Review B* 72.3 (2005), p. 035122.

[80] Philipp Werner et al. "Continuous-time solver for quantum impurity models". In: *Physical Review Letters* 97.7 (2006), p. 076405.

[81] K Held et al. "Realistic investigations of correlated electron systems with LDA+DMFT". In: *physica status solidi (b)* 243.11 (2006), pp. 2599–2631.

[82] Gabriel Kotliar et al. "Electronic structure calculations with dynamical mean-field theory". In: *Reviews of Modern Physics* 78.3 (2006), p. 865.

[83] Gabriel Kotliar and Dieter Vollhardt. "Strongly correlated materials: Insights from dynamical mean-field theory". In: *Physics today* 57.3 (2004), pp. 53–60.

[84] F Aryasetiawan et al. "Frequency-dependent local interactions and low-energy effective models from electronic structure calculations". In: *Physical Review B* 70.19 (2004), p. 195104.

[85] David Pines. *Elementary excitations in solids*. CRC Press, 2018.

[86] O Gunnarsson, MW Haverkort, and G Sangiovanni. "Analytical continuation of imaginary axis data using maximum entropy". In: *Physical Review B* 81.15 (2010), p. 155107.

[87] Gernot J. Kraberger et al. “Maximum entropy formalism for the analytic continuation of matrix-valued Green’s functions”. In: *Phys. Rev. B* 96 (15 Oct. 2017), p. 155128. DOI: 10.1103/PhysRevB.96.155128. URL: https://link.aps.org/doi/10.1103/PhysRevB.96.155128.

[88] Igor Krivenko and Malte Harland. “TRIQS/SOM: Implementation of the stochastic optimization method for analytic continuation”. In: *Computer Physics Communications* 239 (2019), pp. 166–183.

[89] Claude E Shannon. “A mathematical theory of communication”. In: *Bell system technical journal* 27.3 (1948), pp. 379–423.

[90] Stephen F Gull and John Skilling. “Maximum entropy method in image processing”. In: *IEE Proceedings F (Communications, Radar and Signal Processing)*. Vol. 131. 6. IET. 1984, pp. 646–659.

[91] RK Bryan. “Solving oversampled data problems by maximum entropy”. In: *Maximum Entropy and Bayesian Methods*. Springer, 1990, pp. 221–232.

[92] SF Gull and J Skilling. “Maximum entropy and bayesian methods”. In: *J. Skilling* (1989).

[93] Y Maeno et al. “Superconductivity in a layered perovskite without copper”. In: *Nature* 372.6506 (1994), pp. 532–534.

[94] TM Rice and M Sigrist. “Sr2RuO4: an electronic analogue of 3He?” In: *Journal of Physics: Condensed Matter* 7.47 (1995), p. L643.

[95] Andrej Pustogow et al. “Constraints on the superconducting order parameter in Sr 2 RuO 4 from oxygen-17 nuclear magnetic resonance”. In: *Nature* 574.7776 (2019), pp. 72–75.

[96] A. T. Rømer et al. “Knight Shift and Leading Superconducting Instability from Spin Fluctuations in Sr_2RuO_4”. In: *Phys. Rev. Lett.* 123 (24 Dec. 2019), p. 247001. DOI: 10.1103/PhysRevLett.123.247001. URL: https://link.aps.org/doi/10.1103/PhysRevLett.123.247001.

[97] Fumihiko Nakamura et al. “From Mott Insulator to Ferromagnetic Metal: A Pressure Study of Ca2RuO4”. In: *Phys. Rev. B* 65 (2002), p. 220402. DOI: 10.1103/PhysRevB.65.220402.

[98] O. Friedt et al. “Structural and Magnetic Aspects of the Metal-Insulator Transition in Ca[2-x]Sr[x]RuO4”. In: *Phys. Rev. B* 63 (2001), p. 174432. DOI: 10.1103/PhysRevB.63.174432.

[99] Z. Fang and K. Terakura. “Magnetic Phase Diagram of Ca[2-x]Sr[x]RuO4 Governed by Structural Distortions”. In: *Phys. Rev. B* 64 (2001), p. 020509. DOI: 10.1103/PhysRevB.64.020509.

[100] Elbio Dagotto. “Complexity in strongly correlated electronic systems”. In: *Science* 309.5732 (2005), pp. 257–262.

[101] CG Fatuzzo et al. “Spin-orbit-induced orbital excitations in Sr 2 RuO 4 and Ca 2 RuO 4: a resonant inelastic x-ray scattering study”. In: *Physical Review B* 91.15 (2015), p. 155104.

[102] L. Das et al. “Spin-Orbital Excitations in Ca_2RuO_4 Revealed by Resonant Inelastic X-Ray Scattering”. In: *Phys. Rev. X* 8 (1 Mar. 2018), p. 011048. DOI: 10.1103/PhysRevX.8.011048. URL: https://link.aps.org/doi/10.1103/PhysRevX.8.011048.

[103] Giniyat Khaliullin. “Excitonic Magnetism in Van Vleck-Type D4 Mott Insulators”. In: *Phys. Rev. Lett.* 111 (2013), p. 197201. DOI: 10.1103/PhysRevLett.111.197201.

[104] Teresa Feldmaier et al. *Excitonic Magnetism at the intersection of Spin-orbit coupling and crystal-field splitting*. 2019. arXiv: 1910.13977 [cond-mat.str-el].

[105] A Jain et al. “Higgs mode and its decay in a two-dimensional antiferromagnet”. In: *Nature Physics* 13.7 (2017), pp. 633–637.

[106] D. Sutter et al. “Hallmarks of Hunds Coupling in the Mott Insulator Ca2RuO4”. In: *Nat. Commun.* 8 (2017), p. 15176. DOI: 10.1038/ncomms15176.

[107] Guoren Zhang and Eva Pavarini. "Mott transition, spin-orbit effects, and magnetism in Ca_2RuO_4". In: *Phys. Rev. B* 95 (7 Feb. 2017), p. 075145. DOI: 10.1103/PhysRevB.95.075145. URL: https://link.aps.org/doi/10.1103/PhysRevB.95.075145.

[108] Stefan Kunkemöller et al. "Highly anisotropic magnon dispersion in Ca 2 RuO 4: evidence for strong spin orbit coupling". In: *Physical Review Letters* 115.24 (2015), p. 247201.

[109] P. Steffens et al. "High-Pressure Diffraction Studies on Ca2RuO4". In: *Phys. Rev. B* 72 (2005), p. 094104. DOI: 10.1103/PhysRevB.72.094104.

[110] Haruka Taniguchi et al. "Anisotropic Uniaxial Pressure Response of the Mott Insulator Ca2RuO4". In: *Phys. Rev. B* 88 (2013), p. 205111. DOI: 10.1103/PhysRevB.88.205111.

[111] X. Wang et al. "Epitaxial Thin Film Growth of Ca2RuO4+δ by Pulsed Laser Deposition". In: *Appl. Phys. Lett.* 85 (2004), p. 6146. DOI: 10.1063/1.1841451.

[112] C. Dietl et al. "Tailoring the Electronic Properties of Ca2RuO4 via Epitaxial Strain". In: *Appl. Phys. Lett.* 112 (2018), p. 031902. DOI: 10.1063/1.5007680.

[113] Sofia-Michaela Souliou et al. "Raman Scattering from Higgs Mode Oscillations in the Two-Dimensional Antiferromagnet Ca2RuO4". In: *Phys. Rev. Lett.* 119 (2017), p. 067201. DOI: 10.1103/PhysRevLett.119.067201.

[114] Fumihiko Nakamura et al. "Electric-Field-Induced Metal Maintained by Current of the Mott Insulator Ca2RuO4". In: *Sci. Rep.* 3 (2013), p. 2536. DOI: 10.1038/srep02536.

[115] H. Gretarsson et al. "Observation of spin-orbit excitations and Hund's multiplets in Ca_2RuO_4". In: *Phys. Rev. B* 100 (4 July 2019), p. 045123.

[116] Olivier Parcollet et al. "TRIQS: A Toolbox for Research on Interacting Quantum Systems". In: *Comput. Phys. Commun.* 196 (2015), pp. 398–415. DOI: 10.1016/j.cpc.2015.04.023.

[117] Antoine Georges, Luca de'Medici, and Jernej Mravlje. "Strong correlations from Hund's coupling". In: (2013).

[118] Luca de'Medici. *Hund's metals, explained*. 2017. arXiv: 1707.03282 [cond-mat.str-el].

[119] Hyeong Jun Lee, Choong H Kim, and Ara Go. "Interplay between spin-orbit coupling and van Hove singularity in the Hund's metallicity of Sr _2 RuO _4". In: *arXiv preprint arXiv:2002.04825* (2020).

[120] S. Riccò et al. "In Situ Strain Tuning of the Metal-Insulator-Transition of Ca2RuO4 in Angle-Resolved Photoemission Experiments". In: *Nat. Commun.* 9 (2018), p. 4535. DOI: 10.1038/s41467-018-06945-0.

[121] Priyanka Seth et al. "TRIQS/CTHYB: A Continuous-Time Quantum Monte Carlo Hybridisation Expansion Solver for Quantum Impurity Problems". In: *Comput. Phys. Commun.* 200 (2016), pp. 274–284. DOI: 10.1016/j.cpc.2015.10.023.

[122] Jungho Kim et al. "Magnetic excitation spectra of Sr2IrO4 probed by resonant inelastic X-ray scattering: establishing links to cuprate superconductors". In: *Physical Review Letters* 108.17 (2012), p. 177003.

[123] D Betto et al. "Three-dimensional dispersion of spin waves measured in NiO by resonant inelastic x-ray scattering". In: *Physical Review B* 96.2 (2017), p. 020409.

[124] G Fabbris et al. "Doping dependence of collective spin and orbital excitations in the spin-1 quantum antiferromagnet La 2- x Sr x NiO 4 observed by X rays". In: *Physical review letters* 118.15 (2017), p. 156402.

[125] G Ghiringhelli et al. "NiO as a test case for high resolution resonant inelastic soft x-ray scattering". In: *Journal of Physics: Condensed Matter* 17.35 (2005), p. 5397.

[126] Atsushi Hariki, Mathias Winder, and Jan Kuneš. "Continuum charge excitations in high-valence transition-metal oxides revealed by resonant inelastic x-ray scattering". In: *Physical review letters* 121.12 (2018), p. 126403.

[127] Cornelius Lanczos. *An iteration method for the solution of the eigenvalue problem of linear differential and integral operators*. United States Governm. Press Office Los Angeles, CA, 1950.

[128] Daniel Bauernfeind et al. "Fork tensor-product states: efficient multiorbital real-time DMFT solver". In: *Physical Review X* 7.3 (2017), p. 031013.

[129] F Alexander Wolf, Ian P McCulloch, and Ulrich Schollwöck. "Solving nonequilibrium dynamical mean-field theory using matrix product states". In: *Physical Review B* 90.23 (2014), p. 235131.

[130] Y. Lu et al. "Efficient real-frequency solver for dynamical mean-field theory". In: *Phys. Rev. B* 90 (8 Aug. 2014), p. 085102. DOI: 10.1103/PhysRevB.90.085102. URL: https://link.aps.org/doi/10.1103/PhysRevB.90.085102.

[131] Y. Lu et al. "Natural-orbital impurity solver and projection approach for Green's functions". In: *Phys. Rev. B* 100 (11 Sept. 2019), p. 115134. DOI: 10.1103/PhysRevB.100.115134. URL: https://link.aps.org/doi/10.1103/PhysRevB.100.115134.

[132] Israel Klich. "Lower entropy bounds and particle number fluctuations in a Fermi sea". In: *Journal of Physics A: Mathematical and General* 39.4 (Jan. 2006), pp. L85–L91. DOI: 10.1088/0305-4470/39/4/l02. URL: https://doi.org/10.1088%2F0305-4470%2F39%2F4%2Fl02.

[133] Ingo Peschel. "Special review: Entanglement in solvable many-particle models". In: *Brazilian Journal of Physics* 42.3-4 (2012), pp. 267–291.

[134] Gerald Knizia and Garnet Kin-Lic Chan. "Density matrix embedding: A simple alternative to dynamical mean-field theory". In: *Physical review letters* 109.18 (2012), p. 186404.

[135] Sebastian Wouters et al. "A practical guide to density matrix embedding theory in quantum chemistry". In: *Journal of chemical theory and computation* 12.6 (2016), pp. 2706–2719.

[136] MW Haverkort et al. "Bands, resonances, edge singularities and excitons in core level spectroscopy investigated within the dynamical mean-field theory". In: *EPL (Europhysics Letters)* 108.5 (2014), p. 57004.

[137] Martin Eckstein. "The frustrated Hubbard model on the Bethe lattice-an investigation using the self-energy functional approach". PhD thesis. Citeseer, 2006.

[138] Jack Sugar. "Potential-Barrier Effects in Photoabsorption. II. Interpretation of Photoabsorption Resonances in Lanthanide Metals at the 4 d-Electron Threshold". In: *Physical Review B* 5.5 (1972), p. 1785.

[139] Masahiko Matsubara et al. "Charge transfer excitation in resonant X-ray emission spectroscopy of NiO". In: *Journal of the Physical Society of Japan* 74.7 (2005), pp. 2052–2060.

[140] S. Kondo et al. "LiV_2O_4: A Heavy Fermion Transition Metal Oxide". In: *Phys. Rev. Lett.* 78 (19 May 1997), pp. 3729–3732. DOI: 10.1103/PhysRevLett.78.3729. URL: https://link.aps.org/doi/10.1103/PhysRevLett.78.3729.

[141] J. Matsuno, A. Fujimori, and L. F. Mattheiss. "Electronic structure of spinel-type LiV_2O_4". In: *Phys. Rev. B* 60 (3 July 1999), pp. 1607–1610. DOI: 10.1103/PhysRevB.60.1607. URL: https://link.aps.org/doi/10.1103/PhysRevB.60.1607.

[142] H Takagi et al. "Transport properties of metallic LiV2O4 single crystals—heavy mass Fermi liquid behavior". In: *Materials Science and Engineering: B* 63.1-2 (1999), pp. 147–150.

[143] C. Urano et al. "LiV_2O_4 Spinel as a Heavy-Mass Fermi Liquid: Anomalous Transport and Role of Geometrical Frustration". In: *Phys. Rev. Lett.* 85 (5 July 2000), pp. 1052–1055. DOI: 10.1103/PhysRevLett.85.1052. URL: https://link.aps.org/doi/10.1103/PhysRevLett.85.1052.

[144] N. Fujiwara, H. Yasuoka, and Y. Ueda. "Anomalous spin fluctuation in vanadium spinel LiV_2O_4 studied by $^7Li - NMR$". In: *Phys. Rev. B* 57 (6 Feb. 1998), pp. 3539–3542. DOI: 10.1103/PhysRevB.57.3539. URL: https://link.aps.org/doi/10.1103/PhysRevB.57.3539.

[145] Yoshitaka Matsushita, J-I Yamaura, and Yutaka Ueda. "Lithium divanadate spinel, LiV2O4". In: *Acta Crystallographica Section E: Structure Reports Online* 61.8 (2005), pp. i137–i139.

[146] V. I. Anisimov et al. "Electronic Structure of the Heavy Fermion Metal LiV_2O_4". In: *Phys. Rev. Lett.* 83 (2 July 1999), pp. 364–367. DOI: 10.1103/PhysRevLett.83.364. URL: https://link.aps.org/doi/10.1103/PhysRevLett.83.364.

[147] V Eyert et al. "Electronic structure and magnetic interactions in LiV_2O_4". In: *Europhysics Letters (EPL)* 46.6 (June 1999), pp. 762–767. DOI: 10.1209/epl/i1999-00330-9. URL: https://doi.org/10.1209%2Fepl%2Fi1999-00330-9.

[148] H. Kusunose, S. Yotsuhashi, and K. Miyake. "Formation of a heavy quasiparticle state in the two-band Hubbard model". In: *Phys. Rev. B* 62 (7 Aug. 2000), pp. 4403–4407. DOI: 10.1103/PhysRevB.62.4403. URL: https://link.aps.org/doi/10.1103/PhysRevB.62.4403.

[149] C Lacroix. "Heavy-fermion behavior of itinerant frustrated systems: β-Mn, Y(Sc)Mn2, and LiV2O4". In: *Canadian Journal of Physics* 79.11-12 (2001), pp. 1469–1473. DOI: 10.1139/p01-112. URL: https://doi.org/10.1139/p01-112.

[150] M. S. Laad, L. Craco, and E. Müller-Hartmann. "Heavy-fermion behavior of the spinel-based transition-metal oxide LiV_2O_4". In: *Phys. Rev. B* 67 (3 Jan. 2003), p. 033105. DOI: 10.1103/PhysRevB.67.033105. URL: https://link.aps.org/doi/10.1103/PhysRevB.67.033105.

[151] S. Burdin, D. R. Grempel, and A. Georges. "Heavy-fermion and spin-liquid behavior in a Kondo lattice with magnetic frustration". In: *Phys. Rev. B*

66 (4 July 2002), p. 045111. DOI: 10.1103/PhysRevB.66.045111. URL: https://link.aps.org/doi/10.1103/PhysRevB.66.045111.

[152] Yasufumi Yamashita and Kazuo Ueda. "Spin-orbital fluctuations and a large mass enhancement in LiV_2O_4". In: *Phys. Rev. B* 67 (19 May 2003), p. 195107. DOI: 10.1103/PhysRevB.67.195107. URL: https://link.aps.org/doi/10.1103/PhysRevB.67.195107.

[153] R Arita et al. "Doped Mott Insulator as the Origin of Heavy-Fermion Behavior in LiV_2O_4". In: *Physical review letters* 98.16 (2007), p. 166402.

[154] Ilja N Bronstein et al. *Taschenbuch der mathematik*. Vol. 1. Springer-Verlag, 2012.

[155] Yi Lu. "From itinerant to localized: an x-ray spectroscopic study of transition metal oxides". In: (2017).

[156] Luuk JP Ament et al. "Resonant inelastic x-ray scattering studies of elementary excitations". In: *Reviews of Modern Physics* 83.2 (2011), p. 705.

[157] Jun John Sakurai. *Advanced quantum mechanics*. Pearson Education India, 1967.

[158] Hendrik A Kramers and Werner Heisenberg. "Über die streuung von strahlung durch atome". In: *Zeitschrift für Physik* 31.1 (1925), pp. 681–708.